Novel Prospects of Image Restoration Inspired by Concepts of Quantum Mechanics

Sayantan Dutta

THÈSE

En vue de l'obtention du

DOCTORAT DE L'UNIVERSITÉ DE TOULOUSE

Délivré par : *l'Université Toulouse 3 Paul Sabatier (UT3 Paul Sabatier)*

Présentée et soutenue le *09/01/2023* **par :**

Sayantan DUTTA

Novel Prospects of Image Restoration Inspired by Concepts of Quantum Mechanics

Nouvelles Approches de Restauration d'Images Inspirées des Concepts de la Mécanique Quantique

JURY

Stephen MCLAUGHLIN	Professeur des Universités	Rapporteur
Pierre BORGNAT	Directeur de Recherche	Rapporteur
Jean-Philippe THIRAN	Professeur des Universités	Président du Jury
Laure BLANC-FÉRAUD	Directrice de Recherche	Examinateur
Adrian BASARAB	Professeur des Universités	Directeur de thèse
Denis KOUAMÉ	Professeur des Universités	Co-directeur de thèse
Bertrand GEORGEOT	Directeur de Recherche	Invité

École doctorale et spécialité :
ED MITT : Informatique et Télécommunications
Unité de Recherche :
IRIT: Institut de Recherche en Informatique de Toulouse - UMR 5505
LPT: Laboratoire de Physique Théorique de Toulouse - UMR 5152
Directeur(s) de Thèse :
Adrian BASARAB, *Bertrand GEORGEOT* et *Denis KOUAMÉ*
Rapporteurs :
Stephen MCLAUGHLIN et *Pierre BORGNAT*

Dedicated to my parents

ACKNOWLEDGEMENTS

Foremost, my deepest gratitude to my supervisors, Prof. Adrian Basarab, Dr. Bertrand Georgeot, and Prof. Denis Kouamé, for their entire guidance and helpful criticism during my PhD studies. Indeed, I would like to thank them for introducing me to the fascinating topic of quantum mechanics-based image processing during my Master 2 internship (2018-19). I sincerely thank them for teaching me this new topic and motivating me to enter the field of research while preparing my Master 2 Thesis under their supervision. Being a student of physics and mathematics, the field of image processing was very new to me at the beginning, but I received continuous encouragement and support from my supervisors throughout the process. I am grateful to them for making this work possible through their rigorous and tireless supervision. Their doors were always open to me, and they nicely clarified any kind of queries I had. They taught me how to write an article and how to think about and figure out some research problems. Their support was not only limited to academics, but also in several administrative works during my stay in France, and I have always been heartily grateful to them. Working closely with my supervisors has been a tremendously enriching experience and I feel very lucky for it.

I would like to graciously thank Prof. Stephen McLaughlin and Dr. Pierre Borgnat for accepting my manuscript to review and giving nice reports with useful remarks. I wish to thank them and Dr. Laure Blanc-Féraud and Prof. Jean-Philippe Thiran for being the Jury members in my defense. Your suggestions brought in threads of thought that made my research so much richer, and my dissertation something I can be proud of having written. Thank you for your feedback and comments that refined my defense.

I am deeply grateful to the EDMITT committee for offering me the PhD grant during 2019-2022 and to the physics department at Université de Tours for selecting me as a Master 2 Research fellow in fundamental physics during 2018-19.

I have had the privilege of working in the IRIT and LPT labs, which I believe are among the best laboratories around. I would like to thank in particular Vanessa Adjeroud,

Malika Bentour, and Mathilde Rasolomalala for their continuous support, and for having the patience to deal with me on several administrative processes.

My heartfelt love and gratitude to Catherine Stasiulis for helping me out with all kinds of administrative work throughout my staying in France. Concerning the préfecture works, she did almost everything for me. I found lovely motherhood inside her and will remember that forever.

I hereby take the opportunity to express my gratitude to all my professors at The University of Burdwan, Visva Bharati University, and Université de Tours and all my teachers during school life, without whom I would not have reached this point. I would like to give special thanks to Prof. Mikhail Volkov, Prof. Xavier Bekaert, Prof. Amaury Mouchet, and Prof. Enrick Olive of Université de Tours; Prof. Amar Prasad Misra, Prof. Madan Mohan Panja, and Dr. Nikhil Pal of Visva Bharati University; Dr. Anandamoy Mukhopadhyay, and Prof. Arijit Ghoshal of The University of Burdwan for teaching several courses in mathematics and physics, and support for numerous aspects throughout my study. I genuinely enjoyed the courses taught by all of them. I would also like to thank Ujjwal sir, Ananda sir, and Anowar da for teaching me the foundation of mathematics during my school and college days.

Of course, the people we work with become very important in our life. I spent more than three years with people who always helped me when they could, with their advice and their time. And an engine turns well when all its gears work properly. I would like to thank Vassili, François, Arthur, Lorena, Kenule, Farah, Mohammad, Oumaima, Janka, Maen, Martin, Miguel, and Gabriele with whom I shared food and good moments. They have been always there, and they helped me a lot with my work and my life; being at the same time colleagues, friends, psychologists, and French teachers. Merci beaucoup!

Afterward, I would like to express my deepest gratitude to all of my Indian friends Uchchhal, Ashraful, Kuntal, Sravani, Nischal, Avisek, Agnideep, Ravi, and Bhupen, whom I met in Toulouse. Your presence around me and kind cooperation in various situations, helped me fix several things and made me feel at ease. I would like to express my warm appreciation and sense of gratitude to all of my friends especially my childhood friends Kuntal, Bireswar, Soumen, Parimal, Amrik, Soujoy, Arun, Anirdom, Tajkera, and Ardhendu for always being there and for your true, unwavering support and love. I thank all of my classmates for their warm company.

I am heartily grateful to Meziane Si Mohammed and his family. He and his family helped me in every way to cope with this new culture in my early days in France. They made me a family member and protected me just like my parents. I will remember

forever those colorful seven months I spent with my second family in Tours.

Further, my deepest gratitude to Kamalika for supporting me throughout my journey. I would like to warmly thank my sweetest sister Sayanita and Brother-in-law Soumik from the bottom of my heart for their support, constant motivation, and unconditional love. Also, deep thanks to my cousin Saptarshi for giving me several suggestions and advising me on many decisions. I am also deeply grateful to my uncles and aunts for their support and love in my life. Now most importantly, my sincere gratefulness and love to my parents and grandparents for always supporting and motivating me with lots of love and compassion. I am and will always be indebted to my parents for their unconditional love, ultimate care, and commitment. I can not imagine being on this stage without their unrelenting, unwavering, and constant support. Words are insufficient to explain their kindness, devotion, and love for my efforts. I am also grateful to have such loving, caring, and supportive family members and relatives. Thank you for accepting me as I am and where I am at this time. Knowing how much I am genuinely loved gives me a great deal of comfort.

A sincere thank you to everyone!!

সায়ন্তন দত্ত

(Sayantan Dutta)

RÉSUMÉ

La décomposition d'images numériques en d'autres bases ou dictionnaires que les domaines temporel ou spatial est une approche très courante et efficace dans le traitement et l'analyse d'images. Une telle décomposition est couramment obtenue à l'aide de transformations fixes (par exemple, Fourier ou ondelettes) ou de dictionnaires appris à partir de bases de données d'exemple ou à partir du signal ou de l'image eux-mêmes. Ces dernières années, avec la croissance de la puissance de calcul, les stratégies exploitant la redondance des patchs extraits d'une ou de plusieurs images pour faciliter leur décomposition parcimonieuse sont devenues très populaire, notamment grâce à leur efficacité à restaurer des images. Un des objectifs de cette thèse est de savoir comment concevoir une telle transformation adaptative à l'aide de principes de la mécanique quantique.

Cette thèse explore de nouvelles approches de construction de telles bases dépendantes de l'image inspirées de la mécanique quantique. Tout d'abord, nous construisons une base dépendante de l'image en utilisant les solutions d'onde de l'équation de Schrödinger. En particulier, en considérant l'image comme un potentiel dans l'équation de Schrödinger discrétisée, nous obtenons les solutions d'onde qui constitue une base et qui joue le rôle de transformée. L'efficacité de la décomposition proposée est illustrée par des résultats de débruitage dans le cas des bruits Gaussiens, de Poisson et de speckle et par comparaison aux algorithmes de l'état de l'art. Cette décomposition adaptative est ensuite généralisée en s'inspirant de la théorie quantique à plusieurs corps. Sur la base de l'analyse par patchs, les mesures de similarité dans un voisinage d'image local sont formalisées par un terme apparenté à l'interaction en mécanique quantique qui peut efficacement préserver les structures locales des images. La nature polyvalente de cette base adaptative étend la portée de son application à des scénarios de bruit indépendants ou dépendants de l'image sans aucun ajustement. Nous effectuons une comparaison rigoureuse avec les méthodes existantes pour démontrer la capacité de débruitage de l'algorithme proposé, quelles que soient les caractéristiques de l'image, les statistiques

de bruit et l'intensité. Nous montrons la capacité de nos approches à traiter des données médicales réelles telles que le débruitage d'images de tomodensitométrie dentaire clinique et les applications de despeckling d'images d'échographie médicale. Nous étendons encore notre travail aux tâches de déconvolution d'image et de super-résolution en exploitant nos algorithmes de debruitage adaptatifs quantiques proposés. En particulier, suite à des développements récents, nous imposons ces débruiteurs externes comme fonction préalable au sein des approches de type Plug-and-Play et Régularisation par Débruitage.

Enfin, nous présentons une architecture de réseau neuronal profond dépliant notre proposition d'algorithme de débruitage adaptatif, reposant sur la théorie de la physique quantique à plusieurs corps. Les ingrédients clés de la méthode proposée sont d'une part, sa capacité à gérer des structures d'image non locales à travers le terme d'interaction patch et l'opérateur Hamiltonien quantique, et, d'autre part, sa flexibilité pour adapter les hyperparamètres aux caractéristiques de chaque patch. De plus, il est démontré qu'avec de très légères modifications, ce réseau peut être amélioré pour résoudre des tâches de restauration d'image plus difficiles telles que le défloutage d'image, la super-résolution et l'inpainting. Malgré une architecture compacte et interprétable (d'un point de vue physique), le réseau d'apprentissage profond proposé améliore plusieurs algorithmes de référence récents de la littérature, conçus spécifiquement pour chaque tâche. Enfin, nous abordons le problème de l'amélioration des image échocardiographiques clinique pour démontrer le potentiel de notre réseau profond dans des applications médicales réelles.

Mots clés: Mécanique quantique, Interaction quantique à plusieurs corps, Transformation adaptative, Équation de Schrödinger, Apprentissage profond, Débruitage quantique, Traitement d'image quantique, Imagerie médicale, Restauration d'images, Imagerie computationnelle.

ABSTRACT

Decomposition of digital images into other basis or dictionaries than time or space domains is a very common and effective approach in image processing and analysis. Such a decomposition is commonly obtained using fixed transformations (*e.g.*, Fourier or wavelet) or dictionaries learned from example databases or from the signal or image itself. In recent years, with the growth of computing power, data-driven strategies exploiting the redundancy within patches extracted from one or several images to increase sparsity have become more prominent. They have demonstrated very promising image restoration results. The question to pursue in this thesis is how to design such an adaptive transformation based on principles of quantum mechanics.

In this thesis, we explore new possibilities of constructing such image-dependent bases inspired by quantum mechanics. First, we construct an image-dependent basis using the wave solutions of the Schrödinger equation, in particular, by considering the image as a potential in the discretized Schrödinger equation. The efficiency of the proposed decomposition is illustrated through denoising results in the case of Gaussian, Poisson, and speckle noises and compared to the state-of-the-art algorithms. We further generalize our proposed adaptive basis by exploiting the data-driven strategy inspired by quantum many-body theory. Based on patch analysis, the similarity measures in a local image neighborhood are formalized through a term akin to interaction in quantum mechanics that can efficiently preserve the local structures of real images. The versatile nature of this adaptive basis extends the scope of its application to image-independent or image-dependent noise scenarios without any adjustment. We carry out a rigorous comparison with contemporary methods to demonstrate the denoising capability of the proposed algorithm regardless of the image characteristics, noise statistics and intensity. We show the ability of our approaches to deal with real-medical data such as clinical dental computed tomography image denoising and medical ultrasound image despeckling applications. We further extend our work to image deconvolution and super-resolution

tasks exploiting our proposed quantum adaptive denoisers. In particular, following recent developments, we impose these external denoisers as a prior functions within the Plug-and-Play and Regularization by Denoising approaches.

Lastly, we present a deep neural network architecture unfolding our proposed baseline adaptive denoising algorithm, relying on the theory of quantum many-body physics. The key ingredients of the proposed method are on one hand, its ability to handle non-local image structures through the patch-interaction term and the quantum-based Hamiltonian operator, and, on the other hand, its flexibility to adapt the hyperparameters patch wisely, due to the training process. Furthermore, it is shown that with very slight modifications, this network can be enhanced to solve more challenging image restoration tasks such as image deblurring, super-resolution and inpainting. Despite a compact and interpretable (from a physical perspective) architecture, the proposed deep learning network outperforms several recent benchmark algorithms from the literature, designed specifically for each task. Finally, we address the problem of clinical cardiac ultrasound image enhancement to demonstrate the potential of our proposed deep unfolded network in real-world medical applications.

Keywords: Quantum Mechanics, Quantum many-body interaction, Adaptive transformation, Schrödinger equation, Deep learning, Deep unfolding, Quantum denoising, Quantum image processing, Medical imaging, Image restoration, Computational imaging.

Table of Contents

List of Tables

Table **Page**

List of Figures

Figure **Page**

List of Algorithms

NOMENCLATURE

Acronyms / Abbreviations

μCT	Mircro Computed Tomography
AD	Anisotropic Diffusion
ADMM	Alternating Direction Method of Multipliers
AT	Anscombe Transform
ATBM3D	Anscombe Transform Block-Matching and 3D Filtering
AWGN	Additive White Gaussian Noise
BCCB	Block Circulant with Circulant Blocks
BD	Bicubic Downsampling
BM3D	Block-Matching and 3D Filtering
BSNR	Blurred Signal-to-Noise Ratio
CBCT	Cone Beam Computed Tomography
CCD	Charge-Coupled Device
CNN	Convolutional Neural Network
CNR	Contrast-to-Noise Ratio

CPU	Central Processing Unit
CT	Computed Tomography
DCT	Discrete Cosine Transform
De-QuIP	Denoising by Quantum Interactive Patches
DIVA	Deep denoising by quantum InteractiVe pAtches
DIVA-A	Deep denoising by quantum InteractiVe pAtches Advanced
DL	Deep Learning
DR	Douglas-Rachford splitting
FB	Forward-Backward splitting
FISTA	Fast Iterative Shrinkage Thresholding Algorithm
FSR	Fast Super-Resolution
GB	Gaussian Blur
GD	Gaussian Downsampling
GPU	Graphics Processing Unit
GSP	Graph Signal Processing
HR	High-Resolution
IPR	Inverse Participation Ratio
IQFT	Inverse Quantum Fourier Transform
LR	Low-Resolution
MAP	Maximum-a-Posteriori
MB	Motion Blur

MLP	Multi Layer Perceptron
MRI	Magnetic Resonance Imaging
MRS	Magnetic Resonance Spectroscopy
MSE	Mean Squared Error
MUST	MATLAB UltraSound Toolbox
NL	Neural Network
NLM	Non-Local Means
NLSS	Non-Local Self-Similarity
OMP	Orthogonal Matching Pursuit
ONN	Operational Neural Networks
P^4IP	Poisson Plug-and-Play Prior Inverse Problems
PCA	Principal Component Analysis
PnP	Plug-and-Play
PSF	Point Spread Function
PSNR	Peak Signal-to-Noise Ratios
QAB	Quantum Adaptive Basis
QFT	Quantum Fourier Transform
QMBI	Quantum Many Body Interaction
QMPI	Quantum Many Patch Interaction
RED	Regularization by Denoising
ReLU	Rectified Linear Unit

RGB	Red, Green and Blue
RL	Resolution Loss
RMSE	Root Mean Square Error
SIMUS	Ultrasound Simulator
SNR	Signal-to-Noise Ratios
SpaRSA	Sparse Reconstruction by Separable Approximation
SR	Super-Resolution
SSIM	Structure Similarity
TNRD	Trainable Nonlinear Reaction Diffusion
TV	Total Variation
TwIST	Two-step Iterative Shrinkage Thresholding
US	Ultrasound
VST	Variance Stabilizing Transformation

Symbols

$\geq$	Greater than or equal
$\gg$	Much greater
$\hbar$	Planck constant
$\leq$	Less than or equal
$\ll$	Much lower
$\mathbb{C}$	Set of complex numbers
$\mathbb{R}$	Set of real numbers
$\mathbb{R}^+$	Set of positive real numbers
$\mathscr{D}$	Denoiser
$\mathscr{P}$	Poissonian process
∇	Gradient operator
ψ	Wave function
E	Energy
H	Hamiltonian operator
P	Probability distribution
V	Potential of a system

List of Publications

Journal Papers

[1] Sayantan Dutta, Adrian Basarab, Bertrand Georgeot, Denis Kouamé, "**DIVA: Deep Unfolded Network from Quantum Interactive Patches for Image Restoration**," *Arxiv Preprint (Submitted)*, pp. 1-18, 2022, DOI: 10.48550/ARXIV.2301.00247.

[2] Sayantan Dutta, Adrian Basarab, Bertrand Georgeot, Denis Kouamé, "**A Novel Image Denoising Algorithm Using Concepts of Quantum Many-Body Theory**", *Signal Processing*, vol 201, pp. 108690(1-13), 2022, DOI: 10.1016/j.sigpro.2022.108690.

[3] Sayantan Dutta, Adrian Basarab, Bertrand Georgeot, and Denis Kouamé, "**Plug-and-Play Quantum Adaptive Denoiser for Deconvolving Poisson Noisy Images**", *IEEE Access*, vol. 9, pp. 139771-139791, 2021, DOI: 10.1109/ACCESS.2021.3118608.

[4] Sayantan Dutta, Adrian Basarab, Bertrand Georgeot, and Denis Kouamé, " **Quantum Mechanics-Based Signal and Image Representation: Application to Denoising**", *IEEE Open Journal of Signal Processing*, vol. 2, pp. 190-206, 2021, DOI: 10.1109/OJSP.2021.3067507.

Conference Papers

[1] Sayantan Dutta, Adrian Basarab, Bertrand Georgeot, Denis Kouamé, **"Deep Unfolding of Image Denoising by Quantum Interactive Patches"**, in *Proceedings 2022 29th of the IEEE International Conference on Image Processing (ICIP)*, pp. 491-495, 2022, DOI: 10.1109/ICIP46576.2022.9897959.

[2] Sayantan Dutta, Bertrand Georgeot, Denis Kouamé, Damien Garcia, Adrian Basarab, "**Adaptive Contrast Enhancement of Cardiac Ultrasound Images using a Deep Unfolded Many-Body Quantum Algorithm**", in *Proceedings 2022 of the IEEE International Ultrasonics Symposium (IUS)*, pp. 1-4, 2022, DOI: 10.1109/IUS54386.2022.9958691.

[3] Sayantan Dutta, Nwigbo Kenule Tuador, Jérôme Michetti, Bertrand Georgeot, Duong Hung Pham, Adrian Basarab, Denis Kouamé, "**Quantum Denoising-Based Super-Resolution Algorithm Applied to Dental Tomography Images**", in *Proceedings 2022 19th of the IEEE International Symposium on Biomedical Imaging (ISBI)*, pp. 1-4, 2022, DOI: 10.1109/ISBI52829.2022.9761623.

[4] Sayantan Dutta, Adrian Basarab, Bertrand Georgeot, Denis Kouamé, "**Image Denoising Inspired by Quantum Many-Body Physics**", in *Proceedings 2021 28th of the IEEE International Conference on Image Processing (ICIP)*, pp. 1619-1623, 2021, DOI: 10.1109/ICIP42928.2021.9506794.

[5] Sayantan Dutta, Adrian Basarab, Bertrand Georgeot, Denis Kouamé, "**Poisson Image Deconvolution by a Plug-and-Play Quantum Denoising Scheme**", in *Proceedings 2021 29th of the European Signal Processing Conference (EUSIPCO)*, pp. 646-650, 2021, DOI: 10.23919/EUSIPCO54536.2021.9616253.

[6] Sayantan Dutta, Adrian Basarab, Bertrand Georgeot, Denis Kouamé, "**Despeckling Ultrasound Images Using Quantum Many-Body Physics**", in *Proceedings 2021 of the IEEE International Ultrasonics Symposium (IUS)*, pp. 1-4, 2021, DOI: 10.1109/IUS52206.2021.9593778.

CHAPTER 1

INTRODUCTION

Contents

Overview

This chapter introduces, in broad strokes, the framework of inverse problems for imaging applications, in particular, the image restoration problems and the motivation for the explorations of quantum mechanics-based algorithms for solving such tasks. The outline and contribution of this thesis are summarized at the end of this chapter.

1.1 Digital Image

From the perspective of photography history, the development of digital imaging is relatively recent. It originated in the nineteen-fifties with the digitization of newspapers and was accelerated in the nineteen-seventies with the development of the first charge-coupled device (CCD) sensor. Since then devices have continued to improve and have reached very high resolution. In this chapter, we first recall how the CCD sensor works to produce a digital image before identifying the sources of error during the acquisition process.

1.1.1 What is a Digital Image?

The process of digital imaging begins with an optical device. The light rays reflected from the object pass through a series of lenses and are projected onto the CCD sensor. This CCD sensor processes these light rays and converts the light information into electrical information. To do so, the sensor is composed of an array of capacitors that accumulate electric charge proportionally to the light intensity. Next, the charge is converted into a voltage which is converted into digital data for storage. Fig. 1.1 portrays the process of digital image generation. Note that the CCD sensor is solely sensitive to light intensity, captures only that information and provides a grayscale image after acquisition (*i.e.*, sampling and quantization). To produce digital color image, a bare filter is usually placed over the CCD sensor.

This process of acquiring raw digital data often gets affected by various physical phe-

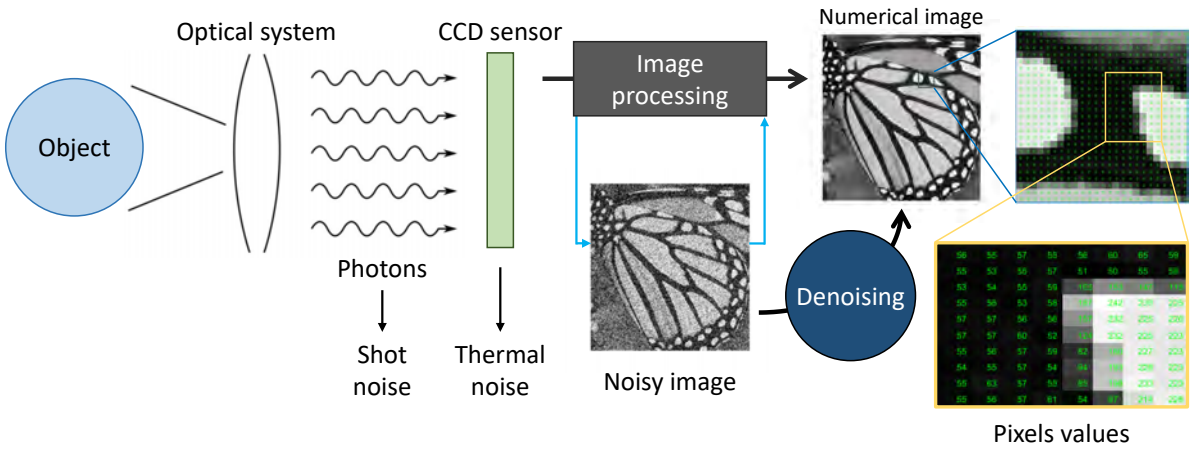

FIGURE 1.1. The process of creating a digital image.

nomena in its surroundings and requires several restoration operations before obtaining the final output image. Other physical circumstances and sensors in different imaging modalities (*e.g.*, tomography and ultrasound imaging that used in this thesis) can exhibit such situations. This process of restoration operations, called digital image restoration, is briefly introduced in the following.

1.2 Digital Image Restoration

Digital images have become omnipresent in our modern age of computers. Their applications are not only limited to photography to capture our life's most memorable moments, but have become an integral part of modern medical science, astronomy, geological science, engineering, and other fields. In a wide range of real world applications, one does not have direct access to the true image of interest but only to its distorted version. These distortions often appear from various unavoidable physical phenomena in hands-on implementation. They may depend on the acquisition process, the physical laws of the phenomenon studied, the devices or sensors used for acquisition, and the mode of communication. In science and engineering, the forward problem is a process of finding observations from the original data, while deriving the original data from the observations is called the inverse problem. The restoration of the original image from a distorted observation is one of the most fundamental tasks in inverse problems. There is a wide range of real-life problems within the range of image restoration, such as image denoising where the observed image is contaminated by random noise, image deblurring where the observed image is blurry caused by motions or optics, image super-resolution (SR) where the spatial resolution of a low-resolution (LR) observed image is improved to obtain a high-resolution (HR) output, image impainting where parts of the observed image are removed or corrupted, etc. For all these imaging applications, recovery of the original latent image from the observed one is the primary objective. Over the past few decades, image restoration techniques have been extensively studied, yet remain an active field of research. In this thesis, the objective is to tackle such imaging problems from a different perspective, specifically using tools inspired by quantum theory.

1.3 Motivation for Quantum Mechanics-Based Algorithms

After the digital revolution, the future might be an age of quantum computers. Quantum computers allow conducting an operation efficiently with enormous parallelism. Furthermore, the exploitation of a logarithmic number of qubits by quantum computation may effectively improve computational efficiency against a classical computer where exponentially more bits are needed. Despite all these advantages, the quantum computer is still far from real-life implementation and only small-scale versions are available. However, the concepts and principles of quantum theory can be used as tools to design algorithms for classical computers. The implementation of such quantum principles can significantly boost the performance of algorithms. Thus, exploiting the concepts of quantum physics, these algorithms may enable to deal with real-life problems such as medical imaging, remote sensing, low-level vision, surveillance, astronomy, geology, etc, much better than the traditional methods.

The objective of this thesis is to explore quantum mechanics-based approaches in the field of image processing and analysis, particularly for image restoration problems, and implement these schemes in real applications.

1.4 Outline of the Thesis

As stated earlier, this thesis aims to design new approaches for image restoration problems inspired by the concepts of quantum physics. The forthcoming chapters are organized as follows:

* **Chapter 2:** This chapter reminds the basic postulates of quantum mechanics. The differences between classical and quantum theory are discussed. In addition, those properties of the wave solutions of the time-independent Schrödinger equation are presented. This quantum picture is illustrated with the very simple example of a particle in a box. Furthermore, we discuss the behavior of these wave functions in the presence of random potentials. Specifically we study the quantum localization of these wave functions under a random potential. Finally, we introduce the concept of quantum interactions in the presence of more than one quantum particle in a system, *i.e.*, a quantum many-body systems.

* **Chapter 3:** In this chapter, we briefly introduce various image restoration problems with a discussion of the existing state-of-the-art methods for solving such imaging tasks using model-based, learning-based, and model-based learning approaches. In addition, the development of quantum mechanics-based imaging algorithms over the past few decades is summarized here.

* **Chapter 4:** Decomposition of digital signals and images into other basis or dictionaries than time or space domains is a very common approach in signal and image processing and analysis. Such a decomposition is commonly obtained using fixed transforms (e.g., Fourier or wavelet) or dictionaries learned from example databases or from the signal or image itself. In this chapter, we propose a new way of generating an adaptive basis from the signal or image itself by exploiting principles of quantum mechanics. In particular the wave solutions of the Schrödinger equation give the adaptive transforms and are used to construct an adaptive basis suitable for signal and image representation applications, where the signal or image acts as the potential of the quantum system. This adaptive basis will be used for signal or image decomposition. To illustrate the potential of the proposed decomposition, we study the signal or image denoising problem.

* **Chapter 5:** This chapter addresses the Poisson image deconvolution problem, a common problem that occurs in several imaging applications, such as limited photon acquisition, X-ray computed tomography or positron emission tomography. A new Plug-and-Play (PnP) alternating direction method of multipliers (ADMM) scheme is introduced based on the adaptive denoiser proposed in Chapter 4 using the Schrödinger equation's solutions of quantum physics. The adaptative nature of this denoiser makes it highly efficient at selectively eliminating noise from higher intensity pixels, without relying on any statistical assumption about the noise, which makes the proposed method capable of handling the Poisson deconvolution task.

* **Chapter 6:** In the context of image decomposition, data-driven dictionaries and, in particular, exploiting the redundancy between patches extracted from one or more images, allowed important improvements. This chapter proposes an original idea of constructing such an image-dependent basis inspired by the principles of quantum many-body physics. The similarity between two image patches is introduced in the formalism through a term akin to interaction terms in quantum mechanics.

The potential of the proposed adaptive decomposition is illustrated through image denoising in presence of image-independent and image-dependent noise scenarios.

* **Chapter 7:** This chapter introduces a blueprint of a new deep network unfolding a baseline quantum mechanics-based adaptive denoising scheme (De-QuIP), proposed in Chapter 6. Furthermore, it is shown that with very slight modifications, this network can be enhanced to solve more challenging image restoration tasks such as image deblurring, SR and inpainting. The proposed deep network embeds both quantum interactions and other quantum concepts, mainly the Hamiltonian operator, which enables the network to predict the possible stationary solutions of the Schrödinger equation by harnessing the power of the convolutional layers during the training process.

* **Chapter 8:** The final conclusions of this thesis and as well as possible directions for future work on these topics are summarized in this chapter.

1.5 Main Contributions

The primary objective of this thesis is to propose new tools and algorithms for image restoration problems integrating or inspired by the concepts and principles of quantum physics. The main contributions of this thesis are as follows.

* **Chapter 4:** The main scope of this chapter is to show how tools from quantum mechanics, in particular the Schrödinger equation, can be used to construct an adaptive transform suitable for signal and image processing applications. The proposed framework reposes on the discrete version of the time-independent Schrödinger equation for a quantum particle in a potential. In our case, the potential is represented by the signal samples or the pixel values. We use a basis of wave functions, *i.e.*, stationary solutions of the Schrödinger equation, directly computed from the signal or image itself, as adaptive basis for signal or image decomposition. A detailed description of the behavior of the wave functions and the proposed adaptive basis with respect to the choice of the hyperparameters is provided, allowing to gain insight about the practical consequences in signal and image processing of the quantum mechanical principles involved. Furthermore, the proposed transform embedded in a denoising algorithm shows promising results in different noise scenarios, such as additive, multiplicative, signal/image dependent and independent noise models. Finally a comprehensive comparison is reported in the case of

Gaussian, Poisson, and speckle noise against several state of-the-art methods from the literature.

* **Chapter 5:** The main novelty of this chapter is to propose an original Poisson image deconvolution scheme using the concepts of quantum mechanics. The primary contributions are the construction of a computationally advanced quantum denoiser compared to Chapter 4, its integration into a PnP-ADMM scheme, and the experimental proof of convergence of the final algorithm. The efficiency of the proposed method regardless of the assumption of Gaussian noise represents the main motivation of its interest in Poisson deconvolution PnP-ADMM algorithms. This performance gain regardless of the amount of noise affecting the observations is explained by the flexibility of the embedded quantum denoiser constructed without assuming any prior statistics about the noise, which is one of the major advantages of this method. Generally, in the literature, while dealing with a Poisson deconvolution task using a PnP scheme, a variance stabilizing transformation (VST) is often used to approximately Gaussianize the Poisson data, although the convolution operation is not invariant under such transformation. The proposed algorithm discards the need for a VST due to its adaptive architecture, a clear advantage of this proposed scheme. Finally, detailed quantitative and qualitative analyses of the proposed scheme have been conducted compared to recent state-of-the-art techniques, for both benchmark and real-life fluorescence microscopy images.

* **Chapter 6:** The main contribution of this chapter is to translate concepts of quantum many-body theory to imaging problems. Interactions in quantum physics correspond to two or more quantum particles present in the system that can influence each other's quantum state. From an image processing perspective, we propose to adapt this theory to extend the idea of interaction between image patches. More precisely, the proposed framework consists in placing a quantum particle in every image-patch, *i.e.*, every image-patch acts like a single particle system, and the whole collection of patches, that is the entire image, behaves like a many-body system where interactions describe local similarities in the neighbouring patches. This chapter includes the characterization of the hyperparameters and their respective effects on the denoising performance, together with automated rules of selecting their values close to the optimal one in experimental setups with ground truth not available, explorations of the denoising possibilities beyond Gaussian statistics without any modification, and a rigorous comparison with contemporary methods

to demonstrate the denoising capability of the proposed algorithm regardless of the image characteristics, noise statistics and intensity. Finally, the chapter highlights the capabilities of the proposed approach to deal with practical image denoising problems such as medical ultrasound (US) image despeckling applications. Furthermore, we address the super-resolution (SR) problem exploiting our proposed quantum adaptive denoiser. In particular, following recent developments, we impose this external denoiser as a prior function within the Plug-and-Play (PnP) and Regularization by Denoising (RED) approaches. Medical Dental computed tomography (CT) images are used to illustrate the potential of the proposed algorithms for high-resolution (HR) image retrieval.

* **Chapter 7:** Designing a deep network architecture unfolding a baseline quantum algorithm called DIVA, relying on the theory of quantum many-body physics, is the main contribution of this chapter. The key ingredients of the proposed method are on one hand, its ability to handle non-local image structures through the patch-interaction term and the quantum-based Hamiltonian operator, and, on the other hand, its flexibility to adapt the hyperparameters patch-wisely, due to the training process. Thus, recasting the De-QuIP algorithm in the framework of a deep learning network while preserving the essence of the baseline structure significantly enhances the adaptability of the model to various challenging image restoration tasks such as image denoising, deblurring, SR and inpainting. In general, the model-based approaches are fairly successful in tackling a variety of image recovery tasks, including proper interpretation of their roles, however, require costlier manual computation process. Deep network structures are in most cases determined empirically, which makes them suffer from a lack of interpretation of their true functionality. Despite a compact and interpretable (from a physical perspective) architecture, the proposed deep learning network outperforms several recent algorithms from the literature, designed specifically for each task. Finally, we show the ability of our approach to deal with clinical cardiac ultrasound image enhancement applications.

CHAPTER 2

Basics of Quantum Mechanics

Contents

Overview

This chapter presents the basic postulates of classical and quantum mechanics. In addition, the concepts of wave-particle duality, matter waves and wave solutions of the time-independent Schrödinger equation are illustrated. We discuss the particle in a box problem in quantum mechanics. Furthermore, we present the behavior of these wave solutions in a random potential. Finally, we recall the notion of a quantum many-body system, where quantum interactions take place in the presence of more than one quantum particles.

2.1 Introduction

Unlike Newtonian mechanics, or Maxwell's electrodynamics, or Einstein's relativity, quantum mechanics was not invented by one individual. Resorting to new ideas, which were radically opposite from classical ideas, to explain some experimental results in the last quarter of the nineteenth century called forth a wholly new and radically counter-intuitive way of thinking about the world. This led to the introduction of quantum mechanics. The physical theory of quantum mechanics was born by the efforts of many scholars, such as Born, Dirac, Jordan, Pauli, Schrödinger, Heisenberg and many more. A series of ad hoc moves by Planck, Bohr, Ehrenfest and many others, now called old quantum theory, to explain some phenomena indicated the need of formulating a new mechanics for microscopic particles, which was subsequently synthesized by Schrödinger, Heisenberg, Dirac and others. Their formulations were physico-mathematical in their own right. Later on, in the middle and second half of the twentieth century, Dirac, Feynman, Schrödinger, Kramers, Bethe, Tomonaga, and many others, made major advancements in the theory that combined classical field theory, special relativity, and quantum mechanics. This modified generalized theory, known as quantum field theory, is the basis of our current understanding of physical particles at the subatomic level, and is the foundation of the *Standard Model* of elementary particles. Nevertheless, a rigorous mathematical formulation was needed in order to reveal full ramification of the quantum revolution. This task was first taken by Hilbert and Neumann during 1926-1927 [166, 358, 359]. Not only did they give a firm mathematical foudation but also introduced the sharp separation between the mathematical formalism - what Hilbert called "der analytische Apparat", the analytical apparatus - and its physical interpretation [166].

2.2 Classical Mechanics

Classical mechanics, narrowly defined, is the study of the motion of systems of particles in Euclidean three-dimensional space, under the influence of specific force laws, the evolution of motion being determined by Newton's second law, a second-order differential equation. That is, given the physical forces at certain times and certain boundary conditions on the positions of the particles at some particular times, the problem is to determine the trajectories of all the particles at all times. Newton's formalism of classical mechanics, together with the investigation of appropriate force laws, provided the basic framework of physics from Newton's time, until the beginning of the last century.

In the eighteenth and nineteenth century, the scope of classical mechanics expanded from Newton's laws to the development of Lagrangian and Hamiltonian formulations of mechanics.

Classical mechanics has a deterministic property, that is, it is possible to determine or measure the position and momentum of a classical particle at any time under a given force and initial conditions. For a system, the positions $\vec{q}$ and momenta $\vec{p}$ provide a complete picture of the trajectories of the classical particles of the system. The space consisting of all such possible values of positions and momenta for the system at all instants is known as phase space. The Hamiltonian formulation of mechanics is the natural description for working in phase space. In general the Hamiltonian $H(\vec{q},\vec{p})$, a function of $\vec{q}$ and $\vec{p}$, is just the sum of the kinetic and potential energies, or the total energy of a system, and the physical motion obeys Hamilton's equations of motion,

$$\dot{\vec{q}} = \frac{\partial H}{\partial \vec{p}}, \qquad \dot{\vec{p}} = -\frac{\partial H}{\partial \vec{q}}, \tag{2.1}$$

where $\dot{\vec{q}}$ and $\dot{\vec{p}}$ represent the time derivatives of $\vec{q}$ and $\vec{p}$, respectively. The kinetic energy is $T = \frac{1}{2}m\dot{\vec{q}}^2$, where m is the mass and given that $\vec{p} = m\dot{\vec{q}}$, so $T = \frac{1}{2m}\vec{p}^2$ is a function of $\vec{p}$. The potential V only depends on the position $\vec{q}$. In general, Hamiltonian H = kinetic energy T + potential energy V, or, $H = \frac{1}{2m}\vec{p}^2 + V(\vec{q})$.

The Hamilton equations (2.1) are generalization of the Newton equation of motion to arbitrary configuration-space coordinate frames. By solving these first-order differential equations with some initial conditions, one can accurately determine the properties (*i.e.*, position and momentum) of classical particles at any instant of time [148, 275].

Starting from Hamilton's equations, it is very easy to derive the Newton equation. Indeed, Hamiltonian H = kinetic energy T + potential energy V, with the kinetic energy $T = \frac{1}{2}m\dot{\vec{q}}^2$, and $\dot{\vec{q}}$ is the velocity of the particle and V is a function of $\vec{q}$ only. Now in Hamiltonian formulation, momentum $\vec{p} = m\dot{\vec{q}}$. Hence, the second equation of the Hamilton's equations of motion (2.1) gives, $m\ddot{\vec{q}} = -\frac{\partial V}{\partial \vec{q}}$, where $\ddot{\vec{q}}$ is the acceleration. Note that, $-\frac{\partial V}{\partial \vec{q}} = F$ is the force acting on the particle. Therefore, one has $m\ddot{\vec{q}} = F$, which is exactly Newton's second law of motion [306].

Following the above discussions, it is clear that in classical mechanics, the position and momentum of a classical particle can be determined precisely, starting from Newton's or Hamilton's equations of motion. Fig. 2.1 illustrates this concept through a pictorial diagram. Suppose a classical particle is moving under a potential V with an energy E in the Euclidean space. At point q_3, the potential energy is higher than the particle's

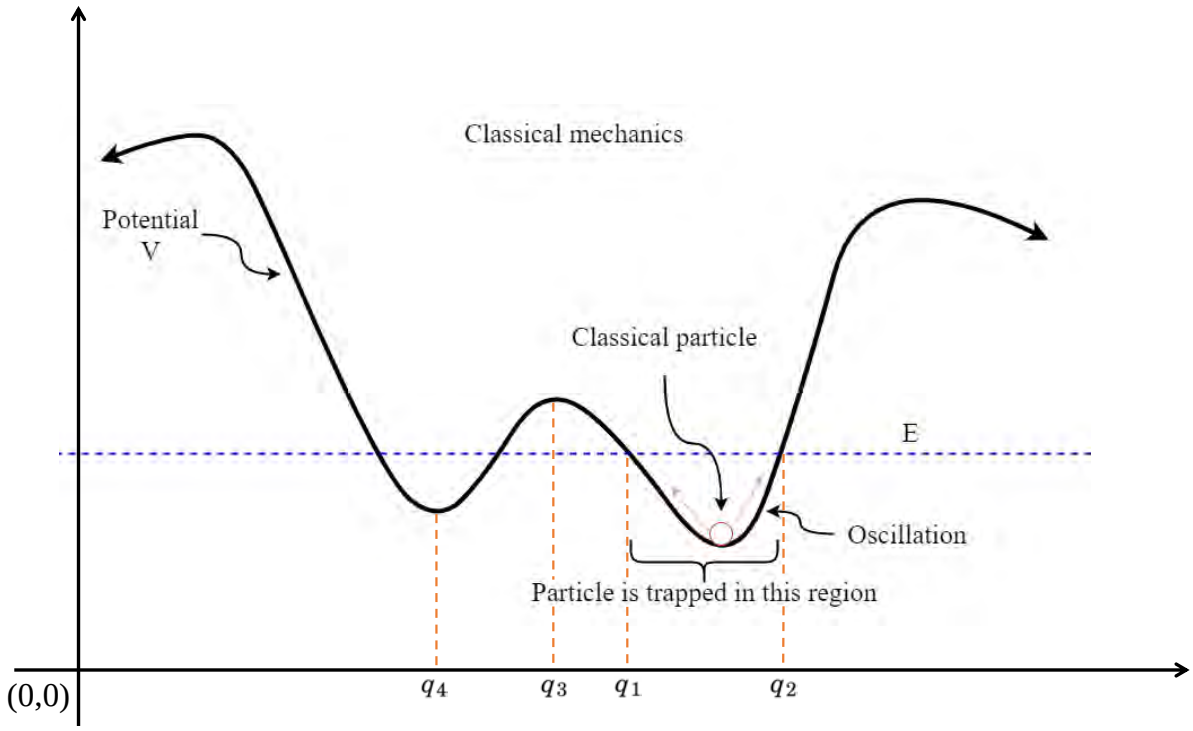

FIGURE 2.1. Motion of a classical particle with an energy E under a potential V. The blue dashed line represents the energy of the classical particle.

energy. Thus this potential energy acts as a potential barrier for the particle and limits its motion. With the given energy E, the classical particle will never cross the potential barrier and reach the point q_4. Indeed, the particle is trapped between the points q_1 and q_2, and remains so while oscillating forever if there is no damping force (*e.g.*, friction) acting on the particle.

2.3 Quantum Mechanics

Until the end of the nineteenth century, the laws of classical mechanics were found to be sufficient to explain the physical phenomena studied up to that time. The universe was conceived as containing matter consisting of particles and radiation (waves). The motions of material bodies were described using the laws of Newtonian mechanics, while the theory of electromagnetism was used to describe radiation. Interactions between radiation and matter were well explained by the Maxwell's equations. This set of laws

was considered satisfactory to explain the experimental data at that time. In this context, it is to be mentioned that by a particle one means a point endowed with some mass. So particles are localized bundles of energy and momentum. At each instant of time a particle has a definite position in space and it follows a trajectory, when it moves from one point to another. A wave, in contrast, is a disturbance spread over the space. It is described by a function which characterizes the disturbance at a point at a particular time t. Diffraction and interference are two properties of a wave, which are not exhibited by particles described by classical mechanics.

2.3.1 Wave-Particle Duality

Newton considered light to be a beam of particles which can bounce back upon reflection from a mirror. But such a concept could not explain the interference effect of light. During the first half of the nineteenth century, interference and diffraction effects of light were successfully explained considering light as a wave. Later on, it was found that visible lights are particular forms of electromagnetic radiation which move in vacuum with a speed of 3×10^8 m/sec. Electromagnetic theory formulated by Maxwell was successful in explaining electromagnetic radiation.

However, it was not possible to explain experimental observations of black body radiation using electromagnetic theory. In order to explain the observed data of black body radiation, Planck had to assume that an electromagnetic radiation of frequency ν could have energies which are only integral multiple of $h\nu$, where h is a constant known as Planck's constant ($h = 6.55 \times 10^{-34}$ Joule-sec). Thus, following Planck, electromagnetic radiation of frequency ν can be considered as consisting of stream of particles or corpuscles each of energy $h\nu$. These particles which can be localized in space are known as photons. Making use of the concept of photons, Einstein was able to explain the characteristics of the photoelectric effect quite successfully. Later on, the corpuscular character of electromagnetic radiation was confirmed by Compton while explaining the scattering of X-ray by a stationary electron.

From the above discussion, we can arrive at the following conclusion. The interaction between radiation and matter takes place by means of an elementary process in which radiation appears to be composed of particles, called photons. We have thus returned to the particle conception of light, though this conception is very much different from that considered by Newton. Reconciliation with the corpuscular nature of radiation leads to a natural question - should we give up the wave theory? The answer is no. Because, we know that interference and diffraction phenomena can not be explained in a purely

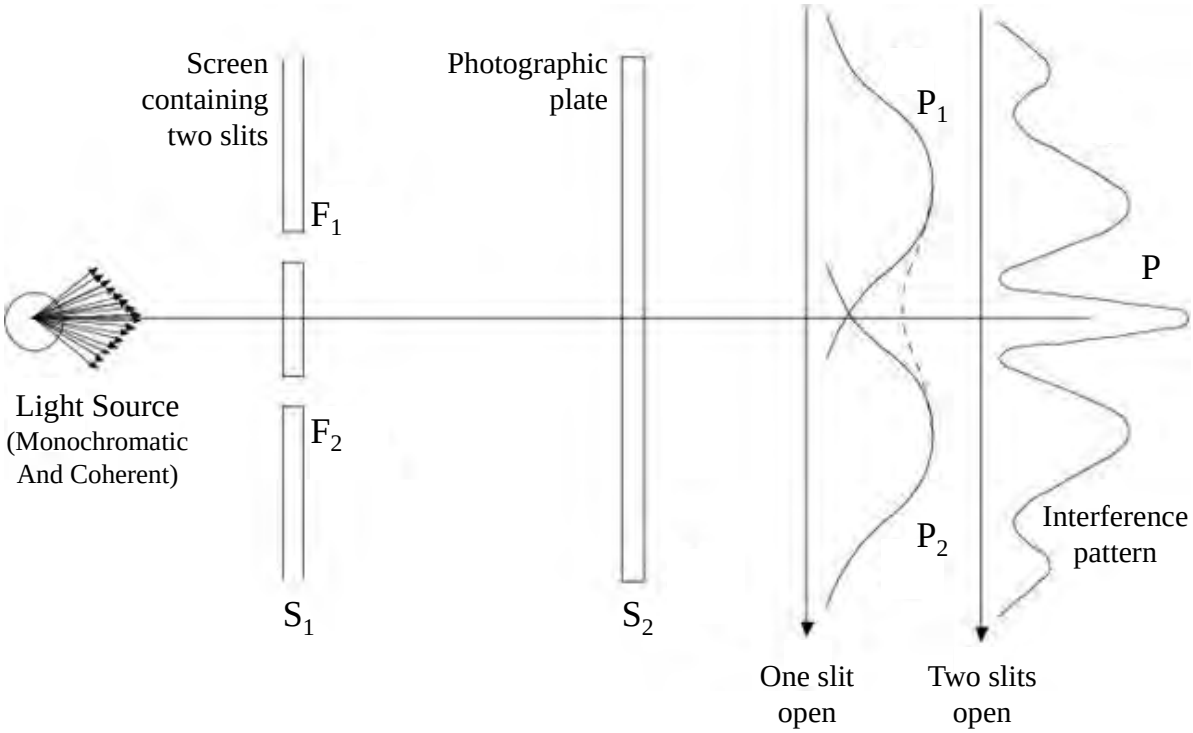

FIGURE 2.2. Pictorial illustration of the double slit experiment. A monochromatic coherent light source emits photons that pass through a two-slit screen and are detected on a photographic plate placed behind the screen. The sum $P_1 + P_2$ of the intensities P_1, when slit F_2 is closed, and P_2 when slit F_1 is closed, is not equal to the intensity P measured when both slits are open.

particle framework. As a matter of fact, a complete interpretation of the phenomena concerning radiation can only be made by assuming both particle and wave aspects of radiation. So we face a paradox, because the concepts of wave and particle are mutually exclusive. This is particularly visible in the double slit experiment.

2.3.1.1 Double Slit Experiment with Single Photons

In the basic version of the experiment, a monochromatic coherent light source (for example, a laser beam) illuminates a screen S_1 containing two slits F_1 and F_2. At some distance beyond this screen a second screen S_2 is placed, incorporating detectors (for example, a photographic plate) which can detect the light that falls on a given point [144, 306].

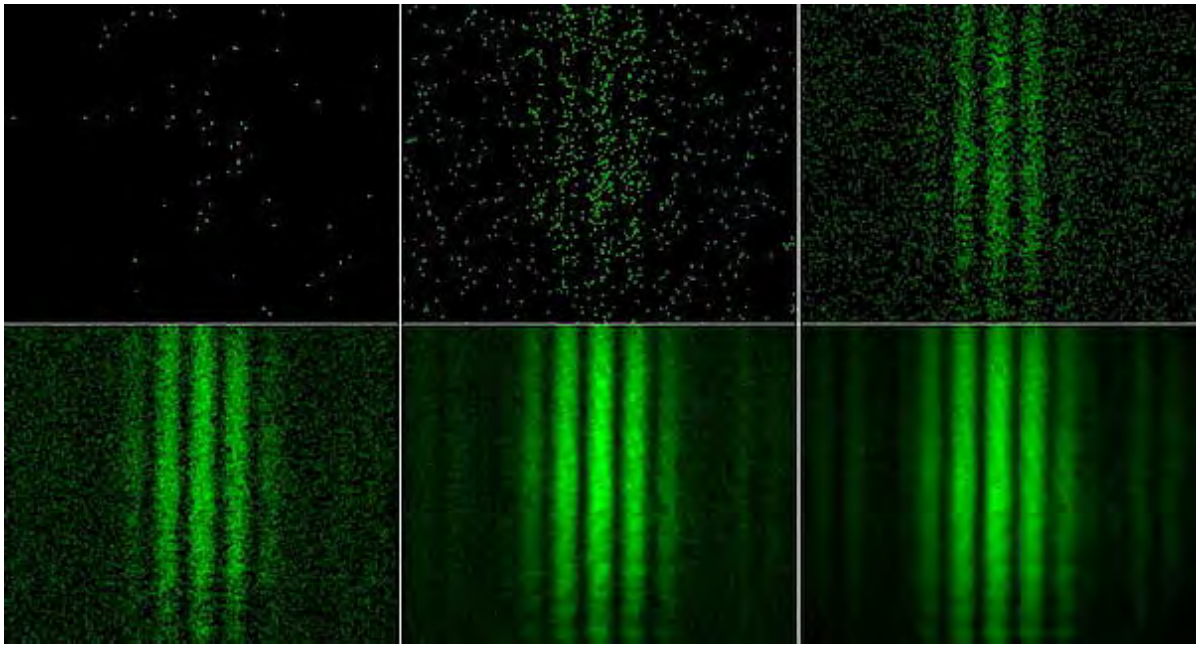

FIGURE 2.3. Double slit experiment with single photons. The top left image is the result after a short exposure time, after around 100 photons have landed on the detector. Each dot of light represents one photon, which behaves as a particle here. With increasing exposure time – top middle and top right, and again from bottom left to bottom right – it becomes clear that the photons are landing at random positions but with a wave-like distribution of probability and generates interference pattern [373].

We observe that with the slits open one at a time, we get a classical distribution, and with both slits open, we get the interference pattern as in Fig. 2.2. Let us now consider the case when both slits are open. At first sight one might think that the interference pattern develops due to the interactions of photons passing through the slits F_1 and F_2. But it is not the case. Because, if the intensity of the source is diminished until the photons strike the screen one by one so that there is no possibility of interaction between the photons, the interference pattern is still found to be developed after a long time (that is, after a large number of photons is recorded). Therefore, purely corpuscular interpretation must be rejected.

Let us now try to explain the results on the basis of wave picture. According to the wave picture, light intensity at a point on the screen S_2 is proportional to the square of the amplitude of the wave at this point. If we consider the case "when the source emits

photons one by one" and analyse the screen S_2 after it has received a few photons, we then observe that each photon produces a localized impact on S_2 (see top left image in Fig.2.3) and not a very weak interference pattern. Therefore, the purely wave interpretation must also be rejected. In reality, the individual impacts of photons on the screen S_2 are distributed in a random manner, and only when a large number of photons has reached the screen S_2, the distribution of the impacts begins to have a continuous aspect or interference fringes (see bottom right image in Fig.2.3).

The top left image in Fig.2.3 is the result after a short exposure time, after around 100 photons have landed on the detector. Each dot of light represents one photon, which behaves as a particle here: it hits exactly one position – one detector pixel. If the wave property would dominate, each photon would be distributed over the whole detector surface, just as a sea wave does not hit the beach at one point only but over the whole length of the beach. With increasing exposure time – in Fig.2.3 top middle and top right, and again from bottom left to bottom right – it becomes clear that the photons are landing at random positions but with a wave-like distribution of probability. A long exposure time with a high number of detected photons leads to the interference pattern which we know from a normal monochromatic light source at the double slit.

It is thus clear that interference pattern is the result of the impacts of a large number of photons. Let us now try to determine through which slit each photon passed before it reached the screen S_2. In order to do this we have to place detectors behind the slit F_1 and F_2. It is then observed that, if the photons arrive one by one, each one passes through a well-determined slit (F_1 or F_2, but not both). But obviously photons, recorded in this way, are absorbed and do not reach the screen. Removing detectors from one of the slit, say from F_2, tells us that about half of the photons emitted from the source pass through the slit F_2. But in this case, no interference pattern is developed, since slit F_1 is blocked. We only obtain a classical distribution of F_2. The content of this paragraph can be summarised by concluding that it is impossible to observe the interference pattern and to know at the same time through which slit each photon has passed. The analysis of the double-slit experiment thus shows that it is not possible to explain all the observed phenomena if only one of the two aspects of light, wave or particle, is considered. Classically, these two aspects are mutually exclusive. We are thus led to the conclusion that this classical idea, although our everyday experience tells us to consider this well-founded, is not valid in the microscopic domain.

2.3.2 Matter Waves

One of the greatest challenges of the nineteenth century was to explain the atomic spectra. It is found that atomic spectra are composed of narrow lines which indicate that a given atom can emit or absorb only photons having well-determined frequencies or energies. Classical mechanics is totally unable to explain this fact.

In 1923, de Broglie put forward a hypothesis which unifies particle and wave. He postulated that material particles, just like photons, can have wavelike aspect. These are called matter waves. What is true for photons should be valid for any type of particle. More specifically, de Broglie conjectured, in analogy with photons, that particles of momentum p will produce an interference pattern corresponding to a wave number $k = p/\hbar$ (where, $\hbar = h/2\pi$) in the double-slit experiment. We therefore associate with a material particle having energy E and momentum p, a wave whose angular frequency ω and wave vector k are given by the same relations as for photons:

$$E = \hbar\omega, \quad \text{and} \quad p = \hbar k. \tag{2.2}$$

This prediction was verified for electrons by Davisson and Germer, shortly thereafter. It is now widely accepted that all particles are described by probability amplitudes ψ, and that the assumption that they move in definite trajectories is ruled out by experiment. But what about common sense, which says that billiard balls and baseballs travel along definite trajectories? How did classical mechanics survive for three centuries? The answer is that the wave nature of matter is not apparent for macroscopic phenomena since $\hbar$ is so small [306].

2.3.3 Wave Functions and Quantum Description of Particle

From the analysis of the double-slit experiment we have learnt that the concept of trajectory of a particle does not make sense at the microscopic scale. In order to describe the motion of a microscopic particle, such as an electron, quantum mechanics introduced the concept that the probability of finding the particle at a given location is proportional to the square of the modulus of the wave function $\psi(z,t)$ which characterizes the state of the particle, z being a spatial coordinate. Thus the probability of finding the particle within the volume element dz about the point z at time t is

$$P(z,t)dz = |\psi(z,t)|^2 dz, \tag{2.3}$$

so that $P(z,t) = |\psi(z,t)|^2$ is the probability density. We thus see that the wave function associated with a particle determines its space-time behaviour which is statistical in

nature. Since the probability of finding the particle somewhere in the space must be unity, we deduce that

$$\int |\psi(z)|^2 \mathrm{dz} = 1, \tag{2.4}$$

So the wave functions are square-integrable functions.

As we have seen in the previous sections, in order to account for the interference effects, it must be possible to superpose wave functions. This means that if ψ_1 and ψ_2 are two possible states of a particle, then any linear combination, $c_1\psi_1 + c_2\psi_2$, is also a possible state of the particle, where c_1 and c_2 are constants.

The equation describing the evolution of ψ should then be linear. It is called the Schrödinger equation. This equation is a fundamental equation of the non-relativistic quantum mechanics. We simply consider this equation as a postulate and for the sake of simplicity we restrict ourself to one dimensional case. For a particle of mass m moving in the field of potential $V(z,t)$, the Schrödinger equation takes the form

$$i\hbar\frac{\partial}{\partial t}\psi(z,t) = -\frac{\hbar^2}{2m}\frac{\partial^2}{\partial z^2}\psi(z,t) + V(z,t)\psi(z,t). \tag{2.5}$$

The Schrödinger equation is linear and homogeneous in ψ. As a result, for material particles there exists a superposition principle which, combined with interpretation of ψ as a probability amplitude, is the source of wavelike effects. Furthermore the equation is of first order in t. So if the state at some time, say t_0, is known we can determine exactly the subsequent state of the particle. Thus there exists a fundamental analogy between matter and radiation - in both cases, a correct description of the phenomena needs the introduction of quantum concepts, in particular the idea of wave-particle duality.

At this point it is clear that wave functions $\psi(z,t)$ describe the states of a quantum particle. Let us assume a wave function $\psi(z,t) = ce^{i(kz-\omega t)}$, where c is a constant [360]. Performing differentiation with respect to z we get

$$\begin{aligned} &\frac{\partial}{\partial z}\psi(z,t) = \frac{\partial}{\partial z}\left(ce^{i(kz-\omega t)}\right) \\ \text{or,}\quad &\frac{\partial}{\partial z}\psi(z,t) = ik\left(ce^{i(kz-\omega t)}\right) \end{aligned}$$

$$\text{or,} \quad -i\hbar\frac{\partial}{\partial z}\psi(z,t) = \hbar k\psi(z,t)$$

$$\text{or,} \quad -i\hbar\frac{\partial}{\partial z}\psi(z,t) = p\psi(z,t) \qquad \text{since } p = \hbar k \text{ from equation (2.2),} \tag{2.6}$$

Again applying differentiation with respect to t we get

$$\frac{\partial}{\partial t}\psi(z,t) = \frac{\partial}{\partial t}\left(ce^{i(kz-\omega t)}\right)$$

$$\text{or,} \quad \frac{\partial}{\partial t}\psi(z,t) = -i\omega\left(ce^{i(kz-\omega t)}\right)$$

$$\text{or,} \quad i\hbar\frac{\partial}{\partial t}\psi(z,t) = \hbar\omega\psi(z,t)$$

$$\text{or,} \quad i\hbar\frac{\partial}{\partial t}\psi(z,t) = E\psi(z,t) \qquad \text{since } E = \hbar\omega \text{ from equation (2.2),} \tag{2.7}$$

Relations (2.6) and (2.7) show that the operators $-i\hbar\frac{\partial}{\partial z}$ and $i\hbar\frac{\partial}{\partial t}$, when acting on the wave function, yield respectively the momentum and energy of the particle as eigenvalues of the operators. This gives hints to the fact that momentum and energy of a free particle can be represented by the differential operators

$$p_{operator} = -i\hbar\frac{\partial}{\partial z}, \quad \text{and} \quad E_{operator} = i\hbar\frac{\partial}{\partial t} \tag{2.8}$$

acting on the wave function ψ. It is a postulate of wave mechanics that when the particle is not free the dynamical variables $\vec{p}$ and E are still represented by these differential operators.

Let us consider a particle moving under the potential $V(z,t)$. So the total energy E of the particle is given by the sum of kinetic energy $T = \frac{p^2}{2m}$ and potential energy V. Therefore,

$$E = \frac{p^2}{2m} + V. \tag{2.9}$$

Since the potential energy $V(z,t)$ does not depend on p or E, using the operators representation (2.8) we obtain

$$i\hbar\frac{\partial}{\partial t} = -\frac{\hbar^2}{2m}\frac{\partial^2}{\partial z^2} + V. \tag{2.10}$$

This leads to the Schrödinger equation,

$$i\hbar\frac{\partial}{\partial t}\psi(z,t) = \left[-\frac{\hbar^2}{2m}\frac{\partial^2}{\partial z^2} + V\right]\psi(z,t). \tag{2.11}$$

The operator $\left[-\frac{\hbar^2}{2m}\frac{\partial^2}{\partial z^2} + V\right]$ appearing on the right hand side of the Schrödinger equation plays a fundamental role in quantum mechanics. It is called the Hamiltonian operator of the particle, and is denoted by H. Thus

$$\begin{aligned} H &= -\frac{\hbar^2}{2m}\frac{\partial^2}{\partial z^2} + V \\ &= \frac{1}{2m}\left(p^2_{operator}\right) + V \\ &= T + V, \end{aligned} \tag{2.12}$$

where $T = \frac{1}{2m}\left(p^2_{operator}\right)$ is the kinetic energy operator. Therefore the time-dependent Schrödinger equation can be written as

$$i\hbar\frac{\partial}{\partial t}\psi(z,t) = H\psi(z,t). \tag{2.13}$$

Note that the quantum mechanical Hamiltonian operator is obtained from classical Hamiltonian by performing the substitution $\vec{p} \rightarrow p_{operator} = -i\hbar\frac{\partial}{\partial z}$.

2.4 The Postulates of Quantum Mechanics

In the following we describe the postulates for the case of a single particle in one space dimension. The quantum postulates are written together with the classical Hamiltonian formalism to provide some perspective [306].

Classical Mechanics	**Quantum Mechanics**
I. The state of a particle at any give time t is specified by the two variables position $\vec{q}(t)$ and momentum $\vec{p}(t)$, that is, as a point in a two-dimensional phase space.	I. The state of a physical system at a fixed time t, is described by a vector $\|\psi(t)\rangle$ belonging to the Hilbert space of square-integrable functions.
II. Every dynamical variable f is a function of $\vec{q}$ and $\vec{p}$, thus $f = f(\vec{q}, \vec{p})$.	II. Every measurable physical quantity is described by an operator in the Hilbert space and this operator is an observable. The independent variables $\vec{q}$ and $\vec{p}$ of classical mechanics are represented by Hermitian operators z and p. Any observable corresponding to the classically defined dynamical variable $f(\vec{q}, \vec{p})$, is obtained as the same function of the operators z and p. Thus the observable is given by Hermitian operators $F(z,p) = f(\vec{q} \to z, \vec{p} \to p)$.
III. If the particle is in a state given by $\vec{q}$ and $\vec{p}$, the measurement of the variable f will yield a value $f(\vec{q}, \vec{p})$. The state will remain unaffected.	III. The only possible result of the measurement of a physical quantity is one of the eigenvalues of the corresponding observable. If the particle is in a state $\|\psi\rangle$, measurement of the variable (corresponding to) F will yield one of the eigenvalues f with probability $P(f) = \|\langle f\|\psi\rangle\|^2$. The state of the system will change from $\|\psi\rangle$ to $\|f\rangle$ as a result of the measurement.

IV. The state variables change with time according to Hamilton's equations of motion,

$$\dot{\vec{q}} = \frac{\partial H}{\partial \vec{p}},$$
$$\dot{\vec{p}} = -\frac{\partial H}{\partial \vec{q}}.$$

IV. The time evolution of the state vector $|\psi(t)\rangle$ is governed by the Schrödinger equation:

$$i\hbar \frac{d}{dt}\psi(t) = H(t)\psi(t),$$

where $H(t)$ is the observable associated with the total energy or Hamiltonian of the system.

2.4.1 Physical Interpretation of the Postulates

In quantum mechanics, the state of a physical system is described by a vector in a Hilbert space. Since the state vectors define a Hilbert space, this implies a superposition principle: a linear combination of state vectors is a possible state vector. Therefore, if $|\psi\rangle$ and $|\psi_1\rangle$ correspond to two different states of a system, $c_1|\psi\rangle + c_2|\psi_1\rangle$ also corresponds to a state of the system. This also follows from the Schrödinger equation. Since Schrödinger equation is a linear equation, linear combination of any number of solutions is again a solution.

In classical mechanics for a given state $(\vec{q},\vec{p})$, one can say that any dynamical variable f has a value $f(\vec{q},\vec{p})$, in the sense that if the variable is measured, the result $f(\vec{q},\vec{p})$ will be obtained. Analogous to that in quantum mechanics for the particle in a state $|\psi\rangle$, every measurable physical quantity is described by an observable. The description of the physical quantities by observables has important consequences. First of all, the Hermitian nature of the observable ensures that measurement of the physical quantity always gives a real value. The quantum theory makes only probabilistic predictions for the result of a measurement of F. Furthermore, from the third postulate, if a state is an eigenstate $|f\rangle$ of some observable F, then the corresponding measurement, surely, yields the value f, the eigenvalue of F corresponding to $|f\rangle$. Thus the only possible values of F are its eigenvalues and these eigenvalues are all real due to the Hermitian nature of F. As a consequence, a collapse of the quantum state $|\psi\rangle$ to one of the eigenstates $|f\rangle$ of the observable F takes place during the measurement process [152].

Finally, Schrödinger equation is a fundamental equation in non-relativistic quantum mechanics since time evolution of the states of physical systems is governed by this equation. The Schrödinger equation is first order in time t. It thus follows that if the

initial state of the system, say $|\psi(t_0)\rangle$, is known, the state $|\psi(t)\rangle$ at any subsequent time t can be easily uniquely determined. So, there is no indeterminacy in the time evolution of a quantum system. Indeterminacy appears only when a physical quantity is measured, the state vector then undergoes an unpredictable modification. However, between two measurements, the state evolves in a perfectly deterministic way in accordance with the equation.

2.5 Stationary States and Time-Independent Schrödinger Equation

If the Hamiltonian operator is time-independent, its eigenstates are called stationary states. In such states, the probability of measurement of any time-independent observable F is independent of time. Thus all the physical properties of a system in a stationary state do not vary over time.

Now the Hamiltonian of a single particle of mass m moving in time-independent potential is given by

$$H = -\frac{\hbar^2}{2m}\frac{d^2}{dz^2} + V(z). \tag{2.14}$$

Thus we have

$$-\frac{\hbar^2}{2m}\frac{d^2}{dz^2}\psi(z) + V(z)\psi(z) = E\psi(z), \tag{2.15}$$

an eigenvalue equation and is known as time-independent Schrödinger equation. Note that equation (2.15) can be written in operator notation as

$$H\psi(z) = E\psi(z) \tag{2.16}$$

and thus the eigenvalue E of H can be identified with the energy of the system. Obviously E is real, since H is a Hermitian operator. Here it is important to note that, since H is time-independent, wave functions $\psi(z)$ are the eigenfunctions of H corresponding to the eigenvalue E. These eigenfunctions $\psi(z)$ of the Hamiltonian operator H give the stationary solutions of the time-independent Schrödinger equation (2.15). Note that the position probability density $|\psi(z)|^2$ of these stationary states are constant in time.

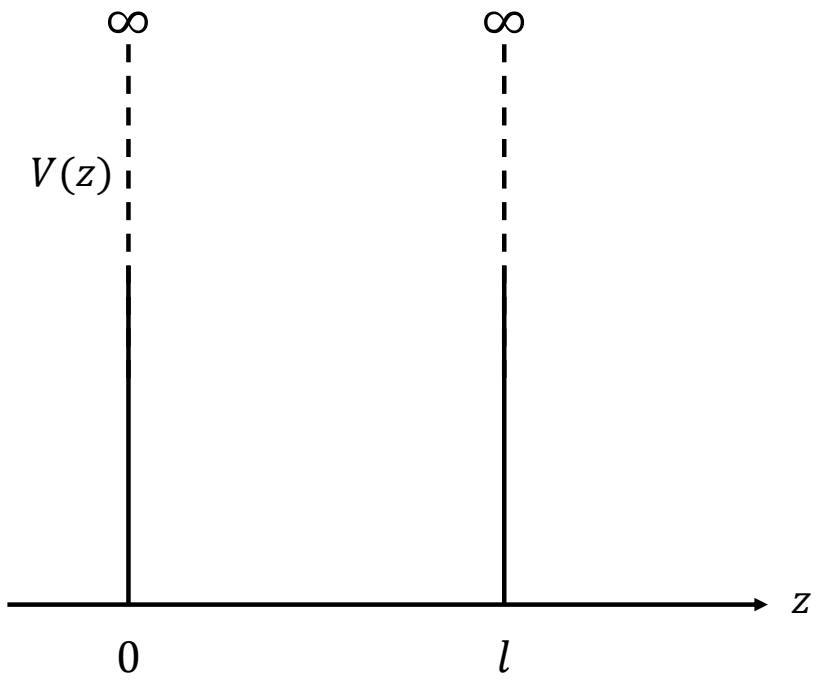

FIGURE 2.4. Infinite potential box.

In this thesis, we exploit these stationary wave solutions $\psi(z)$ of the time-independent Schrödinger equation in the context of signal and image decomposition. In Chapter 4, we use the fact that for a finite-dimensional problem these stationary wave functions will form a complete set of basis functions of the Hilbert space of L^2-integrable functions.

In the next subsection, now let us discuss a simple problem concerning the motion of a single particle in one dimension and see how the Schrödinger equation describes the picture.

2.6 Particle in a Box

Consider a particle of energy E and mass m confined into a region 0 to l of the $z-$axis. At $z = 0$ and $z = l$, there are two absolutely rigid, impenetrable walls of infinite height

[44, 152]. Therefore the potential V is given by

$$V\begin{cases} =0 & \text{for } 0 \le z \le l, \\ =\infty & \text{otherwise.} \end{cases} \tag{2.17}$$

The potential experienced by the particle is shown graphically in Fig. 2.4.

To leave the region $[0,l]$, the particle needs infinite energy. Since this is impossible, one can have the probabilities of finding the particle at $z=0$ and $z=l$ to be zero. As probability is measured by the modulus square of the wave function, so we choose

$$\psi(0) = \psi(l) = 0 \tag{2.18}$$

Similarly, since the particle can not cross the infinite barrier and go outside the box, the wave function $\psi = 0$ everywhere outside the box.

Since the potential V does not depend on time, we use the time-independent Schrödinger equation (2.15), given by

$$\begin{aligned} & -\frac{\hbar^2}{2m}\frac{d^2}{dz^2}\psi(z) + V(z)\psi(z) = E\psi(z) \\ \text{or,} \quad & \frac{d^2}{dz^2}\psi(z) + \frac{2m}{\hbar^2}\big(E - V(z)\big)\psi(z) = 0, \end{aligned} \tag{2.19}$$

to obtain the stationary wave function of the particle. Inside the box $V(z) = 0$, therefore Schrödinger equation (2.19) takes the form

$$\frac{d^2}{dz^2}\psi(z) + k^2\psi(z) = 0, \tag{2.20}$$

where $k = \dfrac{\sqrt{2mE}}{\hbar}$.
The solution of equation (2.20) is of the form

$$\psi(z) = c_1 \sin(kz) + c_2 \cos(kz), \tag{2.21}$$

where c_1 and c_2 are arbitrary constants. Now by the boundary condition $\psi(0) = 0 \Rightarrow c_2 = 0$. Hence we get

$$\psi(z) = c_1 \sin(kz). \tag{2.22}$$

Again the boundary condition $\psi(l) = 0$ gives $c_1 \sin(kl) = 0$ which is satisfied and gives nontrivial solution if

$$\sin(kl) = \sin(r\pi), \qquad r = 1, 2, 3, \cdots. \tag{2.23}$$

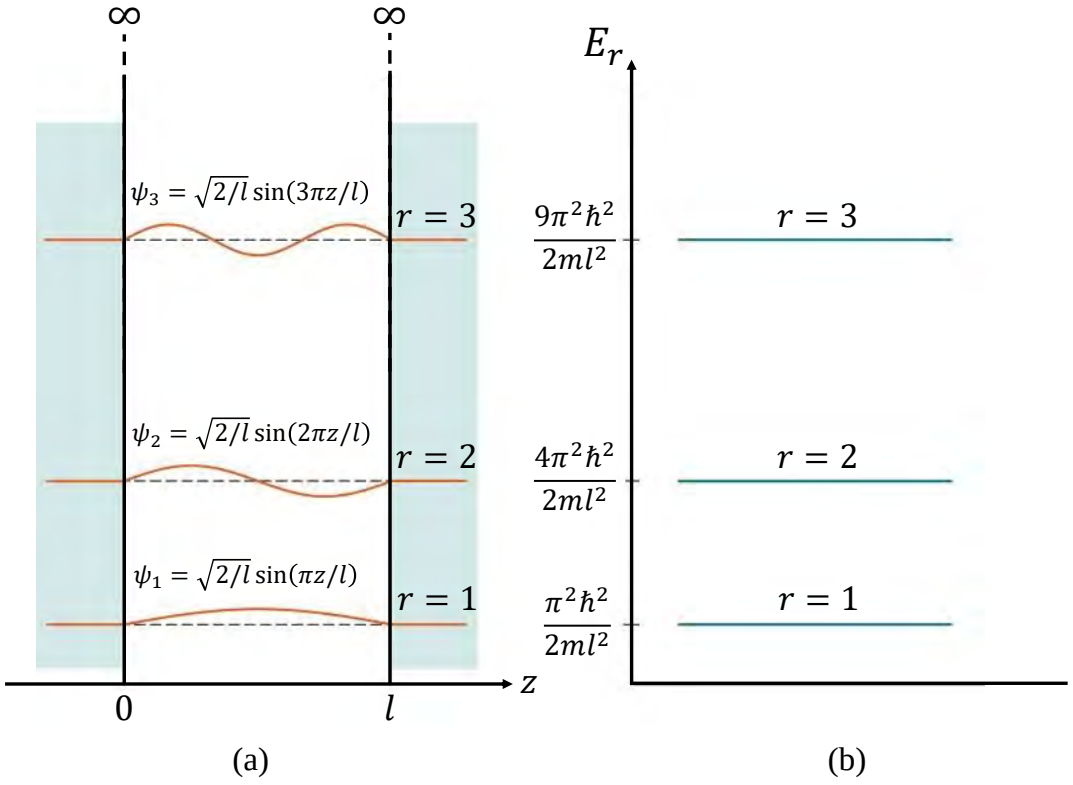

FIGURE 2.5. Wave functions and energy levels of a particle in a potential box. The first three wave functions and energy levels are respectively plotted in subfigures (a) and (b).

So,

$$k_r = \frac{r\pi}{l}, \tag{2.24}$$

and therefore,

$$\psi_r(z) = c_{1r}\sin\left(\frac{r\pi z}{l}\right). \tag{2.25}$$

The subscript r denotes the $r-$dependence of the underlying quantities. The eigenvalues thus form a discrete set as in the problem of a vibrating string with the two ends fixed. We get the energy of the particle as

$$E_r = \frac{\hbar^2 {k_r}^2}{2m} = \frac{r^2\hbar^2\pi^2}{2ml^2}. \tag{2.26}$$

Thus the wave function of a particle confined in an one-dimensional box is given by

$$\begin{aligned}\psi(z) = \psi_r(z) &= c_{1r}\sin\left(\frac{r\pi z}{l}\right), \qquad r = 1,2,3,\cdots \qquad \text{for } 0 \le z \le l,\\ &= 0 \qquad \text{otherwise.}\end{aligned} \tag{2.27}$$

This wave function can be normalized as follows

$$\int_{\infty}^{\infty} |\psi(z)|^2 \mathrm{dz} = 1$$
$$\text{or, } |c_{1r}|^2 \int_0^l \sin^2\Big(\frac{r\pi z}{l}\Big)\mathrm{dz} = 1$$
$$\text{or, } |c_{1r}|^2 \frac{l}{2} = 1$$
$$\text{or, } c_{1r} = \sqrt{\frac{2}{l}}. \tag{2.28}$$

Thus the normalized wave function is given by

$$\psi_r(z) = \sqrt{\frac{2}{l}} \sin\Big(\frac{r\pi z}{l}\Big), \qquad r = 1,2,3,\cdots. \tag{2.29}$$

$\{\psi_r\}$ forms a complete orthonormal set. There is only one independent eigenfunction ψ_r corresponding to each energy level E_r. Thus the energy spectrum is non-degenerate. The energy spectrum E_r as well as ψ_r has been shown in Fig. 2.5.

Now instead of $V = 0$, consider a nonzero potential inside the infinite potential box given by

$$V \begin{cases} = a & \text{for } 0 \le z \le l/2, \\ = b & \text{for } l/2 \le z \le l, \\ = \infty & \text{otherwise,} \end{cases} \tag{2.30}$$

where a and b are positive constants with $b < a$. Fig. 2.6 shows the graphical representation of this potential. Similar to the previous case, the particle can not leave the region $[0,l]$ due to the infinite potential barrier. So we choose $\psi(0) = \psi(l) = 0$ as the boundary conditions.

Since $V \neq 0$ and time-independent, so we get from Schrödinger equation (2.19)

$$\frac{d^2}{dz^2}\psi(z) + k^2\psi(z) = 0, \tag{2.31}$$

where $k = \dfrac{\sqrt{2m(E-V)}}{\hbar}$. All nontrivial solutions of (2.31) have locally the form

$$\psi_r(z) \sim e^{i\frac{\sqrt{2m(E_r-V)}}{\hbar}z}, \qquad r = 1,2,3,\cdots \qquad \text{for } 0 \le z \le l. \tag{2.32}$$

Therefore each solution ψ_r is associated with a specific value of E_r, with $E_r > V$ and takes discrete values. This means that the frequency of the stationary wave solution

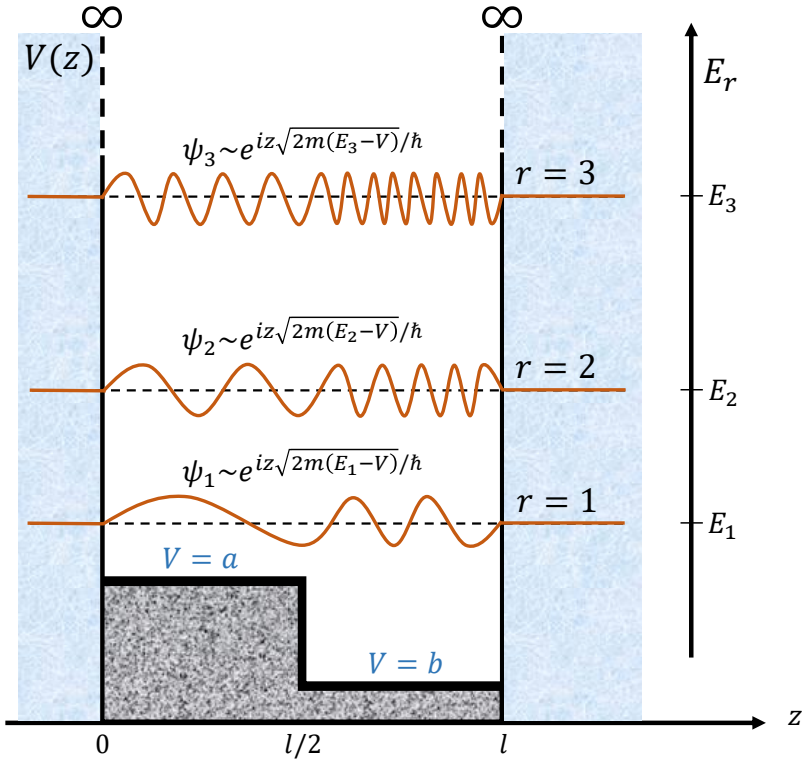

FIGURE 2.6. Wave functions of a particle in a nonzero potential box. Three wave functions and respective energy levels are shown. The frequency of the wave functions are proportional to $\sqrt{E_r - V}$, with $E_r > V$.

ψ_r is proportional to $\sqrt{E_r - V}$. Hence, the stationary solutions are locally oscillatory functions with an oscillation frequency dependent on the local value of V for a given energy E_r. In presence of the nonzero potential V the wave functions ψ_r are shown in Fig. 2.6.

In this thesis, we will calculate these stationary solutions ψ_r in the case of a more intricate potential, where V is no more a simple constant and depends on position. Indeed, we will consider the value of the signal sample or image pixels as the potential V. Therefore, the local oscillation frequency of the stationary wave functions ψ_r will depend on the local value of the signal sample or image pixels. These locally oscillatory stationary wave functions will be exploited for further signal or image decomposition tasks. Chapter 4 will put more insights into this fact.

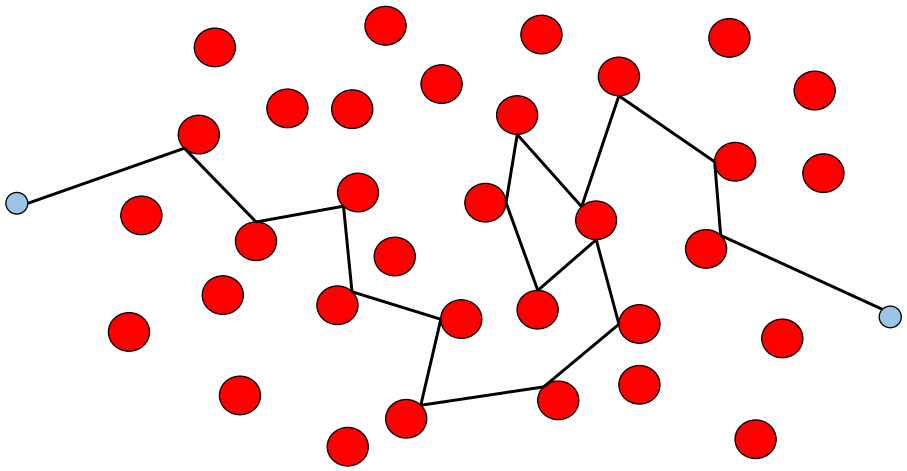

FIGURE 2.7. Motion of an electron in a disordered potential according to classical theory.

2.7 Quantum Localization of Wave Functions

If one considers an electron in a disordered crystal, according to classical theories, the zigzag motion of electrons is directly correlated to the mean free path, which is the average length traveled by an electron before it collides with an impurity. The motion of an electron is shown in Fig. 2.7 according to classical theories. The classical Drude theory tells us that the mean free paths of electrons are directly proportional to the electronic conductivity of a metal. It was clear that if the level of impurity increases, the mean free path becomes smaller and smaller. After the discovery of quantum mechanics, in the late 1950s, Philip Anderson came up with a new picture of electronic conductivity using quantum theory. He proved that beyond a critical amount of impurity scattering the zigzag motion of the electron is not just reduced, it can come to a complete halt. The electron becomes trapped or localized [19, 20] and the conduction is stopped.

Imagine an electron bounded on an one-dimensional lattice. If the lattice is periodic, all sites have the same potential energy, as shown in the top diagram in Fig.2.8. The electron will tunnel through one site to another according to the quantum mechanical laws. This tunneling process becomes efficient in the presence of an ordered lattice where the depth of the wells is the same in the lattice. In other words, we get a good coupling efficiency between neighboring wells, since the energy differences are zeros. As a result, extended Bloch wave functions [19] are present and motion is ballistic.

On the contrary, for a random lattice, each site has random potential energy and nearby wells have very different energies, as shown in the bottom diagram in Fig.2.8.

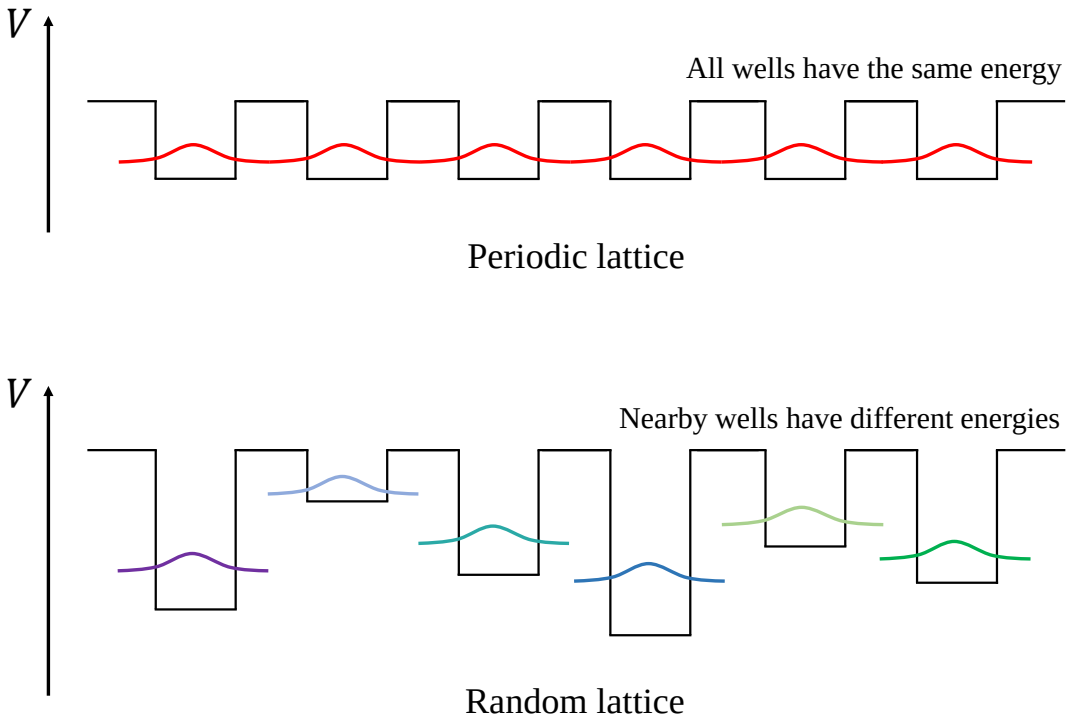

FIGURE 2.8. Periodic and random lattices. Here different colors represent different potential energies.

The electron will still tunnel from one site to another through large energy barriers, but the cross-coupling efficiency becomes very low due to the high energy differences. Thus, a critical amount of randomness in the depth of the wells leads to exponentially localized wave function $|\psi| \sim e^{(z-z_0)/L}$ of the electron [201], where L is the localization length.

According to scaling theory [201], the scaling function $\beta(g)$ describes how or more precisely, with what exponent the average conductance g grows with system size l. The conductance varies as l^{D-2}, for a normal Ohmic conductor with dimension D, correspondingly $\beta(g) \sim D-2$ for large g. Thus for the three-dimensional case the beta function is positive, zero for two dimension and for one dimension beta is negative. In the localized regime, g decays exponentially with sample size so that $\beta(g)$ is negative. In three dimensions, that leads to a critical point [19, 20, 201] at which β vanishes for some special value of g. But the one or two-dimensional systems do not undergo a phase transition because the conductance always decreases with system size [198]. The localization length decreases when the system becomes more and more disordered. Therefore, localization

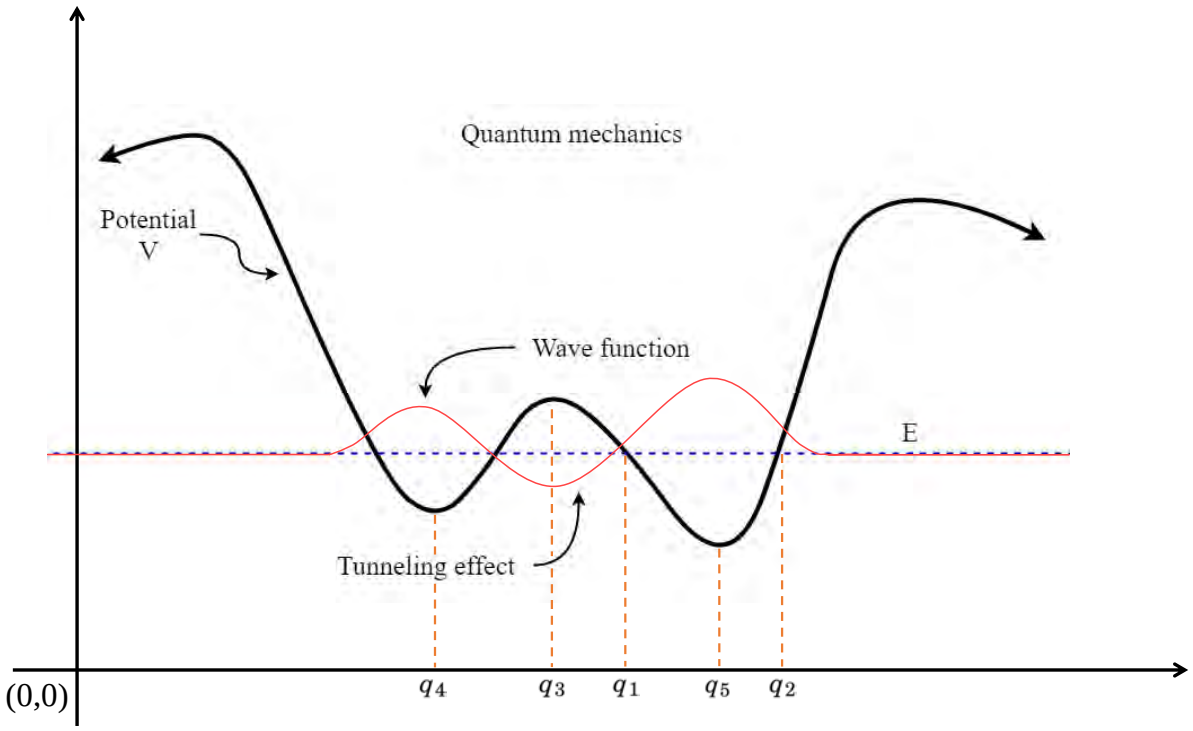

FIGURE 2.9. Wave function with energy E under a smooth potential V. The blue dashed line represents the energy of the quantum particle.

is always present for one or two-dimensional systems. The level of localization can be measured by computing the inverse participation ratio (IPR) of the wave functions, which is directly proportional to the localization length. For a given wave function ψ, the IPR is mathematically defined as:

$$\text{IPR}(\psi) = \frac{\left(\sum_i |\psi_i|^2\right)^2}{\sum_i |\psi_i|^4}. \tag{2.33}$$

The IPR (or localization length) of a wave function ψ decreases with increasing disorder of the system.

Let us illustrate this concept through a pictorial diagram. It is clear that in quantum mechanics, a wave function characterizes the state of a quantum particle where the position and momentum of the particle can not be determined precisely. Suppose a particle is moving under an arbitrary but smooth potential V. For an energy E, the solution of the time-independent Schrödinger equation under the potential V gives the wave solution as shown in Fig. 2.9. Although at point q_3, the potential barrier is higher

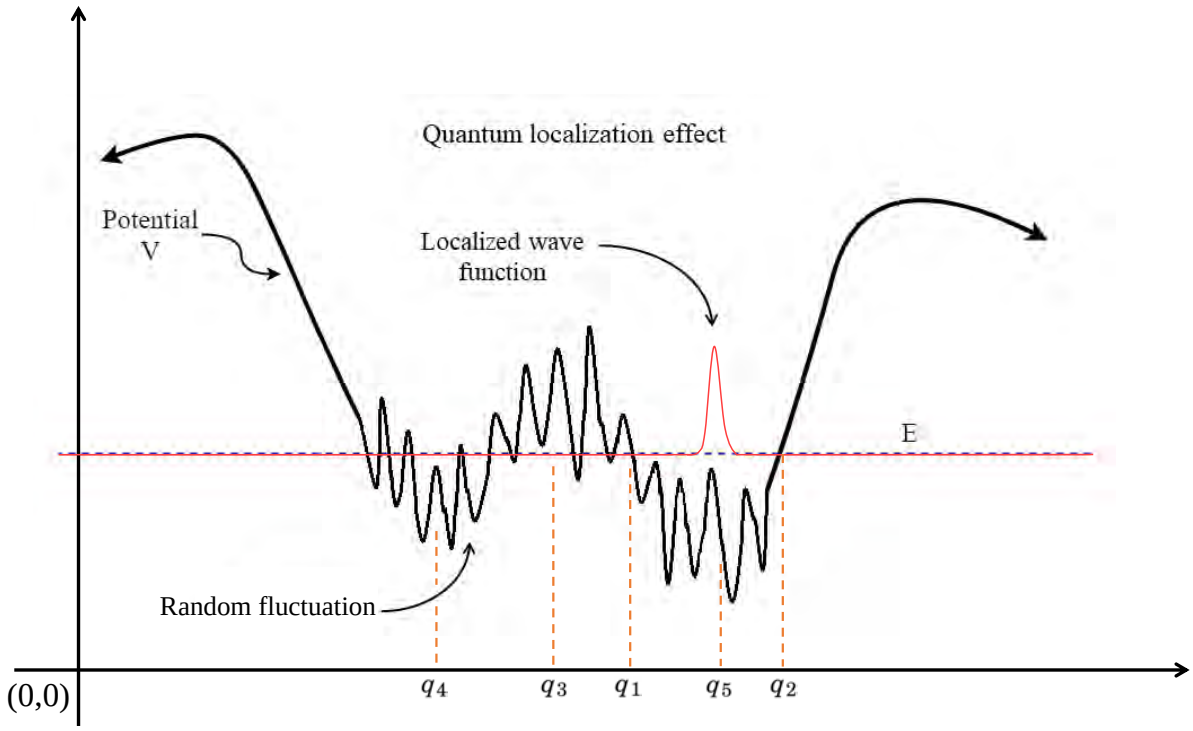

FIGURE 2.10. Slaking wave function with energy E under a random potential V. The blue dashed line represents the energy of the quantum particle.

than the particle's energy E, the particle can tunnel through the barrier and reach reach the point q_4. Thus we get a non-zero probability at point q_5 as well as at point q_4. This phenomenon is impossible for a classical particle.

In the case of a disordered system, *i.e.*, the potential V is not smooth anymore and is affected by random fluctuations, as shown in Fig. 2.10. Due to the random changes of V, the destructive interference between different waves causes an exponential decay of the wave function, resulting in the localization of wave function. Hence, the wave function no longer extends over the entire space and becomes trapped around point q_5.

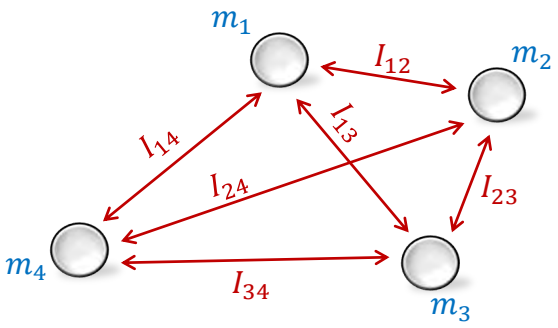

FIGURE 2.11. Interactions between particles in a many-body system.

In the context of signal or image processing, the random noise, that contaminates signal or image represents the disorderness of the system. In other words, a noisy signal or image behaves like a random lattice with random potential energies at each signal value or image pixel. As the noise intensity grows, the signals or images become more and more disordered, causing the waves of that system to become completely localized in some regions of the signals or images. So, for one-dimensional signals and two-dimensional images with random noise, the localization factor plays a crucial role. In Chapter 4, we will elaborate on this in the context of signal and image decomposition.

2.8 Quantum Many-Body Theory

Our discussion so far has been restricted to a system with a single particle in one dimension. We want to deal with the case of several quantum particles generalizing the theory. In reality, the motion of a particle is often influenced by other particles nearby. In general, it is straightforward to understand the underlying physical laws governing the motion of each particle in the absence of such effects, but the complex nature of such influence makes the study of collections of interacting particles extremely difficult. This is a well known as the 'Many-Body Problem' in physics. Our universe is primarily

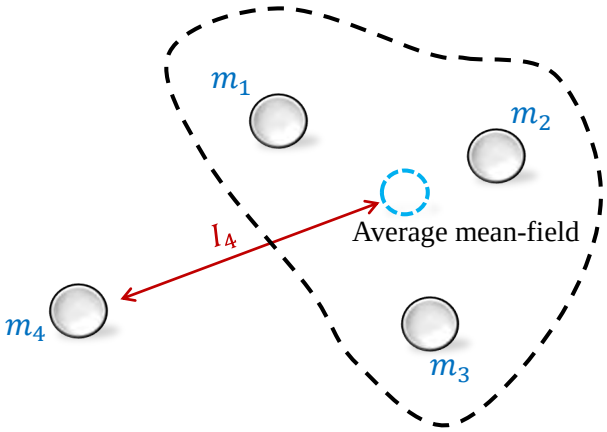

FIGURE 2.12. Interaction between a particle and the average mean-field.

governed by four fundamental interactions, these are gravitational, electromagnetic, weak-nuclear and strong-nuclear interactions. Fig. 2.11 presents a pictorial diagram of such particle-particle interaction in a classical system.

Consider a quantum system with w particles with mass $m_1, m_2, m_3, \cdots, m_w$. Thus the characteristics of each particle depends of others. Hence we then have to solve a Schrödinger equation with a wave function $\psi(z_1, z_2, z_3, \cdots, z_w)$ depending on the w variables corresponding to the w particles, where $z_1, z_2, z_3, \cdots, z_w$ are the spatial coordinates of the w particles. The potential $V = V(z_1, z_2, z_3, \cdots, z_w)$ is also a function of w variables. Therefore, for a system with w particles the Hamiltonian operator becomes [232]:

$$H(z_1, z_2, z_3, \cdots, z_w) = -\sum_{a=1}^{w} \frac{\hbar^2}{2m_a} \frac{d^2}{dz_a^2} + V(z_1, z_2, z_3, \cdots, z_w). \tag{2.34}$$

Thus, for a given energy E the associated wave function $\psi(z_1, z_2, \cdots, z_w)$ satisfies a new Schrödinger equation:

$$H\psi(z_1, z_2, \cdots, z_w) = E\psi(z_1, z_2, \cdots, z_w). \tag{2.35}$$

Solving this equation (2.35) is not straightforward because of the highly nonlinear nature of $V(z_1, z_2, z_3, \cdots, z_w)$. $V(z_1, z_2, z_3, \cdots, z_w)$ contains the original potentials of particles as single particle systems and the external potentials due to the interactions, mathematically given by

$$V(z_1, z_2, \cdots, z_w) = \underbrace{\sum_a V(z_a)}_{\text{1-body term}} + \underbrace{\sum_{a,b} I(z_a, z_b)}_{\text{2-body term}} + \underbrace{\sum_{a,b,c} I(z_a, z_b, z_c)}_{\text{3-body term}} + \cdots + \underbrace{I(z_1, z_2, \cdots, z_w)}_{\text{w-body term}}, \tag{2.36}$$

where the 1-body term $V(z_a)$ is the original potential of a-th particle as single particle system, 2-body term $I(z_a, z_b)$ is the interaction generated by two particles, 3-body term $I(z_a, z_b, z_c)$ is the interaction generated by three particles, and so on.

Considering approximations like the Mean-Field approximation, we can simplify the problem. It assumes that the particles do not interact with each other except through an average self-consistent mean-field [242, 257]. For example, the a-th particle does not interact with other particles of the system one-by-one or one-by-two or so on and only interacts with an average mean-field generated by the other particles of the system. Under this approximation, all higher order terms present in equation (2.36) vanish, and only interaction, say I_a, between the a-th particle with its average mean-field remains (see Fig. 2.12 for a pictorial representation). Therefore, we get an approximated potential given by

$$V(z_1, z_2, \cdots, z_w) \approx \sum_a V(z_a) + \sum_a I_a. \tag{2.37}$$

Hence, the many-body problem reduces into an effective one-body problem and for each particle their respective Hamiltonian operator is given by

$$H_a = \underbrace{-\frac{\hbar^2}{2m_a}\frac{d^2}{dz_a^2} + V(z_a)}_{H_{0_a}} + I_a, \quad \text{for } a = 1, 2, 3, \cdots, w, \tag{2.38}$$

where, H_{0_a} is the Hamiltonian for the a-th particle as a single-particle system. Under this reduced Hamiltonian, the Schrödinger equation gives wave solutions for each particle, providing useful insight into understanding the underlying physics of the many-body system.

We show in Chapter 6 that by exploiting this many-body framework for imaging problems, we can obtain significant improvements in image restoration performance, especially in image denoising, where this quantum interaction plays a crucial role in preserving image features.

Chapter Highlights

In quantum mechanics, (non-relativistic) particles in a potential V are described by wave functions ψ, whose absolute values $|\psi|^2$ correspond to the probability of presence of the particles. The stationary wave functions are the solutions of the time-independent Schrödinger equation and these stationary functions ψ are the eigenfunctions of the Hamiltonian operator H corresponding to the eigenvalue E_r.
For a quantum particle in an infinite potential box, the stationary solutions are locally oscillatory functions with an oscillation frequency dependent on the local value of V for a given energy E_r.
In a disordered system, the random fluctuations of V cause destructive interference between different waves and lead to an exponential decay of the wave function, resulting in the localization of the wave function.
In a quantum many-body system, in general, particle-particle interactions take place and the characteristics of each particle are often influenced by other particles nearby.

In this thesis, we exploit these stationary wave solutions $\psi(z)$ of the time-independent Schrödinger equation to construct a signal or image-dependent basis set, which will be used in the context of signal or image decomposition. Indeed, we will consider the value of the signal sample or image pixels as the potential V. Therefore, the local oscillation frequency of the basis vectors will depend on the local value of the signal sample or image pixels.
In this thesis, a noisy signal or image behaves like a disordered system with random potential energies at each signal value or image pixel. This disorderness increases with the noise intensity, causing the basis vectors of that system to become completely localized in some regions of the signals or images. These localized basis vectors play a crucial role in the signal and image decomposition tasks.
Finally, we exploit the quantum many-body theory for imaging problems, where the quantum interaction plays a crucial role in preserving local image features.

CHAPTER 3

Image Restoration Problems and Related Methods

Contents

Overview

This chapter briefly introduces various image restoration problems with a discussion of the existing state-of-the-art methods for solving such imaging tasks using model-based, learning-based, and model-based learning approaches. In addition, the development of the quantum mechanics based imaging algorithms over the past few decades are summarized here.

3.1 Introduction

The spatial resolution of an imaging system is the capacity to differentiate two closely spaced point sources. In other words, it is the ability of the system to separate two close targets. In almost all practical applications, we do not have direct access to the desired image through observations but only to a degraded version of that ground truth due to various unavoidable phenomena in real-life situations causing such distortions. These distortions that can significantly damage the spatial resolution and image details, *i.e.*, the overall image quality, arise due to the sensors or to the environment of the physical system. In most imaging applications, a high-quality image is always desired as it provides more precise image details that facilitate accurate image analysis. This image analysis becomes very critical, particularly for medical diagnosis, and also has a great impact on astrophysics, geosciences, engineering, etc. Due to this drive, image restoration problems to obtain a high-quality image from a low-quality observation have been extensively studied over the years yet remain an open research domain even in present times.

3.2 Examples of Image Restoration Tasks

The process of retrieving a clean image from a distorted observation is known as image restoration. There is a wide range of practical problems within image restoration. In the following, we discuss the forward models associated with the most common ones.

3.2.1 Image Denoising

Let us consider a physical system acquiring visual information (*e.g.*, by a digital camera) of its surroundings in the form of images. Frequently, the images appear to be noisy, suggesting that they were degraded during the acquisition process, because of various factors depending on the apparatus. Under certain assumptions, the noisy image is assumed to be the sum of two terms, the noise, which depends on the imaging system, and a noiseless version of the observed image, which corresponds to the clear image. Obtaining an estimate of this true image is then an image restoration problem (more generally an inverse problem), known in the literature as image denoising. Note that depending on the noise nature and application specificities, the noise is not necessarily additive.

(a) Gaussian denoising of photographic image [9]

(b) Poissonian denoising of fluorescence microscopic image [1]

FIGURE 3.1. Examples of image denoising.

The random variation of information related to color or brightness value in the images is known as noise. Image noise is caused by the circuitry and sensor of a scanner or digital camera, and also to film grain or quantum fluctuations of photons. One can range image noise from almost invisible specks on a photograph taken in good light, to optical and radio-astronomical images that are extremely noisy, from which one can only collect a small amount of information. Generally the Gaussian noise is generated as an intrinsic noise in the sensor of a scanner or digital camera due to the illumination level and internal temperature of the electronic circuits connected to the sensor. As a different example, in the case of counting process such as limited photon acquisition, the process gets contaminated by Poisson noise, which is a signal-dependent noise. Thus, in several applications such as astronomy, photography, microscopy, medical imaging, etc., the denoising task becomes crucial to acquire a high-quality image by removing unwanted contributions to pixels due to noise. Fig. 3.1 shows denoising applications for photography and microscopy images in the presence of Gaussian and Poissonian noise, respectively. In Chapters 4 and 6, we address this image denoising problem by exploiting the principles of quantum theory using adaptive transform domain shrinkage and a nonlocal data-driven approach, respectively. Furthermore, a quantum-inspired deep neural network is proposed in Chapter 7 for the denoising task.

3.2.2 Image Deblurring

Image deblurring is a process of recovering a sharp and noise-free image from a blurry and noisy observation. For simplicity, let us consider the scenario of acquiring visual information from surroundings by a digital camera. An additional image degradation can occur due to depth-of-field effects or defocusing. These degradation processes produce

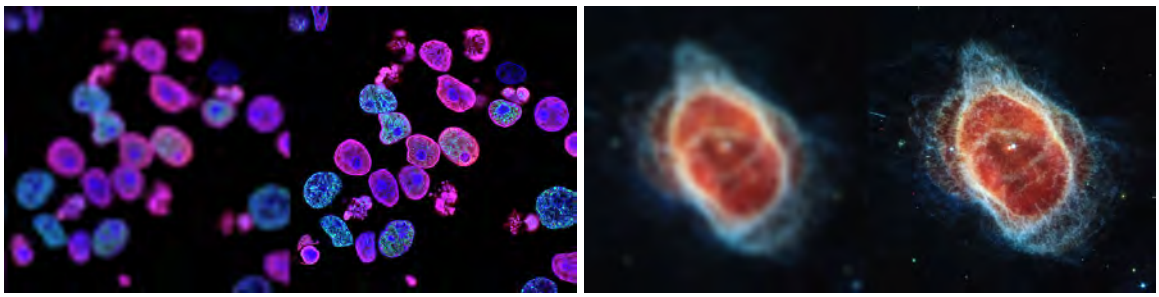

(a) Deblurring of fluorescence microscopy cell image [150]

(b) Deblurring of astronomical image from James Webb Telescope [255]

FIGURE 3.2. Examples of image deblurring.

images that are not only noisy but also blurred. Other phenomena may occur that reduce image sharpness, such as camera motion or light propagation through the atmosphere.

Image deblurring is widely used in many applications including astronomy, microscopy, medical imaging, etc. Fig. 3.2 shows its application for microscopy and astronomy images. Generally, the forward model associated with image blurring consists in a convolution between blur kernel that can be caused by motion or the system impulse response. The blur kernel often corresponds to a filter that causes information loss when applied to an image, especially from the high-frequency spectrum. In our case, the image deblurring algorithm aims to recover lost information under noisy system conditions when the blur kernel itself is known or unknown. Chapters 4 and 7 present image deblurring methods using model-based and neural network-based approaches, respectively.

3.2.3 Single Image Super-Resolution

Imaging beyond the system resolution is referred to as super-resolution (SR). Assume a situation of obtaining information about an object from a distance, typically by using sensors or cameras. These sensors or cameras primarily capture an optical image, which is a set of pixels representing the spatial information of the object. The number of pixels is related to the spatial resolution of the image. Enhancing the resolution of the image is another example of restoration problem, known as the single image SR problem. In this case, the system is usually modeled as a degradation process acting on a sharp high-resolution (HR) image. This degradation is a consequence of the characteristics of the sensor or camera that was used to capture the image. SR techniques are often used

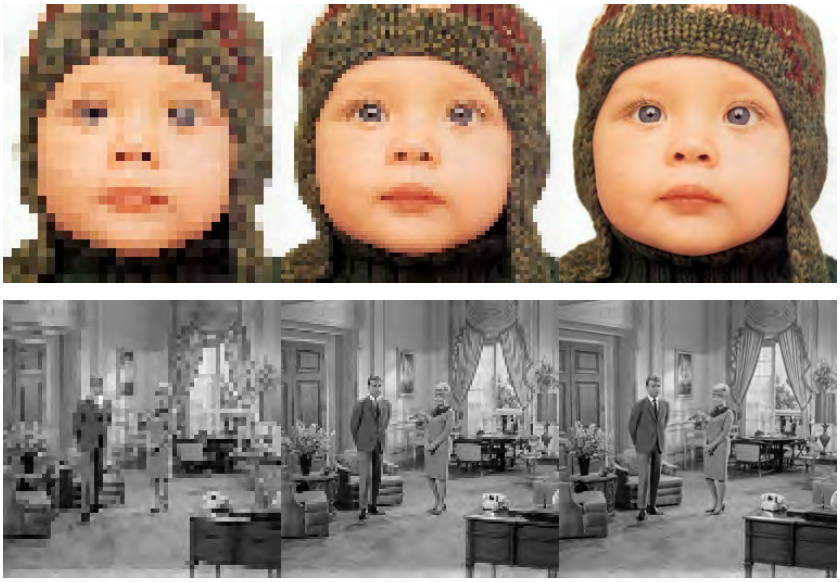

FIGURE 3.3. Examples of image super-resolution. From left to right are low-resolution, restored high-resolution (using nearest-neighbor interpolation), and ground truth images, respectively [405].

in image enhancement, medical imaging and hyper-spectral imaging. The problem of SR can be thought of as a combination of the process of image deblurring and image upsampling. To handle the loss of information, multiple low-resolution (LR) observations are usually used in order to recover a single frame HR image. However, we focus on the single image approach in our work. An example of SR is shown in Fig. 3.3. We discuss this SR problem in Chapters 6 and 7, employing various imaging and quantum tools.

The main advantage of analyzing all the different problems described in the previous paragraphs as restoration problems lie in the fact that this can be done systematically. Note that the ultimate goal of solving a restoration problem (inverse problem) is to retrieve the original underlying data from the degraded observations. This is typically harder to do than the reverse. As an example, consider the problem of image deblurring: it requires estimation of not only a deblurred image but also parameters related to the camera. It can then be helpful to develop ways to use additional information about the system under study.

When formulating a restoration problem, one usually needs to address four different points:

(a) the selection of an observation model describing the underlying physical reality,

(b) the establishment of a criterion quantifying how well the observations are described by the model,

(c) the design of a way to incorporate any additional information about the parameters, if available, and,

(d) the selection of a computational approach to tackle the restoration problem.

In the following, we focus on the mathematical formulation of the image restoration problem.

3.3 Image Formation Model

Often, such a degradation process as those introduced previously, can be formulated mathematically to capture the nature of the contamination or degradation as

$$\boldsymbol{y} = \mathcal{N}(\boldsymbol{O}\boldsymbol{x}), \tag{3.1}$$

where, $\boldsymbol{y}$ and $\boldsymbol{x}$ denote the degraded observation and unobservable image of interest, respectively, $\boldsymbol{O}$ denotes the degradation operator, and $\mathcal{N}$ accounts for the effect of the noise (be it additive, speckle, Poissonian, etc.). The goal is to recover the underlying image $\boldsymbol{x}$ from the observation $\boldsymbol{y}$. Note that $\boldsymbol{y} \in \mathbb{R}^m$ and $\boldsymbol{x} \in \mathbb{R}^n$ are respectively the standard vectorized versions of images $\boldsymbol{Y}$ and $\boldsymbol{X}$ in lexicographical order. Depending on the degradation operator $\boldsymbol{O}$, different restoration problems occur. For example, if $\boldsymbol{O}$ is the identity operator, the resulting problem is an image denoising problem. If $\boldsymbol{O}$ is a blurring operator then restoration becomes a deblurring, or a SR task if $\boldsymbol{O}$ includes a subsampling operator. In practice, estimating $\boldsymbol{x}$ from $\boldsymbol{y}$ by mitigating the effect of the degradation operator $\boldsymbol{O}$ is a challenging ill-posed inverse problem.

3.4 State-of-the-Art Methods

Over time, original methods from various branches of science have enriched the literature of digital image processing, and specifically the fundamental question of image restoration. Such methods are inspired from statistics [157], probability theory [208, 271], graph theory [262, 297, 310] or differential equations [191, 227]. This section will present benchmark techniques reported in the literature for various image restoration problems such as denoising, deblurring and SR. Fig. 3.4 presents a hierarchical representation of various types of inverse problem techniques. Note that it is possible to classify these imaging techniques in several ways, here we choose one way to do it depending on the statistical or learning-based approach.

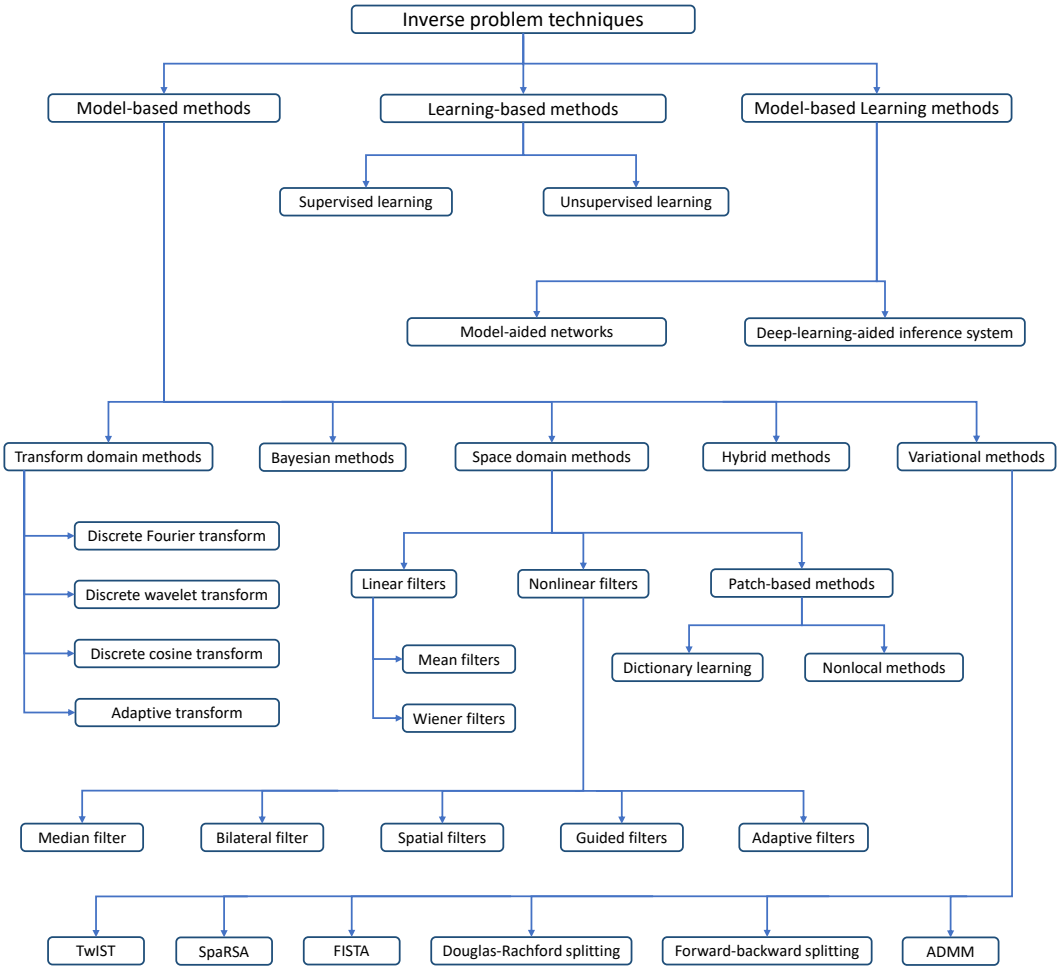

FIGURE 3.4. Hierarchical representation of various types of image restoration techniques.

3.4.1 Model-Based Methods

Traditional signal and image processing is dominated by algorithms based on mathematical models which are hand-designed from domain knowledge. Such knowledge can come from statistical models based on measurements and understanding of the underlying physics, or from deterministic representations of the particular problem at hand. These domain-knowledge-based processing algorithms, known as model-based methods, carry out inference based on knowledge of the underlying model relating the observations at hand and the desired information. Model-based methods do not rely on data to learn their mapping, though data is often used to estimate a small number

of parameters. Fundamental techniques like the Kalman filter and message passing algorithms belong to the class of model-based methods. Classical statistical models rely on simplifying assumptions (*e.g.*, linear systems, Gaussian and independent noise, etc.) that make models tractable and understandable.

3.4.1.1 Filters for Image Denoising

Image denoising is one of the fundamental image restoration challenges that has been extensively studied over the last forty years and is still an active area of research [65, 251]. Nowadays, denoising algorithms are present in all imaging domains. More recently, new denoising challenges have appeared, for instance with the apparition of cameras in smartphones, high-resolution sensors in satellites, or modern imaging equipments in medical diagnosis. Image denoising consists in estimating an unknown noiseless image $\boldsymbol{x}$ from a noisy observation $\boldsymbol{y}$, that obeys the classic image degradation model

$$\boldsymbol{y} = \boldsymbol{x} + \boldsymbol{e}, \tag{3.2}$$

since $\boldsymbol{O}$ in eq. (3.1) is the identity operator for denoising and we consider additive noise $\boldsymbol{e}$ for simplicity.

All denoising methods assume some underlying image regularity. Depending on this assumption, most of them can be divided into transformation-domain and spatial-domain methods.

For the denoising problem, number of methods are based on sparse representations into a given basis, with most of the true image described by the projections on a few basis vectors. This enables to efficiently store and restore the image. Transform domain methods work by shrinking or thresholding the coefficients of some transform domain [147, 217, 320]. The Wiener filter [372] is one of the first such methods operating on the Fourier domain, further extended to the wavelet domain by Donoho *et al.* [106]. Such sparse representations [6, 23, 53, 105, 106, 196, 273, 320] depend on both the transformation chosen and the nature of the image. Fig. 3.5 shows how one can get a denoised image by thresholding these sparse coefficients in the wavelet domain. Traditionally, all these methods exploit few explicit or underlying hypotheses about the image to restore, for example, piece-wise smoothness, but are not strong enough to capture the complex textures present in a true image.

Space-domain methods traditionally use a local notion of regularity with edge-preserving algorithms such as total variation [133, 289, 290, 371], anisotropic diffusion

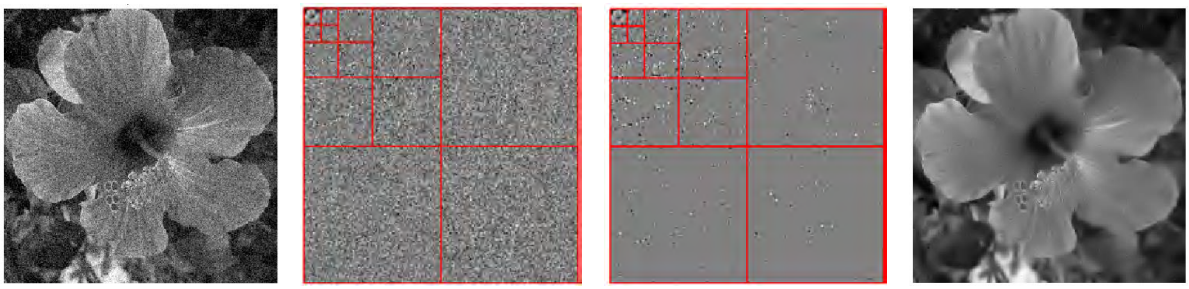

FIGURE 3.5. Examples of image denoising using wavelet transform. Four-scale wavelet transform and hard thresholding are used here [268].

[267, 369, 370], spatial filtering [109, 340], bilateral filter [122, 340, 408], or guided filters [160, 197], etc. In Chapter 4, we exploit this notion of sparsity by an adaptive transformation designed from the principles of quantum mechanics.

With the growth of computing power, data-driven strategies to increase the sparsity and overcome the limitations of general transforms have become more prominent in recent decades. One such approach is to learn overcomplete dictionaries from training image sets [10, 102, 123, 236]. These data-driven methods are non-local as they denoise by averaging similar patches in the image. Patch-based denoising has developed into attempts to model the patch space of an image, or of a set of images. These techniques model the patch as sparse representations on dictionaries [100, 123, 234], using Gaussian Scale Mixtures models [273, 278, 418], or with non-parametric approaches by sampling from a huge database of patches [213, 214, 250, 269].

Another alternative patch-based scheme uses patch neighborhood as a feature vector and takes advantage of both space- and transform-domain approaches [82, 208]. They group similar image patches and jointly denoise them through associative filtering in a transform domain (see Fig. 3.6). Additionally, they proceed by applying two slightly different denoising stages, with the second stage using the output of the first as its guide. For example, block-matching and 3D filtering known as BM3D creates 3D data arrays by grouping similar image fragments before computing a sparse representation applying 3D transformations [82, 83].

Patch-based algorithms exploit the self-similarity model, which takes into account the fact that natural images often represent repetitive patterns. The idea behind these patch-based algorithms is to exploit the non-local self-similarity (NLSS) while processing a group of similar patches. The first, most famous denoising schemes using NLSS is the

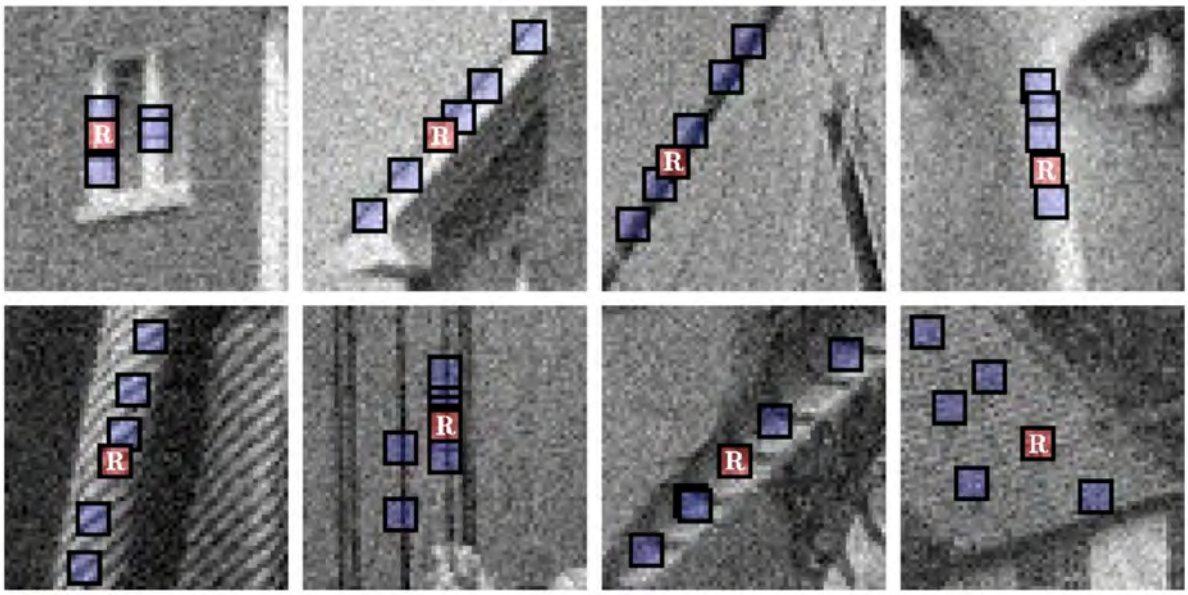

FIGURE 3.6. Illustration of grouping blocks from noisy natural images corrupted by white Gaussian noise with standard deviation 15 and zero mean. Each fragment shows a reference block marked with "R" and a few of the blocks matched to it [82].

Non-Local Means (NLM) algorithm that brought a different perspective to the image denoising problem, where each estimated image pixel intensity is a weighted average of pixels centered at patches that are similar to the patch centered at the estimated pixel [48, 50]. Fig. 3.7 illustrates the principle of NLM filtering algorithm. An alternative patch-based NLM approach projects image patches into a lower dimensional subspace using principal component analysis (PCA) before performing the weighted average for denoising [92, 333]. Later on, various schemes were proposed in the literature to accelerate or to improve the NLM performance, such as a fast NLM algorithm with a probabilistic early termination [355], quadtree-based NLM with locally adaptive PCA [419], fast processing using statistical nearest-neighbor strategy [136], adaptive neighborhoods [187], patch-based locally optimal Wiener filtering [66] and others [102, 216, 233, 350, 397, 399–401]. NLSS-based sparse modeling significantly improves the performance of sparse representation-based image restoration and eventually enhances the denoising process [102, 154, 235]. These NLSS-based schemes are known as a powerful way of denoising exploiting similar patches from the whole image. Hence, the patch neighborhood gives an effective way of preserving the local structures of an image where neighborhood similarity is the key ingredient.

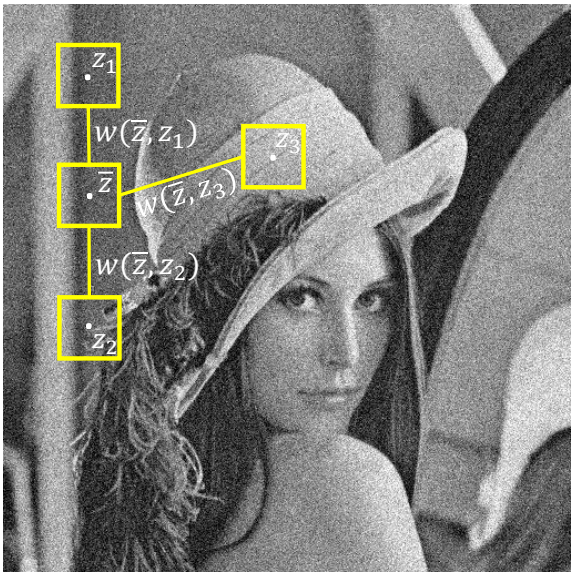

FIGURE 3.7. Principle of Non-Local Means filtering algorithm. Similar pixel neighborhoods give a large weight, $w(\bar{z}, z_1)$ and $w(\bar{z}, z_2)$, while much different neighborhoods give a small weight $w(\bar{z}, z_3)$.

In the last decade, a new way of exploiting the local similarities in an image neighborhood has been introduced through graph theory. The graph image processing methods [73, 259, 262, 282, 307] use a graph Laplacian constructed from the image to build an adaptive basis that can be used to decompose the noisy image. This constructed graph Laplacian emphasizes the similarities between neighboring pixel values that eventually increase the algorithm's performance [243, 342–344]. We introduce a notion of a patch-interaction inspired by the quantum many-body theory in Chapter 6 that can take advantage of NLSS in a local image neighborhood.

In a Poisson noise model, the conventional algorithms fail to recover the latent image since the counting process introduces intensity-dependent noise. This problem is solved by simply transforming Poisson data to produce data with approximate Gaussian noise via, for instance, the variance stabilizing Anscombe transform (VST) [21, 238] or Fisz transform [134, 138]. ATBM3D [238], NLBayes [209], SAFIR [41, 187] are a few such examples where classical Gaussian denoising algorithms are consolidated with the Anscombe transform. In fact, these VST-based refinements exhibit very good performance for low-intensity noise but are less accurate while dealing with high-intensity noise (*i.e.*, low SNR) [296]. The low-dimensional modeling and sparse Poisson intensity reconstruction algorithm [54, 296], or Bayesian approach [15] present different perspectives to

counter Poissonian problem without considering any transformation. In Chapter 4, we present a new denoising algorithm with promising performances in the presence of Poisson noise distribution without using any of these transformations.

3.4.1.2 Generalized Restoration Methods

Image denoising, deblurring or super-resolution (SR) is a restoration problem of recovering the sharp-clean underlying or high-resolution (HR) image $\boldsymbol{x}$ from a noisy blurred degraded or low-resolution (LR) one $\boldsymbol{y}$. We reproduce the forward model eq. (3.1) by considering additive noise $\boldsymbol{e}$ for simplicity,

$$\boldsymbol{y} = \boldsymbol{O}\boldsymbol{x} + \boldsymbol{e}. \tag{3.3}$$

Note that degradation $\boldsymbol{O}$ is an identity operator for image denoising, for a deblurring problem $\boldsymbol{O} = \boldsymbol{G}$, with $\boldsymbol{G}$ is a convolution matrix (which can be chosen as block circulant, block Toeplitz, etc.) to account for boundary conditions and represents the point spread function (PSF), and in case of SR problem $\boldsymbol{O} = \boldsymbol{S}\boldsymbol{G}$, where $\boldsymbol{S}$ and $\boldsymbol{G}$ are respectively the decimation and blurring/convolution operators [5, 84, 94, 102, 103, 125, 141, 174, 175, 318, 328].

The estimation of the underlying hidden image from this distorted observation is often formulated as the optimization of a cost function resulting from the maximum-a-posteriori (MAP) estimator [272], *i.e.*, the maximization of the posterior probability, defined as

$$\hat{\boldsymbol{x}} = \arg\max_{\boldsymbol{x}} \; P(\boldsymbol{x}|\boldsymbol{y}), \tag{3.4}$$

where $P(\boldsymbol{x}|\boldsymbol{y})$ is the posterior probability density function that defines $\boldsymbol{x}$ for a given measurement $\boldsymbol{y}$ and $\hat{\boldsymbol{x}}$ represents the estimation of the unobserved image $\boldsymbol{x}$. Taking $-log(\cdot)$ element-wise and applying Bayes' theorem, the maximization problem above becomes

$$\begin{aligned}
\hat{\boldsymbol{x}} &= \arg\min_{\boldsymbol{x}} - log\,(P(\boldsymbol{x}|\boldsymbol{y})) \\
&= \arg\min_{\boldsymbol{x}} - log\left(\frac{P(\boldsymbol{y}|\boldsymbol{x})P(\boldsymbol{x})}{P(\boldsymbol{y})}\right) \\
&= \arg\min_{\boldsymbol{x}} \big(- log\,(P(\boldsymbol{y}|\boldsymbol{x})) - log\,(P(\boldsymbol{x})) + log\,(P(\boldsymbol{y}))\big). \qquad (3.5)
\end{aligned}$$

In eq. (3.5), $f(\boldsymbol{x}) = -log\,(P(\boldsymbol{y}|\boldsymbol{x}))$ is the negative log-likelihood function whose expression depends on the observation (degradation) model, and $g(\boldsymbol{x}) = -log\,(P(\boldsymbol{x}))$ is the *a priori*

log-distribution of $\boldsymbol{x}$, that only depends on some prior knowledge on the image to estimate and is also called regularization function. Note that $P(\boldsymbol{y})$ does not depend on $\boldsymbol{x}$ and is usually ignored in the estimation of $\hat{\boldsymbol{x}}$.

Often, since the forward model of a particular problem is well defined, most of the design effort of the optimization problem is put into the prior formulation (formulation of $log(P(\boldsymbol{x}))$). Several prior distributions have been well studied in the literature such as ℓ_1 norm (Laplacian distribution prior) that promotes a sparse solution for optimization, ℓ_2 norm (Gaussian distribution prior) promoting smooth solutions, and also total variation norm (Laplacian prior in the derivative or gradient domain) that enforces piece-wise smooth solutions. The choice of the prior depends on the specific problem and characteristics of the latent image.

With these notations, the optimization problem to solve can be expressed as

$$\hat{\boldsymbol{x}} = \arg\min_{\boldsymbol{x}} \ \big(f(\boldsymbol{x}) + g(\boldsymbol{x})\big). \tag{3.6}$$

Using a suitable choice of the regularization function, based for example on the *a priori* statistics of the image to estimate, various proximal operator-based [31] iterative optimization schemes have been extensively studied to solve (3.6), such as the sparse reconstruction by separable approximation (SpaRSA) [375], the two-step iterative shrinkage thresholding (TwIST) [39], the fast iterative shrinkage thresholding algorithm (FISTA) [32–34, 416], the alternating minimization algorithm [384], the Douglas-Rachford splitting method [120, 133, 305, 325], the forward-backward splitting method [277], or the alternating direction method of multipliers (ADMM) [8, 14, 42, 58, 61, 69, 332, 385, 411, 416]. In particular, ADMM, originally introduced around 1975 [140], has been largely used in many applications, by redefining the optimization problem (3.6) into a constrained optimization framework using an Augmented Lagrangian functional to decouple cost functions. ADMM technique will be used in several of the imaging algorithms we present in Chapters 5-6, as it is one of the most versatile method that allows decoupling and shows competitive convergence properties. Therefore the basics of the ADMM optimization algorithm are provided hereafter.

3.4.1.2.1 Alternating Direction Method of Multipliers

ADMM is an iterative convex optimization algorithm, resulting from the fusion of the dual decomposition method with the method of multipliers. The dual decomposition method is a parallelization technique, initially proposed by Dantzig and Wolfe [85, 86], and Benders [35], and consists in splitting a minimization problem into several parallel

minimizations solved separately. The method of multipliers, introduced by Hestenes [165] and Powell [274], originally introduced the use of the augmented Lagrangian for solving constrained optimization problems. ADMM is mainly the blend of the primary ideas behind dual decomposition and method of multipliers techniques. While the seminal ideas of ADMM were proposed by Gabay and Eckstein [140] and Golwinski [146], several developments have been proposed during the last few decades, resulting into a rapidly growing literature [8, 42, 52, 64, 72, 120, 305, 341, 385, 416]. The ADMM algorithm is able to solve constrained optimization problems of the form

$$\begin{aligned} &\underset{\boldsymbol{x},\boldsymbol{z}}{\text{minimize}} \quad f(\boldsymbol{x})+g(\boldsymbol{z}) \\ &\text{subject to} \;\; \boldsymbol{A}\boldsymbol{x}+\boldsymbol{B}\boldsymbol{z}=\boldsymbol{c}, \end{aligned} \tag{3.7}$$

where f and g are assumed to be closed convex functions of variables $\boldsymbol{x}\in\mathbb{R}^n$ and $\boldsymbol{z}\in\mathbb{R}^m$, with $\boldsymbol{A}\in\mathbb{R}^{p\times n}$, $\boldsymbol{B}\in\mathbb{R}^{p\times m}$ and $\boldsymbol{c}\in\mathbb{R}^p$. The associated augmented Lagrangian function is defined as

$$\mathscr{L}_\lambda(\boldsymbol{x},\boldsymbol{z},\boldsymbol{v}) = f(\boldsymbol{x})+g(\boldsymbol{z})+\boldsymbol{v}^T(\boldsymbol{A}\boldsymbol{x}+\boldsymbol{B}\boldsymbol{z}-\boldsymbol{c})+\frac{\lambda}{2}\|\boldsymbol{A}\boldsymbol{x}+\boldsymbol{B}\boldsymbol{z}-\boldsymbol{c}\|_2^2, \tag{3.8}$$

where $\boldsymbol{v}\in\mathbb{R}^p$ is the Lagrangian multiplier, and $\lambda\in\mathbb{R}^+$ is the penalty parameter of the augmented Lagrangian. An equivalent expression of the augmented Lagrangian $\mathscr{L}_\lambda(\boldsymbol{x},\boldsymbol{z},\boldsymbol{v})$ can be obtained by scaling the Lagrangian multiplier $\boldsymbol{u}=(1/\lambda)\boldsymbol{v}$, as follows:

$$\begin{aligned} \mathscr{L}_\lambda(\boldsymbol{x},\boldsymbol{z},\boldsymbol{v}) &= f(\boldsymbol{x})+g(\boldsymbol{z})+\boldsymbol{v}^T(\boldsymbol{A}\boldsymbol{x}+\boldsymbol{B}\boldsymbol{z}-\boldsymbol{c})+\frac{\lambda}{2}\|\boldsymbol{A}\boldsymbol{x}+\boldsymbol{B}\boldsymbol{z}-\boldsymbol{c}\|_2^2 \\ &= f(\boldsymbol{x})+g(\boldsymbol{z})+\frac{\lambda}{2}\left\|\boldsymbol{A}\boldsymbol{x}+\boldsymbol{B}\boldsymbol{z}-\boldsymbol{c}+\frac{\boldsymbol{v}}{\lambda}\right\|_2^2-\frac{1}{2\lambda}\|\boldsymbol{v}\|_2^2 \\ &= f(\boldsymbol{x})+g(\boldsymbol{z})+\frac{\lambda}{2}\|\boldsymbol{A}\boldsymbol{x}+\boldsymbol{B}\boldsymbol{z}-\boldsymbol{c}+\boldsymbol{u}\|_2^2-\text{constant}_{\boldsymbol{v}} \\ &\overset{\text{def}}{=} \mathscr{L}_\lambda(\boldsymbol{x},\boldsymbol{z},\boldsymbol{u}). \end{aligned} \tag{3.9}$$

The ADMM algorithm decouples the augmented Lagrangian into three iterative steps as follows:

$$\boldsymbol{x}^{k+1}\in\arg\min_{\boldsymbol{x}} \;\; \mathscr{L}_\lambda(\boldsymbol{x},\boldsymbol{z}^k,\boldsymbol{u}^k), \tag{3.10}$$

$$\boldsymbol{z}^{k+1}\in\arg\min_{\boldsymbol{z}} \;\; \mathscr{L}_\lambda(\boldsymbol{x}^{k+1},\boldsymbol{z},\boldsymbol{u}^k), \tag{3.11}$$

$$\boldsymbol{u}^{k+1}=\boldsymbol{u}^k+\boldsymbol{A}\boldsymbol{x}^{k+1}+\boldsymbol{B}\boldsymbol{z}^{k+1}-\boldsymbol{c}. \tag{3.12}$$

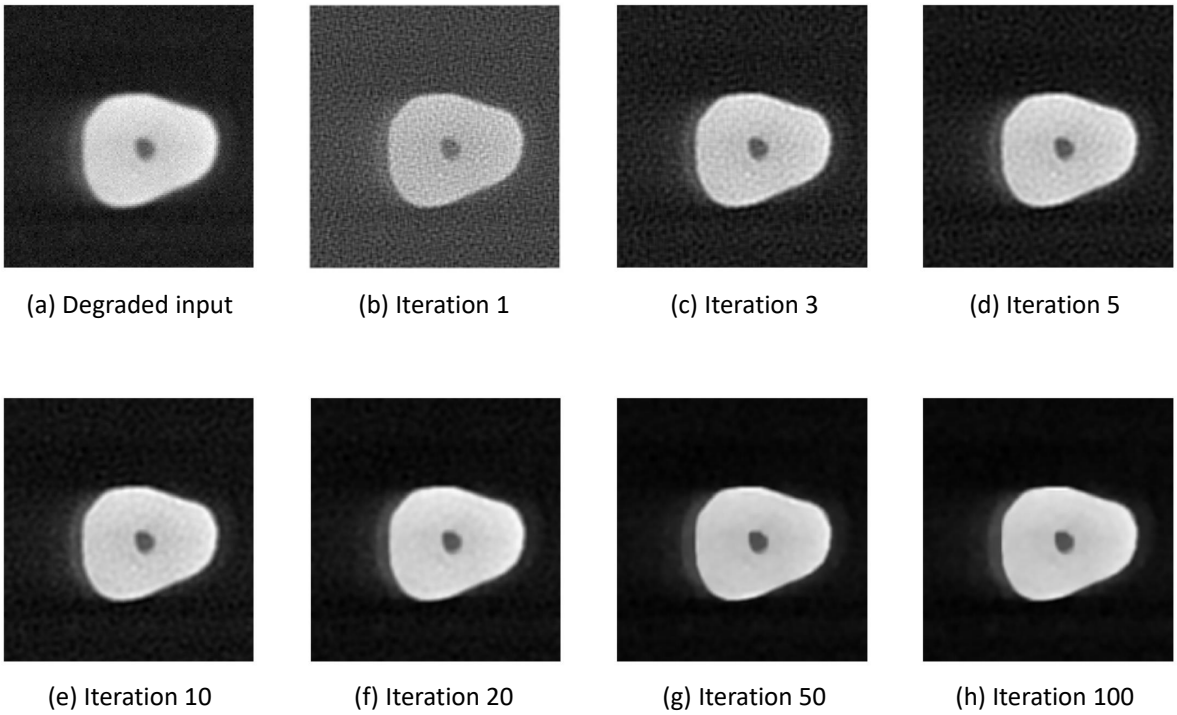

FIGURE 3.8. Iterations of PnP ADMM algorithm for image super-resolution problem using proposed quantum adaptive denoiser (from Chapter 6) as the PnP prior.

The convergence of this iterative scheme has been widely discussed in the literature of convex programming and within various statistical problems [128, 139, 159]. The ADMM technique has a broad spectrum of applications in the context of signal and image restoration applications [61, 133, 168, 249, 325, 416]. Fig. 3.8 shows an example of the ADMM algorithm in the image SR problem.

3.4.1.2.2 ADMM Application to Image Restoration

Let us consider the following general image restoration problem, characterized by the forward model eq. (3.1), where $\boldsymbol{y}$ is the observed image related to the underlying image $\boldsymbol{x}$ through the degradation operator $\boldsymbol{O}$ (remind that, for image denoising $\boldsymbol{O}$ is an identity operator, for image deblurring $\boldsymbol{O} = \boldsymbol{G}$ is generally assumed to be a block circulant with circulant blocks (BCCB) matrix, and for SR problem $\boldsymbol{O} = \boldsymbol{SG}$ is a product of decimation and blurring operator). ADMM can be used to estimate the MAP solution of such an

image restoration task by reformulating it as (3.7) using the following parameterization: $\boldsymbol{z} = \boldsymbol{x}$, thus $\boldsymbol{A} = -\boldsymbol{B} = \boldsymbol{I}_{n\times n}$, $\boldsymbol{c} = \boldsymbol{0}_n$, where $\boldsymbol{I}_{n\times n}$ is the identity matrix of size $n \times n$ and $\boldsymbol{0}_n$ is a zero vector of size n. The associated augmented Lagrangian is given by

$$\mathscr{L}_\lambda(\boldsymbol{x},\boldsymbol{z},\boldsymbol{u}) = f(\boldsymbol{x}) + g(\boldsymbol{z}) + \frac{\lambda}{2}\|\boldsymbol{x}-\boldsymbol{z}+\boldsymbol{u}\|_2^2, \tag{3.13}$$

where $f(\boldsymbol{x}) = -log(P(\boldsymbol{y}|\boldsymbol{x}))$ is the data fidelity term depending on $\boldsymbol{O}$ and $g(\boldsymbol{z})$ the regularization function. To accelerate the convergence, the penalty parameter λ is usually increased at each iteration, by multiplication by a factor of $\gamma > 1$ [62], instead of using a fixed value. At each iteration, ADMM performs the following steps:

$$\boldsymbol{x}^{k+1} = \arg\min_{\boldsymbol{x}} \; f(\boldsymbol{x}) + \frac{\lambda^k}{2}\left\|\boldsymbol{x}-\boldsymbol{z}^k+\boldsymbol{u}^k\right\|_2^2, \tag{3.14}$$

$$\boldsymbol{z}^{k+1} = \arg\min_{\boldsymbol{z}} \; g(\boldsymbol{z}) + \frac{\lambda^k}{2}\left\|\boldsymbol{x}^{k+1}-\boldsymbol{z}+\boldsymbol{u}^k\right\|_2^2, \tag{3.15}$$

$$\boldsymbol{u}^{k+1} = \boldsymbol{u}^k + \boldsymbol{x}^{k+1} - \boldsymbol{z}^{k+1}, \tag{3.16}$$

$$\lambda^{k+1} = \gamma\lambda^k. \tag{3.17}$$

3.4.1.2.3 Plug-and-Play (PnP) Framework

Recently, a breakthrough was made in the literature, enabling the use of state-of-the-art denoisers instead of the proximal operator $g(\boldsymbol{z})$ in eq. (3.15) in the ADMM framework, known as the plug-and-play (PnP) scheme [354]. PnP paves the way of using a wide range of state-of-the-art denoisers such as patch-based dictionary learning methods [123], block-matching 3D filtering (BM3D) [82], non-local means (NLM) [47], high-order variational models [230], etc. Since its initial development, the PnP scheme [354] is largely accepted for signal and image restoration problems due to its extremely promising performance [26, 27, 46, 60, 62, 77, 200, 287, 293, 319, 335, 337, 347, 364, 380, 404]. The primary goal of PnP is to consider a state-of-the-art denoiser as the prior of a constrained optimization process. Interestingly, no prior knowledge is required about the image to estimate to derive the regularization function g, since g is intrinsically defined through the external denoiser used.

The efficiency of ADMM algorithm mainly reposes on its ability of decoupling the optimization processes over each variable, as shown in the previous section. ADMM steps performed at each iteration, (3.14), (3.15) and (3.16), can be interpreted as follows. Eq. (3.14) is originally an inversion step to get the best possible primary image satisfying the data through the data fidelity function $f(\boldsymbol{x})$, while the third step (3.16) updates the

Lagrangian multiplier. The second step (3.15) can be rewritten as

$$\boldsymbol{z}^{k+1} = \arg\min_{\boldsymbol{z}} \; g(\boldsymbol{z}) + \frac{\lambda^k}{2} \left\| \boldsymbol{z} - (\boldsymbol{x}^{k+1} + \boldsymbol{u}^k) \right\|_2^2. \tag{3.18}$$

The expression on the right hand side of (3.18) fundamentally intends to find the solution that optimizes the compromise between the difference between $\boldsymbol{z}$ and $(\boldsymbol{x}^{k+1} + \boldsymbol{u}^k)$ and the regularization function $g(\boldsymbol{z})$. Thus, it can be associated to a denoising problem designed to denoise $(\boldsymbol{x}^{k+1} + \boldsymbol{u}^k)$. Therefore it is possible to rewrite this step as

$$\boldsymbol{z}^{k+1} = \mathscr{D}\left(\boldsymbol{x}^{k+1} + \boldsymbol{u}^k\right), \tag{3.19}$$

where $\mathscr{D}(\cdot)$ is a denoising operator. Hence it is feasible to implement a state-of-the-art denoiser to handle the denoising operation as proposed in [354]. The most interesting feature representing the key benefit of this approach is that this PnP model does not require the prior term $g(\boldsymbol{z})$ explicitly, rather it is indirectly related to the choice of the denoiser $\mathscr{D}(\cdot)$ (see, e.g., [47, 67, 82, 193]). In the literature, it is well established that a state-of-the-art denoiser [47, 67, 82, 193] without having an explicit formulation from an optimization problem shows very good performance compared to a prior based regularization method [14, 58, 332, 385, 411] for image denoising. In Chapter 5, we study this prospect for the Poisson image deconvolution problem, exploiting a quantum adaptive basis as the PnP denoiser.

3.4.1.2.4 Convergence of PnP-ADMM Algorithms

One major challenge of PnP-ADMM algorithms is to prove their convergence, due to the implicit relation between the regularization function $g(\boldsymbol{z})$ and the denoising operator $\mathscr{D}(\cdot)$. Note that the convergence of conventional ADMM has been largely discussed in the literature, primarily in [139] and [120] and more recently in [42] based on the proximal operator [248] or in [167]. The proof of global convergence of PnP-ADMM algorithm [319] has been shown in the case of non-expansive denoisers belonging to the family of symmetric smoothing filters [63, 188, 246, 338]. Yet these conditions are too restrictive for generalisation to all the denoisers. To overcome this issue, a series of works has been published during the last few years showing the fixed point convergence of PnP-ADMM algorithms for bounded denoisers not necessarily symmetric and non-expansive [60, 62, 77, 293, 337, 380, 404], but we stress that all these algorithms were constructed for Gaussian noise model. Still, the convergence of a PnP algorithm is not straightforward as the operation is highly sensitive to the hyperparameter tuning process and can lead to bad outcomes for slight changes in their values. Fig. 3.9 presents such a diverging PnP

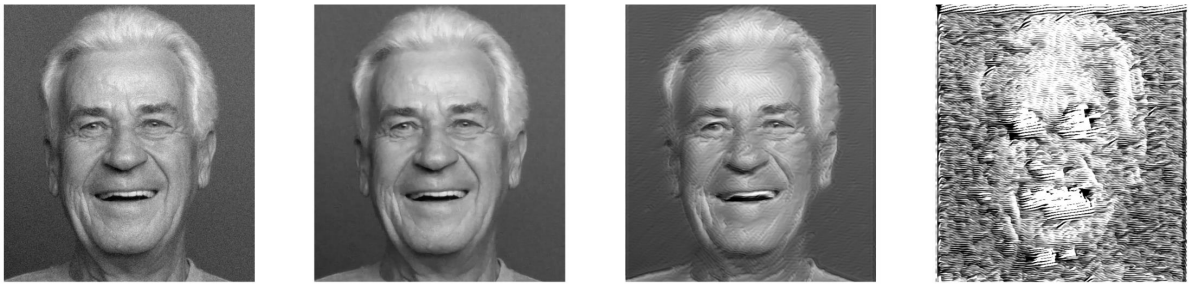

(a) Noisy (b) Iteration 1 (c) Iteration 100 (d) Iteration 800

FIGURE 3.9. Example of a diverging PnP algorithmic scheme [314].

scenario, where with each iteration, the algorithm gradually diverge, and after some iterations, the image gets completely destroyed [314]. We will show that the algorithm we build in Chapter 5 is more robust to the hyperparameter choice and shows numerical proof of convergence for general images.

3.4.1.2.5 Regularization by Denoising (RED) Framework

Although the PnP scheme may sound like an appealing solution for the image retrieval problem, in reality it is a bit complicated. First, this method is not always accompanied by a clear definition of the objective function, since the regularization being effectively used is only implicit, implied by the denoising algorithm. In fact, it is not at all clear that there is an underlying objective function behind the PnP scheme if arbitrary denoising engines are used [59]. Second, parameter tuning of the ADMM scheme is a delicate matter, and especially so under a nonprovable convergence regime, as is the case when using sophisticated denoising algorithms. Finally, being closely coupled with ADMM, the PnP scheme does not provide an easy and flexible way to replace the optimization nature. For this reason, the PnP scheme is not a general tool for treating an arbitrary retrieval problem. Nevertheless, the PnP method has drawn much attention, and rightfully so, as it offers a clear and more efficient path towards harnessing a given off-the-shelf denoising architecture for restoration tasks [46, 62, 87, 294, 336, 354, 380].

The Regularization by Denoising (RED) [286] scheme is a variation of the PnP framework, with a more flexible alternative of the optimization method to use, not as tightly coupled to a specific strategy, as in the case of the PnP relying on ADMM. The RED generalizes the PnP scheme, offering a systematic use of such off-the-shelf denoising engines as regularizers, relying on a general structured smoothness penalty term harnessed to regularize any desired restoration problem. Unlike PnP, RED proposes

an explicit construction of the regularization function of the form of an image-adaptive Laplacian based on an external denoiser. More specifically, the regularization function is defined as

$$g(\boldsymbol{z}) = \frac{1}{2}\boldsymbol{z}^T\Big(\boldsymbol{z} - \mathscr{D}(\boldsymbol{z})\Big), \tag{3.20}$$

in which the denoising engine itself is applied on the candidate image $\boldsymbol{z}$, and the penalty induced is proportional to the inner product between this image and its denoising residual. This defined smoothness regularization is effectively done using an image-adaptive Laplacian, which in turn draws its definition from the arbitrary $\mathscr{D}(\cdot)$ image denoising engine. Furthermore, the gradient of the regularization term is manageable, given as the denoising residual [286], *i.e.*, $\nabla g(\boldsymbol{z}) = \boldsymbol{z} - \mathscr{D}(\boldsymbol{z})$, and leads to a reasonable expression for any restoration task while calling the denoising engine iteratively.

Apart from adding more flexibility to the process, RED offers an explicit adaptive Laplacian-based regularization functional, making the overall Bayesian objective function clearer and better defined. RED can incorporate any image denoising scheme and can treat general restoration problems very effectively when an overall algorithm with a simple framework is developed. The potential of the RED scheme has been demonstrated in various restoration works using steepest descent method [286], fixed-point strategy [78, 329], ADMM [280, 286], etc. However, RED denoisers should be symmetric Hessian matrices, which is a limitation of this approach. In Chapter 6, we will show that the real medical computed tomography image SR problems can be solved efficiently under this RED framework exploiting a quantum denoiser as the RED prior.

3.4.1.2.6 Convergence of RED-ADMM Algorithms

An important advantage of RED over the PnP scheme is that it guarantees a more reliable and stable convergence of the iterative algorithms under some circumstances. For convex data-fidelity terms and non-expansive denoisers the fixed-point convergence of the RED scheme is proven in [286, 330]. The convergence of RED algorithms can also be analyzed using monotone operator theory. In particular, it can be shown that for a convex function g and a nonexpansive denoiser $\mathscr{D}(\cdot)$, RED steepest descent converges sublinearly to a set of $\boldsymbol{z}$ satisfying the equilibrium condition $\nabla g(\boldsymbol{z}) = \boldsymbol{z} - \mathscr{D}(\boldsymbol{z})$ [329], in this setting ∇g is known as the "score" of this distribution. This negative gradient describes the steepness of the log-likelihood function and hence the sensitivity to changes in $\boldsymbol{z}$. From this, we see that it balances changes in the log-likelihood against the update step $\boldsymbol{z} - \mathscr{D}(\boldsymbol{z})$ [280]. Very recently the works [169, 226] extend this limit even for nonconvex

data-fidelity terms and expansive image denoisers, offering a stable convergence for a monotone RED algorithm.

3.4.2 Learning-Based Methods

Complementary to the aforementioned approaches, learning-based methods for determining a non-linear mapping that restores the image while adapting parameter choices to an underlying training image set have been developed. Particularly important in this class are techniques that employ deep neural networks. The history of using neural networks for blind deblurring actually dates back to the last century [326]. The incredible success of deep learning over traditional image processing algorithms, for example, on vision [161, 210], as well as challenging games such as Go [311] and Starcraft [357], has initiated a general data-driven mindset. It is currently prevalent to replace simple principled models with purely datadriven pipelines, trained with massive labeled data sets. In particular, deep neural networks can be trained in a supervised way end-to-end to map inputs to predictions. The benefits of data-driven methods over model-based approaches are twofold: first, purely data-driven techniques do not rely on analytical approximations and thus can operate in scenarios where analytical models are not known. Second, for complex systems, data-driven algorithms are able to recover features from observed data which are needed to carry out inference [36].

More recently, deep learning (DL)-based methods, especially the convolutional neural network (CNN) based architectures have been known for their very competitive denoising performance. Large modeling capacity and robust training procedure make CNN attractive for image denoising and has been explored with various networks, such as a fast flexible learning method [71], deep residual learning [162, 405], a fast and flexible denoising with a tunable noise level [407], denoising autoencoders with a local unsupervised criterion [356], multi layer perceptron (MLP) method applied to image patches

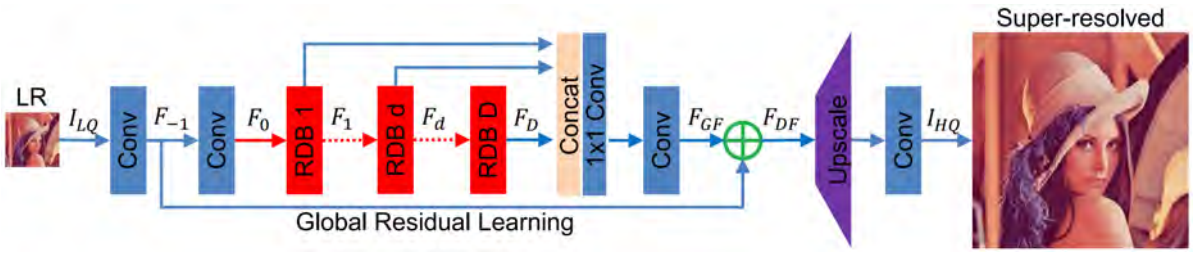

FIGURE 3.10. The architecture of a residual dense network for image super-resolution [414].

[51], random shrinkage field-based architecture combining the image model and the optimization algorithm in a single unit [301], operational neural networks (ONN) based models [192, 240, 241] with non-linear generalized CNN architecture, and others. These benchmark DL networks have proven their efficiency in image denoising, exploiting noisy-clean image pairs in the learning process.

Due to the successes in many computer vision and denoising applications in the past few years, deep neural networks have been used more frequently for solving image restoration tasks [28, 40, 96, 163, 223, 231, 252, 283, 291, 339, 379, 402]. Fig. 3.10 shows an example of a deep network architecture for image super-resolution problem. To overcome the non-interpretability of end-to-end deep learning-based restoration approaches [379], many approaches resort to unrolling an optimization algorithm as a static cascade scheme with a fixed number of steps in which specific neural networks are integrated into different steps [199, 303, 402, 406]. The deep neural network components usually model the operators only corresponding to the priors/regularizers (*e.g.*, proximal projectors [283]). In these static model structures, the deep neural network-based operators in each step are learned specifically for the intermediate output from the previous step. Based on this philosophy, DL algorithms [96, 97, 183, 331, 398] achieved state-of-the-art performances learning the mapping functions from observed degraded or low-resolution (LR) images to the original or high-resolution (HR) images. Deep image prior [346], deep CNN denoiser prior [101, 402], deep gradient descent optimization [149], sparse coding based deep network [368], residual learning [224, 362], dense residual network [414], self-organized operational neural networks [241], variational expected maximization network to quantify the uncertainty of learned image prior [254], deep network for guided super-resolution for single-photon depth imaging [292], accelerated convolutional neural network by reformulate the mapping layer [98], deep feature alignment using geometric information and depth information [43], deep convolutional network inspired by VGG-net [190], densely connected residual network with Laplacian attention [22], deep residual network with block channel attention mechanism [410], etc., are some of the well-known DL networks with proven efficiency in image restoration over the conventional model-based approaches, exploiting a training dataset in the learning process.

3.4.3 Model-Based Deep Learning or Hybrid Methods

Completely separating existing literature into model-based versus data-driven is a daunting, subjective and debatable task. In general, all model-based approaches are

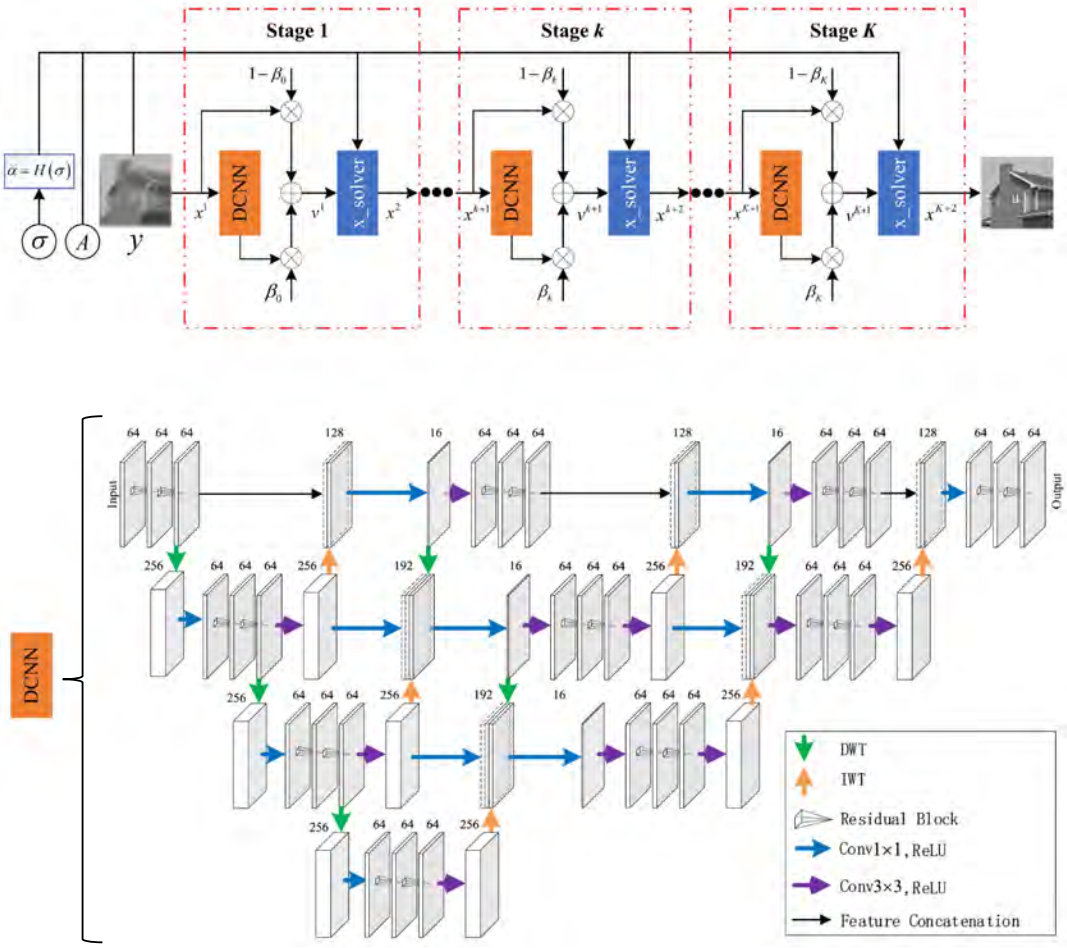

FIGURE 3.11. The architecture of a deep learning-aided inference system for image restoration using the DCNN network as the RED denoiser in the iterative algorithm [194].

fairly successful in tackling the image denoising tasks, including proper interpretation of their roles. However, these schemes require conducting a costlier computation process and manual tuning of several hyperparameters, which are the primary challenges of these strategies. On the other side, training a CNN is not straightforward. The performance largely depends on the number of layers, the kernel size and the learning rate. Deeper network structures may provide better results but exponentially increase the training complexity [162]. Thus, network structures are in most cases determined empirically, which makes them suffer from a lack of interpretation of their true functionality. Instead of tilting towards any one these approaches a recent breakthrough lies in the middle ground giving a useful overview of these landscapes. The considered families of methods incorporate domain knowledge in the form of an established model-based algorithm

which is suitable for the problem at hand, while combining capabilities to learn from data via deep learning techniques. Benefiting from CNN's powerful representation ability, this new concept, known as unfolding [151], gathering the advantages of both model and DL-based approaches, is currently gaining more attention due to its explanatory properties.

Techniques for studying and designing inference rules in a hybrid model-based/data-driven fashion can be divided into two main strategies: the first is to use model-aided networks, which utilize deep neural networks for inference; however, rather than using conventional DL network architectures, here a specific network tailored for the problem at hand is designed by following the operation of suitable model-based methods. The second strategy DL-aided inference systems, uses conventional model-based methods for inference; however, unlike purely model-based schemes, specific parts of the model-based algorithm are augmented with DL tools, allowing the resulting system to implement the algorithm while learning to overcome partial or mismatched domain knowledge from data. Fig. 3.11 shows such a DL-aided inference system for image restoration. More precisely, the main idea of such frameworks is to construct a DL network starting from a classical algorithm.

This approach has been recently successfully explored in the literature, leading to superior restoration performance over the classical peer for denoising, such as BM3D-NET [383] network is designed on the BM3D framework, LKSVD [300] scheme follows the principles of dictionary-learning, Deep-NLM [225] model built on a NLM architecture, the deep graph-convolutional network GCDN [348] generalizes the classic convolution to arbitrary graphs, to cite few.

There has been exciting recent explorations of neural network architectures by unrolling iterative algorithms [183, 304, 308, 352]. During the past few years the implementation of the Deep-CNN networks [28, 40, 163, 223, 231] has been introduced for image denoising [402, 405] and further extended to the PnP or RED schemes [70]. These Deep-CNN networks give several advantages such as reconstruction accuracy and convergence speed [145]. However, more often they suffer from some drawbacks. First, such denoisers should be trained using the noise variance in each iteration. Hence, during the iterative process of the PnP or RED framework, the noise variance is usually unknown since it varies at each iteration, and leads to a divergence of the algorithm for a pre-trained Deep-CNN architecture [314]. Second, the training procedure is very costly since Deep-CNN denoisers require expensive retraining whenever the noise level or noise type change. Also, each iteration involves a Deep-CNN denoising process, so using a large

neural network and/or too many iterative operations leads to a time consuming task. Third, the theoretical aspects of Deep-CNN denoiser-based PnP or RED models are still not clear. Later on more robust unfolded PnP or RED networks have been introduced in the literature, for example, deep plug-and-play network combining physical and learned models [186], an unfolded PnP network with three complementary deep priors [396], deep RED unfolded network [194], deep equilibrium learning for regularization by denoising [226, 376], that solve the convergence problem. Other widely known deep unfolded image restoration networks are deep Wiener deconvolution network [99], unfold optimization scheme with deep priors [95], deep unfolded network for total-variation regularization in the gradient domain [221, 222], deep unfolded robust principle component analysis [313], regularized residual networks with long and short skip-connections [315], unfolded one-bit quantizers [189], deep network for alternating direction method of multipliers [387], deep unfolding of the MAP inference via a half-quadratic splitting algorithm [403], deep network that exploit the inherent non-local self-similarity via variational methods [212], deep neural networks as beamformers in ultrasound imaging [351], statistical Bayesian algorithm into a new deep learning architecture [195], hierarchical graph representation with unsupervised learning [37], and unfolded graph neural networks for weighted minimum mean squared error [75], graph-based temporal network structures [156]. Exploiting the advantages of model-and data-driven strategies, these unfolded deep models demonstrated benchmark performances in the literature. In Chapter 7, we explore this direction of model-based deep learning or hybrid methods by unfolding a baseline algorithm based on the principles of quantum many-body physics. We thus show that we can build a robust DL model inspired by the algorithm of Chapter 6, which compares favorably with other state-of-the-art DL methods from the literature.

3.4.4 Related Works on Quantum Mechanics-Based Algorithm

In 1982, Feynman proposed a novel computation model, named quantum computers, which can efficiently solve some problems that are believed to be intractable on classical computers [131]. He suggested that the superposition principle of quantum mechanics enables exponentially many computations to be performed in parallel [121, 324]. Thus, in principle, quantum processors using the full power of quantum mechanics may be enormously faster than today's classical computers. After that, many researchers have specified various aspects of such quantum computers. Later, a significant breakthrough came with the Shor's algorithm [309], which factors large numbers with exponential efficiency compared to any known classical algorithm. Another such example is the

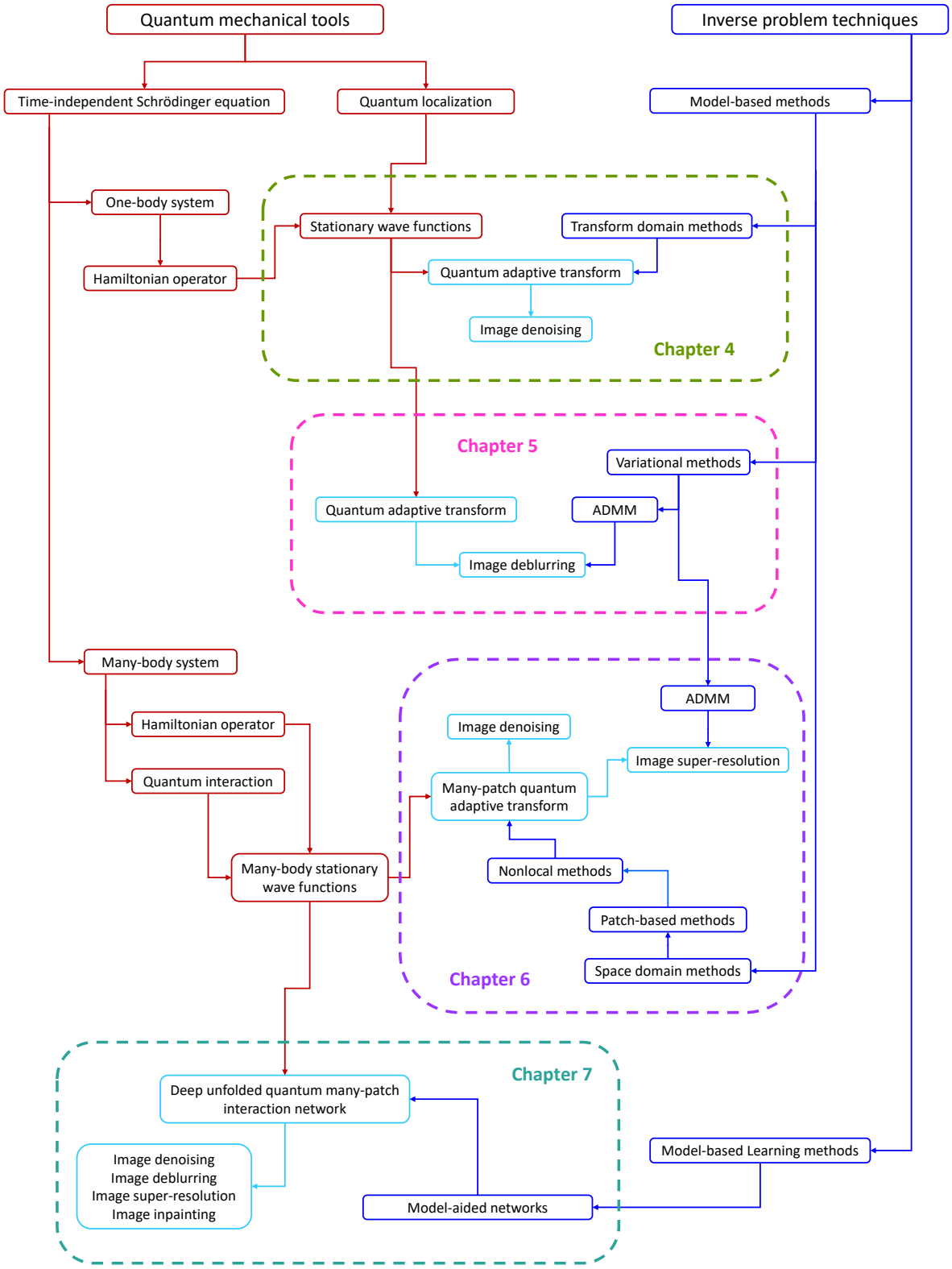

FIGURE 3.12. Schematic structure of this thesis by exploiting various image restoration techniques and quantum mechanical tools.

Grover's algorithm [153], which speeds up the search in an unsorted database. These ground-breaking results have attracted much attention in the scientific community and many experimental proposals have been explored to realize such a quantum computer.

The development of quantum computer caused people's interest to study quantum imaging which refers to the use of quantum computers to process images. Many researchers have proposed several kinds of quantum imaging algorithms, such as geometric transformation [177, 179, 207, 361], color transformation [180, 412], image scrambling [178, 181, 181], quantum image watermark [173, 182, 316, 317, 409], image segmentation [218, 353], feature extraction [413], edge detection [388], quantum image encryption [171, 363, 417], quantum sound processing [284, 285], quantum image processing [172, 176, 327, 382], computational imaging [18], quantum convolutional neural networks [2, 55, 81], etc. Their efficiency are theoretically higher than their corresponding classical schemes. Despite these gains, all these schemes remain primarily theoretical achievements and present abstract frameworks. To date, the large-scale quantum computer is still a distant goal and seems to remain so in the near future.

A new point of view was presented in the early 2000s by Y. Eldar *et al.* [126], introducing a new concept called quantum mechanics-based algorithm in the imaging domain. In [126], they propose the concept of a quantum measurement for a signal processing tasks. In contrast to works in fields like quantum computing and quantum information theory, quantum mechanics-based algorithms do not entirely depend on the physics associated with quantum mechanics and give us the freedom to impose quantum mechanical constraints that we find useful for imaging problems. Indeed, the implementation of such quantum principles in imaging problems can significantly boost the performance of classical algorithms. The next big breakthrough came in 2013 by Ç. Aytekin *et al.* [24], where they proposed an algorithm for automatic object extraction using the solutions of Schrödinger equation. After that, A. Youssry *et al.* published a series of papers on object detection [389] and vessel segmentation in retinal images [390] by using the time-dependent Hamiltonian operator as an unitary time evolution operator, and classical image segmentation algorithm by associating each pixel with a quantum harmonic oscillator [391]. Other proposed works in this domain are signal reconstruction algorithms using spectral quantities associated with some self-adjoint realization of the Schrödinger operator [127, 164], pulse shaped signal processing using the discrete spectrum of the Schrödinger operator [203, 270], image representation and denoising by decomposing the images into 1D signals before applying the Schrödinger operator in 1D [185], the region-of-interest characterization based on the Schrödinger

equation's solutions for Magnetic Resonance Imaging (MRI) [57] and Magnetic Resonance Spectroscopy (MRS) [56], and spectral data denoising using localized wave functions for MRS images [204]. From the literature survey we can observe that all these quantum mechanics-based algorithms are primarily designed for image segmentation problem or the characterization of 1D signals. Not only that, the exploitation of the quantum theory in these works is quite limited.

The quantum mechanical framework opens up great opportunities for developing new or modifying existing signal or imaging processing algorithms by drawing a parallel between quantum tools and signal or imaging processing schemes and exploiting the rich mathematical structure of quantum mechanics without requiring a physical implementation based on quantum theory. In this thesis, we will explore this paradigm of quantum mechanics-based signal or image processing algorithm borrowing principles and axioms of quantum mechanics. This framework provides a structure to deal with various traditional imaging problems, leading to new tools for image processing with applications in areas of computer vision, medical imaging, surveillance, etc. In the following chapters, we will study these different prospects of quantum mechanics-based algorithms for signal or image processing. Fig. 3.12 schematizes the structure of this thesis and gives an overview of how quantum mechanical tools are combined with imaging techniques to solve image restoration problems.

CHAPTER 4

Quantum Mechanics-Based Signal and Image Representation: Application to Denoising

Contents

* This chapter presents material from the journal paper [114].

Overview

Decomposition of digital signals and images into other basis or dictionaries than time or space domains is a very common approach in signal and image processing and analysis. Such a decomposition is commonly obtained using fixed transformations (e.g., Fourier or wavelet) or dictionaries learned from example databases or from the signal or image itself. In this chapter, we investigate in detail a new approach of constructing such a signal or image-dependent bases inspired by quantum mechanics tools, i.e., by considering the signal or image as a potential in the discretized Schrödinger equation. To illustrate the potential of the proposed decomposition, denoising results are reported in the case of Gaussian, Poisson, and speckle noise and compared to the state-of-the-art algorithms based on wavelet shrinkage, total variation regularization or patch-wise sparse coding in learned dictionaries, non-local means image denoising, and graph signal processing. Finally, application to clinical CBCT dental image denoising is presented.

4.1 Introduction

4.1.1 Image Representation and Related Works

In number of applications, processing or analyzing signals and images require the use of other representations than time or space. While the most famous transformation still remains the Fourier transform, other representations have been proposed to overcome the non-localization in time or space of the Fourier basis vectors. The most used time-frequency representations are the short time Fourier and the wavelet transforms [104, 106]. Most often (*e.g.*, image compression, restoration, reconstruction, denoising or compressed sensing), such transforms are associated with the concept of sparsity, *i.e.*, their ability to concentrate most of the signal or image energy in a few coefficients. To reinforce the sparsity, overcomplete dictionaries have also been explored over the last decades, such as the wavelet frames or more recently patch-based or convolutional dictionaries learned from a set of training signals or images [11]. The latter has been shown to be of particular interest in image denoising [124].

4.1.2 Contributions

In this chapter, we investigate a novel signal and image representation, through a dedicated basis extracted from the signal or image itself, using concepts from quantum mechanics. Compared to fixed basis such as Fourier, discrete cosinus, wavelets, curvelets, etc, or dictionary learning that generally needs a training database, the proposed approach has the advantage of computing a transform adapted to the signal or image of interest.

Several attempts of translating quantum principles in image or signal processing applications have been proposed in the literature. One may note the seminal work in [126], or, more recently, the interest of quantum mechanics in image segmentation [24, 389] or in pulse-shaped signal analysis [203, 204]. More related to our work, we note that there was a recent attempt to use quantum mechanics in the same context in [57, 185]. Although there are similarities between the two approaches, there are also some important differences. The authors in [57, 185] start from a continuous mathematical representation of the signal, and the discretization only occurs at the end of the process. The processing of a large image in these papers is done by decomposing it into lines and columns to get 1D signals, while the proposed work is applied block-wisely, which offers a more efficient solution for image denoising given that the correlation between

neighbouring pixels is preserved. Additionally, unlike [57, 185], our method fully takes into account the quantum localization phenomenon, a subtle effect due to quantum interference which makes the distribution of the eigenfunctions of the Schrödinger operator strongly dependent on noise, and has important effects on the denoising process. We also use the physics of the problem to identify the optimal domain of applicability of such methods.

The proposed framework reposes on the discrete version of the Schrödinger equation for a quantum particle in a potential. In our case, the potential is represented by the signal samples or the pixel values. The bases used to decompose the signal or the image are directly computed from the signal and image itself and correspond to the wave function representing the stationary solutions of the Schrödinger equation. These wave functions have interesting properties of temporal or spatial localization and of frequency dependence on the value of the potential. In particular, they present higher frequencies for low potential values, thus allowing an original signal or image decomposition.

The proposed method has a certain formal similarity with graph signal processing methods [73, 243, 259, 262, 307], which use a graph Laplacian constructed from the signal to build an adaptive basis. However, graph signal processing constructs the graph Laplacian to emphasize the similarities between neighbouring pixel values, while in the proposed method the adaptive basis is solely related to the individual pixel values, resulting into very different adaptive bases with different properties.

Within the proposed framework, the frequency and localization properties of the basis can be controlled through several parameters, thus ensuring flexibility in applications such as denoising. A detailed description of the behavior of the proposed transform and denoising method with respect to the choice of these parameters is provided, allowing to gain insight about the practical consequences in signal and image processing of the quantum mechanical principles involved. Furthermore, the proposed transform embedded in a denoising algorithm shows promising results in different noise scenarios (additive Gaussian, Poisson or speckle noise). Finally using different signals and images, comparisons with several state-of-the-art methods are performed.

The remainder of the chapter is organized as follows. Section 4.2 and 4.3 respectively give the details of the adaptive transform design and its application to denoising. Results and comparisons are provided in Section 4.4. Application to clinical CBCT dental image denoising is presented in Section 4.5 and concluding remarks are finally reported in Section 4.6.

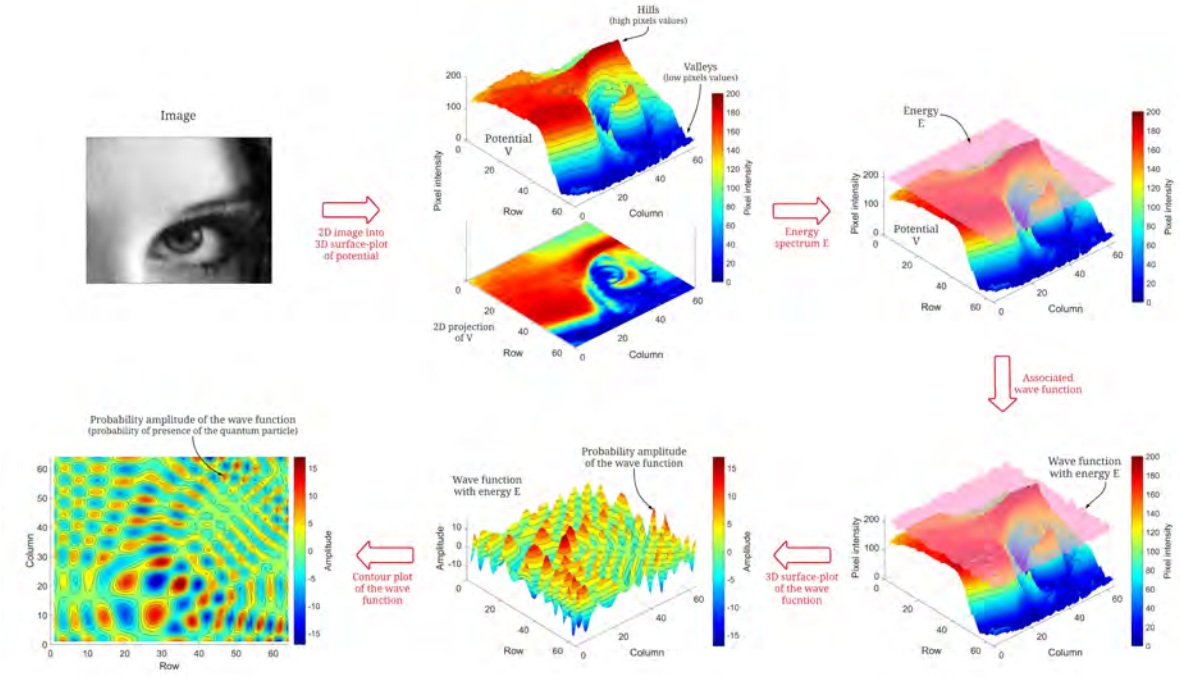

FIGURE 4.1. Relationship between quantum mechanics and image representation: example on *Lena* image.

4.2 Adaptive Basis from Quantum Mechanics

4.2.1 General Framework

The main idea of the proposed method is to describe a signal or an image onto a specific basis which is constructed through the resolution of a related problem of quantum mechanics: the probability of presence of a quantum particle in a potential related to the signal or image. While the motivation of using quantum mechanics in this particular context is not straightforward, its main purpose is to produce a basis of oscillating functions with the following properties: 1) the oscillation frequency increases with a parameter of the basis corresponding to the energy, 2) for a given basis function, the oscillation frequency is higher for low values of the signal. The adopted strategy will then be to threshold a noisy signal in energy once expanded in this basis: this will automatically keep higher frequencies for low pixel values, and lower frequencies for high pixel values. Intuitively, one could expect that this method is especially efficient for signal-dependent noise, stronger for high signal values, such as, for instance, Poisson noise.

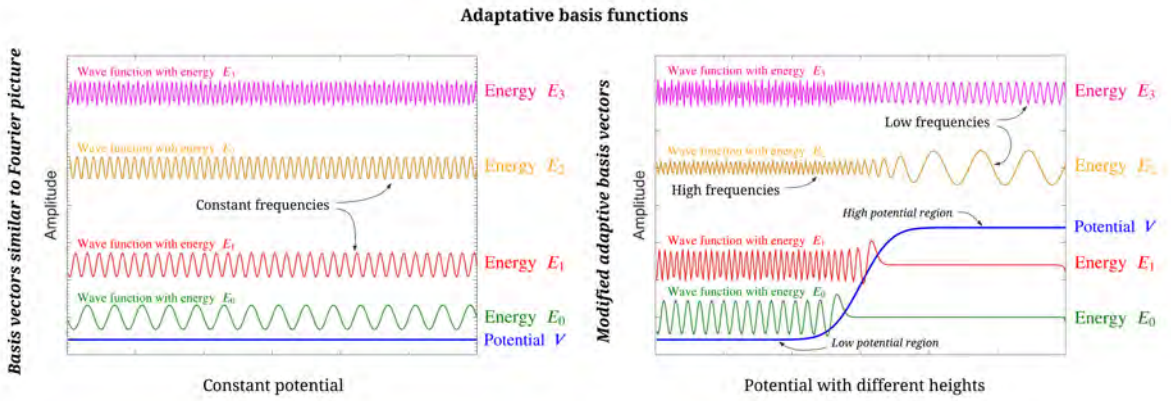

FIGURE 4.2. Relationship between the frequency of the adaptive basis functions and the height of the potential.

4.2.2 Adaptive Transform for Signals or Images

Our method uses quantum mechanics as a tool for building an adaptive basis suitable for denoising applications. The basics of quantum mechanics which are useful for our purpose have already been explained in Chapter 2, we refer the interested reader to more extensive introductions to this vast field of physics [80, 132, 206]. Our formalism is based on the resolution of the Schrödinger equation of non-relativistic quantum mechanics. This equation determines the wave function $\psi(z)$ which belongs to the Hilbert space of L^2-integrable functions, z being *e.g.* a spatial coordinate. The function $|\psi(z)|^2$ gives the probability of presence of the particle, which implies that $\int |\psi(z)|^2 \mathrm{dz} = 1$. In Chapter 2, we discussed the properties of these wave functions.

The basic idea of the proposed method is to consider the signal or image as a potential $V(z)$ for a quantum system, as illustrated in Fig. 4.1. The 3D surface plot of a 2D image is shown in Fig. 4.1. This surface will act as the potential of the system, where we consider pixel intensity as the height of the potential (*i.e.,* along the z-axis). It is clearly visible that there are many hills and valleys in the potential which are associated with the high and low pixel values respectively. If a quantum particle with energy E probes this surface, then the probability of presence of this quantum particle at some position on the surface will be determined by the wave function $\psi(z)$. Unlike the classical picture where one can precisely determine the position of a classical particle, the quantum theory only gives a probability of finding a quantum particle at some point. The stationary Schrödinger equation corresponds to the probability of presence of a stationary quantum

particle with energy E in a potential $V(z)$, the associated wave function $\psi(z)$ satisfying [302]:

$$-\frac{\hbar^2}{2m}\nabla^2\psi = -V(z)\psi + E\psi, \tag{4.1}$$

with m the mass of the quantum particle, $\hbar$ the Planck constant that are both parameters of the problem, and ∇^2 the Laplacian operator.

To illustrate the nature of the solution of (4.1), let us consider a simple case corresponding to a constant potential V and to the wave function $\psi(z)$ following a periodic boundary condition, *i.e.,* $\psi(z+L) = \psi(z)$, where L is the periodicity. Solving equation (4.1) under the above conditions is trivial, all solutions having the form:

$$\psi(z) = A\ e^{i\frac{\sqrt{2m(E-V)}}{\hbar}z}, \tag{4.2}$$

where A is a given amplitude. Each solution ψ is associated with a specific value of E, with E taking discrete values, all higher than V. If space is discretized in n values, there will be n solutions and E takes only n different values.

In the case of a more intricate 1D potential, where V is no more a simple constant and depends on position, (4.1) implies that the relation (4.2) will still hold locally, with an amplitude and phase depending on position. This means that the stationary solutions of (4.1) are locally oscillatory functions with an oscillation frequency dependent on the local value of V for a given energy E, with a frequency proportional to $\sqrt{E-V}$. This is illustrated in Fig. 4.2, where two different potentials are taken into account in the Schrödinger equation (4.1): a constant potential and a potential with non-uniform heights. For the constant potential, the solutions are just plane waves satisfying (4.2). All solutions are indexed by the values of the associated energy, and higher energy translates in higher frequency of oscillations. This frequency is the same for all positions for a given wavefunction. For a non constant potential which depends on position (right panel of Fig. 4.2), the oscillation frequency still increases with higher values of E, but at the same time a given stationary solution of (4.1), which corresponds to the physical wavefunction, contains different local oscillation frequencies according to the local value of V. Thus, although at each local position the frequency increases with E, it does so in a different way from place to place according to the local value of V. In other words, for a given energy E the wave function $\psi(z)$ associated with a quantum particle will use a higher frequency to probe a low potential region in comparison with a high potential region. In the regions where $E-V$ is negative, (4.2) leads to exponentially decreasing functions which quickly become constant (see e.g. the solutions for E_0 and E_1 in the right side of Fig. 4.2).

In 2D, (4.2) is not exactly valid, but the solutions of (4.1) will still have typically an oscillation frequency proportional to $\sqrt{E-V}$. This is illustrated in Fig. 4.1 (bottom panels) where the wave function frequency of oscillation is clearly seen to increase in the regions of low potential.

To summarize, the global properties of the wavefunctions which form the proposed adaptive basis are the following:

(i) they are oscillating functions indexed by the energy E,

(ii) the local frequency is typically proportional to $\sqrt{E-V}$, thus increasing with E while differing locally for the same wavefunction depending on the local value of $E-V$,

(iii) the precise dependence on the frequency of oscillation with respect to $E-V$ is tuned by the parameter $\hbar^2/2m$.

In the application addressed herein, the Schrödinger equation (4.1) is just a way to obtain an adaptive basis possessing these properties, which can further be used independently of its quantum mechanical nature as a tool for signal or image processing.

The basis of eigenvectors of (4.1) naturally describes with different frequencies the different parts of the signal or image, in contrast to e.g the Fourier or wavelet bases. As said above, the precise relation between the local frequency of the eigenvectors and the value of the signal or image pixel is governed by the parameter $\hbar^2/2m$. In the physical problem of quantum mechanics, this quantity is linked to Planck's constant and the particle mass, but in our framework it is a free parameter. It should be chosen with care, as extreme values are clearly inadequate. Indeed, as the problem is discretized there is a maximal frequency in the problem, linked to the inverse of the discretization step. If $\hbar^2/2m$ is very small, the local frequencies $\sqrt{2m(E-V)}/\hbar$ become very high even for low values of the energy, the maximal energy becomes very low, and the basis does not explore properly high values of the signal or pixels of the image. On the other side for very large values of $\hbar^2/2m$, the local frequencies become smaller and smaller at fixed energy, the maximal energy becomes larger and larger, and eventually when $\hbar^2/2m$ tends to infinity most vectors of the adaptive basis are so high above the signal or image pixel that they do not discriminate between low and high values, becoming closer and closer to the standard Fourier basis vectors. Therefore it is crucial to tune the free parameter $\hbar^2/2m$ in the right way.

4.3 Proposed Method for Denoising Applications

4.3.1 Explicit Construction of the Adaptive Basis

In operator notation, (4.1) corresponds to $H\psi = E\psi$ with $H = -\frac{\hbar^2}{2m}\nabla^2 + V$ the Hamiltonian operator. The energy E of the particle in (4.1) labels the solutions of the problem. Solutions of this stationary Schrödinger equation in a bounded domain correspond to a discrete set of energy levels, from a minimal energy to infinity.

Solutions of (4.1) form a basis of the Hilbert space to which the wavefunctions belong. This space is infinite-dimensional for continuous values of the position y in (4.1). However, we are interested in signal or image processing applications, where the space is discretized in a finite number of points. Specifically, we assume that the potential V is represented by the value of signal sample or image pixel $\boldsymbol{x}$. In the case of a discretized problem, the operators become finite matrices and the resolution of (4.1) is equivalent to diagonalizing the Hamiltonian matrix.

Specifically, one has, following (4.1), $\boldsymbol{H} = -\dfrac{\hbar^2}{2m}\nabla^2 + \boldsymbol{x}$, with:

- the potential V represented by $\boldsymbol{x}$ (the signal or the image),
- if $\boldsymbol{x}$ is a signal of size n, then the size of $\boldsymbol{H}$ is $n \times n$,
- if $\boldsymbol{x}$ is an image of size $n \times n$, it is transformed into a vector (in lexicographical order) of size n^2 and $\boldsymbol{H}$ is a $n^2 \times n^2$ matrix,
- in both cases ($\boldsymbol{x}$ is a signal or an image), $\boldsymbol{x}$ is considered in a vector form.

For a 1D signal, we have:

- numerical derivatives of $\boldsymbol{\psi}$: $(\nabla\boldsymbol{\psi})_i = \boldsymbol{\psi}[i+1] - \boldsymbol{\psi}[i]$,
- numerical Laplacian of ψ: $(\nabla^2\boldsymbol{\psi})_i = \boldsymbol{\psi}[i+1] - 2\boldsymbol{\psi}[i] + \boldsymbol{\psi}[i-1]$.

Thus, $(\boldsymbol{H}\boldsymbol{\psi})_i = -\dfrac{\hbar^2}{2m}(\boldsymbol{\psi}[i+1] - 2\boldsymbol{\psi}[i] + \boldsymbol{\psi}[i-1]) + \boldsymbol{x}[i]\boldsymbol{\psi}[i]$
$\Longrightarrow (\boldsymbol{H}\boldsymbol{\psi})_i = \left(\boldsymbol{x}[i] + 2\dfrac{\hbar^2}{2m}\right)\boldsymbol{\psi}[i] - \dfrac{\hbar^2}{2m}(\boldsymbol{\psi}[i+1] - \dfrac{\hbar^2}{2m}\boldsymbol{\psi}[i-1])$.
Therefore, $(\boldsymbol{H}\boldsymbol{\psi})_i = \sum_{j=i-1}^{i+1}\boldsymbol{H}[i,j]\boldsymbol{\psi}[j]$, for $i = 1, 2, 3, \cdots, n$.

where,

$$\boldsymbol{H}[i,j] = \begin{cases} \boldsymbol{x}[i] + 2\dfrac{\hbar^2}{2m} & \text{for } j = i, \\ -\dfrac{\hbar^2}{2m} & \text{for } j = i \pm 1, \\ 0 & \text{otherwise.} \end{cases} \tag{4.3}$$

where $\boldsymbol{x}[i]$ represents the i-th component of a signal and $\boldsymbol{H}[i,j]$ is the (i,j)-th element of the Hamiltonian matrix.

The resolution of (4.1) is thus equivalent to finding eigenvectors and eigenvalues of the discretized Hamiltonian matrix $\boldsymbol{H} \in \mathbb{R}^{n \times n}$ written as:

$$\boldsymbol{H} = \begin{bmatrix} \boldsymbol{x}[]1] + 2\dfrac{\hbar^2}{2m} & -\dfrac{\hbar^2}{2m} & & & \\ -\dfrac{\hbar^2}{2m} & & & & \\ & \ddots & \ddots & \ddots & \\ & & & & -\dfrac{\hbar^2}{2m} \\ & & & -\dfrac{\hbar^2}{2m} & \boldsymbol{x}[n] + 2\dfrac{\hbar^2}{2m} \end{bmatrix}$$

For a 2D image $\boldsymbol{x} \in \mathbb{R}^{n \times n}$ the methodology is similar. In (4.1), the Laplacian operator should be replaced by its discrete version, following the standard numerical definitions of the gradient operator:

$$\begin{aligned} \nabla_{\mathrm{h}} \boldsymbol{x}[i,j] &= \boldsymbol{x}[i+1,j] - \boldsymbol{x}[i,j] && \text{if } i < n \\ \nabla_{\mathrm{v}} \boldsymbol{x}[i,j] &= \boldsymbol{x}[i,j+1] - \boldsymbol{x}[i,j] && \text{if } j < n \end{aligned}$$

where ∇_{h} and ∇_{v} are associated to the horizontal and vertical gradients. The boundary conditions correspond simply to a zero padding of the image.

The Hamiltonian matrix is thus:

$$\boldsymbol{H}[i,j] = \begin{cases} \boldsymbol{x}[i] + 4\dfrac{\hbar^2}{2m} & \text{for } i = j, \\ -\dfrac{\hbar^2}{2m} & \text{for } i = j \pm 1, \\ -\dfrac{\hbar^2}{2m} & \text{for } i = j \pm n, \\ 0 & \text{otherwise,} \end{cases} \tag{4.4}$$

where $\boldsymbol{x}[i]$ represents the i-th component of a vectorized image $\boldsymbol{x}$ in the lexicographical order and and $\boldsymbol{H}[i,j]$ represents the (i,j)-th element of the operator $\boldsymbol{H} \in \mathbb{R}^{n^2 \times n^2}$.

TABLE 4.1. The Hamiltonian matrix of size 16×16 corresponding to an image of size 4×4.

1	2	3	4	5	6	7	8	9	10	11	12	13	14	15	16
$\boldsymbol{x}[1]+2\frac{\hbar^2}{2m}$	$-\frac{\hbar^2}{2m}$	0	0	$-\frac{\hbar^2}{2m}$	0	0	0	0	0	0	0	0	0	0	0
$-\frac{\hbar^2}{2m}$	$\boldsymbol{x}[2]+3\frac{\hbar^2}{2m}$	$-\frac{\hbar^2}{2m}$	0	0	$-\frac{\hbar^2}{2m}$	0	0	0	0	0	0	0	0	0	0
0	$-\frac{\hbar^2}{2m}$	$\boldsymbol{x}[3]+3\frac{\hbar^2}{2m}$	$-\frac{\hbar^2}{2m}$	0	0	$-\frac{\hbar^2}{2m}$	0	0	0	0	0	0	0	0	0
0	0	$-\frac{\hbar^2}{2m}$	$\boldsymbol{x}[4]+2\frac{\hbar^2}{2m}$	0	0	0	$-\frac{\hbar^2}{2m}$	0	0	0	0	0	0	0	0
$-\frac{\hbar^2}{2m}$	0	0	0	$\boldsymbol{x}[5]+3\frac{\hbar^2}{2m}$	$-\frac{\hbar^2}{2m}$	0	0	$-\frac{\hbar^2}{2m}$	0	0	0	0	0	0	0
0	$-\frac{\hbar^2}{2m}$	0	0	$-\frac{\hbar^2}{2m}$	$\boldsymbol{x}[6]+4\frac{\hbar^2}{2m}$	$-\frac{\hbar^2}{2m}$	0	0	$-\frac{\hbar^2}{2m}$	0	0	0	0	0	0
0	0	$-\frac{\hbar^2}{2m}$	0	0	$-\frac{\hbar^2}{2m}$	$\boldsymbol{x}[7]+4\frac{\hbar^2}{2m}$	$-\frac{\hbar^2}{2m}$	0	0	$-\frac{\hbar^2}{2m}$	0	0	0	0	0
0	0	0	$-\frac{\hbar^2}{2m}$	0	0	$-\frac{\hbar^2}{2m}$	$\boldsymbol{x}[8]+3\frac{\hbar^2}{2m}$	0	0	0	$-\frac{\hbar^2}{2m}$	0	0	0	0
0	0	0	0	$-\frac{\hbar^2}{2m}$	0	0	0	$\boldsymbol{x}[9]+4\frac{\hbar^2}{2m}$	$-\frac{\hbar^2}{2m}$	0	0	$-\frac{\hbar^2}{2m}$	0	0	0
0	0	0	0	0	$-\frac{\hbar^2}{2m}$	0	0	$-\frac{\hbar^2}{2m}$	$\boldsymbol{x}[10]+4\frac{\hbar^2}{2m}$	$-\frac{\hbar^2}{2m}$	0	0	$-\frac{\hbar^2}{2m}$	0	0
0	0	0	0	0	0	$-\frac{\hbar^2}{2m}$	0	0	$-\frac{\hbar^2}{2m}$	$\boldsymbol{x}[11]+4\frac{\hbar^2}{2m}$	$-\frac{\hbar^2}{2m}$	0	0	$-\frac{\hbar^2}{2m}$	0
0	0	0	0	0	0	0	$-\frac{\hbar^2}{2m}$	0	0	$-\frac{\hbar^2}{2m}$	$\boldsymbol{x}[12]+3\frac{\hbar^2}{2m}$	0	0	0	$-\frac{\hbar^2}{2m}$
0	0	0	0	0	0	0	0	$-\frac{\hbar^2}{2m}$	0	0	0	$\boldsymbol{x}[13]+2\frac{\hbar^2}{2m}$	$-\frac{\hbar^2}{2m}$	0	0
0	0	0	0	0	0	0	0	0	$-\frac{\hbar^2}{2m}$	0	0	$-\frac{\hbar^2}{2m}$	$\boldsymbol{x}[14]+3\frac{\hbar^2}{2m}$	$-\frac{\hbar^2}{2m}$	0
0	0	0	0	0	0	0	0	0	0	$-\frac{\hbar^2}{2m}$	0	0	$-\frac{\hbar^2}{2m}$	$\boldsymbol{x}[15]+3\frac{\hbar^2}{2m}$	$-\frac{\hbar^2}{2m}$
0	0	0	0	0	0	0	0	0	0	0	$-\frac{\hbar^2}{2m}$	0	0	$-\frac{\hbar^2}{2m}$	$\boldsymbol{x}[16]+2\frac{\hbar^2}{2m}$

As the boundary conditions correspond to zero padding of the image, a few individual coefficients of the matrix H follow specific rules. Indeed, $\boldsymbol{H}[i,j] = \boldsymbol{x}(i) + 2\frac{\hbar^2}{2m}$ for $i = j$ and $i \in \{1, n, n^2-n+1, n^2\}$, $\boldsymbol{H}[i,j] = \boldsymbol{x}(i) + 3\frac{\hbar^2}{2m}$ for $i = j$ and $i \in \{2,3,...,n-1, n^2-n+2, n^2-n+3, ..., n^2-1\}$, $\boldsymbol{H}[i,j] = \boldsymbol{x}(i) + 3\frac{\hbar^2}{2m}$ for $i = j$ and $i \mod n \in \{0,1\}$, except for $i \in \{1,2,...,n, n^2-n+1, n^2-n+2, ..., n^2\}$ in order to respect the boundary conditions, and $H[i,i+1] = H[i+1,i] = 0$ for any i multiple of n apart from n^2.

In the specific case of $n = 4$, *i.e.* for an image of size 4×4 the discretized Hamiltonian is of size 16×16. This Hamiltonian matrix is explicitly shown in Table 4.1.

The set of eigenvectors gives a basis of the Hilbert space, with each eigenvector associated to an energy E, which is the corresponding eigenvalue of the Hamiltonian operator. The n^2 eigenvectors, denoted by $\boldsymbol{\psi}_i \in \mathbb{R}^{n^2 \times 1}$, each with components $\boldsymbol{\psi}_i^j$ with $j = 1, \cdots, n^2$, are the main tool for the proposed adaptive transform in this work. Indeed, our method consists in projecting the signal or image on this particular basis and use the energy associated to each eigenfunction as a parameter on which we perform the thresholding of these coefficients.

4.3.2 A Technical Problem for Noisy Signals or Images: the Problem of Quantum Localization

In order to use the adaptive basis for various problems of signal or image processing, including denoising, the procedure should be adapted for noisy signals and images. A technical problem then arises, linked to the phenomenon of quantum localization. As explained in Chapter 2, the quantum localization is a property of wave functions in a disordered potential which makes the adaptive basis localized in position space, which in turn makes it less useful for our purpose. In this subsection, we propose a way to mitigate this technical problem which will be implemented throughout the chapter.

Indeed, it is known in quantum mechanics that a disordered potential localizes the wavefunctions in one and two dimensions. Due to destructive interference, the different wave functions are exponentially localized at different positions of the potential, an effect known as Anderson localization, which earned the Nobel prize in 1977 to its discoverer [19]. If the signal or image are not smooth, which certainly arises in the case of a noisy signal or image, we expect the vectors of the basis to be localized, with a localization length which will be smaller and smaller for increasing noise intensity.

Let us start from a wave function defined as eigenfunction of (4.4), $\boldsymbol{\psi}_i \in \mathbb{R}^{n^2 \times 1}$ with components $\boldsymbol{\psi}_i^j$. The level of localization is measured by computing the inverse participa-

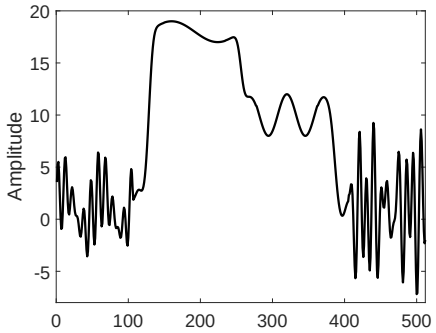

FIGURE 4.3. Synthetic signal used to illustrate the localization property of the wave functions.

tion ratio (IPR) of the wave functions, mathematically defined for a given wave function as:

$$\mathrm{IPR}(\boldsymbol{\psi}_i) = \frac{\left(\sum_{j=1}^{n^2} |\boldsymbol{\psi}_i^j|^2\right)^2}{\sum_{j=1}^{n^2} |\boldsymbol{\psi}_i^j|^4}, \tag{4.5}$$

where n^2 is the dimension of the Hilbert space. For a vector uniformly spread over P indices and zero elsewhere, this quantity is exactly P. For an exponentially localized vector such as the wavefunctions in a disordered potential, it is proportional to the localization length for each vector in the adaptive basis. In this case, these vectors will still be oscillating functions, but will no longer have different frequencies at different locations since they are localized in a specific part of the potential.

In Fig. 4.4 the averaged IPR of all functions of the adaptive basis is shown for a synthetic signal (Fig. 4.3) degraded by an additive Gaussian noise with different signal to noise ratios (SNR). The localization property is clearly seen: the IPR decreases with decreasing SNR, indicating that noisy signals tend to localize the basis.

To modify this characteristic of the basis, we use a smoothed adaptation of the noisy signal or image to construct the Hamiltonian matrix, computed by a simple convolution with a Gaussian kernel whose standard deviation is denoted by σ. This is not part of the denoising process, it is just a technical trick to delocalize the adaptive basis while keeping the main features of the signal/image. In our framework, this standard deviation σ is an additional free parameter. If σ is chosen too large, then the noisy signal or image becomes so smooth that many characteristics needed for the adaptive basis will be lost. On the opposite, if σ is too small the basis vector will remain strongly localized. To balance both sides one needs to tune the parameter σ to get the best achievable outcome.

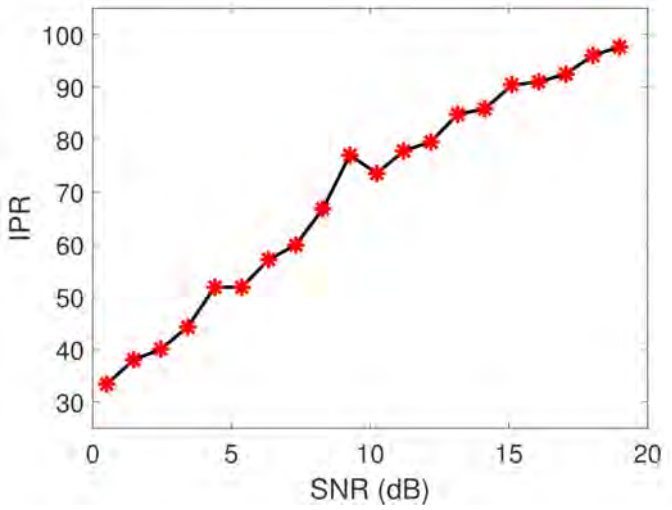

FIGURE 4.4. Quantum localization effect: IPR corresponding to the wave functions calculated from the signal in Fig. 4.3 degraded by an additive Gaussian noise for several SNR. The size of the signal was 512. The IPR is computed through (4.5) and averaged over all 512 wave functions of the adaptive basis.

Fig. 4.5(b) and Fig. 4.6(b-c) show examples of wave functions calculated from a noisy signal and image. From these examples, one observes again that the wave functions are completely localized in a specific location and present a fast decrease due to the destructive interference. On the contrary, in the case where the same wave functions are calculated from low-pass filtered versions of the noisy signal and image (i.e. a smoothed version of the potential), they are shown to delocalize and spread over the whole available space as illustrated in Fig 4.5(d) and Fig. 4.6(e-f).

4.3.3 Application to the Denoising Problem

This section explains in detail the application of the proposed adaptive basis from quantum mechanics to the denoising problem. The significant difficulties for signal or image denoising are to sharpen the edges without blurring and preserve the image textures without generating artifacts. The most common denoising strategies are based on three primary steps. To distinguish the useful information and the noise, the noisy signal or image is projected onto a dictionary. This is then accompanied by a hard or soft thresholding process in the transformed space. Finally, the revised coefficients are back projected to the time or space domain, so that the denoised signal or image could

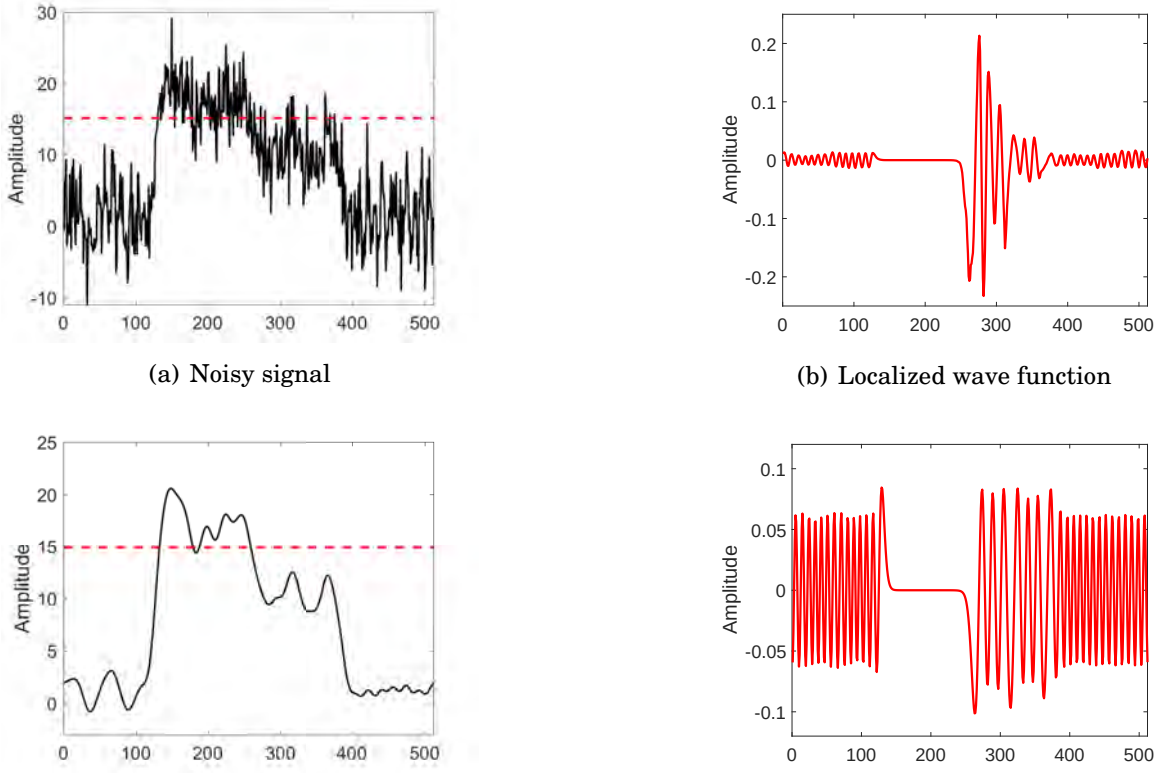

(a) Noisy signal

(b) Localized wave function

(c) Blurred signal

(d) Delocalized wave function

FIGURE 4.5. Role of the hyperparameter σ and localization: (a) Signal in Fig. 4.3 contaminated by additive Gaussian noise corresponding to a SNR of 15 dB, (b) localized wave function number 68 calculated from the noisy signal with energy level illustrated by the dashed line in (a), (c) blurred version of the noisy signal in (a) obtained by Gaussian low-pass filter corresponding to $\sigma^2 = 10$, (d) delocalized wave function number 68 calculated from the low-pass filtered signal with the same energy level illustrated by the dashed line in (c).

be retrieved. We will apply the same procedure using the adaptive basis defined by the eigenvectors $\boldsymbol{\psi}_i$ obtained by solving the Schrödinger equation (4.1).

The basic assumptions is that the noise is more present in high frequency components of the signal or image, corresponding to eigenvectors associated with large energy eigenvalues. The thresholding will therefore be performed in energy, leaving out the components of the signal or image on high energy eigenvectors. The fact that our basis has frequencies which vary depending on the position should be an asset, especially for signal or image dependent noise (e.g. Poisson noise). In the following, we will show that it is indeed the case in some examples of signals and images with various types of noise.

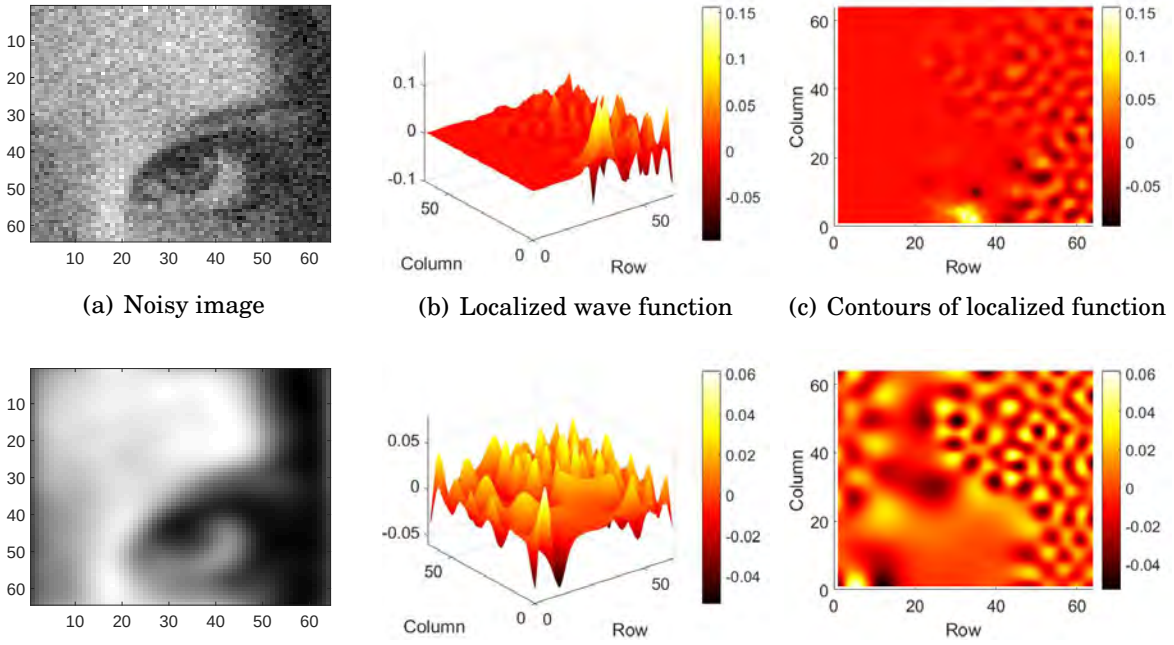

(a) Noisy image (b) Localized wave function (c) Contours of localized function

(d) Blurred image (e) Delocalized wave function (f) Contours of delocalized function

FIGURE 4.6. Role of the hyperparameter σ and localization: (a) *Lena* image used in Fig. 4.1, contaminated by additive Gaussian noise corresponding to a SNR of 15 dB, (b,c) localized wave function number 195 calculated from the noisy *Lena* image (a), (d) blurred version of the noisy *Lena* image in (a) obtained by Gaussian low-pass filter corresponding to $\sigma^2 = 6$, (e,f) the same wave function but delocalized due to the low pass Gaussian filter applied to the noisy image.

The denoising process is expressed as follows; for a noisy signal or image denoted by $\boldsymbol{y}$, the denoised signal or image $\hat{\boldsymbol{x}}$ is rebuilt through:

$$\hat{\boldsymbol{x}} = \sum_{i=1}^{n^2} \boldsymbol{\alpha}_i \boldsymbol{\psi}_i \tau_i, \tag{4.6}$$

with

$$\tau_i = \begin{cases} 1 & \text{for } i \leq s, \\ 1 - \dfrac{i-s}{\rho} & \text{for } i > s \text{ and for } 1 - \dfrac{i-s}{\rho} > 0, \\ 0 & \text{otherwise.} \end{cases} \tag{4.7}$$

where $\boldsymbol{\alpha}_i = \langle \boldsymbol{y}, \boldsymbol{\psi}_i \rangle$ are the coefficients representing the signal or image $\boldsymbol{y}$ in the proposed adaptive basis. s and ρ are two hyperparameters, used to define the thresholding function for the proposed denoising algorithm.

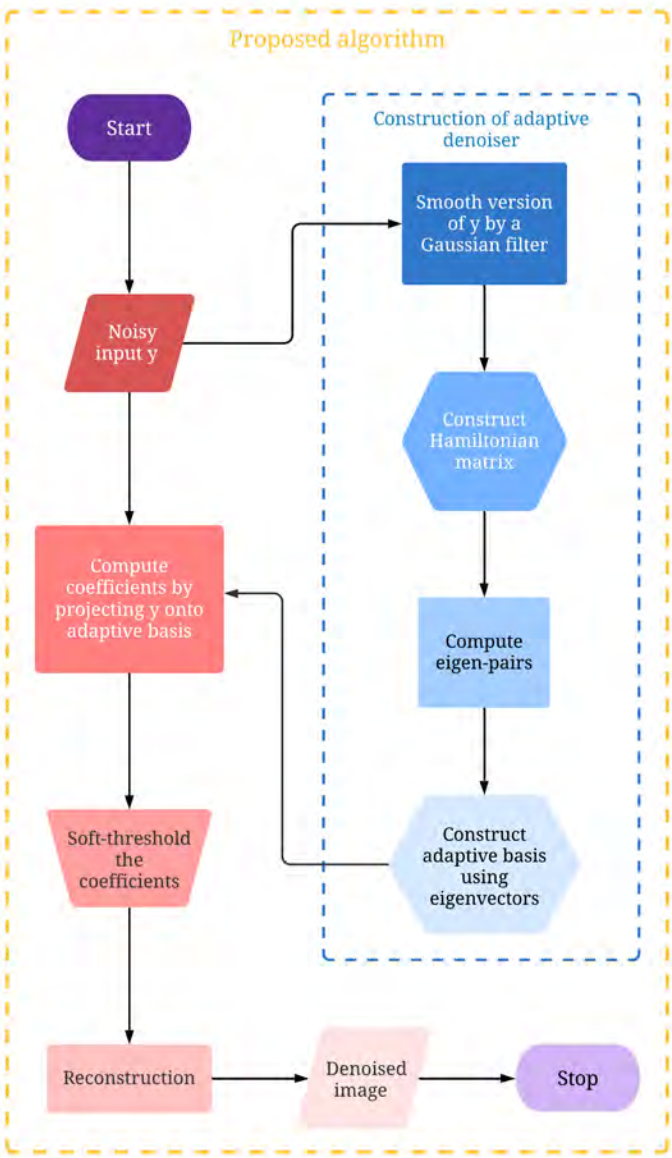

FIGURE 4.7. Flowchart of the proposed denoising algorithm.

In order to use this procedure, we will need to specify which values of the parameter $\hbar^2/2m$ should be selected. As we will see, there is a relatively large range of values where the algorithm is efficient, meaning that it can be set to a specific value independent of the signal or image on which the algorithm is used.

4.3.4 Algorithm Description

Denoising a signal or an image using the proposed method requires the computation of eigenvalues and eigenvectors of the discretized Hamiltonian matrix (4.4) for appropriate values of the parameters $\hbar^2/2m$ and σ, project the signal or image on this basis, threshold the coefficients by an appropriate threshold in energy, and reconstruct from this a denoised signal or image. These steps are summarized in Algorithm 4.1 and Fig. 4.7.

For very large signals and images, where the size of the matrix (4.4) becomes too large for practical simulations, we implement a modified version of the algorithm where the matrix (4.4) is diagonalized for subparts of the signal or image independently, and then a complete signal or image is reconstructed:

- The noisy signal or image is divided into sub-blocks of equal size, using in particular square sub-blocks in the case of images.
- Use algorithm 4.1 for each sub-block.
- Reconstruct the denoised signal or image by integrating each denoised sub-block.

Algorithm 4.1: Denoising algorithm using the proposed adaptive transform.

Input: $\boldsymbol{y}$, $\hbar^2/2m$, s, ρ, σ

1 Compute a smooth version of $\boldsymbol{y}$ by Gaussian filtering
2 Construct the Hamiltonian matrix $\boldsymbol{H}$ based on the smoothed version of $\boldsymbol{y}$ using equation (4.4)
3 Calculate the eigenvectors $\boldsymbol{\psi}_i$ of $\boldsymbol{H}$
4 Compute the coefficients $\boldsymbol{\alpha}_i$ by projecting $\boldsymbol{y}$ onto the basis formed by $\boldsymbol{\psi}_i$
5 Threshold the coefficients $\boldsymbol{\alpha}_i$ and recover the denoised signal or image following equations (4.7) and (4.6)

Output: Denoised $\hat{\boldsymbol{x}}$

4.4 Results

This section regroups results showing the interest of the proposed approach in signal and image denoising and analyze the optimal choice of parameters. Subsection 4.4.1 elaborates the dependence of the proposed denoising method on the choice of the hyper-parameters $\hbar^2/2m$, σ, s and ρ. Subsection 4.4.2 compares the denoising results obtained with the proposed approach to several state of the art methods.

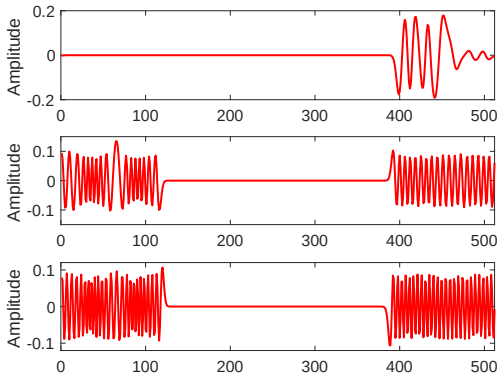

(a) Hyperparameter $\hbar^2/2m = 0.08$

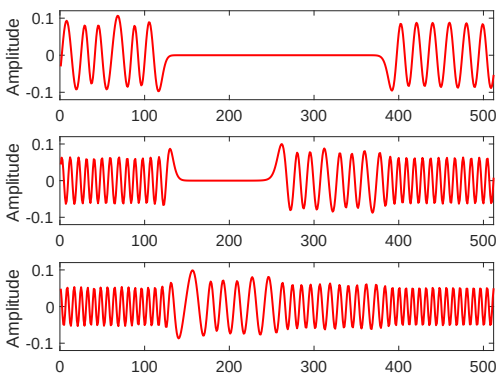

(b) Hyperparameter $\hbar^2/2m = 1$

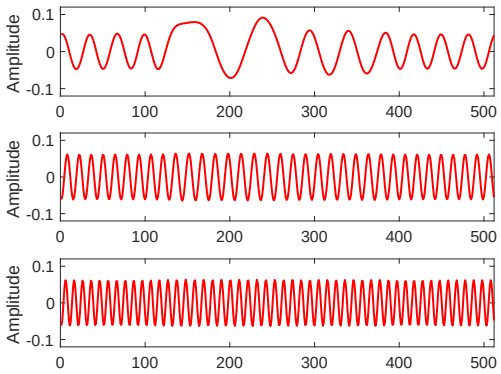

(c) Hyperparameter $\hbar^2/2m = 15$

FIGURE 4.8. Role of the hyperparameter $\hbar^2/2m$: adaptive basis functions (wave functions) number 25, 70 and 100 calculated from the signal Fig. 4.3 are shown from top to bottom with different values of the hyperparameter $\hbar^2/2m$.

4.4.1 Influence of Hyperparameters $\hbar^2/2m$, σ, s and ρ on the Efficiency of the Algorithm

In this subsection, we provide a detailed discussion about the influence of the hyperparameters on the proposed adapative bases.

4.4.1.1 Properties of Hyperparameter $\hbar^2/2m$

As mentioned above, the parameter $\hbar^2/2m$ specifies how the local frequencies of the vectors of the basis vary with the amplitude of the signal or image pixel value. To illustrate this relationship, the effect of $\hbar^2/2m$ on local frequencies is shown in Fig. 4.8 for

three distinct values of this parameter. For each case, three wave functions (number 25, 70 and 100) computed from the synthetic signal in Fig. 4.3 are displayed. For low values of $\hbar^2/2m$ (i.e., 0.08 for the results in Fig. 4.8(a)), one may remark that the wave functions are oscillating at very high frequencies, even for higher values of the potential (i.e., of the signal). The presence of a maximal oscillation period due to the discretization of the signal implies that in this limit the high values of the signal are not taken properly into account. For very high values of $\hbar^2/2m$ (15 for the results in Fig. 4.8(c)), most of the wave functions are at an energy well above the potential values, and they discriminate less and less between the regions with different potential height. In this limit, wave functions behave very similarly to cosine functions with increasing frequencies, thus reducing the interest of the proposed bases that becomes very similar to the Fourier transform. At intermediate values of $\hbar^2/2m$ (1 for the results in Fig. 4.8(b)), wave functions explore the different regions but with clearly different oscillation frequencies, *i.e.* wave vectors have significantly larger frequencies or short wavelengths for the low potential valued regions as opposed to high potential regions.

4.4.1.2 Properties of the Gaussian Smoothing Hyperparameter σ

The second hyperparameter studied in this section that has a strong impact on the proposed denoising algorithm is the paramater σ which makes the adaptive basis delocalized on the system (signal or image). As explained above in Subsection 4.3.2, this parameter corresponds to the cut-off frequency of the Gaussian low pass filter used to smooth the noisy signal or images before computing the wave functions through (4.1).

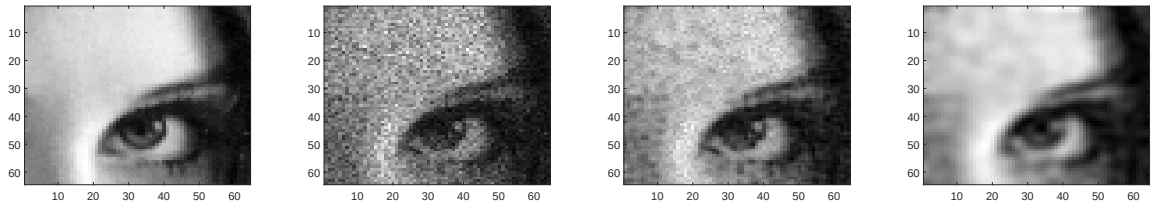

FIGURE 4.9. Role of the hyperparameter σ: (a) Cropped version of clean *Lena*, (b) cropped version of noisy *Lena* contaminated by Poisson noise corresponding to a SNR of 15 dB, (c) denoised result with hyperparameter $\sigma^2 = 0$, giving a PSNR = 25.37 dB, of the image (b), (d) denoised result with hyperparameter $\sigma^2 = 4$, giving a PSNR = 28.81 dB. The hyperparameters are $\hbar^2/2m = 0.6$, $\rho = 1$, and $s = 600$ for each set of experiment.

This cutoff frequency is fixed through the choice of the standard deviation σ of the Gaussian filter. Again, we highlight that this parameter is not related to the denoising process itself, but to the definition of the adaptive basis to be used for denoising.

The localization of the wave functions in the presence of noise has an important impact on the proposed signal or image representation and furthermore on the efficiency of the denoising process. To illustrate this claim, Fig 4.9 shows a denoising result with and without the use of the low pass Gaussian filter prior to the computation of the wave functions. In this example, the cropped version of *Lena* in Fig. 4.9(a) was degraded by a Poisson noise resulting into a SNR of 15 dB. The denoised images in Fig. 4.9(c,d) were obtained using the algorithm detailed in Algo. 4.1. However, while the result in Fig. 4.9(c) exploits the image decomposition through localized wave functions computed directly from the noisy image, the result in Fig. 4.9(d) was obtained by filtering the noisy image by a low pass Gaussian filter before using (4.1), in order to delocalize the wave functions. The interest of such delocalization can be visually appreciated in this example and allows a peak SNR (PSNR) gain of more than 3 dB. In the following, we will always use a pre-smoothed signal or image in (4.1), and the parameter σ of the smoothing is thus an important parameter of the algorithm.

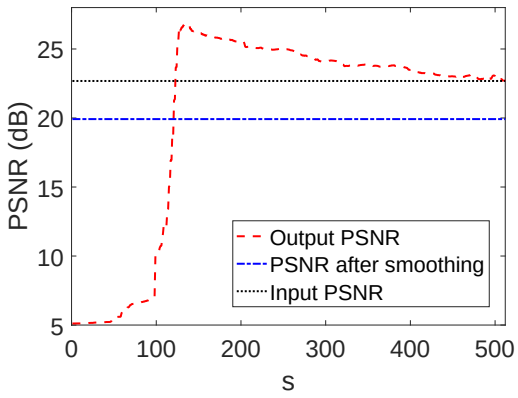

(a) PSNR as a function of the thresholding hyperparameter s, for $\sigma^2 = 20$, $\rho = 1$ and $\hbar^2/2m = 0.5$.

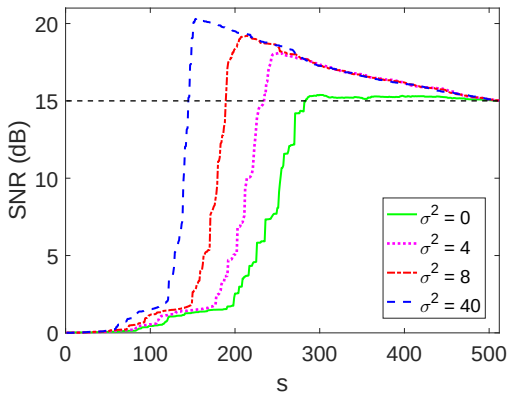

(b) SNR as a function of the thresholding hyperparameter s, for $\rho = 1$, $\hbar^2/2m = 0.4$ and four different values of σ^2 (0, 4, 8 and 40).

FIGURE 4.10. Role of the hyperparameters s and σ. Simulations with the 1D signal Fig. 4.3 corrupted by additive Gaussian noise corresponding to a SNR of 15 dB.

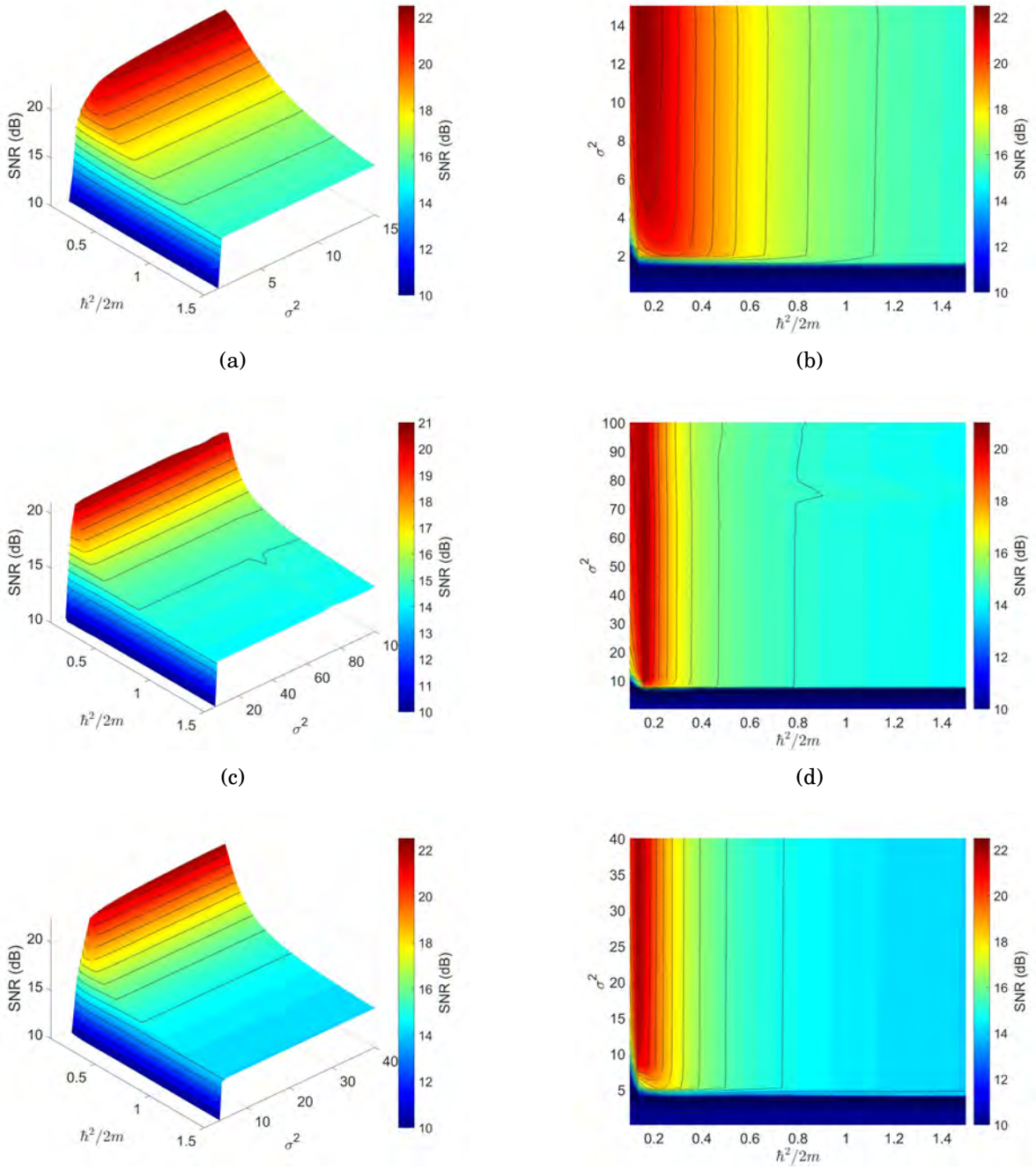

FIGURE 4.11. Influence of the hyperparameters $\hbar^2/2m$ and σ on the proposed decomposition performed on the 1D system Fig. 4.3 in presence of (a,b) Poisson noise, (c,d) Gaussian noise and (e,f) speckle noise corresponding to a SNR of 15 dB respectively. The hyperparameters are $\rho = 1$ and $s = 110$ for each set of experiment.

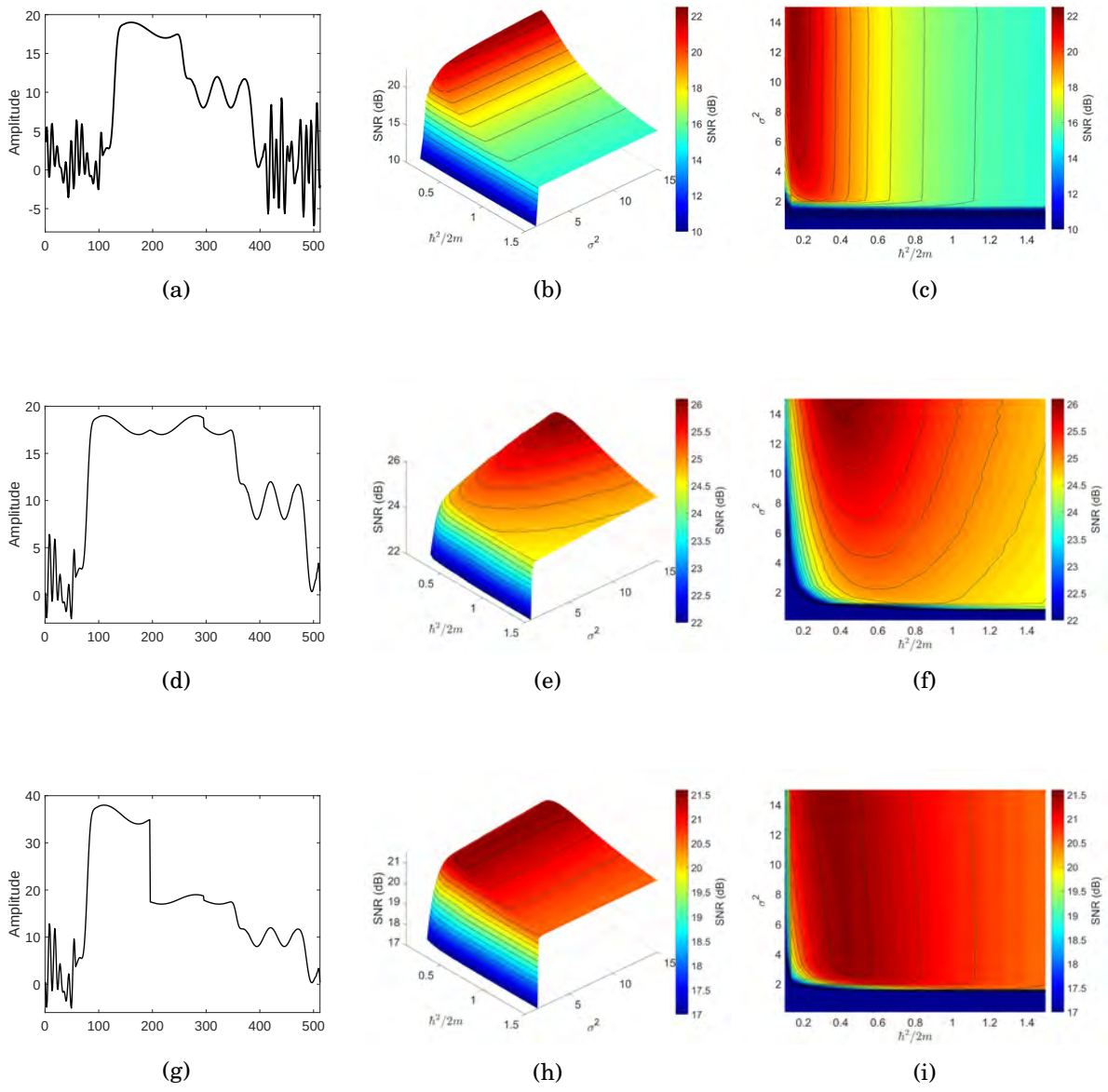

FIGURE 4.12. (a) Sample A, (b,c) influence of the hyperparameters $\hbar^2/2m$ and σ on the proposed method performed on the sample A corrupted with Poisson noise corresponding to a SNR of 15 dB, (d) sample B, (e,f) influence of the hyperparameters $\hbar^2/2m$ and σ on proposed method performed on the sample B corrupted with Poisson noise corresponding to a SNR of 15 dB, (g) sample C, (h,i) influence of the hyperparameters $\hbar^2/2m$ and σ on proposed method performed on the sample C corrupted with Poisson noise corresponding to a SNR of 15 dB. The hyperparameters are $\rho = 1$ and $s = 110$ for each set of experiment.

4.4.1.3 Properties of the Thresholding Hyperparameters s and ρ

At last, in order to denoise the signal or image one has to threshold the coefficients of the signal or image on the adaptive basis; this process uses two thresholding hyperparameters s and ρ defined in (4.7), which define respectively the threshold value and the abruptness of the cutoff. In particular, the parameter s corresponds to the threshold in energy of the wave functions taken into account in the expansion (4.6) to reconstruct the signal or image.

Fig. 4.10(a) illustrates the PSNR as a function of the thresholding hyperparameter s while reconstructing the denoised result corresponding to the signal in Fig. 4.3 contaminated by additive Gaussian noise of 15 dB. It is clear from that figure that initially PSNR decreases due to the low pass filtering, whereas the thresholding operation on the adaptive basis shows improvement in PSNR value. Fig. 4.10(b) illustrates the variation of the SNR for changing values of the hyperparameter s. For $\sigma^2 = 0$, the reconstructed signal has a SNR worse or similar to the original noisy one, indicating once more the importance of the smoothing process before computing the adaptive basis through (4.1). For nonzero values of σ^2, there is a relatively small range of optimal s values, where the SNR is much better than in the original noisy signal. Of course this threshold value should eventually depend on the level of noise. The adaptive transform makes the filtering of high frequencies stronger at high values of the potential, but the overall level of filtering should still depend on the noise properties.

4.4.1.4 Effects of the Hyperparameters $\hbar^2/2m$ and σ on the Denoising Performance

Numerical experiments on the synthetic signal of Fig. 4.3 and on the *Lena* image in Fig. 4.1 were carried out to analyze the impact of $\hbar^2/2m$ and σ on the denoising quality and subsequently to adjust these parameters to their best values for assessment of the efficiency of the algorithm. Three different types of noise were considered: Poisson, additive Gaussian and multiplicative speckle noise. In all cases, the level of noise was adjusted to correspond to a SNR of 15 dB.

Fig. 4.11 show the quality of the denoising results for the synthetic signal Fig. 4.3, in terms of SNR, versus the value of the hyperparameters $\hbar^2/2m$ and σ^2 for different types of noise: Poisson noise, Gaussian noise and speckle noise. Several observations can be made from these results. As expected, an optimal value arises in each case. In particular, the hyperparameter σ should clearly be chosen to be nonzero, indicating the importance

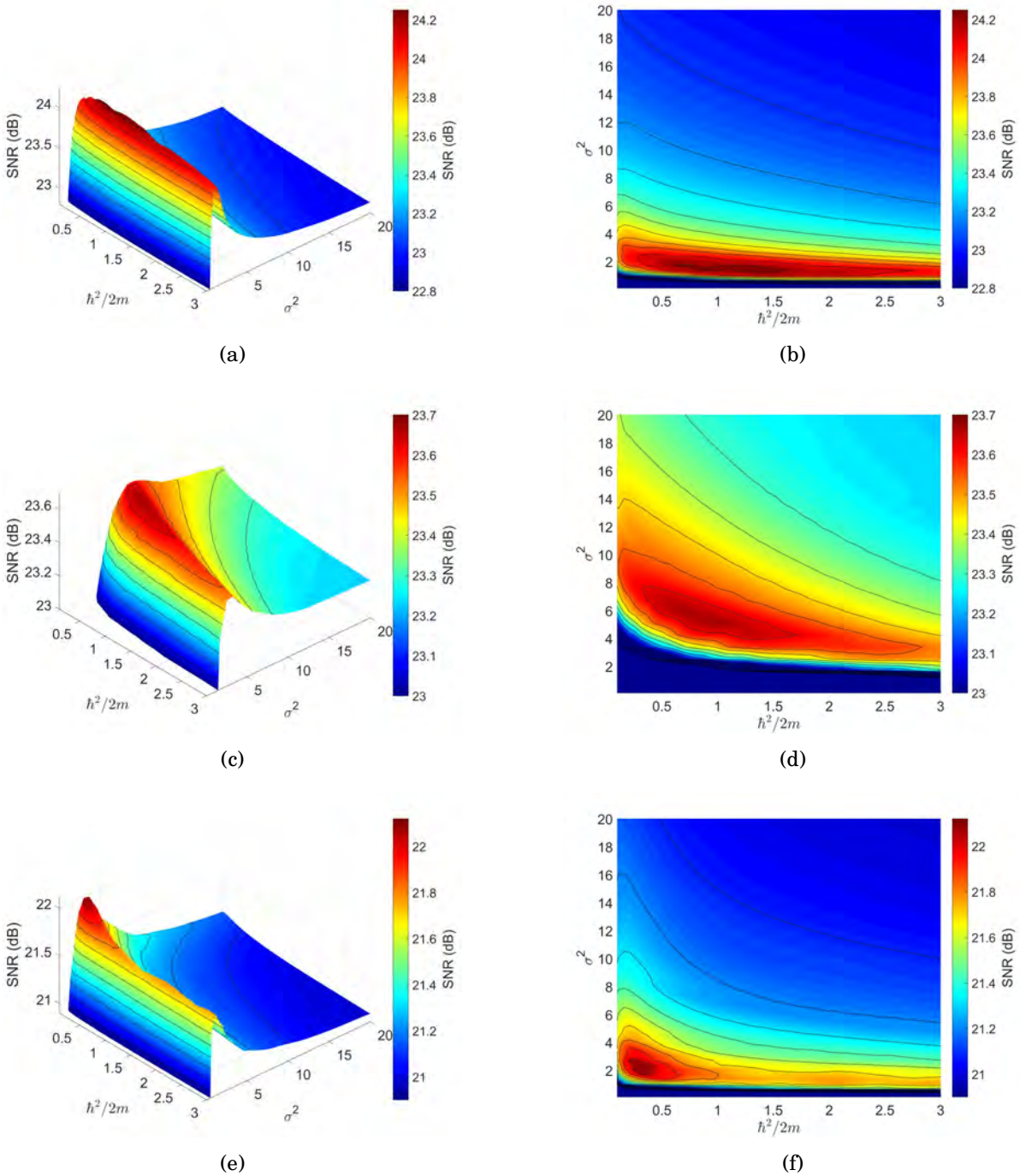

FIGURE 4.13. Influence of the hyperparameters $\hbar^2/2m$ and σ on the proposed decomposition carried out on the 2D *Lena* image in Fig. 4.1 in presence of (a,b) Poisson noise, (c,d) Gaussian noise and (e,f) speckle noise corresponding to a SNR of 15 dB respectively. The hyperparameters are $\rho = 1$ and $s = 600$ for each set of experiment.

of taking into account the localization effects. However, even if an optimal value exists for the different hyperparameters, a small variation in the choice of these hyperparameters around the optimal values only slightly influences the quality of the denoising. Moreover, the optimal values are only slightly dependent on the nature of the noise. This means that for this type of signal the hyperparameters could be fixed beforehand at a fixed value which can be chosen independently of the type of noise present.

Next, the dependence of $\hbar^2/2m$ and σ hyperparameters on the shape of the signals is analyzed. For this purpose, two additional synthetic signals were generated as shown in Fig. 4.12(d)(g) together with Fig. 4.12(a), which corresponds to the same synthetic signal used previously, further normalized to 1 and corrupted by Poisson noise. From the results in Fig. 4.12(b-c)(e-f)(h-i), it can be clearly observed that the quality of the denoising does depend on the shape of the signals, which can be expected given the nature of the adaptive basis used by the proposed approach. However, the denoising process is efficient for a fairly large interval around the optimal values. As there is a big overlap in the acceptable range of values of the hyperparameters for various signal shape, again this means that the hyperparameters could be fixed beforehand at a fixed value which can be chosen independently of the signal.

Finally, Fig. 4.13 regroups the results for the cropped *Lena* image for the three types of noise. The same conclusions can be drawn as from the results on 1D signals in Fig. 4.11: as expected and similar to any other denoising method, the choice of the hyperparameters does have an impact on the results, and the optimal range of parameters depend on the noise. However, even though the acceptable range of parameters seems smaller than for the 1D signal, there is still a relatively large parameter region where the denoising is very effective. This again makes realistic the possibility to set these parameters beforehand in the algorithm independently from the signal or image. Additionnally, there is a large overlap between the optimal parameter ranges for Poisson and speckle noise, with a marked difference for Gaussian noise. This seems to indicate that the choice of the parameters may differ according to the broad class to which the noise of interest belongs, an information that is usually known beforehand in many cases.

4.4.2 Efficiency of the Denoising Process

This section presents denoising results on a synthetic signal, a synthetic image and six standard testing images of size 512×512 and 320×320 pixels, shown in Fig. 4.14.

Denoising is an extensively explored research field that prevents an exhaustive comparison of the proposed approach to all the existing methods. Moreover, we remind

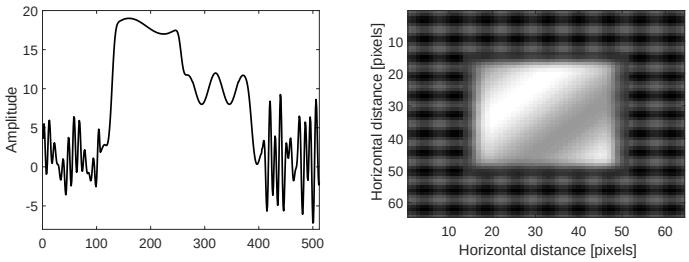

(a) Synthetic signal (b) Synthetic image

(c) Boat (512 × 512) (d) Elaine (512 × 512) (e) Lena (512 × 512)

(f) Lighthouse (512 × 512) (g) Fruits (512 × 512) (h) Moon (320 × 320)

FIGURE 4.14. Signal and images used to compare the proposed denoising method to existing algorithms. The size in number of pixels is indicated for each considered image.

that the most important contribution herein is to investigate a novel way of decomposing signals or images, which is not meant to outperform all the denoising algorithms in any scenario. Five algorithms from the literature were used for comparison purpose: i) wavelet denoising based on hard and soft thresholding of detail coefficients [104, 106], ii) the variance stabilization transform (VST) relevant for data dependent noise models [237], iii) an optimization-based approach using the total variation (TV) semi-norm to regularize the solution [133, 289], iv) a graph signal processing (GSP) method by

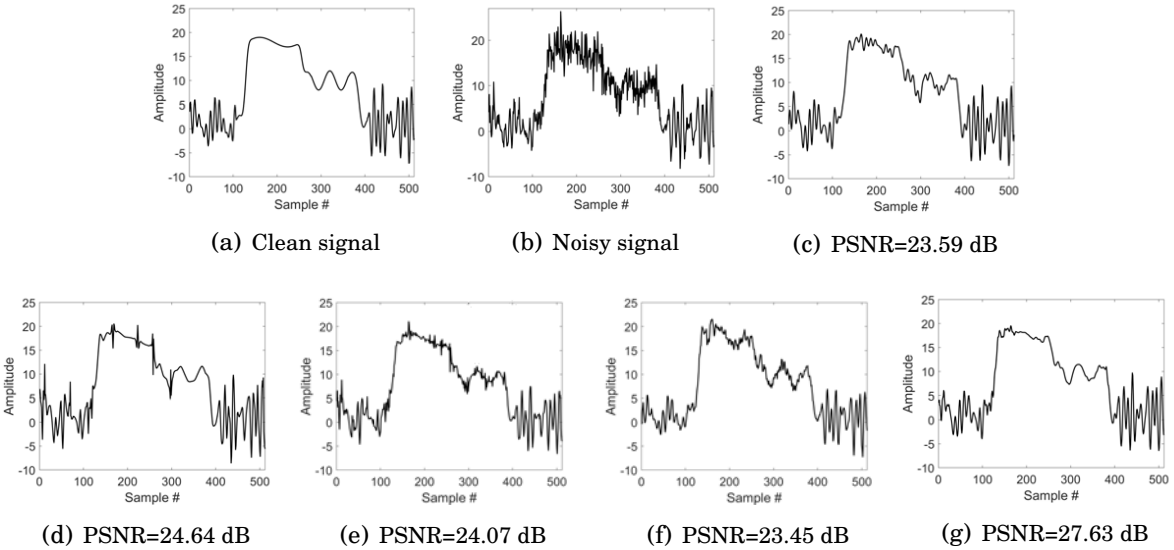

(a) Clean signal (b) Noisy signal (c) PSNR=23.59 dB

(d) PSNR=24.64 dB (e) PSNR=24.07 dB (f) PSNR=23.45 dB (g) PSNR=27.63 dB

FIGURE 4.15. Result of the denoising algorithm compared with other methods: (a) Clean synthetic signal, (b) Signal corrupted with Poisson noise corresponding to a SNR of 15 dB. Denoising results obtained using, (c) Fourier transformation, (d) wavelet hard thresholding, (e) wavelet soft thresholding, (f) total variation regularization and (g) proposed method. The proposed adaptive transform was computed with the hyperparameters $\hbar^2/2m = 1.2$, $\sigma^2 = 20$, $\rho = 1$ and $s = 180$.

constructing an optimal graph and corresponding graph Laplacian regularizer [262], v) a non-local means (NLM) image denoising method that uses principal component analysis approach [333], and vi) a dictionary learning (DL) method exploiting sparse and redundant representations over learned patch-based dictionaries [123]. Note that for all the methods and for all the simulation scenarios, their hyperparameters were manually tuned to obtain optimal denoising results in the sense of the quantitative measurements employed. We used the Matlab implementations available in the Numerical tours website [268].

Three quantitative measurements were used to evaluate the denoised images: the signal to noise ratio (SNR), the peak signal to noise ratios (PSNR) and the structure similarity (SSIM) [365]. All the quantitative results are regrouped in Table 4.2 where the best and the second best values have been highlighted by red and blue colors respectively for each dataset. Note that VST is only used for data-dependent noise, whereas GSP and NLM is used only for Gaussian noise. Moreover, VST, GSP, NLM, and DL were only tested for images, as initially suggested by the seminal papers. Illustrative results for

TABLE 4.2. Quantitative denoising results.

Sample	Method	Gaussian Noise (15dB)			Poisson Noise (15 dB)			Speckle Noise (15dB)		
		SNR (dB)	PSNR (dB)	SSIM	SNR (dB)	PSNR (dB)	SSIM	SNR (dB)	PSNR (dB)	SSIM
Synthetic Signal	Wavelet hard	**18.84**	**25.21**	-	17.21	**24.64**	-	**17.36**	**24.13**	-
	Wavelet soft	18.53	24.21	-	**17.79**	24.07	-	17.02	22.70	-
	TV	16.20	23.01	-	15.94	23.45	-	15.92	22.92	-
	Proposed	**22.21**	**27.50**	-	**22.51**	**27.63**	-	**20.75**	**26.86**	-
Synthetic Image	Wavelet hard	15.01	24.46	0.61	15.01	25.68	0.69	15.01	25.34	0.76
	Wavelet soft	15.71	25.05	0.64	15.61	26.20	0.70	15.49	25.80	0.77
	VST	-	-	-	15.09	25.83	0.69	15.06	25.58	0.76
	TV	15.74	25.07	0.64	15.62	26.23	0.71	15.53	25.78	0.77
	GSP	**20.28**	**28.78**	**0.79**	-	-	-	-	-	-
	NLM	18.70	26.88	0.71	-	-	-	-	-	-
	DL	17.35	26.15	0.71	**17.14**	**27.22**	**0.75**	**17.21**	**27.48**	**0.80**
	Proposed	**23.42**	**31.78**	**0.89**	**23.92**	**32.78**	**0.92**	**25.32**	**33.50**	**0.95**
Boat	Wavelet hard	20.28	26.87	0.62	19.92	27.26	0.61	19.71	25.85	0.59
	Wavelet soft	21.50	27.83	0.59	21.35	27.82	0.59	21.08	26.16	0.58
	VST	-	-	-	21.77	28.62	0.62	22.80	28.03	0.68
	TV	22.46	28.77	0.71	22.25	29.00	**0.64**	**23.11**	**28.19**	0.71
	GSP	**23.88**	**29.36**	**0.78**	-	-	-	-	-	-
	NLM	23.56	29.27	0.77	-	-	-	-	-	-
	DL	**24.02**	**29.52**	**0.80**	**23.44**	**29.77**	**0.77**	22.64	27.71	**0.73**
	Proposed	23.15	28.88	0.77	**23.51**	**29.29**	**0.77**	**23.65**	**28.73**	**0.78**
Elaine	Wavelet hard	20.52	27.02	0.52	20.08	28.17	0.49	19.75	25.99	0.48
	Wavelet soft	21.99	27.69	0.53	21.67	28.59	0.51	21.31	26.61	0.50
	VST	-	-	-	21.71	28.64	0.53	22.51	**27.81**	0.56
	TV	23.67	29.63	0.62	22.03	28.84	0.55	**23.06**	27.61	**0.59**
	GSP	**25.89**	**30.73**	**0.72**	-	-	-	-	-	-
	NLM	24.67	**30.70**	0.67	-	-	-	-	-	-
	DL	**24.97**	29.92	**0.68**	**23.96**	**29.84**	**0.62**	22.99	27.58	0.58
	Proposed	24.70	29.87	**0.68**	**23.89**	**29.03**	**0.65**	**23.52**	**28.32**	**0.64**
Lena	Wavelet hard	20.84	28.17	0.72	20.01	28.89	0.68	19.22	27.49	0.66
	Wavelet soft	21.23	28.12	0.71	20.75	28.54	0.67	20.29	27.31	0.66
	VST	-	-	-	20.82	29.50	**0.73**	21.24	28.55	0.69
	TV	21.95	29.32	0.70	21.34	29.58	0.68	**21.83**	**28.71**	**0.72**
	GSP	22.43	29.32	**0.78**	-	-	-	-	-	-
	NLM	22.92	**30.58**	**0.77**	-	-	-	-	-	-
	DL	**23.14**	**30.02**	**0.77**	**21.89**	**29.61**	0.71	20.35	27.24	0.71
	Proposed	**23.01**	29.89	**0.78**	**22.86**	**29.95**	**0.77**	**23.21**	**30.10**	**0.78**
Lighthouse	Wavelet hard	18.89	26.39	0.63	18.15	26.47	0.58	17.70	25.14	0.57
	Wavelet soft	19.76	26.82	0.65	18.62	26.58	0.56	18.85	25.36	0.59
	VST	-	-	-	18.40	26.76	0.61	**19.99**	**26.46**	0.64
	TV	20.90	27.85	0.73	19.01	**27.31**	0.61	**19.99**	26.03	**0.68**
	GSP	**21.30**	**29.01**	**0.77**	-	-	-	-	-	-
	NLM	**20.98**	**28.54**	**0.75**	-	-	-	-	-	-
	DL	20.09	26.84	0.67	**19.78**	27.29	**0.65**	19.19	25.40	0.63
	Proposed	20.82	28.40	0.73	**20.59**	**27.56**	**0.70**	**20.45**	**26.77**	**0.72**
Fruits	Wavelet hard	18.60	25.07	0.65	18.59	25.53	0.65	18.38	24.86	0.64
	Wavelet soft	18.84	25.08	0.71	18.81	25.29	0.72	18.51	24.50	0.71
	VST	-	-	-	19.37	25.96	**0.76**	19.01	25.61	**0.76**
	TV	20.69	26.86	**0.79**	20.60	26.71	0.75	20.18	26.34	0.74
	GSP	**21.44**	27.43	**0.81**	-	-	-	-	-	-
	NLM	**21.48**	**28.02**	0.77	-	-	-	-	-	-
	DL	21.30	27.37	**0.79**	**20.87**	**27.16**	0.71	**20.39**	**27.08**	0.72
	Proposed	21.39	**28.07**	0.77	**21.93**	**28.31**	**0.79**	**21.83**	**28.29**	**0.82**
Moon	Wavelet hard	22.91	30.02	0.70	21.45	29.90	0.72	21.19	29.07	0.71
	Wavelet soft	23.09	30.98	0.74	22.14	30.51	0.80	21.90	29.79	0.79
	VST	-	-	-	22.58	31.17	**0.85**	22.11	30.01	0.84
	TV	23.35	32.19	0.80	**23.51**	**32.21**	**0.86**	**22.91**	**30.84**	**0.86**
	GSP	23.33	31.22	**0.85**	-	-	-	-	-	-
	NLM	**25.79**	**33.94**	**0.86**	-	-	-	-	-	-
	DL	23.82	32.71	0.81	22.95	31.65	**0.85**	22.32	30.07	0.84
	Proposed	**24.81**	**33.11**	0.83	**24.65**	**33.34**	**0.86**	**23.48**	**31.55**	**0.89**

∗*The symbol - denotes that the methods are not suitable for a particular experiment, as suggested by the seminal papers.*

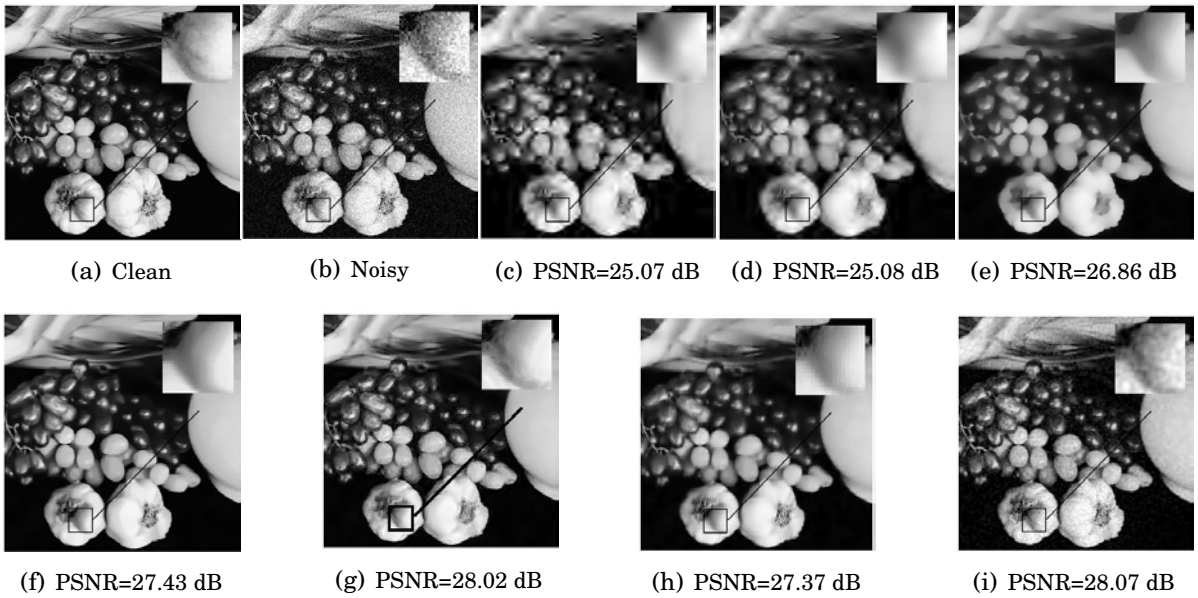

(a) Clean (b) Noisy (c) PSNR=25.07 dB (d) PSNR=25.08 dB (e) PSNR=26.86 dB

(f) PSNR=27.43 dB (g) PSNR=28.02 dB (h) PSNR=27.37 dB (i) PSNR=28.07 dB

FIGURE 4.16. Result of the denoising algorithm compared with other methods: (a) Clean *Fruits* image, (b) Image corrupted with Gaussian noise corresponding to a SNR of 15 dB. Denoising results obtained using, (c) wavelet hard thresholding, (d) wavelet soft thresholding, (e) total variation regularization, (f) graph signal processing, (g) non-local means, (h) dictionary learning and (i) proposed method. The proposed adaptive transform was computed with the hyperparameters $\hbar^2/2m = 0.23$, $\sigma^2 = 7.5$, $\rho = 2$ and $s = 560$.

synthetic signal (Fig. 4.14 (a)) contaminated with Poisson noise, *Fruits* image (Fig. 4.14 (e)) corrupted by Gaussian noise, *Moon* image (Fig. 4.14 (f)) with Poisson noise and *Lena* image (Fig. 4.14 (d)) with speckle noise are shown respectively in Fig. 4.15, 4.16, 4.17 and 4.18. All these results allow us to draw some conclusions. First, one may remark that in almost all the cases, regardless of the noise nature and the image, the proposed method is one of the two best ones. This proves its adaptability to different scenarios and general applicability which can be considered a strong point in number of practical applications. Second, we may remark that for the synthetic signal and image, our method outperforms all the others. The main reason is that the synthetic signal and image were generated to provide a best case for the proposed decomposition, that keeps preferentially higher frequencies for low gray levels and lower frequencies for high gray levels. For such images or signals, the proposed method is very efficient. On the contrary, TV and DL, for example, fail in these cases because of the non piece-wise constant nature of the synthetic data. Finally, we remark that the proposed denoising algorithm provides competitive

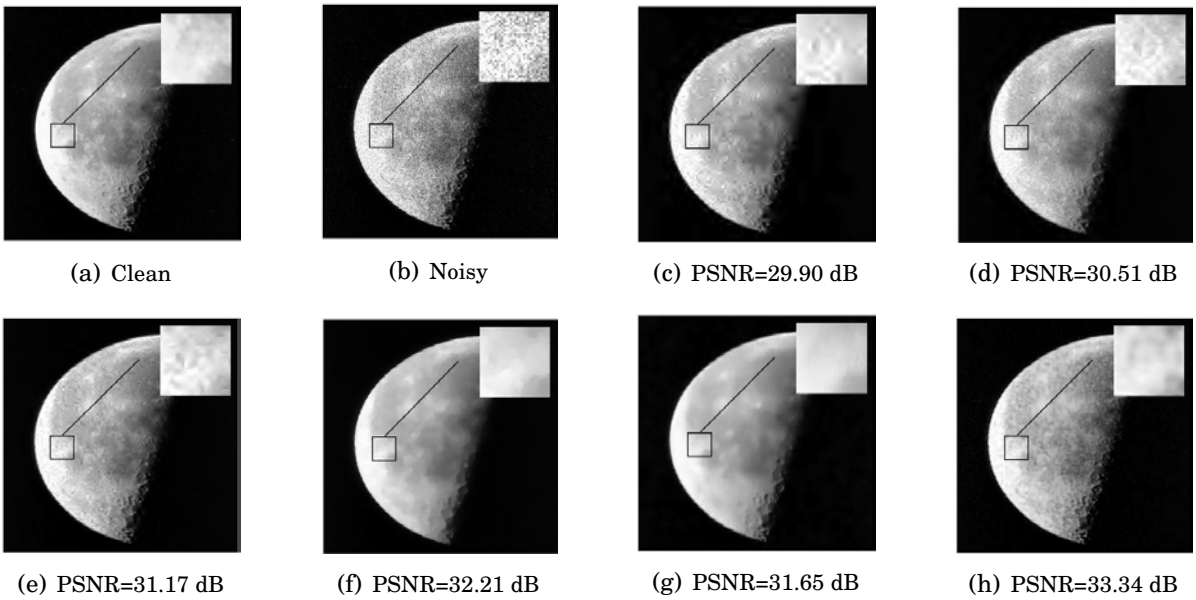

(a) Clean (b) Noisy (c) PSNR=29.90 dB (d) PSNR=30.51 dB

(e) PSNR=31.17 dB (f) PSNR=32.21 dB (g) PSNR=31.65 dB (h) PSNR=33.34 dB

FIGURE 4.17. Result of the denoising algorithm compared with other methods: (a) Clean *Moon* image, (b) Image corrupted with Poisson noise corresponding to a SNR of 15 dB. Denoising results obtained using, (c) wavelet hard thresholding, (d) wavelet soft thresholding, (e) variance stabilization transform, (f) total variation regularization, (g) dictionary learning and (h) proposed method. The proposed adaptive transform was computed with the hyperparameters $\hbar^2/2m = 0.32$, $\sigma^2 = 2.5$, $\rho = 1$ and $s = 520$.

results compared to DL that learns the redundant dictionary from a database of clean images. Of course the proposed method does not need such a database. In summary, the results show that while our method is clearly the best for some specific types of signals or images for which it is well-adapted, it is also competitive for general types of images, being in almost all cases one of the two best methods. This indicates that the algorithm we propose can be used reliably for denoising applications in a variety of contexts.

4.5 Application to CBCT Dental Image Denoising

This section illustrates the ability of the proposed method to denoise real medical images. In particular, the application considered in this work for illustration purpose is CBCT dental imaging. CBCT is a medical imaging modality that allows tooth visualization with low radiation doses, and is thus suitable for dental applications. However, the low radiation prevents the current scanners to provide images with high SNR. In [245], the

(a) Clean (b) Noisy (c) PSNR=27.49 dB (d) PSNR=27.31 dB

(e) PSNR=28.55 dB (f) PSNR=28.71 dB (g) PSNR=27.24 dB (h) PSNR=30.10 dB

FIGURE 4.18. Result of the denoising algorithm compared with other methods: (a) Clean *Lena* image, (b) Image corrupted with speckle noise corresponding to a SNR of 15 dB. Denoising results obtained using, (c) wavelet hard thresholding, (d) wavelet soft thresholding, (e) variance stabilization transform, (f) total variation regularization, (g) dictionary learning and (h) proposed method. The proposed adaptive transform was computed with the hyperparameters $\hbar^2/2m = 0.36$, $\sigma^2 = 1.35$, $\rho = 2$ and $s = 600$.

TABLE 4.3. Quantitative denoising results for CBCT image.

Sample	CNR (dB)	SSIM
Noisy CBCT image	23.89	0.66
Denoised CBCT image	25.26	0.75

quality of CBCT dental image within phantom and *in vivo* data were evaluated. Fig. 4.19 shows a noisy image resulting from that study, as well as the denoised images with the proposed approach. The region of interest in this image is the dark region in the middle of the tooth, that represents the canal root. The results displayed show that the method has some practical applications in this field. For a quantitative analysis the contrast-to-noise ratio (CNR) computed between the dark region representing the canal root and the bright region representing the dentine, and the SSIM values comparing the noisy and the denoised image to the clean one, are presented in Table 4.3. They clearly show the ability of the proposed method to enhance the noisy CBCT image.

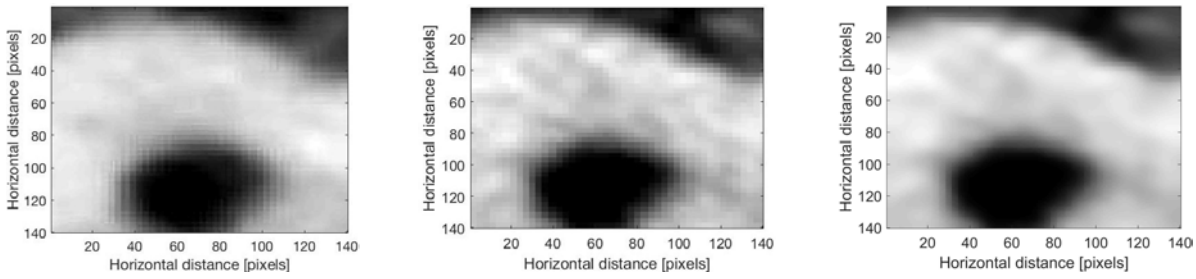

(a) Clean CBCT image (b) Noisy CBCT image (c) Denoised CBCT image

FIGURE 4.19. Result of the denoising algorithm for a biomedical image: (a) Clean CBCT dental image, (b) Noisy CBCT dental image, (c) CBCT dental image after denoising considering the hyperparameters $\hbar^2/2m = 0.5$, $\sigma^2 = 20$, $\rho = 1$ and $s = 3000$.

4.6 Conclusions

We investigated in this chapter an original approach of constructing an adaptive transform in the context of signal and image processing based on the resolution of a quantum mechanical problem. More precisely, the signal or image was used as the potential in a quantum problem, the resolution of which gives as eigenvectors the proposed adaptive basis. The basis vectors automatically use a different range of frequencies to explore low potential valued regions compare to the regions corresponding to the high potential values. Therefore, thresholding the coefficients of the signal or image expanded in this basis will process differently high and low values of the signal or image. This framework has been illustrated through denoising applications on different signals and images in presence of Gaussian, Poisson and speckle noise. We have performed a detailed investigation of the impact of the hyperparameters on the denoising accuracy. We have also presented a quantitative comparison of the denoising efficiency of the proposed adaptive method compared to state-of-the-art methods on synthetic signals and standard images. The results show that our method has interesting potential to denoise signals and images, especially for Poisson and speckle noise to which it is well adapted; indeed, as a vector in the adaptive basis naturally uses higher frequencies for low values of the signal compared to low values, the thresholding process keeps more frequencies for low values than for high values. The results show that our denoising procedure outperforms standard methods in specific cases, and ranks among the best methods in most cases. In general, the method should be optimal for signals or images with large contrasts in presence of Poisson-like noise. Our study of the hyperparameters shows that they

cannot be chosen at random, but that the range of optimality is large enough to allow to set them beforehand independently of the signal or image, although the choice may be modified according to the type of noise present in the application.

4.6.1 Limitations

In presence of strong noise, the wave functions become localized due to the quantum localization phenomenon and make the image restoration tasks more challenging. To mitigate this quantum effect a Gaussian smoothing was considered before the computation of the wave functions from the Hamiltonian operator. Although accumulation of this Gaussian smoothing significantly enhances the potential of the adaptive basis for imaging problems, it increases the number of tunable hyperparameters of the algorithm. Furthermore, the computational time of the eigenvectors of the Hamiltonian operator is the major drawback of this method. For a large-scale signal or image, this computation of the adaptive vectors becomes very costly and makes the practical implementations of our proposed algorithm difficult.

4.6.2 Perspectives

The issue of computational complexity can be tackled by more refined algorithms or by adapting the patch-based processing to the proposed framework, using for example the theory of multiple-particle quantum mechanics. It should be also noted that in many applications the computational efficiency of the algorithm, while important, is less crucial than the efficiency to denoise the signal or image considered. Moreover, implementing a patch-based architecture that relies on the quantum many-body theory can mitigate the problem of the quantum localization phenomenon of the adaptive vectors. In Chapter 6, we will illustrate this many-body quantum theory and its implementation in imaging tasks. This improved scheme profoundly enhances the efficiency of the proposed algorithm at a significantly lesser cost and without any Gaussian smoothing.

Using more complex quantum mechanical tools/concepts, such as the time-dependent Schrödinger equation, *i.e.,* the wave functions and the potential change with time, gives a very fascinating direction for further research. As another perspective of this study, it would be very interesting to extend this framework to three dimensional data or color images. It could be also extended to other reconstruction applications available in the literature, such as deconvolution, super-resolution or compressed sensing. In the succeeding Chapter 5, we will study the image deconvolution problem by plugging

our proposed quantum adaptive basis (QAB) as an off-the-shelf denoiser following the Plug-and-Play (PnP) scheme [354] described in Section 3.4.1.2.

CHAPTER 5

PLUG-AND-PLAY QUANTUM ADAPTIVE DENOISER FOR DECONVOLVING POISSON NOISY IMAGES

Contents

* This chapter presents materials from the journal paper [112] and conference paper [113].

Overview

A new alternating direction of multipliers (ADMM) Plug-and-Play (PnP) scheme is proposed in this chapter, by embedding the adaptive denoiser introduced in the previous chapter using the Schrödinger equation's solutions of quantum physics. The potential of the proposed model is studied for Poisson image deconvolution, which is a common problem occurring in number of imaging applications, such as limited photon acquisition or X-ray computed tomography. Numerical results show the efficiency and good adaptability of the proposed scheme compared to recent state-of-the-art techniques, for both high and low signal-to-noise ratio scenarios. This performance gain regardless of the amount of noise affecting the observations is explained by the flexibility of the embedded quantum denoiser constructed without anticipating any prior statistics about the noise, which is one of the main advantages of this method. The main novelty of this work resides in the integration of a modified quantum denoiser into the PnP-ADMM framework and the numerical proof of convergence of the resulting algorithm. A more computationally efficient algorithm for the quantum mechanics-based scheme of Chapter 4 is also presented. Finally, we show the ability of the proposed method to enhance real-life fluorescence microscopy images.

5.1 Introduction

5.1.1 Maximum-a-Posteriori (MAP) Estimation

In number of applications such as limited photon acquisition, X-ray computed tomography, positron emission tomography, etc., the noise degrading the acquired data follows a Poisson distribution. These Poissonian models have been extensively studied in the fields of astronomical [321–323], photographic [135, 155] or biomedical [90, 94, 129, 258, 299, 374] imaging. The inversion process is expressed as the estimation of a clean image $\boldsymbol{x} \in \mathbb{R}^n$ from observed degraded image $\boldsymbol{y} \in \mathbb{R}^m$. As stated in Chapter 3, we often formulate this estimation problem as a maximum-a-posteriori (MAP) estimation [272], where the goal is to maximize the posterior probability:

$$\begin{aligned} \hat{\boldsymbol{x}} &= \arg\max_{\boldsymbol{x}} \; P(\boldsymbol{x}|\boldsymbol{y}) \\ &= \arg\min_{\boldsymbol{x}} \big(-log(P(\boldsymbol{y}|\boldsymbol{x})) - log(P(\boldsymbol{x})) \big). \end{aligned} \tag{5.1}$$

for some conditional probability $P(\boldsymbol{y}|\boldsymbol{x})$ defining the forward imaging model, and a prior distribution $P(\boldsymbol{x})$ defining the probability distribution of the latent image, with $f(\boldsymbol{x}) = -log(P(\boldsymbol{y}|\boldsymbol{x}))$ as the negative log-likelihood function depends on the degradation (forward) model, and $g(\boldsymbol{x}) = -log(P(\boldsymbol{x}))$ as the *a priori* log-distribution of $\boldsymbol{x}$ or a regularization function. The optimization in eq. (5.1) is a generic unconstrained optimization. Thus, standard optimization algorithms can be used to solve the problem. In this chapter, we focus on the alternating direction method of multiplier (ADMM) [8, 14, 42, 58, 332, 385, 411], which has become the workhorse for a variety of problems in the form of (5.1).

5.1.2 ADMM Algorithm

As discussed in Chapter 3, the idea of ADMM is to convert (5.1), an unconstrained optimization, into a constrained problem

$$\begin{aligned} \underset{\boldsymbol{x},\boldsymbol{z}}{\text{minimize}} \quad & f(\boldsymbol{x}) + g(\boldsymbol{z}) \\ \text{subject to} \quad & \boldsymbol{x} = \boldsymbol{z}, \end{aligned} \tag{5.2}$$

and considering its augmented Lagrangian function, we can reproduce the sequence of subproblems (3.14)-(3.17):

$$\boldsymbol{x}^{k+1} = \arg\min_{\boldsymbol{x}} \; f(\boldsymbol{x}) + \frac{\lambda^k}{2} \left\| \boldsymbol{x} - \boldsymbol{z}^k + \boldsymbol{u}^k \right\|_2^2, \tag{5.3}$$

$$\boldsymbol{z}^{k+1} = \arg\min_{\boldsymbol{z}} \; g(\boldsymbol{z}) + \frac{\lambda^k}{2} \left\| \boldsymbol{x}^{k+1} - \boldsymbol{z} + \boldsymbol{u}^k \right\|_2^2, \tag{5.4}$$

$$\boldsymbol{u}^{k+1} = \boldsymbol{u}^k + \boldsymbol{x}^{k+1} - \boldsymbol{z}^{k+1}, \tag{5.5}$$

$$\lambda^{k+1} = \gamma \lambda^k. \tag{5.6}$$

where $\boldsymbol{u} \in \mathbb{R}^p$ is the Lagrangian multiplier, $\lambda \in \mathbb{R}^+$ is the penalty parameter of the augmented Lagrangian, and the constand $\gamma > 1$ accelerates the convergence.

5.1.3 Plug-and-Play (PnP) ADMM

The interest of PnP schemes have been extensively studied in image restoration problems, *e.g.*, [26, 27, 46, 60, 62, 77, 200, 287, 293, 319, 335, 337, 347, 364, 380, 404]. The key benefit of this process is that the regularizer does not need to be defined explicitly because of its implicit dependence on the denoising operator. More precisely, one may observe that (5.4) is associated with a denoising process, and can be rewritten as

$$\boldsymbol{z}^{k+1} = \arg\min_{\boldsymbol{z}} \; g(\boldsymbol{z}) + \frac{\lambda^k}{2} \left\| \boldsymbol{z} - (\boldsymbol{x}^{k+1} + \boldsymbol{u}^k) \right\|_2^2. \tag{5.7}$$

Treating $(\boldsymbol{x}^{k+1} + \boldsymbol{u}^k)$ as the "noisy" image, (5.7) minimizes the residue between $(\boldsymbol{x}^{k+1} + \boldsymbol{u}^k)$ and the "clean" image $\boldsymbol{z}$ using the prior $g(\boldsymbol{z})$, and is thus associated with a denoising problem designed to denoise $(\boldsymbol{x}^{k+1} + \boldsymbol{u}^k)$. Therefore (5.7) can be replaced by using an off-the-shelf image denoising algorithm, denoted by $\mathscr{D}(\cdot)$ [354], as illustrated in Chapter 3 to yield

$$\boldsymbol{z}^{k+1} = \mathscr{D}\left(\boldsymbol{x}^{k+1} + \boldsymbol{u}^k\right). \tag{5.8}$$

5.1.4 Contributions

This chapter focuses on PnP-ADMM algorithms applied to Poisson deconvolution problems, *i.e.*, recover an image from a blurred observation contaminated by Poisson noise. Since the state-of-the-art denoisers (*e.g.*, BM3D [82]) used within PnP schemes were primarily designed for additive Gaussian noise, they consequently exhibit inconsistency with a non-Gaussian model. Furthermore, decoupling the restoration and denoising steps within PnP frameworks converts the noise distribution affecting the observed

distorted image into a possibly different noise model, and in particular into a non-Gaussian noise. To mitigate this limitation, a variance stabilizing transformation (VST) [21, 108, 237, 239], known as the Anscombe transformation, was embedded in several PnP-ADMM algorithms to adapt them to a data-dependent model. Indeed, VST was designed to remodel approximately a random data-dependent noise into an additive Gaussian noise, before processing through a Gaussian denoiser. Although these refined VST-based PnP schemes exhibit very good performance for low-intensity noise [26, 27, 287] and outperform existing state-of-the-art prior based models, they are less accurate while dealing with high-intensity noise (*i.e.,* low SNR) [296]. Furthermore, the nonuniform nature of the convolution operator under a VST leads to fundamental flaws in the deconvolution algorithms [27, 91, 287]. Therefore, a versatile denoiser adapted to different noise models, without *a priori* hypothesis about the noise statistics, is desirable to be efficient regardless of the prior noise distribution in this PnP framework.

In this chapter, we address these shortcomings by embedding into a PnP-ADMM scheme a new adaptive denoiser designed in the previous Chapter 4 by borrowing tools from quantum mechanics. The adaptive nature of this denoiser makes it highly efficient at selectively eliminating noise from higher intensity pixels, without relying on any statistical assumption about the noise. Its efficiency regardless of the assumption of Gaussian noise represents the main motivation of its interest in Poisson deconvolution PnP-ADMM algorithms, discarding the necessity of a VST. To summarize, the main novelty of the work is the use of quantum mechanical concepts in the field of image restoration. The primary contributions are the quantum denoiser, its integration into a PnP-ADMM scheme, and the experimental proof of convergence of the final algorithm.

The remainder of the chapter is organized as follows. Section 5.2 proposes the PnP-ADMM algorithm for Poisson inverse problems. The numerical experiments and results are regrouped in Section 5.3. Section 5.4 shows the ability of the proposed method to enhance experimental fluorescence microscopy images before drawing conclusions in Section 5.5 with perspectives.

5.2 Proposed PnP-ADMM Algorithm

5.2.1 Poissonian Deconvolution Model

Let us denote by $\boldsymbol{x} \in \mathbb{R}^{n^2}$ the image to be recovered from the observation $\boldsymbol{y} \in \mathbb{R}^{n^2}$, a degraded version by a point spread function (PSF) and Poisson process denoted by $\mathscr{P}(\cdot)$.

Without loss of generality, we consider herein square images of size $n \times n$, written as vectors in lexicographical order. The resulting image formation model is

$$\boldsymbol{y} = \mathscr{P}(\boldsymbol{G}\boldsymbol{x}), \tag{5.9}$$

where $\boldsymbol{G} \in \mathbb{R}^{n^2 \times n^2}$ is a block circulant with circulant blocks (BCCB) matrix acounting for 2D circulant convolution with the PSF. The pixels of the observed blurry and noisy image $\boldsymbol{y}$ are denoted by $\boldsymbol{y}[i], i = 1,2,\cdots,n^2$, and are treated as independent realizations of a Poisson process with parameter $(\boldsymbol{G}\boldsymbol{x})[i] \geq 0$ given by

$$P\big(\boldsymbol{y}[i]\big|\boldsymbol{x}[i]\big) = \begin{cases} \dfrac{e^{-(\boldsymbol{G}\boldsymbol{x})[i]}(\boldsymbol{G}\boldsymbol{x})[i]^{\boldsymbol{y}[i]}}{\boldsymbol{y}[i]!} & \text{if } \boldsymbol{y}[i] \geq 0, \\ 0 & \text{elsewhere,} \end{cases} \quad \text{for } i=1,2,\cdots,n^2 \tag{5.10}$$

where $(\cdot)[i]$ represents the i-th component of a vectorized image. The restoration of $\boldsymbol{x}$ from the noisy-blurred observation $\boldsymbol{y}$ is the primary objective of Poisson deconvolution methods.

One standard way to estimate $\boldsymbol{x}$ from the observation model (5.9) is to use the MAP estimator in (5.1). The Poisson noise probability density function is defined as

$$P(\boldsymbol{y}|\boldsymbol{x}) = \prod_i \frac{e^{-(\boldsymbol{G}\boldsymbol{x})[i]}(\boldsymbol{G}\boldsymbol{x})[i]^{\boldsymbol{y}[i]}}{\boldsymbol{y}[i]!}. \tag{5.11}$$

Thus, the log-likelihood term, *i.e.,* the data fidelity term $f(\boldsymbol{x})$ used within the MAP estimator, is given by

$$\begin{aligned} f(\boldsymbol{x}) &= -log\,(P(\boldsymbol{y}|\boldsymbol{x})) \\ &= -\sum_i log\left(\frac{e^{-(\boldsymbol{G}\boldsymbol{x})[i]}(\boldsymbol{G}\boldsymbol{x})[i]^{\boldsymbol{y}[i]}}{\boldsymbol{y}[i]!}\right) \\ &= -\boldsymbol{y}^T log(\boldsymbol{G}\boldsymbol{x}) + \mathbf{1}^T\boldsymbol{G}\boldsymbol{x} + \text{constant}, \end{aligned} \tag{5.12}$$

where $\mathbf{1}$ is a vector of length n^2 with all elements equal to 1. As explained previously, the function $g(\boldsymbol{x})$, a prior of $\boldsymbol{x}$, depends on some prior knowledge on the image to estimate. In a PnP framework, this prior is intrinsically defined through the external denoiser, removing the need of defining the prior term $g(\boldsymbol{x})$ explicitly. Hence, using the data fidelity term $f(\boldsymbol{x})$ in (5.12), the PnP-ADMM steps depicted in (5.3), (5.5), (5.6) and (5.8) become:

$$\boldsymbol{x}^{k+1} = \arg\min_{\boldsymbol{x}}\Big(-\boldsymbol{y}^T log(\boldsymbol{G}\boldsymbol{x}) + \mathbf{1}^T\boldsymbol{G}\boldsymbol{x} + \frac{\lambda^k}{2}\left\|\boldsymbol{x} - \boldsymbol{z}^k + \boldsymbol{u}^k\right\|_2^2\Big), \tag{5.13}$$

$$\boldsymbol{z}^{k+1} = \mathscr{D}\Big(\boldsymbol{x}^{k+1} + \boldsymbol{u}^k\Big), \tag{5.14}$$

$$\boldsymbol{u}^{k+1} = \boldsymbol{u}^k + \boldsymbol{x}^{k+1} - \boldsymbol{z}^{k+1}, \tag{5.15}$$

$$\lambda^{k+1} = \gamma\lambda^k, \tag{5.16}$$

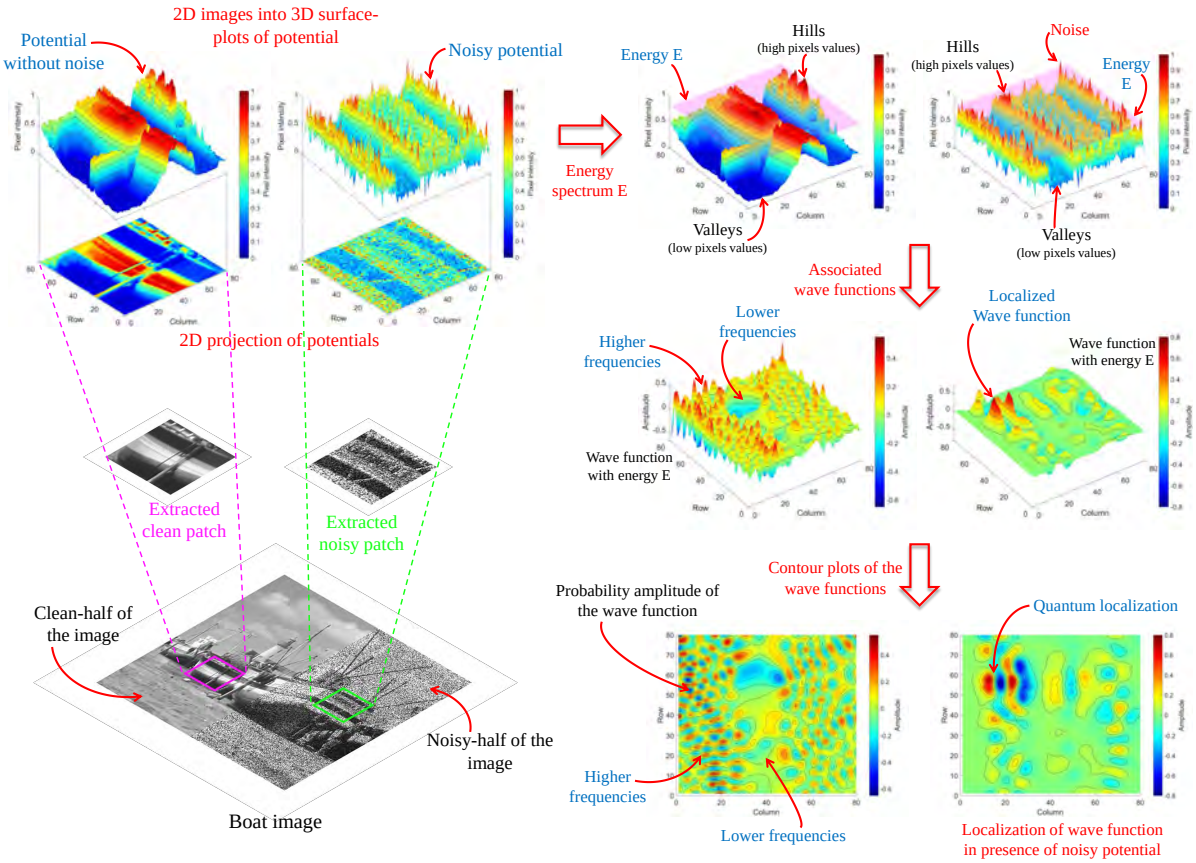

FIGURE 5.1. Relationship between the clean and noisy images under the quantum mechanical framework and their effects on the wave functions: example of the *Boat* image.

where $\mathscr{D}(\cdot)$ is the denoising operator considered within the PnP-ADMM algorithm. In this work, following [288], a gradient descent algorithm is used to solve the minimization problem (5.13), that requires the use of the gradient of the augmented Lagrangian $\mathscr{L}_\lambda$ given by

$$\nabla_{\boldsymbol{x}} \mathscr{L}_\lambda = -\boldsymbol{G}^T\left(\boldsymbol{y}/(\boldsymbol{G}\boldsymbol{x})\right) + \boldsymbol{G}^T\mathbf{1} + \lambda^k(\boldsymbol{x} - \boldsymbol{z}^k + \boldsymbol{u}^k), \tag{5.17}$$

where $\nabla_{\boldsymbol{x}}$ represents the derivative with respect to $\boldsymbol{x}$ and $\boldsymbol{y}/(\boldsymbol{G}\boldsymbol{x})$ stands for element-wise division.

The following subsection describes the Poisson denoiser inspired from quantum mechanics used within the proposed PnP-ADMM algorithm for Poisson image deconvolution, to solve the step in (5.14).

5.2.2 Quantum Adaptive Basis (QAB) Denoiser

As said before, in the last decade, several works have been conducted to use quantum mechanical principles in signal [126] and image processing applications. More precisely, the interest in image segmentation [24, 389–391], restoration [395] and denoising [114, 204, 312] have been studied in the literature.

The denoiser embedded in the proposed method is based on the construction of an adaptive basis inspired by quantum mechanics, as originally proposed in the preceding Chapter 4. An illustration of the adaptive basis construction is given in Fig. 5.1. It displays the relationship between a clean and a noisy image in the quantum mechanical framework. The basic idea is to use the image as a potential of a quantum system, where the height of the potential is determined by the pixel intensity. For illustration purpose, we considered the *Boat* image with half of it contaminated by Gaussian noise. Two patches, one clean and one noisy, are extracted from the image and plotted as 3D surfaces, which will ultimately act as the potentials of the system. In this system, the wave function governs the probability of presence of a quantum particle with energy E at some position on the surface. For a clean image, the wave function uses a broad range of frequencies to probe the surface. In presence of random noise, the wave function becomes localized at some particular position on the surface, as highlighted in Fig. 5.1. The salient feature of the adaptive basis is the fact that the pixel intensity is directly linked to the local frequency of the wave. The localization property in the presence of noise is actually a hindrance, cured by performing a pre-smoothing of the noisy potential in order to create an adaptive basis extended over the whole image. For more details on the construction of the basis, we refer the reader to the previous Chapter 4. For self-consistency, we recall hereafter the main steps of the QAB (quantum adaptive basis) technique.

5.2.2.1 Background on the Adaptive QAB Transform

In the non-relativistic quantum mechanics, the time-independent Schrödinger equation yields an equation for the stationary wave solution $\boldsymbol{\psi}(z)$, given by

$$-\frac{\hbar^2}{2m}\nabla^2\boldsymbol{\psi} = -V(z)\boldsymbol{\psi} + E\boldsymbol{\psi}, \tag{5.18}$$

where $\hbar$ is the Planck constant and $\boldsymbol{\psi}(z)$ characterizes the energy state E of the particle with mass m in a potential V. The probability amplitude of the particle is given by $|\boldsymbol{\psi}(z)|^2$, normalized under $\int |\boldsymbol{\psi}(z)|^2 dz = 1$. The wave function $\boldsymbol{\psi}(z)$ is an element of the

Hilbert space of square-integrable functions. It is possible to rewrite the equation (5.18) as

$$\boldsymbol{H}\boldsymbol{\psi} = E\boldsymbol{\psi}, \tag{5.19}$$

where $\boldsymbol{H} = -\frac{\hbar^2}{2m}\nabla^2 + V$ is the Hamiltonian operator. One can conclude from (5.19) that the solution $\boldsymbol{\psi}(z)$ of the equation (5.18) represents an eigenstate of the system described by the Hamiltonian operator. These eigenstates of (5.19) are oscillatory functions and primarily have two properties: i) the oscillation frequency increases with energy and ii) for the same eigenfunction, the local frequency depends on the local value of the potential, and this dependence is regulated by the value of $\hbar^2/2m$ which acts as a hyperparameter herein.

As in Chapter 4, in the perspective of designing an adaptive transformation for image processing, one may consider the image pixels' values as the potential V in the Schrödinger equation (5.18) for a discretized space. We recall here, for easiness, the stationary solutions of (5.18) can be obtained by computing the eigenpairs of the discretized Hamiltonian operator defined as:

$$\boldsymbol{H}[i,j] = \begin{cases} \boldsymbol{x}[i] + 4\dfrac{\hbar^2}{2m} & \text{for } i = j, \\ -\dfrac{\hbar^2}{2m} & \text{for } i = j \pm 1, \\ -\dfrac{\hbar^2}{2m} & \text{for } i = j \pm n, \\ 0 & \text{otherwise,} \end{cases} \tag{5.20}$$

where $\boldsymbol{x} \in \mathbb{R}^{n^2}$ is an image (*i.e.,* $V = \boldsymbol{x}$), vectorized in lexicographical order and $\boldsymbol{H}[i,j]$ represents the (i,j)-th element of the operator $\boldsymbol{H} \in \mathbb{R}^{n^2 \times n^2}$. Note that zero padding is used to handle the boundary conditions. As a consequence some violations of the rule (5.20) can be observed. More precisely, $\boldsymbol{H}[i,j] = \boldsymbol{x}[i] + 2\frac{\hbar^2}{2m}$ for $i = j$ and $i \in \{1, n, n^2 - n + 1, n^2\}$, $\boldsymbol{H}[i,j] = \boldsymbol{x}[i] + 3\frac{\hbar^2}{2m}$ for $i = j$ and $i \in \{2, 3, ..., n-1, n^2 - n + 2, n^2 - n + 3, ..., n^2 - 1\}$, $\boldsymbol{H}[i,j] = \boldsymbol{x}[i] + 3\frac{\hbar^2}{2m}$ for $i = j$ and $i \mod n \in \{0, 1\}$, except for $i \in \{1, 2, ..., n, n^2 - n + 1, n^2 - n + 2, ..., n^2\}$ in order to respect the boundary conditions, and $\boldsymbol{H}[i, i+1] = \boldsymbol{H}[i+1, i] = 0$ for any i multiple of n apart from n^2. More details about the construction of the Hamiltonian operator associated to an image can be found in Subsection 4.3.1 of the Chapter 4.

The corresponding eigenbasis of the Hamiltonian operator (5.20) represents the adaptive transform. In the previous Chapter 4, it was shown that this adaptive basis gives an efficient way of image denoising, especially in the presence of Gaussian, Poisson

or speckle noise. In this chapter, this adaptive basis, referred to as QAB, is used to construct the denoiser $\mathscr{D}_{\mathscr{QAB}}(\cdot)$ embedded in the proposed PnP-ADMM scheme.

These basis vectors belong to the family of oscillating functions along with the Fourier and wavelet bases, but with a local frequency depending on the local value of $\sqrt{2m(E-V)}/\hbar$. Due to its dependence on the difference between the energy E and potential V, in the same basis vector the lower values of the potential are associated with oscillations of higher frequency. Thus, the property of these adaptive basis vectors able to describe different image pixels' values using different frequency levels, makes it fundamentally distinct from the Fourier and wavelet bases. From the above discussion it is understandable that the local frequency depends on the value of $\hbar^2/2m$, which is a hyperparameter. Apart from that, the level of noise also has an impact on the basis vectors. Indeed, the presence of random noise in the system leads to a subtle quantum phenomenon [19] which makes these vectors localize exponentially at different positions of the potential in the system. To mitigate this phenomenon which degrades the denoising, it is important to low-pass the corrupted image using, for example, a Gaussian filter with suitable standard deviation $\sigma_{\mathscr{QAB}}$, before the computation of the QAB from the Hamiltonian operator (5.20). The reader may refer to Subsection 4.3.2 of the previous chapter for an in-depth discussion about the QAB vector localization in the presence of noise.

The QAB explained above is used to denoise an image, as follows: project the noisy image onto the QAB to identify the valuable information and the noise, followed by a soft-thresholding of the projection coefficients, before taking the inverse projection of the modified coefficients to recover the noise-free image. The denoised image $\hat{\boldsymbol{x}}$ is retrieved as following:

$$\hat{\boldsymbol{x}} = \sum_{i=1}^{n^2} \tau_i \boldsymbol{\alpha}_i \boldsymbol{\psi}_i, \tag{5.21}$$

with

$$\tau_i = \begin{cases} 1 & \text{for } i \leq s, \\ 1 - \dfrac{i-s}{\rho} & \text{for } i > s \text{ and for } 1 - \dfrac{i-s}{\rho} > 0, \\ 0 & \text{otherwise,} \end{cases} \tag{5.22}$$

where $\boldsymbol{\alpha}_i$ are the coefficients representing the image $\boldsymbol{x}$ in QAB, whose basis vectors are $\boldsymbol{\psi}_i$. s and ρ are two thresholding hyperparameters. The denoising process thus corresponds to expanding the signal in the adaptive basis and thresholding the coefficients according to an energy criterion (see Chapter 4 for a detailed discussion of this procedure).

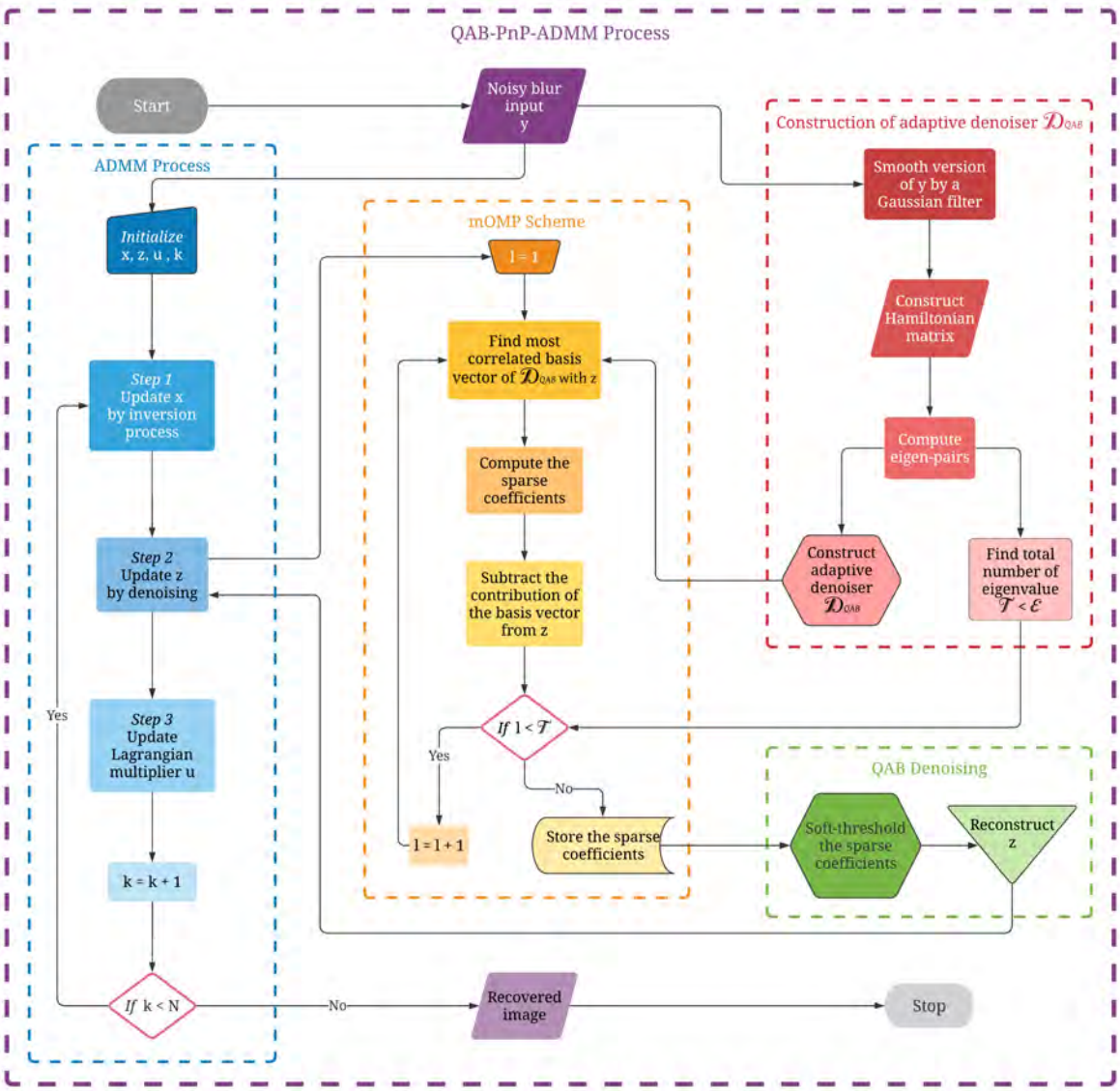

FIGURE 5.2. Flowchart of the proposed QAB-PnP algorithm.

5.2.3 QAB-PnP Algorithm

This section illustrates, in the context of Poisson image deconvolution, the proposed PnP-ADMM algorithm, denoted as QAB-PnP, incorporating the QAB denoiser introduced in the previous section. In this particular context, various state-of-the-art denoisers have been introduced in the literature, such as Gaussian denoisers (*e.g.,* BM3D [82], etc) fused with VST-like transforms or not. Using QAB $\mathscr{D}_{\mathscr{QAB}}$ instead of a classical denoiser is the main contribution of this chapter. It consists in including a modified version of the QAB denoiser into the deconvolution PnP-ADMM method from Section 5.2.1, more precisely

to solve (5.14).

The denoising process integrated in the proposed QAB-PnP algorithm requires the computation of the coefficients $\boldsymbol{\alpha}_i$, obtained by projecting the noisy image onto the QAB. This is a time consuming task for a large image and affects the computational load of the deconvolution algorithm given that the denoising process is performed at each iteration. However, one may note that most of the $\boldsymbol{\alpha}_i$ are not used for reconstructing the denoised image given that they are discarded by the threshohlding operation. To increase the computational efficiency of the proposed algorithm, only the coefficients which contribute the most in the restoration process are computed. To this end, let us focus on $\mathscr{T}$ basis vectors $\boldsymbol{\alpha}_i$ from $\mathscr{D}_{\mathscr{QAB}}$, corresponding to an energy level below $\mathscr{E}$, assuming that higher energy levels naturally correspond to higher frequencies, where $\mathscr{E}$ is considered as a free hyperparameter. The corresponding $\mathscr{T}$ coefficients will be the most significant for the reconstruction of the clean image, and can be computed using the orthogonal matching pursuit (OMP) algorithm [88, 256, 295, 345].

The OMP algorithm was fundamentally designed to obtain a sparse approximation $\hat{\boldsymbol{\alpha}}_i$ with sparsity $\mathscr{T}$ of the corresponding coefficients $\boldsymbol{\alpha}_i$ while projecting the noisy image, say $\boldsymbol{v} \in \mathbb{R}^{n^2}$ onto the denoising basis $\mathscr{D}_{\mathscr{QAB}}$. Therefore the primary goal of OMP is to recover coefficients $\hat{\boldsymbol{\alpha}}_i$ with $\mathscr{T}$ non-zero elements, such that $\boldsymbol{v} \simeq \mathscr{D}_{\mathscr{QAB}}\hat{\boldsymbol{\alpha}}_i$. To get the best possible approximation, it is important to identify the columns $\boldsymbol{\psi}_i \in \mathscr{D}_{\mathscr{QAB}}$ which contribute in the reconstruction of $\boldsymbol{v}$. The basic idea is to choose the column of $\mathscr{D}_{\mathscr{QAB}}$ which is mostly correlated with $\boldsymbol{v}$, followed by subtracting its contribution and repeat

Algorithm 5.1: Modified Orthogonal Matching Pursuit algorithm.

Input: $\boldsymbol{v}$, $\mathscr{T}$, $\mathscr{D}_{\mathscr{QAB}}$

Initialization: $\boldsymbol{r}^0 = \boldsymbol{v}$, $\Lambda^0 = \emptyset$, Φ^0 is an empty matrix
for *l from* 0 *to* $\mathscr{T} - 1$ **do**
  $l = l + 1$
  $\lambda^l = \underset{j=1,2,\ldots,\mathscr{T}}{\arg\max} \; |\langle \boldsymbol{r}^{l-1}, \boldsymbol{\psi}_j \rangle|$, for $\boldsymbol{\psi}_j \in \mathscr{D}_{\mathscr{QAB}}$ (Break ties deterministically)
  $\Lambda^l = \Lambda^{l-1} \bigcup \lambda^l$
  $\Phi^l = [\Phi^{l-1} \quad \psi_{\lambda^l}]$
  $a^l = \underset{a}{\arg\min} \; \left\| \boldsymbol{v} - \Phi^l a \right\|_2^2$
  $\boldsymbol{r}^l = \boldsymbol{v} - \Phi^l a^l$

Output: $\hat{\boldsymbol{\alpha}}$, which has nonzero elements only at Λ^l, *i.e.,* $\hat{\boldsymbol{\alpha}}_{\Lambda^l} = a^l$

Algorithm 5.2: QAB denoising algorithm.

Input: $\boldsymbol{z}$, $\mathscr{D}_{\mathscr{QAB}}$, $\mathscr{T}$, s , ρ

1 Compute the sparse coefficients $\hat{\boldsymbol{\alpha}}_i$ with sparsity $\mathscr{T}$ by using the measurement data $\boldsymbol{z}$ and the operator $\mathscr{D}_{\mathscr{QAB}}$ following the modified orthogonal matching pursuit method as illustrated in Algorithm 5.1.
2 Threshold the coefficients $\hat{\boldsymbol{\alpha}}_i$.
3 Compute $\hat{\boldsymbol{z}}$ following (5.22) and (5.21).

Output: $\hat{\boldsymbol{z}}$

Algorithm 5.3: Poisson deconvolution using QAB-PnP algorithm.

Input: $\boldsymbol{y}$, $\mathscr{E}$, λ_0 , γ, $\dfrac{\hbar^2}{2m}$, $\sigma_{\mathscr{QAB}}$, N

1 **Initialization:** $\boldsymbol{x}^0$, $\boldsymbol{z}^0$, $\boldsymbol{u}^0$
2 Compute a smooth version of $\boldsymbol{y}$ by low-pass Gaussian filter with standard deviation $\sigma_{\mathscr{QAB}}$
3 Form the Hamiltonian matrix $\boldsymbol{H}$ based on the smoothed version of $\boldsymbol{y}$ using (5.20)
4 Calculate the eigen-pairs of $\boldsymbol{H}$
5 Construct $\mathscr{D}_{\mathscr{QAB}}$ using the eigenvectors $\boldsymbol{\psi}_i$ of $\boldsymbol{H}$
6 Find the total number of eigenvalue $\mathscr{T}$, less than the energy level $\mathscr{E}$
7 **begin**
8 **ADMM process:**
9 **for** *k from* 0 *to* $N-1$ **do**
10 *Step 1:*
11 $\boldsymbol{x}^{k+1} = \arg\min_{\boldsymbol{x}} \; -\boldsymbol{y}^T log(\boldsymbol{G}\boldsymbol{x}) + \mathbf{1}^T \boldsymbol{G}\boldsymbol{x} + \dfrac{\lambda^k}{2} \left\| \boldsymbol{x} - \boldsymbol{z}^k + \boldsymbol{u}^k \right\|_2^2$
12 *Step 2:*
13 $\boldsymbol{z}^{k+1} = \mathscr{D}_{\mathscr{QAB}}(\boldsymbol{x}^{k+1} + \boldsymbol{u}^k)$, following QAB denoising Algorithm 5.2
14 *Step 3:*
15 $\boldsymbol{u}^{k+1} = \boldsymbol{u}^k + \boldsymbol{x}^{k+1} - \boldsymbol{z}^{k+1}$
16 $\lambda^{k+1} = \gamma \lambda^k$

Output: $\hat{\boldsymbol{x}} = \boldsymbol{x}^N$

the step on the residual. After $\mathscr{T}$ iterations one can have the desired set of basis vectors and projection coefficients. Within the adaptive basis $\mathscr{D}_{\mathscr{QAB}}$, the basis eigenvectors are organized in ascending order, the first $\mathscr{T}$ basis vectors with energy less than $\mathscr{E}$ being the most correlated with $\boldsymbol{v}$. Therefore, the OMP algorithm is modified herein so that it

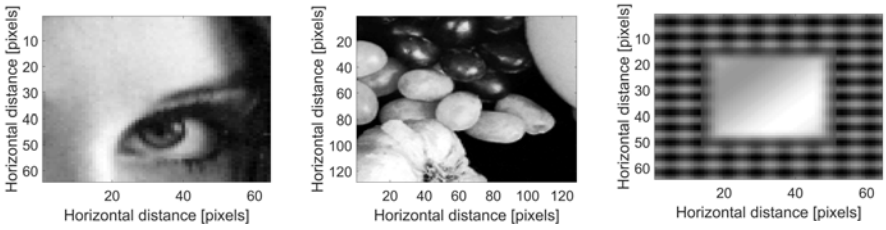

(a) Lena (b) Fruits (c) Synthetic

FIGURE 5.3. Images used for deconvolution simulations.

estimates only the projection coefficients onto the subspace formed by these $\mathscr{T}$ basis vectors. This modified OMP algorithm is detailed in Algorithm 5.1.

The sparse coefficients $\hat{\boldsymbol{\alpha}}_i$ estimated by Algorithm 5.1 are further used by the denoising method detailed in Algorithm 5.2, integrated in the proposed QAB-PnP deconvolution method in Fig. 5.2 and Algorithm 5.3.

5.2.3.1 Computational Complexity

The computational complexity of the algorithm is dominated by the eigendecomposition of the high dimensional Hamiltonian matrix and the QAB image projection. For a $n \times n$ image, the Hamiltonian matrix is of size $n^2 \times n^2$. Usual textbook diagonalization methods would require $O(n^6)$ operations (time complexity) and $O(n^4)$ storage space. However, the Hamiltonian matrix is extremely sparse, and is more efficiently diagonalized by iterative methods such as the Lanczos method (as we actually did). In this case the computational complexity would be $O(n^4)$ if we compute all eigenvalues and eigenvectors (and still $O(n^4)$ in storage space). If we compute only $\mathscr{T}$ of these eigenvalues and eigenvectors (with $\mathscr{T} \leq n^2$), the time complexity becomes $O(\mathscr{T} n^2)$ and the storage space (space complexity) also $O(\mathscr{T} n^2)$. The QAB image projection is $O(n^4)$ with the simplest algorithm, and becomes $O(\mathscr{T} n^2)$ in time and space with the OMP algorithm. We thus conclude that our algorithm requires $O(\mathscr{T} n^2)$ time and space resources, with $\mathscr{T} \leq n^2$, for a $n \times n$ image. To further decrease the complexity, a block-wise approach could be used as proposed in the Chapter 4, where a large image is divided into smaller patches denoised independently by the QAB denoiser. In this the complexity is $O(\mathscr{T} P \overline{n}^2)$ for P patches of size $\overline{n}$ ($<< n$). Moreover, such a patch-based architecture can be improved by considering the dependence between neighboring patches by borrowing tools from the quantum interaction theory and will be discussed in Chapter 6.

5.2.4 Convergence Analysis of QAB-PnP Algorithm

Despite their popularity during the last decade, the proof of convergence of PnP-ADMM algorithms may still be an issue. Some interesting developments have been proposed during the last few years on global [319] and fixed point [60, 62, 77, 293, 337, 380, 404] convergence of these algorithms, while imposing restrictions on the denoising operator. In this section, our goal is to analyse the fixed point convergence of the proposed QAB-PnP algorithm.

To enable the fixed point convergence and in particular to avoid the issue of unbounded gradient in (5.17) for pixel values equal to 0, i.e., to overcome the singularity problem at $\boldsymbol{x} = 0$, we slightly modify the observation model (5.9) by introducing a small positive constant $\epsilon \ll 1$, as suggested in [158]:

$$\boldsymbol{y} = \mathscr{P}(\boldsymbol{G}\boldsymbol{x} + \epsilon\mathbf{1}). \tag{5.23}$$

Therefore the negative Poisson log-likelihood (5.12) becomes

$$f(\boldsymbol{x}) = -\boldsymbol{y}^T log(\boldsymbol{G}\boldsymbol{x} + \epsilon\mathbf{1}) + \mathbf{1}^T\boldsymbol{G}\boldsymbol{x}, \tag{5.24}$$

and the corresponding gradient

$$\nabla f(\boldsymbol{x}) = -\boldsymbol{G}^T(\boldsymbol{y}/(\boldsymbol{G}\boldsymbol{x} + \epsilon\mathbf{1})) + \boldsymbol{G}^T\mathbf{1}. \tag{5.25}$$

One should note that within practical experiments, ϵ is much smaller than any background value, so that its influence on the final output is negligible [158].

Remark 5.1. *For $f(\boldsymbol{x}) : [0,1]^{n^2} \to \mathbb{R}^+$, with nontrivial constant vector $\boldsymbol{y} \in \mathbb{R}^{n^2}$ and operator $\boldsymbol{G} \in \mathbb{R}^{n^2 \times n^2}$, the gradient $\nabla f(\boldsymbol{x})$ is bounded.*

Proof. Since ϵ is the lower bound of $(\boldsymbol{G}\boldsymbol{x} + \epsilon\mathbf{1})$, therefore $1/\epsilon$ is the upper bound of $1/(\boldsymbol{G}\boldsymbol{x} + \epsilon\mathbf{1})$. Since $\boldsymbol{y}$ and $\boldsymbol{G}$ are constants, they are bounded. Hence one can write:

$$\begin{aligned} \|\nabla f(\boldsymbol{x})\|_2 &= \left\| -\boldsymbol{G}^T(\boldsymbol{y}/(\boldsymbol{G}\boldsymbol{x} + \epsilon\mathbf{1})) + \boldsymbol{G}^T\mathbf{1} \right\|_2 \\ &\leq \left\| \boldsymbol{G}^T \right\|_2 \left\| \frac{\boldsymbol{y}}{\boldsymbol{G}\boldsymbol{x} + \epsilon\mathbf{1}} \right\|_2 + \left\| \boldsymbol{G}^T \right\|_2 \\ &\leq \frac{\delta_1}{\epsilon} + \delta_2 \\ &\leq L < \infty \end{aligned} \tag{5.26}$$

where $\delta_1, \delta_2, L \in \mathbb{R}^+$.

■

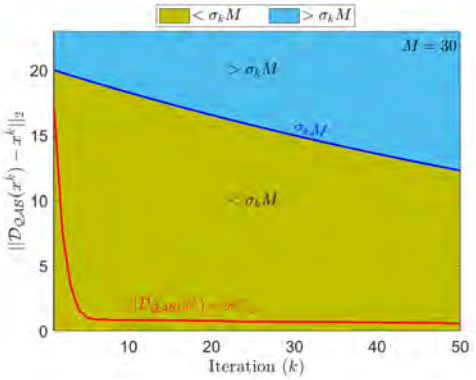

(a) Performed on the image in Fig. 5.3(a).

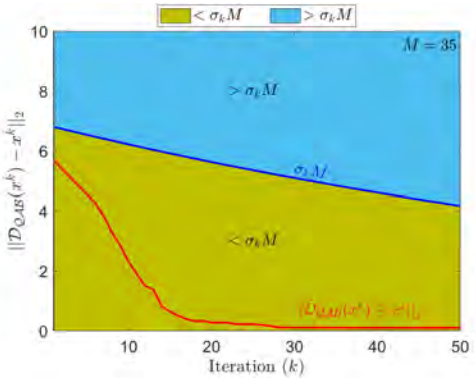

(b) Performed on the image in Fig. 5.3(b).

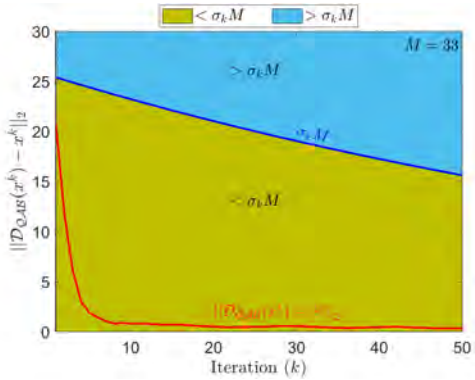

(c) Performed on the image in Fig. 5.3(c).

FIGURE 5.4. Numerical validation of the criteria, $\left\|\mathscr{D}_{\mathscr{QAB}}(\boldsymbol{x}^k) - \boldsymbol{x}^k\right\|_2 \leq \sigma_k M$ for any $\boldsymbol{x}^k \in \mathbb{R}^{n^2}$, performed on the sample images in Fig. 5.3(a-c).

Remark 5.2. *Denoiser $\mathscr{D}_{\mathscr{QAB}}$ is a bounded denoising operator with a parameter σ_k.*

We cannot offer a general proof of this statement, also it intuitively appears highly likely. The denoising process denoted by $\mathscr{D}_{\mathscr{QAB}}$ certainly reduces the level of noise at each iteration and gets $\mathscr{D}_{\mathscr{QAB}}(\boldsymbol{x}^k)$ closer and closer to $\boldsymbol{x}^k$. It is therefore fair to consider that $\left\|\mathscr{D}_{\mathscr{QAB}}(\boldsymbol{x}^k) - \boldsymbol{x}^k\right\|_2$ decreases with k. It is also bounded by $\left\|\boldsymbol{x}^k\right\|_2$ since $\mathscr{D}_{\mathscr{QAB}}$ is a projection operator.

The rate of decrease is not a priori easy to bound, but we offer numerical evidence that the decrease is fast. Indeed, in all three examples shown in Fig. 5.4 the decrease is very fast. In particular, it is much faster that the rate of decrease of $\sigma_k \overset{\text{def}}{=} 1/\lambda^k$. We thus generalize this result and take as generic that $\left\|\mathscr{D}_{\mathscr{QAB}}(\boldsymbol{x}^k) - \boldsymbol{x}^k\right\|_2 \leq \sigma_k M$ where M is a system-dependent constant.

Remark 5.3 (Fixed Point Convergence of QAB-PnP algorithm)**.** *If*

1. *$f(\boldsymbol{x}):[0,1]^{n^2}\to\mathbb{R}^+$ is analytic and has bounded gradient, i.e., for all $\boldsymbol{x}\in[0,1]^{n^2}$, there exists $L<\infty$ such that $\|\nabla f(\boldsymbol{x})\|_2\le L$, and*

2. *$\mathscr{D}_{\mathscr{QAB}}$ is a bounded denoising operator with a parameter σ_k,*

then QAB-PnP converges to a fixed point. That is, there exists $(\boldsymbol{x}^*,\boldsymbol{z}^*,\boldsymbol{u}^*)$ such that $\left\|\boldsymbol{x}^k-\boldsymbol{x}^*\right\|_2\to\mathbf{0}$, $\left\|\boldsymbol{z}^k-\boldsymbol{z}^*\right\|_2\to\mathbf{0}$, $\left\|\boldsymbol{u}^k-\boldsymbol{u}^*\right\|_2\to\mathbf{0}$ as $k\to\infty$.

Proof. $*$ *First condition:* The first condition holds as shown in Remark 5.1.

$*$ *Second condition:* The second condition should hold generically as discussed in Remark 5.2.

Given that the two conditions are satisfied within the proposed framework, let us move to the proof of the fixed point convergence in Remark 5.3. We start by proving the following statements:

$$\left\|\boldsymbol{z}^{k+1}-\boldsymbol{z}^k\right\|\le\frac{C_2}{\lambda^k} \tag{5.27}$$

$$\left\|\boldsymbol{x}^{k+1}-\boldsymbol{x}^k\right\|\le\frac{C_1}{\lambda^k} \tag{5.28}$$

$$\left\|\boldsymbol{u}^{k+1}-\boldsymbol{u}^k\right\|\le\frac{C_3}{\lambda^k} \tag{5.29}$$

where C_1, C_2 and C_3 are constants and λ^k is the penalty parameter with $\lambda^{k+1}=\gamma\lambda^k$, where $\gamma>1$.

$*$ *First step:* Proof of condition (5.27).

From (5.3), we have

$$\boldsymbol{x}^{k+1}=\arg\min_{\boldsymbol{x}}\ f(\boldsymbol{x})+\frac{\lambda^k}{2}\left\|\boldsymbol{x}-\boldsymbol{z}^k+\boldsymbol{u}^k\right\|_2^2. \tag{5.30}$$

The first order optimality implies

$$\boldsymbol{x}-(\boldsymbol{z}^k-\boldsymbol{u}^k)=-\frac{\nabla f(\boldsymbol{x})}{\lambda^k}. \tag{5.31}$$

Since the minimizer is obtained in $\boldsymbol{x}=\boldsymbol{x}^{k+1}$, replacing $\boldsymbol{x}$ by $\boldsymbol{x}^{k+1}$ and using the boundedness property of $\nabla f(\boldsymbol{x})$, we have

$$\left\|\boldsymbol{x}^{k+1}-(\boldsymbol{z}^k-\boldsymbol{u}^k)\right\|_2=\frac{\left\|\nabla f(\boldsymbol{x}^{k+1})\right\|_2}{\lambda^k}\le\frac{L}{\lambda^k}. \tag{5.32}$$

Furthermore, since the denoiser $\mathscr{D}_{\mathscr{Q}\mathscr{A}\mathscr{B}}$ is bounded and $\boldsymbol{z}^{k+1} = \mathscr{D}_{\mathscr{Q}\mathscr{A}\mathscr{B}}(\boldsymbol{x}^{k+1} + \boldsymbol{u}^k)$, one can write

$$\begin{aligned} &\left\| \boldsymbol{z}^{k+1} - (\boldsymbol{x}^{k+1} + \boldsymbol{u}^k) \right\|_2 \\ &= \left\| \mathscr{D}_{\mathscr{Q}\mathscr{A}\mathscr{B}}(\boldsymbol{x}^{k+1} + \boldsymbol{u}^k) - (\boldsymbol{x}^{k+1} + \boldsymbol{u}^k) \right\|_2 \\ &\leq \sigma_k M = \frac{M}{\lambda^k}. \end{aligned} \tag{5.33}$$

One also has

$$\begin{aligned} \left\| \boldsymbol{z}^{k+1} - \boldsymbol{z}^k \right\|_2 \leq &\left\| \boldsymbol{z}^{k+1} - (\boldsymbol{x}^{k+1} + \boldsymbol{u}^k) \right\|_2 \\ &+ \left\| (\boldsymbol{x}^{k+1} + \boldsymbol{u}^k) - \boldsymbol{z}^k \right\|_2. \end{aligned} \tag{5.34}$$

Finally, using (5.32) and (5.33), we obtain

$$\left\| \boldsymbol{z}^{k+1} - \boldsymbol{z}^k \right\|_2 \leq \frac{L}{\lambda^k} + \frac{M}{\lambda^k} = \frac{C_2}{\lambda^k}. \tag{5.35}$$

∗ *Second step:* Proof of condition (5.29).

From (5.5), we get

$$\begin{aligned} \left\| \boldsymbol{u}^{k+1} \right\|_2 &= \left\| \boldsymbol{u}^k + \boldsymbol{x}^{k+1} - \boldsymbol{z}^{k+1} \right\|_2 \\ &= \left\| (\boldsymbol{x}^{k+1} + \boldsymbol{u}^k) - \mathscr{D}_{\mathscr{Q}\mathscr{A}\mathscr{B}}(\boldsymbol{x}^{k+1} + \boldsymbol{u}^k) \right\|_2 \\ &\leq \frac{M}{\lambda^k}. \end{aligned} \tag{5.36}$$

Using (5.36), we have

$$\left\| \boldsymbol{u}^{k+1} - \boldsymbol{u}^k \right\|_2 \leq \left\| \boldsymbol{u}^{k+1} \right\| + \left\| \boldsymbol{u}^k \right\|_2 \leq \frac{M}{\lambda^k} + \frac{M}{\lambda^k} = \frac{C_3}{\lambda^k}. \tag{5.37}$$

∗ *Third step:* Proof of condition (5.28).

(5.5) can be written as

$$\boldsymbol{x}^{k+1} = \boldsymbol{u}^{k+1} - \boldsymbol{u}^k + \boldsymbol{z}^{k+1}. \tag{5.38}$$

Using (5.38), we have

$$\begin{aligned} &\left\| \boldsymbol{x}^{k+1} - \boldsymbol{x}^k \right\|_2 \\ &= \left\| (\boldsymbol{u}^{k+1} - \boldsymbol{u}^k + \boldsymbol{z}^{k+1}) - (\boldsymbol{u}^k - \boldsymbol{u}^{k-1} + \boldsymbol{z}^k) \right\|_2 \\ &\leq \left\| \boldsymbol{u}^{k+1} - \boldsymbol{u}^k \right\|_2 + \left\| \boldsymbol{z}^{k+1} - \boldsymbol{z}^k \right\|_2 + \left\| \boldsymbol{u}^k - \boldsymbol{u}^{k-1} \right\|_2 \\ &\leq \frac{C_3}{\lambda^k} + \frac{C_2}{\lambda^k} + \frac{C_3}{\lambda^{k-1}} \leq \frac{C_3}{\lambda^k} + \frac{C_2}{\lambda^k} + \frac{\gamma C_3}{\lambda^k} = \frac{C_1}{\lambda^k} \end{aligned} \tag{5.39}$$

Hence all three conditions (5.27), (5.28) and (5.29) are true.

Next, we aim at proving that $\{\boldsymbol{x}^k\}_{k=1}^{\infty}$ is a Cauchy sequence. Therefore, one has to show that for all integer $n > k$, $\left\|\boldsymbol{x}^n - \boldsymbol{x}^k\right\|_2 \to \mathbf{0}$ as $n \to \infty$ and $k \to \infty$.

For any finite n and k, one can write using the condition (5.28)

$$\left\|\boldsymbol{x}^n - \boldsymbol{x}^k\right\|_2 \leq \sum_{l=k}^{n-1} \frac{C_1}{\lambda^l} = C_1 \sum_{l=k}^{n-1} \frac{1}{\lambda_0 \gamma^l} = \frac{C_1}{\lambda_0 \gamma^k} \sum_{l=0}^{n-k-1} \frac{1}{\gamma^l}. \tag{5.40}$$

Therefore, as $n \to \infty$ and $k \to \infty$, $\left\|\boldsymbol{x}^n - \boldsymbol{x}^k\right\|_2 \to \mathbf{0}$, since $\gamma > 1$, so $\{\boldsymbol{x}^k\}_{k=1}^{\infty}$ is a Cauchy sequence. Hence, the sequence $\{\boldsymbol{x}^k\}_{k=1}^{\infty}$ is convergent, thus there exits $\boldsymbol{x}^* \in [0,1]^{n^2}$ such that $\left\|\boldsymbol{x}^k - \boldsymbol{x}^*\right\|_2 \to \mathbf{0}$ as $k \to \infty$.

Similarly, one can show that the sequence $\{\boldsymbol{z}^k\}_{k=1}^{\infty}$ and $\{\boldsymbol{u}^k\}_{k=1}^{\infty}$ are convergent, so there exit $\boldsymbol{z}^*, \boldsymbol{u}^* \in [0,1]^{n^2}$ such that $\left\|\boldsymbol{z}^k - \boldsymbol{z}^*\right\|_2 \to \mathbf{0}$ and $\left\|\boldsymbol{u}^k - \boldsymbol{u}^*\right\|_2 \to \mathbf{0}$ as $k \to \infty$.

Therefore we can conclude that the proposed QAB-PnP algorithm converges to a fixed point.

■

The proof we propose is not a convergence proof in the mathematical sense, since it reposes on Remark 5.2 for which we only have plausibility arguments and numerical evidence. Nevertheless, the discussion above and the numerical results in Fig. 5.4 for three very different images, indicate that with high confidence the algorithm should converge in practice for any image.

5.3 Simulation Results

This section illustrates the efficiency of the proposed QAB-PnP algorithm for Poisson image deconvolution. An analysis of the influence of the hyperparameters on the deconvolution accuracy is first provided in Subsection 5.3.1, before comparing its performance to several state-of-the-art methods in Subsection 5.3.2. In Chapter 4, we already performed a detailed analysis of the hyperparameters $\sigma_{\mathscr{QAB}}$, s and ρ for the efficiency of the denoiser. We recall that these hyperparameters control respectively the smoothing of the potential to avoid localization effects in the expansion basis, and the cutoff in energy which leads to denoising. We therefore chose these hyperparameters to be optimal according to the study in the previous Chapter 4. However, the computational method used in the present work (OMP algorithm) introduces a new hyperparameter $\mathscr{E}$ which controls the accuracy and efficiency of the OMP process. The accuracy of OMP increases for increasing $\mathscr{E}$, but at the cost of higher computational time. A trade-off is

thus necessary, and we will show that the optimal value of $\mathscr{E}$ is also influenced by the value of the hyperparameter $\hbar^2/2m$, which fixes how the local frequencies of the basis vectors vary as a function of pixels' amplitudes.

The simulations are conducted on three images, shown in Fig. 5.3. Two of them represent cropped versions of the standard Lena and fruits images. The third one was synthetically constructed so that it contains high frequencies for low gray levels and, vice versa, low frequencies for high intensity pixels. Its purpose is to illustrate the ability of the proposed deconvolution method, and in particular of the embedded quantum-based denoiser, to handle such images. All the sample images are distorted with two Gaussian blurring kernel $h_\sigma^{4\times4}$ of size 4×4 and standard deviation $\sigma=3$ and $\sigma=5$ respectively. The study was conducted with three different Poisson noise levels corresponding to SNRs of 20, 15 and 10 dB. Note that the noise was image-dependent Poisson distributed and that the SNRs of the observations was computed a posteriori to emphasize the amount of noise.

5.3.1 Hyperparameter Analysis

This subsection presents a detailed analysis on the influence of the hyperparameters on the proposed method. In particular, the role of the hyperparameter $\mathscr{E}$ will be evaluated, given its important impact on the compromise between accuracy and computational time, and its relationship with the hyperparameter $\hbar^2/2m$ will be assessed. It is important

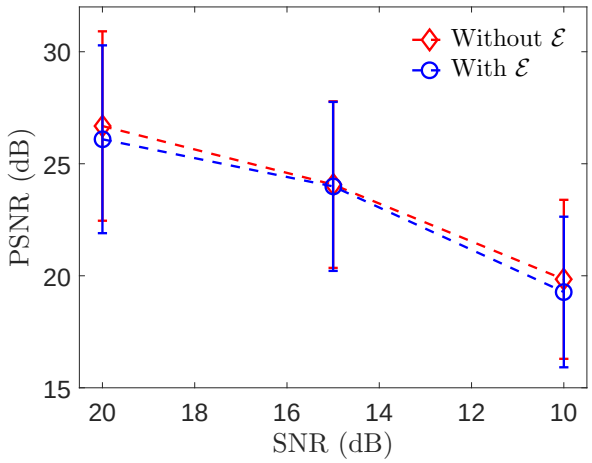

FIGURE 5.5. PSNR mean and standard deviation values for all the three sample images in Fig. 5.3 as a function of Poisson noise levels.

TABLE 5.1. Quantitative measurements obtained using the proposed QAB-PnP algorithm with and without modified OMP

Sample	Noise	Without OMP		With OMP, best $\mathscr{E}$	
		PSNR (dB)	SSIM	PSNR (dB)	SSIM
Synthetic	20 dB	**30.1724**	**0.9179**	29.9497	0.8934
	15 dB	**26.8101**	0.8604	26.7300	**0.8620**
	10 dB	**23.1674**	0.7489	23.1006	**0.7493**
Lena	20 dB	**29.1330**	**0.8112**	28.9842	0.8091
	15 dB	**26.5853**	**0.7712**	26.5805	0.7709
	10 dB	**21.4328**	**0.6989**	19.8070	0.6942
Fruits	20 dB	**20.7366**	**0.6908**	20.1657	0.6817
	15 dB	**18.8144**	0.6471	18.6564	**0.6474**
	10 dB	**14.9236**	0.6114	14.9200	**0.6117**

TABLE 5.2. Average computation time (all the algorithms have been implemented in Matlab and tested on a computer with an Intel(R) Core(TM) i7-10510U CPU of 4 cores each with 1.80 GHz, 16 GB memory and using Windows 10 Pro version 20H2 as operating system) and required number of iterations for different images.

Method	Run time (sec)			Number of iterations		
	Synthetic	Lena	Fruits	Synthetic	Lena	Fruits
TV-ADMM	0.111	0.107	0.130	26	17	23
ADMM+BM3D	0.017	0.017	0.022	27	20	26
ADMM+TNRD	78.375	81.980	104.179	17	22	25
ADMM+VST+TNRD	77.310	82.630	112.070	20	19	17
P^{4}IP	0.037	0.039	0.049	18	8	19
QAB-PnP (Without OMP)	190.284	186.677	266.221	17	7	14
QAB-PnP (With OMP, best $\mathscr{E}$)	37.425	35.732	48.568	18	7	15

to mention that in general the hyperparameter $\hbar^2/2m$ and the number of significant wave vectors $\mathscr{T}$ vary in an opposite way, one of them increasing when the other one decreases. In addition, there is a linear relation between $\mathscr{T}$ and the processing time. Therefore, to achieve an optimal behaviour of the algorithm, a good balance between the hyperparameters $\hbar^2/2m$ and $\mathscr{E}$ needs to be achieved. We will also discuss the choice of the hyperparameter λ_0 which controls the iterations of the ADMM algorithm described in Section 5.1.

From this perspective, we first show that considering the wave vectors up to the energy level $\mathscr{E}$ and evaluating only the corresponding coefficients $\boldsymbol{\alpha}_i$ following the modified

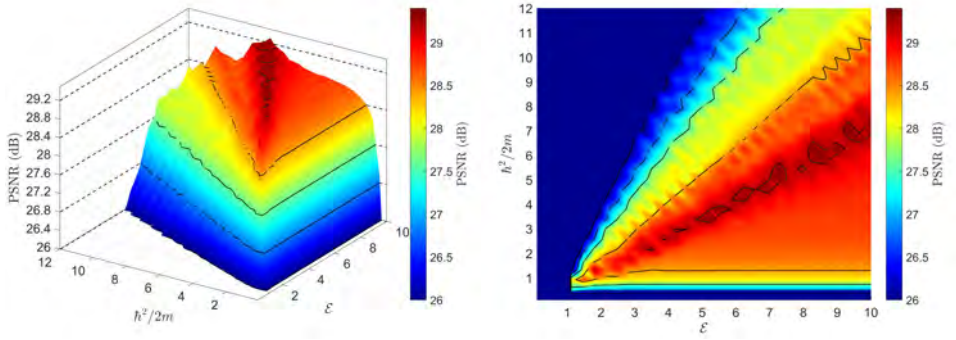

(a) Influence of the hyperparameters $\mathcal{E}$ and $\hbar^2/2m$ on the proposed method in terms of PSNR (dB)

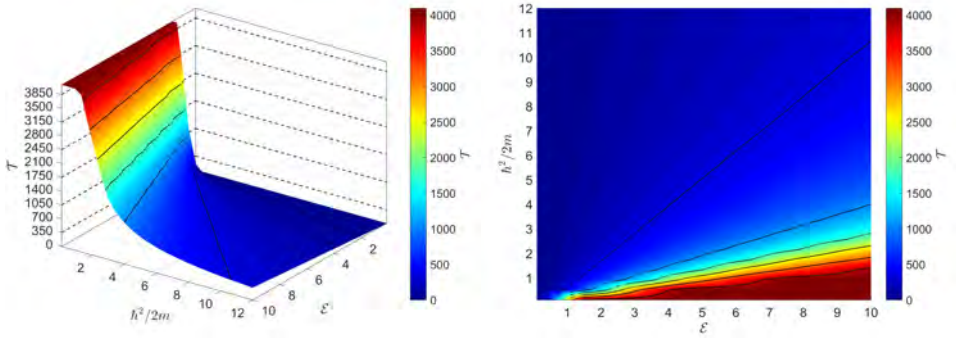

(b) Number of significant wave vectors $\mathcal{T}$ for different values of the hyperparameters $\mathcal{E}$ and $\hbar^2/2m$

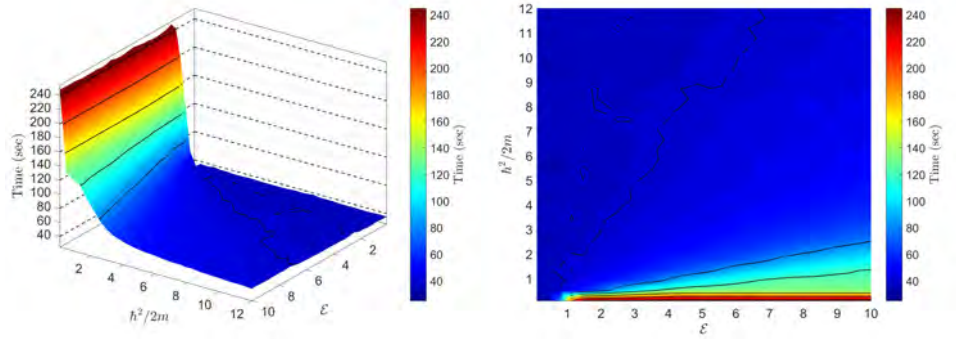

(c) Computation time for different values of the hyperparameters $\mathcal{E}$ and $\hbar^2/2m$

FIGURE 5.6. Experiment performed on the image in Fig. 5.3(a) blurred by a Gaussian kernel $h_\sigma^{4\times4}$ of size 4×4 with standard deviation $\sigma = 3$, and corrupted by Poisson noise corresponding to a SNR of 20 dB. QAB-PnP was performed with $\lambda_0 = 1.5$, and γ, $\sigma_{\mathcal{QAB}}$, s and ρ manually tuned to their best possible values for each set of experiments.

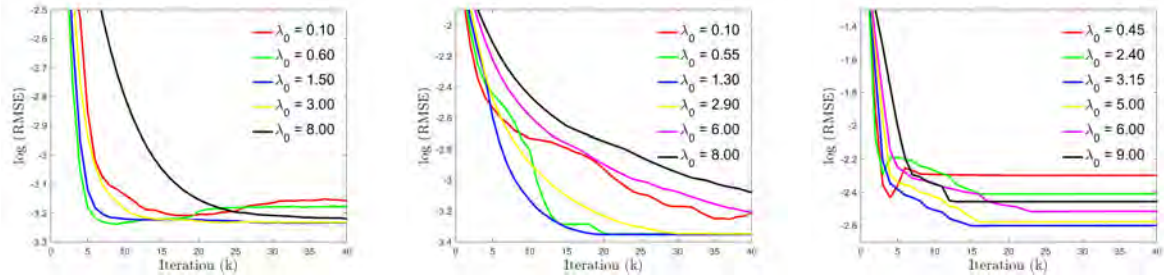

(a) Performed on the image in Fig. 5.3(a) with $\mathscr{E} = 3.9$, $\hbar^2/2m = 4$

(b) Performed on the image in Fig. 5.3(b) with $\mathscr{E} = 4.1$, $\hbar^2/2m = 4$

(c) Performed on the image in Fig. 5.3(c) with $\mathscr{E} = 4.5$, $\hbar^2/2m = 4.3$

FIGURE 5.7. Evolution of the RMSE (logarithmic scale) for different values of the hyperparameter λ_0, for a Gaussian blurring kernel $h_\sigma^{4\times4}$ of size 4×4 with standard deviation $\sigma = 3$ and Poisson noise corresponding to a SNR of 20 dB. The other hyperparameters γ, $\sigma_{\mathscr{QAB}}$, s and ρ have been manually tuned to their best possible values for each set of experiments.

OMP algorithm in Algo. 5.1 helps reducing the computation time with minimal accuracy loss. Quantitative results showing the influence of $\mathscr{E}$ on the simulations performed over the three sample images in Fig. 5.3, distorted by a Gaussian blurring kernel $h_\sigma^{4\times4}$ of size 4×4 and standard deviation $\sigma = 3$, and corrupted by Poisson noise corresponding to a SNR of 20 dB, 15 dB, and 10 dB, have been regrouped in Table 5.1, where the best results have been highlighted in bold. Similarly, the average peak signal to noise ratios (PSNR) values for different SNR, obtained with the proposed deconvolution method with and without the modified OMP algorithm, are shown in Fig. 5.5. The results in Fig. 5.5 and Table 5.1 prove that the accuracy loss, caused by the use of the parameter $\mathscr{E}$ within the modified OMP algorithm, is very limited. This accuracy loss is caused by the denoising process that reconstructs the denoised image only from the wave functions associated with an energy level lower than $\mathscr{E}$. Indeed, although wave functions associated with higher energies are dominated by noise, they may still carry information about certain features of the clean image. The average computation time for different images obtained with a Matlab implementation on a desktop computer, with and without $\mathscr{E}$, given in Table 5.2, confirms the computational efficiency gain enabled by the modified OMP algorithm embedded in QAB-PnP method.

In addition to $\mathscr{E}$, as stated previously, $\hbar^2/2m$ is also an important hyperparameter of the proposed deconvolution technique. The hyperparameter $\hbar^2/2m$ dictates how the local frequencies of the basis vectors vary with the amplitude of the image pixel values. On the other hand, $\mathscr{E}$ is associated with the sparsity. Given their mutual dependence,

Fig. 5.6(a) shows the accuracy of QAB-PnP algorithm for different couple values of these two hyperparameters over an acceptable range. This experiment consisted in recovering the image in Fig. 5.3(a) from a degraded version blurred by a 4×4 Gaussian kernel with standard deviation equal to 3 and Poisson noise corresponding to a SNR of 20 dB.

Similarly, Figs. 5.6(b) and (c) show the variation of the number of the significant wave vectors $\mathscr{T}$ and of the computation time. These results also justify the linear proportionality of $\mathscr{T}$ and processing time. Note that as explained previously, the other hyperparameters, $\sigma_{\mathscr{QAB}}$, s and ρ, were chosen as suggested in the previous Chapter 4.

Finally, the choice of the hyperparameter λ_0 used within the iterations of the ADMM algorithm is important to accelerate the convergence. The curves in Fig. 5.7 show, within a logarithmic scale, the evolution of the root mean square error (RMSE) over the iterations of the proposed deconvolution method, for different values of λ_0. These simulations were performed for the three images in Fig. 5.3, distorted by a Gaussian blurring kernel $h_\sigma^{4\times4}$ of size 4×4 and standard deviation $\sigma = 3$, and corrupted by Poisson process corresponding to a SNR of 20 dB.

The studies performed in this subsection show that a certain range of optimal choice of the hyperparameters considered is possible. Without a priori knowledge, it should be possible to use values in this range for arbitrary images, taking care to choose $\mathscr{E}$ and $\hbar^2/2m$ in a correlated way. As a further note, keeping the hyperparameters constant to the same values for all the images considered hereafter leads to a very low PSNR degradation of about 0.1 dB. From the discussions above, one may note that the hyperparameters $\hbar^2/2m$ and $\mathscr{E}$ are primarily associated with the construction of the quantum adaptive basis and the sparsity of the clean image in this basis, both related to the denoising process. In contrast, λ_0, the penalty parameter, regulates the restoration process by accelerating the convergence. Therefore, the optimal choice of $\hbar^2/2m$ and $\mathscr{E}$ discussed above is independent of the value of λ_0.

5.3.2 Poisson Deconvolution Results

Poisson deconvolution is a well discussed domain in the literature where PnP algorithms implanting a Gaussian denoiser with or without a VST transformation have exhibited promising outcomes [27, 287]. The proposed method is intrinsically adaptive, which makes it well-adapted to different noise statistics for the problem addressed and does not require using any additional transformation in the denoising step.

This subsection regroups image deconvolution results obtained with the proposed method and five approaches from the literature. The experiments consisted in recover-

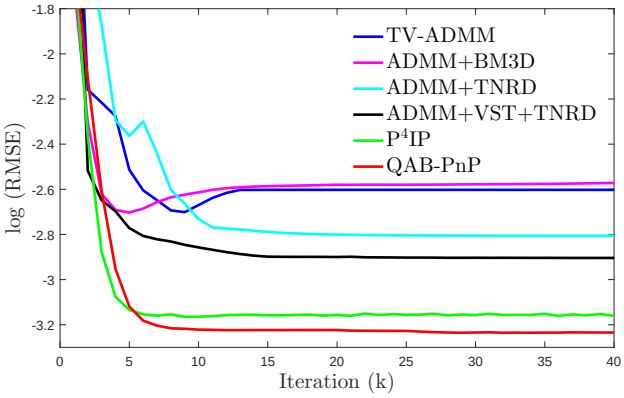

FIGURE 5.8. RMSE in logarithmic scale as a function of iteration number for TV-ADMM, ADMM+BM3D, ADMM+TNRD, ADMM+VST+TNRD, P^{4}IP and proposed QAB-PnP methods. The results correspond to the restoration of the image in Fig. 5.3(a) from a degraded image by a Gaussian blurring kernel $h_\sigma^{4\times4}$ of size 4×4 and standard deviation $\sigma=3$, and Poisson noise corresponding to a SNR of 20 dB. All hyperparameters were manually tuned to their best possible values for all the methods.

ing the images in Fig. 5.3 from degraded versions by Gaussian blurring kernels with different variances and Poisson noise at different SNRs. The first comparative method

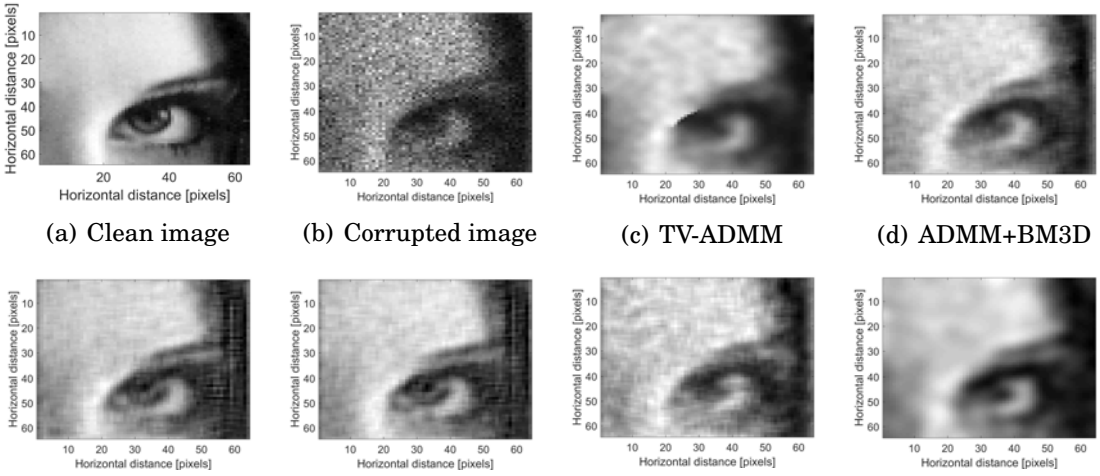

(a) Clean image (b) Corrupted image (c) TV-ADMM (d) ADMM+BM3D

(e) ADMM+TNRD (f) ADMM+VST+TNRD (g) P^{4}IP (h) QAB-PnP

FIGURE 5.9. Deconvolution result for Lena image, blurred by a Gaussian kernel $h_{\sigma=3}^{4\times4}$ and corrupted by Poisson noise corresponding to a SNR of 10 dB. The proposed QAB-PnP algorithm used $\mathscr{E}=3.9$, $\lambda_0=1.5$, $\hbar^2/2m=4$ and $\gamma=1.01$, $\sigma_{\mathscr{QAB}}=7$.

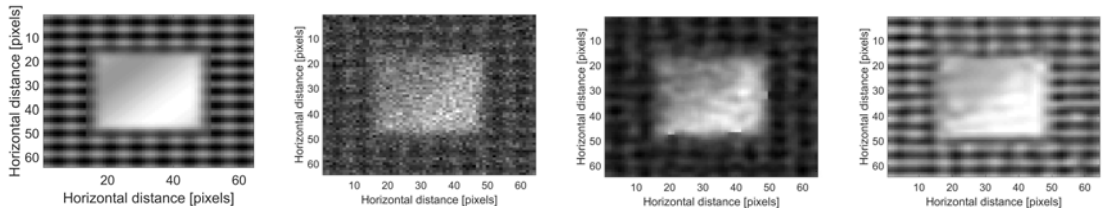

(a) Clean image (b) Corrupted image (c) TV-ADMM (d) ADMM+BM3D

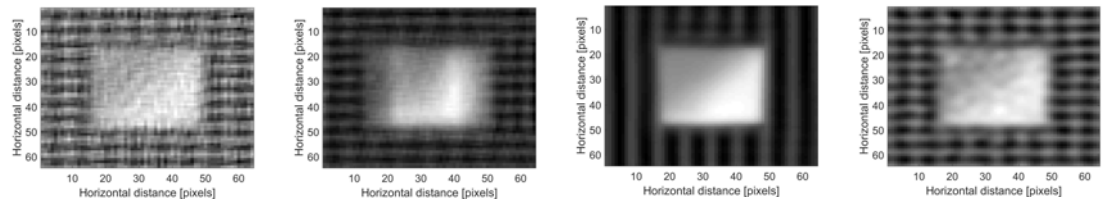

(e) ADMM+TNRD (f) ADMM+VST+TNRD (g) P^{4}IP (h) QAB-PnP

FIGURE 5.10. Deconvolution result for Synthetic image, blurred by a Gaussian kernel $h^{4\times4}_{\sigma=5}$ and corrupted by Poisson noise corresponding to a SNR of 15 dB. The proposed QAB-PnP algorithm used $\mathscr{E} = 4.1$, $\lambda_0 = 1.3$, $\hbar^2/2m = 4$ and $\gamma = 1.01$, $\sigma_{\mathscr{QAB}} = 7$.

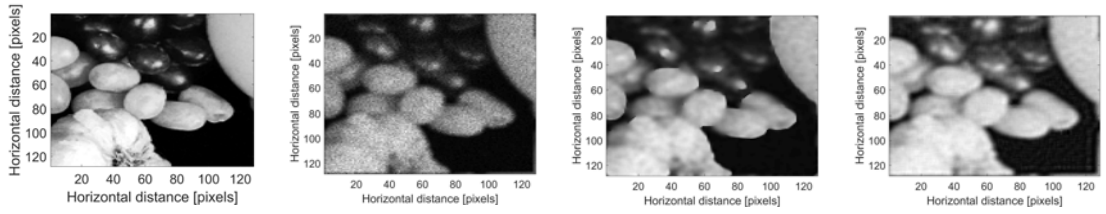

(a) Clean image (b) Corrupted image (c) TV-ADMM (d) ADMM+BM3D

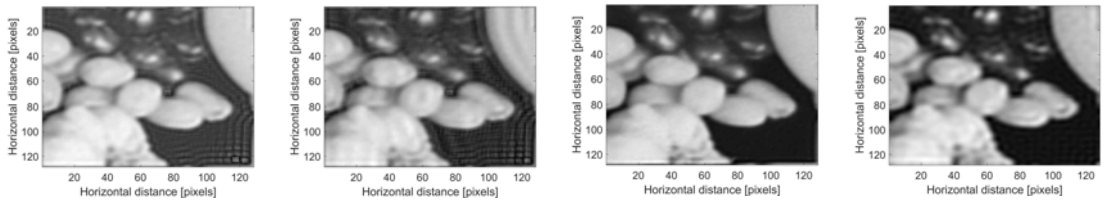

(e) ADMM+TNRD (f) ADMM+VST+TNRD (g) P^{4}IP (h) QAB-PnP

FIGURE 5.11. Deconvolution result for Fruits image, blurred by a Gaussian kernel $h^{4\times4}_{\sigma=3}$ and corrupted by Poisson noise corresponding to a SNR of 20 dB. The proposed QAB-PnP algorithm used $\mathscr{E} = 4.5$, $\lambda_0 = 3.15$, $\hbar^2/2m = 4.3$ and $\gamma = 1.01$, $\sigma_{\mathscr{QAB}} = 8$.

is a standard Poisson deconvolution method that consists in estimating the image that minimizes a cost function formed by the data fidelity term in (5.12) and the classical total

variation regularization [90]. This method will be denoted by TV-ADMM hereafter. The second method denoted by ADMM+BM3D is an integration of the BM3D denoiser in the PnP-ADMM algorithm. Similarly, a deep learning denoiser trained on natural images was integrated into the PnP-ADMM scheme and used as comparison method. In particular, the CNN-based flexible learning method, known as the trainable nonlinear reaction diffusion (TNRD) [71], was used given its efficiency within regularization by denoising approaches [286]. Finally, a PnP-ADMM algorithm coupled with an Anscombe transformation (VST) and a BM3D denoiser, denoted by P^{4}IP in [287] was used for comparison. Note that TNRD has been also used with and without VST. The resulting algorithms are denoted by ADMM+TNRD and ADMM+VST+TNRD. It is important to mention that the methods used for comparisons such as TV-ADMM, P^{4}IP and ADMM+VST+TNRD are particularly designed for handling data degraded by Poisson noise, and are therefore appropriate choices as comparative methods to the proposed Poisson deconvolution algorithm.

As explained previsouly, the proposed method does not require such a VST-like transformation due to the adaptive nature of the embedded denoiser. Therefore, the proposed algorithm is expected to present better generic convergence properties compared to P^{4}IP. In the example in Fig. 5.8, where P^{4}IP had fast convergence, the rate of convergence of QAB-PnP is similar to P^{4}IP and faster than TV-ADMM, ADMM+BM3D, ADMM+TNRD and ADMM+VST+TNRD. To evaluate the computational complexity of the proposed algorithm in comparison with other standard techniques, the average computational time and required number of iterations before convergence are given in Table 5.2 with respect to different images. The results confirm the faster convergence of the proposed method, albeit, at the cost of higher computational time per iteration.

The deconvolution results obtained with the six methods can be visually appreciated in Figs. 5.9, 5.10 and 5.11. The PSNR and the structure similarity (SSIM) [366] were used to evaluate the deconvolution accuracy. The resulting numerical results, for two different blurring kernels and three different SNRs, are regroupped in Table 5.3. In particular, average and standard deviation values are reported for 200 noise realizations. For further investigation, the quantitative results obtained with the proposed method in presence of very high-intensity noise, in particular, with SNRs close to 5 dB and 0 dB, are provided in Table 5.4.

One may observe that the proposed scheme is capable to adapt both to low and high level of noise and outperforms the five other methods in almost all the simulations. It is important to note that QAB-PnP not only provides the best average values, but also the

TABLE 5.3. Quantitative results (average over 200 noise realizations). Best results are shown in bold.

Gaussian kernel $h_{\sigma=3}{}^{4\times4}$

Sample	Method	Poisson Noise (20 dB)		Poisson Noise (15 dB)		Poisson Noise (10 dB)	
		PSNR (dB)	SSIM	PSNR (dB)	SSIM	PSNR (dB)	SSIM
Synthetic	TV-ADMM	26.46±0.10	0.66±0.01	24.80±0.34	0.58±0.01	22.52±1.55	0.52±0.02
	ADMM+BM3D	23.37±0.16	0.73±0.01	19.70±0.23	0.54±0.01	17.67±0.37	0.47±0.02
	ADMM+TNRD	23.94±0.14	0.65±0.01	21.55±0.31	0.56±0.01	18.88±0.40	0.40±0.01
	ADMM+VST+TNRD	23.96±0.11	0.71±0.02	21.73±0.19	0.54±0.02	19.02±0.23	0.38±0.03
	P^{4}IP	23.90±1.37	0.74±0.06	20.91±2.18	0.59±0.11	18.96±3.34	0.48±0.18
	QAB-PnP	**29.86±0.12**	**0.92±0.00**	**27.18±0.43**	**0.86±0.01**	**24.23±1.34**	**0.74±0.03**
Lena	TV-ADMM	27.37±0.31	0.74±0.01	24.52±0.65	0.66±0.01	19.97±1.32	0.52±0.02
	ADMM+BM3D	25.87±0.40	0.75±0.01	23.59±0.66	0.66±0.03	17.59±1.02	0.50±0.05
	ADMM+TNRD	25.76±0.19	0.71±0.01	24.67±0.21	0.69±0.01	19.22±0.38	0.50±0.02
	ADMM+VST+TNRD	25.85±0.23	0.69±0.01	24.73±0.39	0.60±0.01	19.11±0.80	0.42±0.07
	P^{4}IP	27.32±0.44	**0.81**±0.01	24.87±2.76	**0.76**±0.07	18.67±4.83	0.55±0.16
	QAB-PnP	**28.97±0.19**	**0.81±0.00**	**27.04±0.44**	0.75±0.01	**20.18±3.39**	**0.65±0.08**
Fruits	TV-ADMM	20.51±0.38	0.57±0.01	19.02±0.23	0.55±0.01	**17.54±0.93**	0.51±0.01
	ADMM+BM3D	19.75±0.42	0.61±0.01	17.07±0.20	0.53±0.01	13.59±0.35	0.51±0.02
	ADMM+TNRD	19.73±1.91	**0.64±0.02**	17.41±0.57	**0.59±0.01**	16.67±0.79	0.51±0.06
	ADMM+VST+TNRD	20.65±0.39	**0.64±0.01**	18.40±1.19	0.58±0.02	16.51±1.36	0.43±0.08
	P^{4}IP	20.42±1.79	0.59±0.04	17.22±4.62	0.52±0.11	14.35±3.85	**0.53±0.04**
	QAB-PnP	**21.37±0.94**	0.62±0.01	**19.35±0.96**	0.57±0.02	17.28±3.55	0.51±0.12

Gaussian kernel $h_{\sigma=5}{}^{4\times4}$

Sample	Method	Poisson Noise (20 dB)		Poisson Noise (15 dB)		Poisson Noise (10 dB)	
		PSNR (dB)	SSIM	PSNR (dB)	SSIM	PSNR (dB)	SSIM
Synthetic	TV-ADMM	26.47±0.07	0.59±0.01	25.23±0.14	0.54±0.01	23.15±0.29	0.44±0.01
	ADMM+BM3D	22.95±0.18	0.70±0.01	19.78±0.24	0.53±0.01	17.89±0.34	0.46±0.02
	ADMM+TNRD	23.81±0.18	0.66±0.01	21.72±0.22	0.58±0.02	19.03±0.44	0.41±0.01
	ADMM+VST+TNRD	23.89±0.12	0.69±0.01	21.82±0.22	0.52±0.02	18.96±0.34	0.37±0.04
	P^{4}IP	22.35±2.15	0.67±0.09	20.60±2.87	0.56±0.12	18.67±3.42	0.49±0.21
	QAB-PnP	**29.44±0.13**	**0.91±0.00**	**27.24±0.58**	**0.86±0.01**	**24.06±1.07**	**0.73±0.02**
Lena	TV-ADMM	27.17±0.25	0.74±0.01	25.11±0.46	0.61±0.01	19.41±0.42	0.44±0.01
	ADMM+BM3D	25.02±0.48	0.73±0.01	23.51±0.78	0.65±0.02	17.64±1.47	0.48±0.06
	ADMM+TNRD	25.44±0.17	0.71±0.01	24.43±0.26	0.68±0.02	19.20±0.23	0.51±0.02
	ADMM+VST+TNRD	25.46±0.29	0.69±0.01	24.53±0.32	0.60±0.01	19.41±0.49	0.43±0.05
	P^{4}IP	27.26±0.34	**0.81±0.01**	25.07±2.90	**0.77±0.06**	17.99±4.73	0.54±0.21
	QAB-PnP	**28.80±0.21**	**0.81±0.00**	**26.63±1.01**	0.76±0.03	**20.20±3.89**	**0.67±0.05**
Fruits	TV-ADMM	19.94±0.25	0.57±0.01	17.24±0.28	0.55±0.01	16.58±0.34	0.50±0.01
	ADMM+BM3D	19.15±0.58	0.60±0.01	17.11±0.33	0.54±0.01	13.45±0.55	0.50±0.02
	ADMM+TNRD	19.68±1.10	0.63±0.02	17.95±0.96	**0.58±0.01**	16.13±0.74	0.51±0.06
	ADMM+VST+TNRD	20.18±0.29	**0.65±0.01**	18.16±0.87	**0.58±0.01**	16.45±1.04	0.45±0.03
	P^{4}IP	**20.47±1.99**	0.61±0.05	17.49±3.44	0.56±0.04	13.83±4.22	0.51±0.05
	QAB-PnP	20.24±1.09	0.60±0.01	**18.83±0.71**	**0.58±0.01**	**17.44±2.09**	**0.53±0.02**

lowest standard deviations, in particular compared to P^{4}IP. This observation is confirmed by the results in Fig. 5.12, that displays, for a given simulation, the best, the worst and an intermediate result over 200 noise realizations. While the difference between these three results is barely observable for the proposed method, this is not the case for P^{4}IP. Finally, one may observe the big accuracy difference between the proposed method and the five others for the synthetic image. Indeed, in presence of strong noise intensities the methods particularly associated with the VST (or the Anscombe transformation) exhibit more volatility compared to others. This VST only provides a Gaussian approximation of

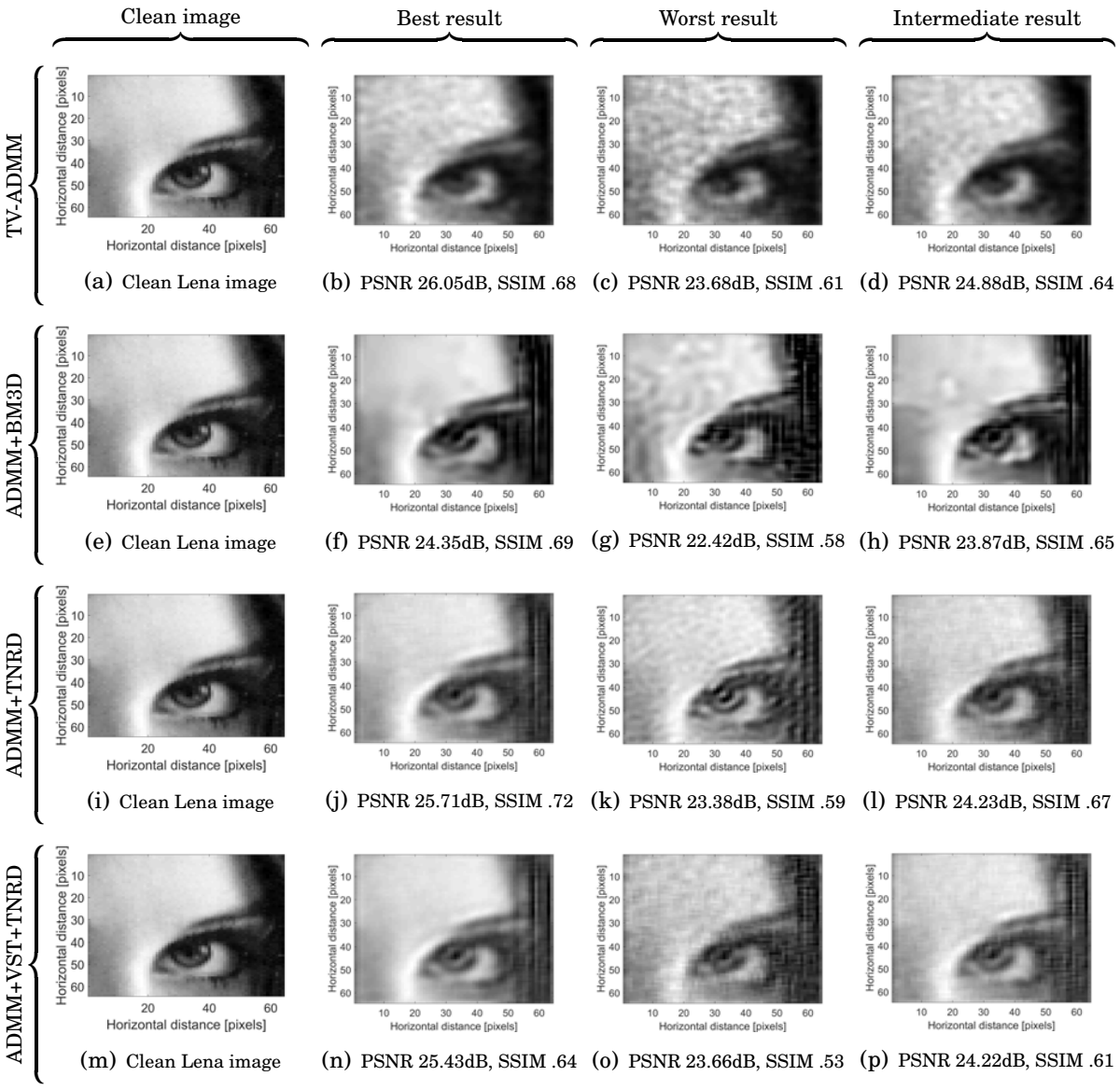

(a) Clean Lena image (b) PSNR 26.05dB, SSIM .68 (c) PSNR 23.68dB, SSIM .61 (d) PSNR 24.88dB, SSIM .64

(e) Clean Lena image (f) PSNR 24.35dB, SSIM .69 (g) PSNR 22.42dB, SSIM .58 (h) PSNR 23.87dB, SSIM .65

(i) Clean Lena image (j) PSNR 25.71dB, SSIM .72 (k) PSNR 23.38dB, SSIM .59 (l) PSNR 24.23dB, SSIM .67

(m) Clean Lena image (n) PSNR 25.43dB, SSIM .64 (o) PSNR 23.66dB, SSIM .53 (p) PSNR 24.22dB, SSIM .61

···Continued on next page.

···Continued from previous page.

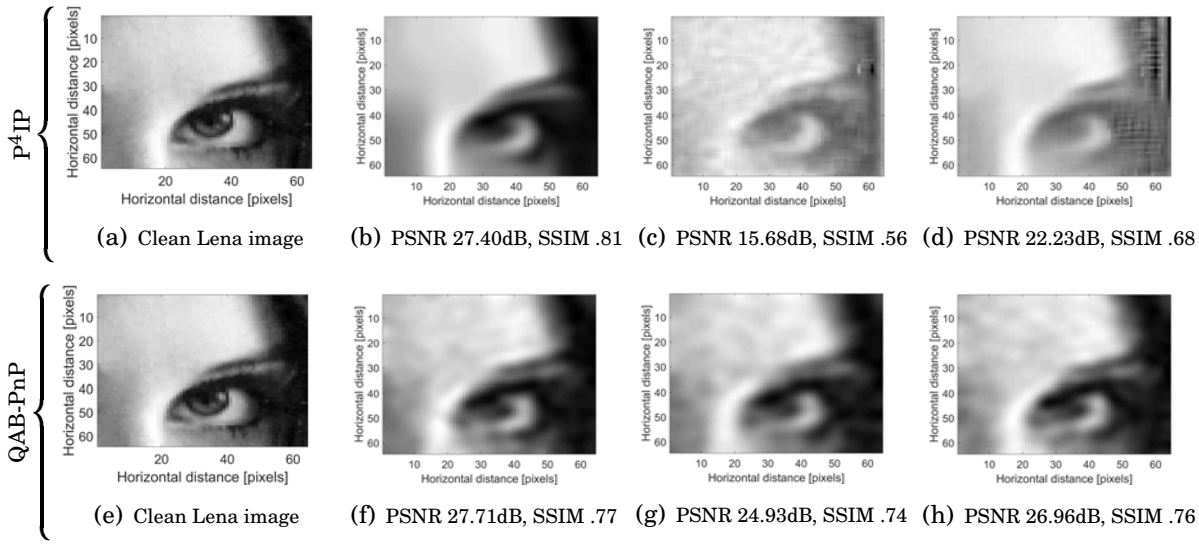

(a) Clean Lena image (b) PSNR 27.40dB, SSIM .81 (c) PSNR 15.68dB, SSIM .56 (d) PSNR 22.23dB, SSIM .68

(e) Clean Lena image (f) PSNR 27.71dB, SSIM .77 (g) PSNR 24.93dB, SSIM .74 (h) PSNR 26.96dB, SSIM .76

FIGURE 5.12. The best, the worst and an intermediate deconvolution results over 200 noise realizations obtained using TV-ADMM, ADMM+BM3D, ADMM+TNRD, ADMM+VST+TNRD, P^{4}IP and the proposed QAB-PnP method for Lena image degraded by a Gaussian blurring kernel $h_{\sigma=3}^{4\times4}$ and Poisson noise corresponding to a SNR of 15 dB.

TABLE 5.4. Quantitative deconvolution results when images are corrupted with high intensity noise.

Gaussian kernel ${h_{\sigma=3}}^{4\times4}$ + Poisson Noise				
Sample	SNR ≈ 5 dB		SNR ≈ 0 dB	
	PSNR (dB)	SSIM	PSNR (dB)	SSIM
Synthetic	18.76	0.41	16.48	0.35
Lena	16.25	0.49	15.72	0.42
Fruits	15.04	0.39	13.32	0.30

a Poissonian distribution and is contaminated with higher inaccuracies as noise intensity increases. Our method does not suffer from such issues and provides a stable output despite the noise level and realization.

5.4 Application to Fluorescence Microscopy Imaging

This section highlights the applicability of the proposed deconvolution method to real-life imaging applications, in particular to fluorescence microscopy imaging using, *e.g.*,

confocal [263] or two-photon [93] microscopes. Fluorescence microscopy images are intrinsically noisy, contaminated by Poisson-Gaussian noise. Poisson noise is the dominating source of noise [90, 253, 415], due to a limited number ($\sim 10^2$ per pixel) of quantized photons captured by a microscopic detector compared to normal photography ($\sim 10^5$ per pixel). Therefore, enhancing such contaminated fluorescence images is of interest for many modern biological studies.

Herein, we used three microscopy images from the online available data-set[1] to illustrate the potential of the proposed method. Fig. 5.13 regroups the observed distorted images, their corresponding ground truth, and the deblurred images estimated by the six methods. PSNR and SSIM values comparing the observed and the deblurred images to the clean ones are given in Table 5.5. These results clearly show the efficiency of the proposed algorithm in real fluorescence microscopy image enhancement.

5.5 Conclusions

This chapter proposed a new PnP-ADMM scheme to handle Poisson deconvolution problems. Although Gaussian denoiser-based PnP-ADMM algorithms have achieved enormous success in the domain of image restoration, they are still facing a theoretical limitation related to the Anscombe transformation used to approximately transform the Poisson noise into additive Gaussian noise. Under this transformation, the convolution

[1] http://tinyurl.com/y6mwqcjs

TABLE 5.5. Quantitative results for experimental fluorescence microscopy images. Best results are shown in bold.

	Methods	Data	Confocal microscopy		Two-photon microscopy
			Zebra Fish	Mouse Brain	Mouse Brain
Observed Data		PSNR (dB)	20.20	27.37	24.07
		SSIM	0.37	0.59	0.40
Deblurred Results	TV-ADMM	PSNR (dB)	24.27	30.27	26.57
		SSIM	0.61	0.88	0.70
	ADMM+BM3D	PSNR (dB)	24.74	32.97	27.66
		SSIM	0.74	0.90	0.81
	ADMM+TNRD	PSNR (dB)	25.85	34.26	31.04
		SSIM	0.79	0.91	0.89
	ADMM+VST+TNRD	PSNR (dB)	25.88	34.44	**31.23**
		SSIM	0.79	0.90	**0.90**
	P^4IP	PSNR (dB)	25.18	33.06	27.09
		SSIM	0.77	0.92	0.85
	QAB-PnP	PSNR (dB)	**28.91**	**35.68**	30.14
		SSIM	**0.82**	**0.93**	0.79

operation is not invariant. To overcome this drawback, we proposed in this work the QAB denoiser derived from principles of quantum mechanics, whose architecture makes it well adapted to different noise statistics, explaining its good behavious as denoiser embedded in a PnP-ADMM algorithm. The simulation results allowed to provide an in-depth analysis of the impact of the hyperparameters on the accuracy and computation efficiency of the proposed method. They also allowed to show its interest compared to five existing methods.

Zebra Fish (Confocal microscopy imaging)

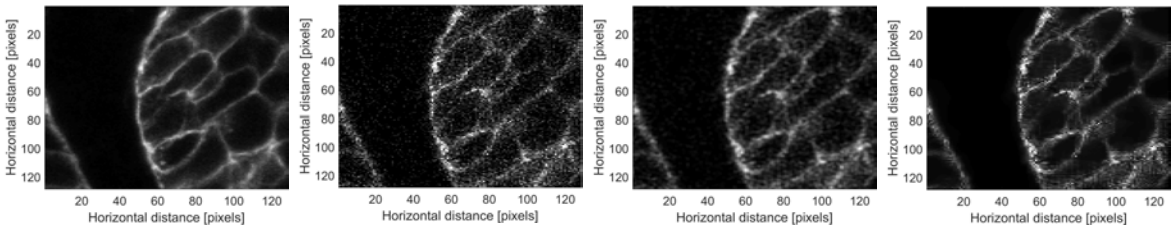

(a) Ground truth (b) Observed image (c) TV-ADMM (d) ADMM+BM3D

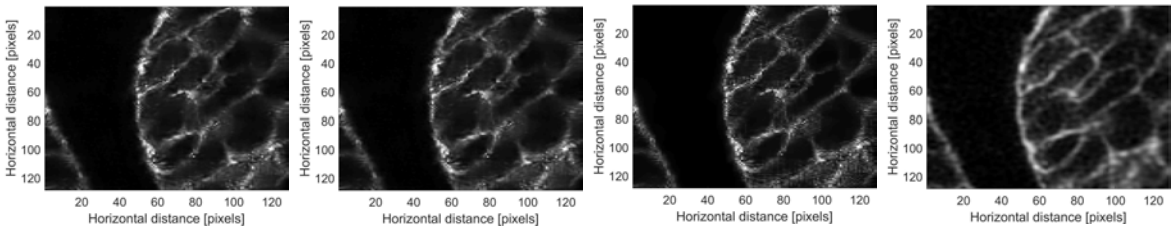

(e) ADMM+TNRD (f) ADMM+VST+TNRD (g) P^{4}IP (h) QAB-PnP

Mouse Brain (Confocal microscopy imaging)

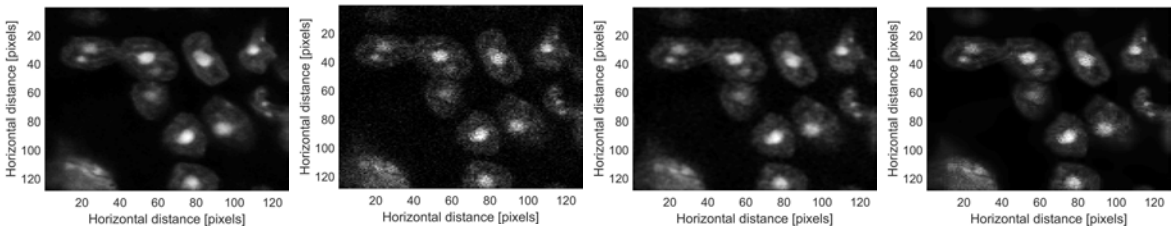

(i) Ground truth (j) Observed image (k) TV-ADMM (l) ADMM+BM3D

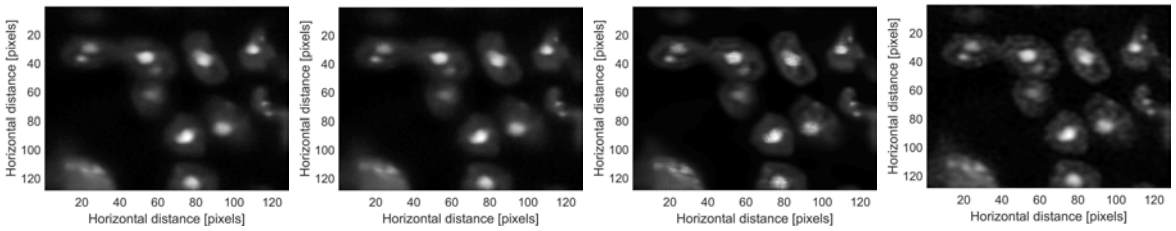

(m) ADMM+TNRD (n) ADMM+VST+TNRD (o) P^{4}IP (p) QAB-PnP

···Continued on next page.

···Continued from previous page.

Mouse Brain (Two-photon microscopy imaging)

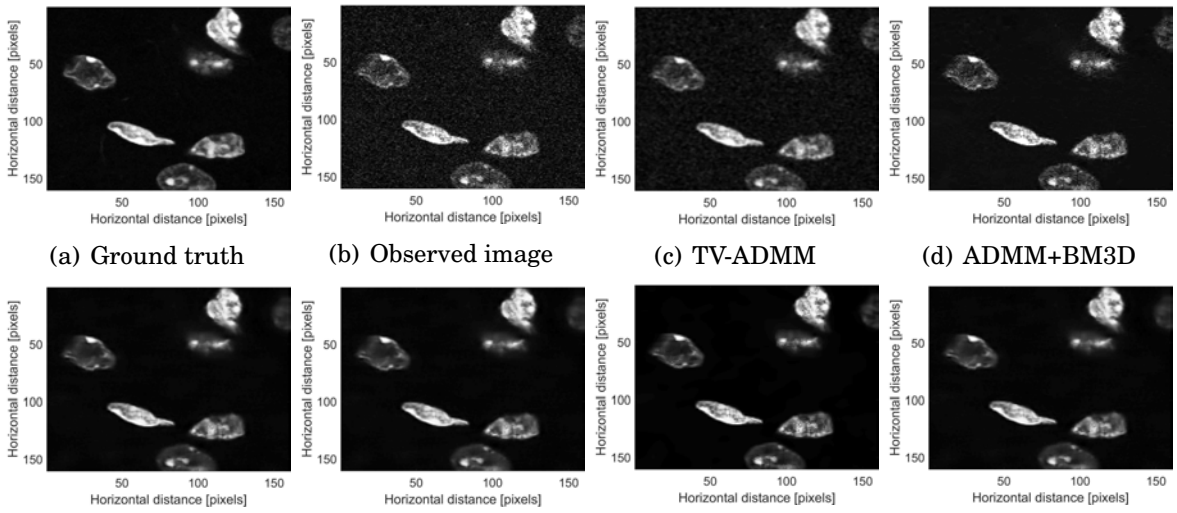

(a) Ground truth (b) Observed image (c) TV-ADMM (d) ADMM+BM3D

(e) ADMM+TNRD (f) ADMM+VST+TNRD (g) P^4IP (h) QAB-PnP

FIGURE 5.13. Deconvolution results for experimental fluorescence microscopy images using TV-ADMM, ADMM+BM3D, ADMM+TNRD, ADMM+VST+TNRD, P^4IP and the proposed QAB-PnP method. The proposed QAB-PnP algorithm used $\mathscr{E} = 4.1$, $\lambda_0 = 1.3$, $\hbar^2/2m = 4$ and $\gamma = 1.01$, $\sigma_{\mathscr{QAB}} = 7$.

5.5.1 Limitations

An issue of our method is the computational burden. The use of the OMP algorithm already dramatically decreases this time compared to earlier implementation in Chapter 4, but other improvements are certainly possible. For small-scale images, the proposed algorithm is computational efficient but for a larger image, this process still demands higher computing resources. Moreover, processing a large-scale image in a block-wise fashion as proposed in Chapter 4, is done independently for each block. However, this strategy of processing each block separately cannot benefit from the idea of structural similarities in a local image neighborhood, which is a key feature of natural images. Furthermore, in presence of random noise, a Gaussian smoothing is required to avoid the phenomenon of quantum localization. In absence of this smoothing, the localized adaptive vectors become less efficient for an imaging task as discussed in Chapter 4.

5.5.2 Perspectives

The computational limitation can be solved by incorporating a many-patch architecture based on the many-body quantum theory. Such an algorithm will be proposed in the subsequent Chapter 6. The advantage of such many-patch construction is not limited to the computing power but also removes the effect of quantum localization and efficiently preserves the structural similarities from a local image neighborhood. As shown in Chapter 4, the proposed quantum adaptive basis is equally efficient for Gaussian, Poisson and speckle noise removal problems without considering any prior information about the noise statistics. Therefore, the proposed deconvolution method could be suitable for other noise degradation than Poisson, and its evaluation in such conditions represents an interesting perspective. As another future perspective of this work one may think of implementing a more advanced inversion algorithm for a Poissonian model (*e.g.,* SPIRAL-TAP [158]) instead of using a gradient descent method. Moreover, blind deconvolution is also an interesting perspective for future study, by coupling the proposed deconvolution algorithm with a PSF estimation method [107, 392]. Finally, such a PnP scheme can be further extended to other reconstruction problems, such as compressed sensing or super-resolution, using more efficient quantum mechanics based algorithms or by including the patch-based procedure to the proposed framework, using for example the multiple-particle quantum theory. In the following Chapter 6, we will illustrate the image-resolution task following the PnP and a more robust version of the PnP scheme, known as regularisation by denoising (RED), in combination with an advanced QAB denoised based on the many-body quantum theory.

CHAPTER 6

A Novel Image Denoising Algorithm Using Concepts of Quantum Many-Body Theory

Contents

* This chapter presents materials from the journal paper [117] and conference papers [110, 111, 119].

Overview

Sparse representation of real-life images is a very effective approach in imaging applications, such as denoising. In recent years, with the growth of computing power, data-driven strategies exploiting the redundancy within patches extracted from one or several images to increase sparsity have become more prominent. This chapter presents a novel image denoising algorithm exploiting such an image-dependent basis inspired by the quantum many-body theory. Based on patch analysis, the similarity measures in a local image neighborhood are formalized through a term akin to interaction in quantum mechanics that can efficiently preserve the local structures of real images. The versatile nature of this adaptive basis extends the scope of its application to image-independent or image-dependent noise scenarios without any adjustment. We carry out a rigorous comparison with contemporary methods to demonstrate the denoising capability of the proposed algorithm regardless of the image characteristics, noise statistics and intensity. We illustrate the properties of the hyperparameters and their respective effects on the denoising performance, together with automated rules of selecting their values close to the optimal one in experimental setups with ground truth not available. Finally, we show the ability of our approach to deal with real-medical imaging problems such as medical ultrasound image despeckling applications and clinical dental computed tomography image super-resolution (SR) problems using Plug-and-Play (PnP) and Regularization by Denoising (RED) approaches.

6.1 Introduction

6.1.1 Image Representation and Related Works

As detailed in Chapter 3, during the past two decades, the redundancy between patches extracted from one or several images has been shown to be a key aspect for number of imaging techniques to increase the sparsity and overcome the limitations of the traditional transforms. Data-driven techniques to exploit the non-local self-similarity (NLSS) while processing a group of similar patches is big breakthrough in recent decades. With the growth of computing power, these patch-based algorithms exploiting NLSS have demonstrated state-of-the-art performance in image denoising, For example, dictionary learning [10, 123], block-matching and 3D filtering (BM3D) [82, 83], Non-Local Means (NLM) [48, 50], etc. This chapter explores such an approach of exploiting the image neighborhood by borrowing tools from quantum mechanics, precisely, the quantum interactions.

6.1.2 Contributions

In this chapter, we propose a novel image representation algorithm well adapted for denoising based on the theory of quantum many-body interaction. In the case of a system containing two or more quantum particles, they can influence each other's quantum state through quantum interactions. The main idea of this work is to adapt ideas from this theory to extend the concept of interaction to imaging problems. More precisely, the proposed framework consists in quantum interactions between image patches where interactions reflect patch similarity measures in a local neighborhood. In this way, each patch acts as a single-particle system, and the whole collection, that is the entire image, behaves as a many-body system where interactions describe regional similarities to neighboring patches. Herein, we show that this method constitutes a robust generalized formalism for image-independent and image-dependent noise models with an extensive study in:

(i) the characterization of the hyperparameters and automated ways to predict their optimal values with limited knowledge about the input image,

(ii) investigation on the denoising possibilities beyond Gaussian statistics without any modification of the algorithms,

(iii) a detailed discussion of denoising performance compared to state-of-the-art methods for both image-independent and image-dependent scenarios,

(iv) application on real medical data for ultrasound (US) image despeckling,

(v) application on clinical dental computed tomography image super-resolution (SR) problems using Plug-and-Play (PnP) and Regularization by Denoising (RED) approaches.

Earlier proposed single-particle based schemes [25, 112–114, 185, 389, 391] have proven their good restoration abilities for different noise models, but are too simple to take advantage of the structural properties of the image and are computationally costly at large scale. As we will show, the proposed generalized framework based on the use of quantum many-body physics improves the previous methods on both counts, building a more versatile computationally efficient adaptive basis that considers similarities between neighboring image patches.

In general, it may seem that there is a close architectural resemblance between the NLM and the proposed many-body scheme since similarity measure is the key for both cases. However, the two methods are different from several perspectives. The NLM image denoising algorithm exploits the self-similarities among the image patches to obtain the similarity weights resulting into a non-local weighted average scheme for denoising. The proposed approach brings non-local characteristics within the quantum framework, where interactions between neighboring patches preserve the local structural similarities. For each patch, these interactions convey the structural information into a quantum adaptive basis offering a good sparsifying transformation at a patch level further used for denoising. It turns out that such a theory can be elegantly written using multi-particle quantum theory instead of the single-particle one.

In the chapter, we first remind briefly of the previously proposed decomposition concept in Chaptre 4 using a quantum adaptive basis based on single-particle theory with its limitations in Section 6.2.1, and then introduce its generalization using many-body quantum theory for imaging problems in Section 6.2.2. Our image denoising algorithm is described in detail in Section 6.3. We then turn to numerical implementation of the method on several examples in Section 6.4. We first explore ways to propose automated rules for hyperparameters selection, and then display numerical results showing that the ability of the proposed method in reducing low and high intensity noise regardless of the noise statistics. We also show its good performance in real-life medical US image despeckling in Section 6.5 and clinical dental computed tomography image super-resolution

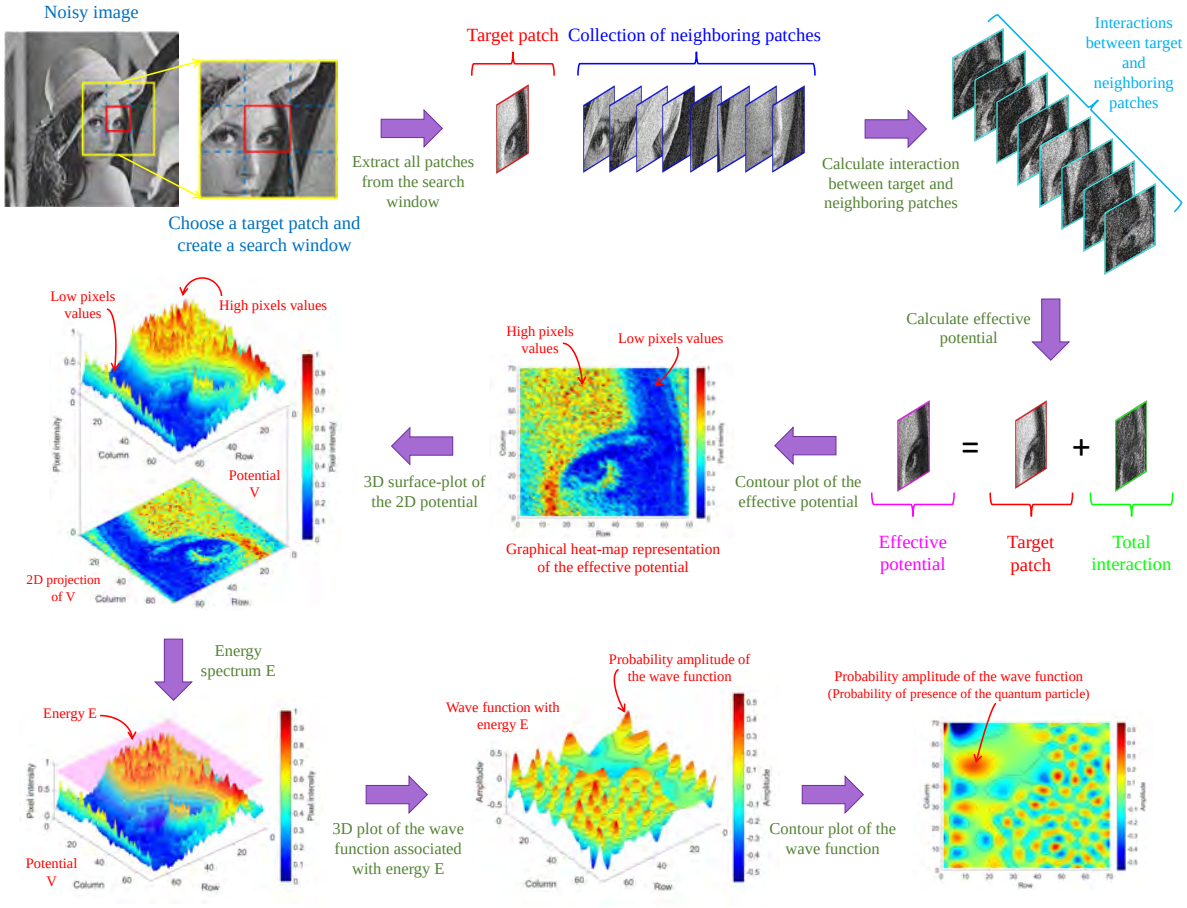

FIGURE 6.1. A simple example of the construction of adaptive vectors from many-patch interaction.

(SR) applications in Section 6.6, which highlight the potential of the proposed scheme for real-world problems. Finally we end with conclusions and perspectives in Section 6.7.

6.2 Quantum Many-Body Theory for Imaging

6.2.1 Quantum Theory for a Single-Particle System

6.2.1.1 Quantum Theory

Before detailing the proposed method, we briefly review, for self consistency, the quantum mechanical method for denoising built on single-particle theory introduced in [114]. For more details on quantum theory, one may refer to one of the many textbooks on this

subject, e.g. [79, 130, 205].

In a non-relativistic single-particle quantum system the wave function $\psi(z)$ describes a particle with energy E in a potential $V(z)$ and satisfies the stationary Schrödinger equation:

$$-\frac{\hbar^2}{2m}\nabla^2\psi(z)+V(z)\psi(z)=E\psi(z), \tag{6.1}$$

with m, $\hbar$, ∇, and z are respectively the mass of the quantum particle, the Planck constant, the gradient operator, and the spatial coordinate. The wave function $\psi(z)$ is an element of the Hilbert space of L^2-integrable functions, and its modulus square *i.e.*, $|\psi(z)|^2$, gives the probability of presence of the particle at some point z on the potential $V(z)$.

The wave function solutions of (6.1) form a complete set of basis vectors of the Hilbert space with the following properties: i) Wave vectors are oscillating functions. ii) Oscillation frequency increases with increasing energy E. iii) The basis vectors oscillate with a local frequency proportional to $\sqrt{E-V(z)}$, thus for the same wave function the frequency differs locally depending on the local value of $E-V(z)$. iv) The hyperparameter $\hbar^2/2m$ controls the dependence of the local frequency on $E-V(z)$. These properties of the basis vectors are the key features to use them as an adaptive basis for an imaging problem. For a more detailed illustration of these features, we refer readers to Chapter 4.

6.2.1.2 Application to Imaging Problems

To adapt these concepts to image processing applications, the wave equation (6.1) is rewritten in operator notation leading to $\boldsymbol{H}\boldsymbol{\psi}(z)=E\boldsymbol{\psi}(z)$ with Hamiltonian operator $\boldsymbol{H}=-(\hbar^2/2m)\nabla^2+\boldsymbol{V}(z)$. The eigenvectors of the Hamiltonian operator are the stationary solutions of (6.1).

For imaging applications, the space is finite and discretized, and the potential $\boldsymbol{V}$ of the system may be defined as the image pixel values $\boldsymbol{x}$. This leads to a discretized problem, where the Hamiltonian operator becomes a finite matrix and can be used as a tool for constructing an adaptive basis [114]. This discretized Hamiltonian operator reads:

$$\boldsymbol{H}[i,j]=\begin{cases}\boldsymbol{x}[i]+4\dfrac{\hbar^2}{2m} & \text{for } i=j,\\ -\dfrac{\hbar^2}{2m} & \text{for } i=j\pm 1,\\ -\dfrac{\hbar^2}{2m} & \text{for } i=j\pm n,\\ 0 & \text{otherwise,}\end{cases} \tag{6.2}$$

where $\boldsymbol{x} \in \mathbb{R}^{n^2}$ is an image (*i.e.*, $\boldsymbol{V} = \boldsymbol{x}$), and $\boldsymbol{x}[i]$ and $\boldsymbol{H}[i,j]$ represent respectively the i-th component of the image $\boldsymbol{x}$, vectorized in lexicographical order and the (i,j)-th component of the operator. Note that standard zero padding is used to handle the boundary conditions. A more detailed description of the Hamiltonian construction can be found in Chapter 4. The corresponding set of eigenvectors of the Hamiltonian operator (6.2) serves as the quantum adaptive basis on which the image is decomposed before denoising is performed by thresholding the coefficients in energy.

6.2.1.3 Shortcomings of the Single-Particle Theory in Image Processing

This method of constructing an adaptive basis using quantum principles in a single-particle setting has already been studied in some of our previous works, notably for image denoising in Chapter 4 and deconvolution in Chapter 5. This adaptive method not only is effective for handling different noise statistics (*e.g.*, Gaussian, Poisson) but also equally efficient for different levels of noise (low as well as high-intensity noise). Nevertheless, there are some technical and intrinsic challenges, such as:

i) Structural features are crucial for imaging applications, but this adaptive approach does not take advantage of them.

ii) The random noise present in the system leads to the well-known phenomenon of quantum localization [19] of the wave vectors. The presence of this subtle quantum phenomenon gives additional structures to the adaptive basis and makes it less effective for image denoising. This problem was cured in Chapter 4 by adding an additional step of low-pass filtering, for example, through a Gaussian filter with appropriate standard deviation, of the noisy image. This complicates the method and in particular entails the integration of a new hyperparameter (standard deviation) in the algorithm, which increases the complexity of hyperparameter tuning.

iii) The computational burden of such a method can be quite large compared to other sophisticated state-of-the-art methods, thus preventing it from implementation in large-scale images.

In the following, we will show that these drawbacks can be addressed by constructing a new adaptive basis by exploiting quantum many-body theory, more precisely the physics of quantum interactions.

6.2.2 Quantum Many-Body Theory for Image Processing

6.2.2.1 Quantum Theory for Many Particles

The quantum theory described above is modified for a system with more than one particle as illustrated in Chapter 2 Section 2.8. In particular, particle-to-particle interactions take place inside the quantum system. For a system with w particles the Hamiltonian operator for the many-body system becomes [232]:

$$H(z_1, z_2, z_3, \cdots, z_w) = -\sum_{a=1}^{w} \frac{\hbar^2}{2m_a}\nabla^2 + V(z_1, z_2, z_3, \cdots, z_w), \tag{6.3}$$

where m_a is the mass of the a-th particle and the potential $V = V(z_1, z_2, z_3, \cdots, z_w)$ is a function of $z_1, z_2, \cdots, z_w$, the spatial coordinates of the w particles. Thus, for a given energy E the associated wave function ψ depends on $z_1, z_2, \cdots, z_w$, and satisfies a new Schrödinger equation:

$$H\psi(z_1, z_2, \cdots, z_w) = E\psi(z_1, z_2, \cdots, z_w). \tag{6.4}$$

6.2.2.2 Application to Image Processing

We propose to extend this multi-body theory to build an adaptive basis for imaging applications by assimilating similarities between patches into the quantum framework using the hypothesis as proposed in Chapter 2 Section 2.8. Similar to non-local means filter-based approaches, the proposed algorithm splits the image or a local region into into small patches ranging from 1 to w. Each of these patches acts as a single-particle quantum system, which allows the Hamiltonian operator to be defined for each patch as follows:

$$\boldsymbol{H}_a = \underbrace{-\frac{\hbar^2}{2m_a}\nabla^2 + \overbrace{\boldsymbol{V}(z_a)}^{\boldsymbol{V}_a^{effective}}}_{\boldsymbol{H}_{0_a}} + \boldsymbol{I}_a, \quad a = 1, \cdots, w, \tag{6.5}$$

where $\boldsymbol{H}_{0_a}$ is the Hamiltonians in the patch $\boldsymbol{A}$ for a single particle system (as discretized in (6.2)). $\boldsymbol{I}_a = \sum_{b=1, b\neq a}^{w} \boldsymbol{I}_{ab}$ represents the total interaction between the patch $\boldsymbol{A}$ and the other patches in the system, where $\boldsymbol{I}_{ab}$ is the interaction between the $\boldsymbol{A}$ and $\boldsymbol{B}$ patches. Thus, inside the patch $\boldsymbol{A}$ the effective potential $\boldsymbol{V}_a^{effective}$ is

$$\boldsymbol{V}_a^{effective} = \boldsymbol{V}(z_a) + \boldsymbol{I}_a = \boldsymbol{V}(z_a) + \sum_{b=1, b\neq a}^{w} \boldsymbol{I}_{ab}. \tag{6.6}$$

Therefore, we have a different adaptive basis for each patch containing a unique effective potential $\boldsymbol{V}_a^{effective}$ associated with an energy E_a. Fig. 6.1 depicts one such simple example of constructing adaptive vectors from the many-patch interaction concept. Thus the problem of finding the adaptive basis is transformed into the solution of a system of w equations, as follows:

$$\boldsymbol{H}_a \boldsymbol{\psi}(z_a) = E_a \boldsymbol{\psi}(z_a), \quad a = 1,2,\cdots,w. \tag{6.7}$$

where similar discretization procedures should be used in each patch as in (6.2).

6.2.2.3 Definition of the Quantum Interaction Between two Image Patches

Interaction between two or more objects is a universal phenomenon that governs the world at a very basic level, fundamentally classified into four groups: gravitational, electromagnetic, strong, and weak interactions. The gravitational and electromagnetic interactions have long-range properties characterized by power laws. We extend this concept to an imaging problem by introducing the interaction between two image patches, as follows:

- There is an inverse proportionality between the interaction and the square of the Euclidean distance (*i.e.*, physical distance) between the patches, *i.e.,* $\boldsymbol{I}_{ab} \propto \frac{1}{D_{ab}^2}$, where D_{ab} is the Euclidean distance between two patches denoted by $\boldsymbol{A}$ and $\boldsymbol{B}$.
- There is a linear proportionality between the interaction and the absolute value of the pixel-wise difference between the patches. This process is defined pixel-wise, *i.e.,* $\boldsymbol{I}_{ab}^i \propto |\boldsymbol{A}^i - \boldsymbol{B}^i|$, $i = 1,2,\cdots,P_{dim}$, where superscript i and P_{dim} are associated with the i-th pixel and the number of pixels in every image patch respectively.

Hence, within the proposed image processing framework, the power law for an interacting many-patch system can be defined as

$$\boldsymbol{I}_{ab}^i = p\frac{|\boldsymbol{A}^i - \boldsymbol{B}^i|}{D_{ab}^2}, \quad i = 1,2,\cdots,P_{dim}, \tag{6.8}$$

where the proportionality constant p acts as a hyperparameter for the proposed formalism.

6.2.2.4 Interaction and Patch Similarity in Image Processing

In our many-patch model the proposed mathematical formalism of the power law interaction can be interpreted in the following way:

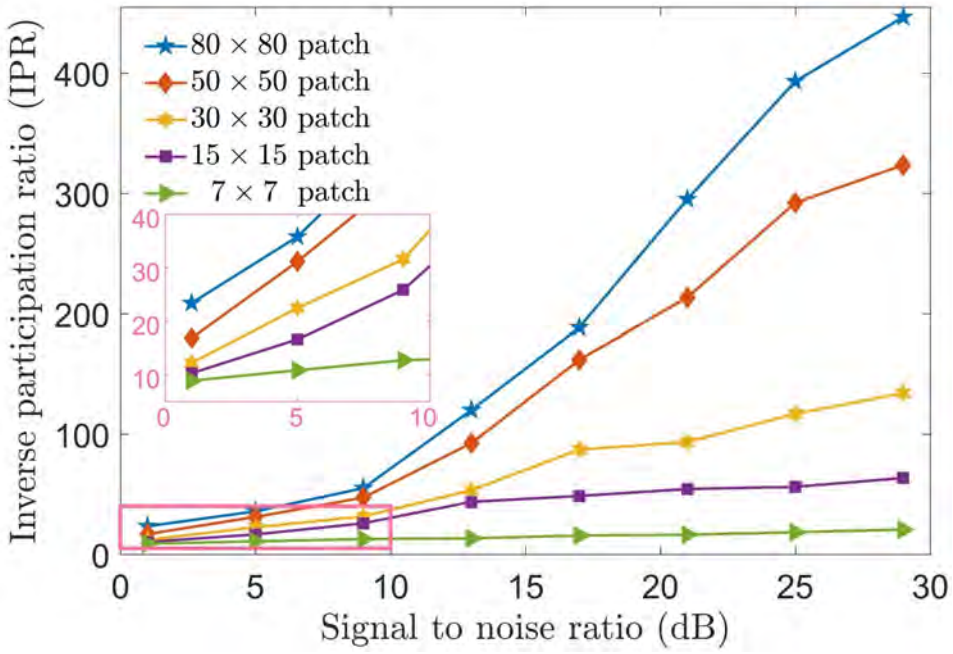

FIGURE 6.2. Average inverse participation ratio (IPR) of all the adaptive basis vectors as a function of signal to noise ratio for the *Lena* image degraded by AWGN using different sizes of the image patch.

(i) two patches with similar pixel values have smaller interaction than the ones with very different values,
(ii) patches located far from each other have small interaction regardless of their pixel values.
In other words, neighboring patches show high interactions if they are very different from each other based on pixel values, while distant patches are always less interactive despite their possible dissimilarity. Based on these principles, the power law manifests itself in such a way that the effective potential of the patch $\boldsymbol{A}$ is $\boldsymbol{V}_a^{effective}$. This is obtained after the combination of the initial potential (*i.e.*, the target patch itself) with the total interaction between the target patch and its neighboring patches, exploiting the concept of patch similarity in the local neighborhood. This local-similarity is a fundamental building block of real images that preserves structural features [48]. We note that power laws other than the inverse square law could be used, thus modifying the importance of distant patches compared to the nearby ones in the proposed methodology.

6.2.2.5 Why the Many-Patch Theory Avoids the Quantum Localization Problem

The presence of random fluctuations in the potential of a quantum system leads to the phenomenon of quantum localization, also known as Anderson localization [19]. This is a property of wave functions in a disordered potential which makes them exponentially localized due to destructive interference. As a consequence, the adaptive basis vectors for various imaging problems are localized at different positions of the potential in presence of random noise, which makes the adaptive basis less suitable for image decomposition tasks. In Chapter 4, this challenge was solved by adding a cumbersome first step of image low-pass filtering, with an additional hyperparameter involved. A more detailed discussion of this phenomenon, in particular for image decomposition and denoising, can be found in the previous Chapter 4.

In the framework of the many-patch theory described above, the decomposition is done at the level of the individual patch, much smaller than the full image. The inverse participation ratio (IPR) of the wave functions, defined as $\left(\sum_i |\boldsymbol{\psi}(i)|^2\right)^2 / \sum_i |\boldsymbol{\psi}(i)|^4$ for a wave function $\boldsymbol{\psi}$, gives a measure of the localization. For a vector uniformly spread over L indices and zero elsewhere, the IPR is exactly L. More generally, the localization length of localized wave functions is proportional to the IPR. It is known from localization theory that this localization length decreases with the intensity of the disorder. Thus unless the noise is extremely strong, the localization length may be larger than the patch size, making the localization irrelevant for our problem. Fig. 6.2 shows the average IPR (measuring the localization length) of all the adaptive basis vectors for the *Lena* image degraded by additive white Gaussian noise (AWGN) with increasing signal to noise ratio (SNR) using different patch sizes. This illustration confirms that the IPR decreases with the SNR, but this effect reduces with patch size. For example, for a 80×80 patch, the IPR decreases rapidly with decreasing SNR (increasing noise intensity) and becomes less than the patch size for SNR ≤ 12 dB, making the system extremely localized. However, for smaller patches like 7×7, almost no such effect is visible for similar noise intensities. In other words, the localization effect becomes less important in a small patch than in a large one and turns out to be irrelevant below a certain level of patch size. We found out that even for fairly strong noise it is always possible to find a patch size smaller than the average IPR that makes irrelevant the localization effect, avoiding the need of the low-pass filtering to create the adaptive basis.

6.3 Quantum Many-Patch Interaction for Imaging Applications: Problem of Image Decomposition

6.3.1 Key Principles of the Proposed Many-Patch Model

The objective of this work is to propose a methodology of an explicit construction of an adaptive basis related to the many-body interaction theory under the principles:

- Every small patch extracted from an image corresponds to a quantum particle; each of these image-patches or potential surfaces with a quantum particle acts like a single-particle system.
- These single-particle systems are not isolated from each others, on the contrary, the interaction between them and other patches occurs within the whole image, like a quantum many-body system, where a particle-to-particle interaction takes place in the quantum system.
- As a consequence of these interactions, the effective potential (see (6.6)) of quantum particles changes, thus the local oscillation frequency of the wave function depends on these interactions.
- These interactions transmit structural features to the wave functions through the effective potential.
- The effective potentials will be used to construct an adaptive basis for each individual patch, in particular used for the decomposition of that patch.
- As an element of the set of oscillatory functions, this basis function uses low oscillation frequencies to probe higher values of the effective potential and vice-versa, *i.e.*, local frequencies depend on the effective potential, and thus on the pixel values and inter-patch interactions.

6.3.2 Denoising Algorithm using Quantum Many-Patch Interactions

This subsection illustrates in detail the application of the proposed many-patch scheme to address image denoising. In this application, the construction of an adaptive basis for each individual image-patch is the primary objective, which leads to a three step

denoising strategy: decomposition of that patch using the adaptive basis, thresholding of the projection coefficients, and finally recovery of the denoised patch by back-projection. These basis vectors are the eigenvectors of the Hamiltonian matrix (6.2), constructed from the effective potential (6.6).

These adaptive vectors belong to the Hilbert space of oscillatory functions with: i) the frequency of oscillation increases with increasing energy value (*i.e.*, eigenvalue in (6.7)), and ii) a given basis vector uses low oscillation frequencies to probe higher values of the effective potential and vice-versa. It is now assumed that the noise primarily rules the high-frequency components of the image, *i.e.*, eigenvectors corresponding to higher energy eigenvalues. Therefore as in the single-particle algorithm, thresholding in energy should be done to eliminate the image components associated with the high energy eigenvectors.

In the proposed interaction framework, the structural similarity between neighboring image patches is assumed to be an innate property of the image. Hence two neighboring patches are assumed to be similar to the extent of random noise. Following the definition (6.8), two adjacent patches show high interaction if they are pixel-wise dissimilar (*i.e.*, random noise is present), thus further contributing to the effective potential (6.6). In other words, the interaction term or ultimately the effective potential increases if the noise intensity increases, which eventually shifts the high-frequency noise components of the image to even higher energy eigenvectors. Thus, in order to have a denoised patch, a noisy patch is projected onto a d-dimensional subspace that is constructed by the lowest energy solutions of (6.7) and the denoised patch is rebuilt from these projection coefficients. In this way, a lack of similarity between pixels leads to a stronger denoising, since for the same value of the energy these regions will have lower frequencies than the ones with more similarity. Here, d acts as a thresholding hyperparameter. Combining all the denoised patches, following a path similar to the one proposed in the non-local means architecture, one can obtain the final denoised image. Hereafter this proposed adaptive quantum denoiser which integrates the quantum theory of interactions to imaging problems is called Denoising by Quantum Interactive Patches (De-QuIP). The whole denoising process is displayed in Algorithm 6.1.

6.3.3 Computational Complexity

In the precedingly developed algorithm based on single particle quantum physics (in Chapter 4), the computational complexity of the algorithm was essentially controlled by the diagonalization of a large Hamiltonian matrix and the identification of its eigenvec-

Algorithm 6.1: De-QuIP algorithm.

Input: $\boldsymbol{y}$, P_h, W_h, d, p, $\hbar^2/2m$

Divide the noisy image $\boldsymbol{y}$ into small patches of size P_h; say total number is T_{patch}. So, the patch dimension $P_{dim} = {P_h}^2$

for $w = 1 : T_{patch}$ **do**

- Choose one small image patch $\boldsymbol{J}_w$
- Create a search window of size W_h centering at $\boldsymbol{J}_w$ and using cyclic boundary conditions
- Collect all the small image patches inside this search window; say the total number is S_{patch}
- **for** $l = 1 : S_{patch}$ **do**
  - Calculate Euclidean distance D_{wl} between the $\boldsymbol{J}_w$ and $\boldsymbol{J}_l$ patch inside the search window
  - Calculate interaction $\boldsymbol{I}_{wl}$ between the $\boldsymbol{J}_w$ and $\boldsymbol{J}_l$ patch inside the search window as, $\boldsymbol{I}_{wl}^k = p\dfrac{|\boldsymbol{J}_w^k - \boldsymbol{J}_l^k|}{D_{wl}^2}, \;\; k = 1, \cdots, P_{dim}$
- Calculate total interaction $\boldsymbol{I}_w^{total}$ between the patch $\boldsymbol{J}_w$ and the patches inside the search window by taking sum over all l; *i.e.*, $\boldsymbol{I}_w^{total^k} = \sum_{l=1}^{S_{patch}} \boldsymbol{I}_{wl}^k, \;\; k = 1, \cdots, P_{dim}$
- Effective potential for the $\boldsymbol{J}_w$ patch is $\boldsymbol{V}_w^{effective^k} = \boldsymbol{J}_w^k + \boldsymbol{I}_w^{total^k}, \;\; k = 1, \cdots, P_{dim}$
- Construct the Hamiltonian matrix $\boldsymbol{H}_w$ using the effective potential $\boldsymbol{V}_w^{effective}$
- Calculate the eigenvalues and eigenvectors of $\boldsymbol{H}_w$
- Construct adaptive basis $\boldsymbol{B}_w^{adaptive}$ using the eigenvectors $\boldsymbol{\psi}_w^k, \;\; k = 1, \cdots, P_{dim}$
- Project the noisy patche $\boldsymbol{J}_w$ onto this adaptive basis $\boldsymbol{B}_w^{adaptive}$
- Calculate projection coefficients $\boldsymbol{c}_w$ in the P_{dim}-dimensional space. Note that, $P_{dim} > d$
- Redefine the projection coefficients in the d-dim subspace as $\boldsymbol{c}_w^{new^k} = \boldsymbol{c}_w^k, k = 1, \cdots, d$
- Reconstruct the patch by $\boldsymbol{R}_w = \sum_{k=1}^{d} \boldsymbol{c}_w^{new^k} \boldsymbol{\psi}_w^k$

Combining all T_{patch} number of small denoised image patches $\boldsymbol{R}_w$ restores the full denoised image $\hat{\boldsymbol{x}}$

Output: $\hat{\boldsymbol{x}}$

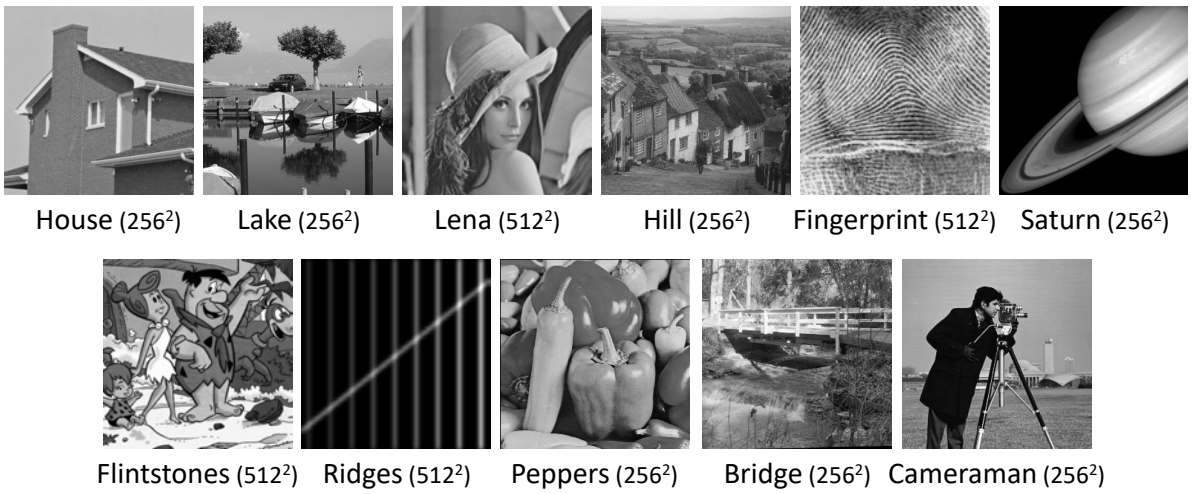

FIGURE 6.3. Sample images (sizes in parentheses).

tors. For an image of size $n \times n$, this matrix is $n^2 \times n^2$. In general, for an arbitrary matrix, the diagonalization process would require $O(n^6)$ operations and $O(n^4)$ storage space. However, for a highly sparse matrix (like the Hamiltonian matrix), efficient iterative methods such as the Lanczos method reduce the computational complexity to $O(n^4)$ operations with $O(n^4)$ space complexity required for the diagonalization.

In the case of the many patch algorithm, the denoising is done patch-wisely (of size $P_h \times P_h$), the time and space complexity become $O(P_h^4)$ for each denoise region, much smaller than the previous one for $P_h \ll n$. Yet, the best time complexity one can achieve is $O(dP_h^2)$ if one computes only the d eigenvectors used for the restoration task (with $d \leq P_h^2$), with a space complexity also in $O(dP_h^2)$.

Apart from the diagonalization, the second major contribution comes from the computations of the transform coefficients using an iterative scheme that would require $O(dP_h)$ operations for each denoise region.

The interaction count for each denoise region gives a complexity in total of $O((S_{patch} + 1)P_h)$ if there are S_{patch} patches inside the $W_h \times W_h$ size search window.

Therefore, if the image consists of T_{patch} regions (patches), then the dominant computational cost of the proposed denoising algorithm is $O(T_{patch} dP_h^2)$. Additionally, parallel computation can be used to boost up the process even further.

6.4 Simulation Results

This section illustrates the interest of the proposed approach in image denoising problems and explores ways to choose the suitable hyperparameters. At the outset, Subsection 6.4.1 explains the reliance of the proposed denoising scheme on the optimal choice of the hyperparameters P_h, W_h, p, $\hbar^2/2m$ and d, and explores rules for their possible estimations. For a thorough investigation, we explore cases of four different noise intensities (low to high) with image independent (*e.g.*, Gaussian) and dependent (*e.g.*, Poisson) noise models. The subsequent Subsection 6.4.2 provides denoising results and a comparison between the proposed approach and several standard state-of-the-art methods.

6.4.1 Influence of Hyperparameters P_h, W_h, p, $\hbar^2/2m$ and d and How to Select Them

6.4.1.1 Effect of the Patch Size P_h

The effect of localization of the basis vectors is associated with the length of the image patch, as explained in Subsection 6.2.2.5. The respective localization length or IPR decreases for increasing noise intensity. To deal with this quantum localization phenomenon, the size of the patch should be always less than or equal to the localization length of the basis vectors for different levels of noise. If the localization length is greater than the size of the patch, the basis vectors probe the entire region of the image patch with different ranges of oscillation frequencies depending on the intensity of the image pixels. On the contrary, a smaller localization length leads to an exponential localization of the basis vectors on a specific part of the image patch. Thus, these localized vectors will not have different frequencies at different pixel values and lose a key asset of this formalism. The drastic effect of this localization phenomenon on image denoising is shown in the previous Chapter 4, where an additional Gaussian smoothing was necessary before computing the quantum adaptive basis (QAB), used as a denoiser in that process. On the contrary, the current formalism eliminates this issue without any additional computational requirements.

Furthermore, a smaller patch size helps to reduce the computational complexity, as discussed in the section above. As a consequence, De-QuIP denoiser is more computationally efficient than the previously proposed QAB denoiser in Chapter 4, applied patch by patch independently. Table 6.1 summarizes the run time using the QAB and De-QuIP denoiser with increasing patch size. The peak signal to noise ratios (PSNR)

TABLE 6.1. Simulation data with different patch sizes for the *Lake* image contaminated by AWGN (SNR = 16dB). For the proposed De-QuIP method hyperparameters $\hbar^2/2m = 1.5$, and p and d are estimated from the equations (6.9) and (6.10) respectively.

	Data	Patch size							
		1×1	3×3	5×5	7×7	11×11	17×17	27×27	63×63
QAB	PSNR(dB)	11.36	12.78	21.56	24.40	26.54	27.12	27.33	28.09
	SSIM	0.43	0.46	0.48	0.48	0.63	0.70	0.74	0.79
	Time(sec)	30.56	17.09	41.31	70.32	161.96	328.97	881.69	5800.72
De-QuIP	PSNR(dB)	22.12	28.16	28.73	28.84	28.58	28.23	28.16	27.77
	SSIM	0.37	0.78	0.83	0.83	0.82	0.81	0.80	0.79
	Time(sec)	21.93	22.75	82.61	108.01	490.52	3829.31	5644.90	22765.18

and the structure similarity (SSIM), used as denoising quality metrics, are given to have a quantitative analysis concerning the patch size. All the algorithms have been implemented in Matlab and tested on a computer with an Intel(R) Core(TM) i7-10510U CPU of 4 cores each with 1.80 GHz, 16 GB memory and using Windows 10 Pro version 20H2 as operating system. From Table 6.1, one can see that the computational time for both denoisers increases as the patch size increases but the denoising performance (*i.e.*, PSNR and SSIM values) for De-QuIP first increases with the patch size and then begins to decrease gradually after size 11×11. Whereas, QAB requires much larger patches to achieve a similar performance, which essentially imposes a huge computational burden on the process. The gradual decrease in the performance of the De-QuIP denoiser for increasing patch size is expected due to the localization phenomenon, which is discussed above. Therefore, a smaller patch size preserves the fundamental features of these adaptive vectors and reduces the computational complexity and run time. Herein, we will only focus on the patch sizes 5×5, 7×7 and 11×11 for further investigations.

6.4.1.2 Effect of the Search Window Size W_h

The search window is the image region aroung the current patch regrouping all the patches interacting with it. Following the discussion in Subsection 6.2.2.3, the size of the search window plays an important role in preserving the structural similarities in a local neighborhood. This search window is usually defined as a square window of limited size so that the implementation is restricted to a small neighborhood centered on the target patch (to be denoised) instead of the whole image. In the literature, mostly two types of approaches are used, based on a fixed search window size [92, 233, 333, 355] or

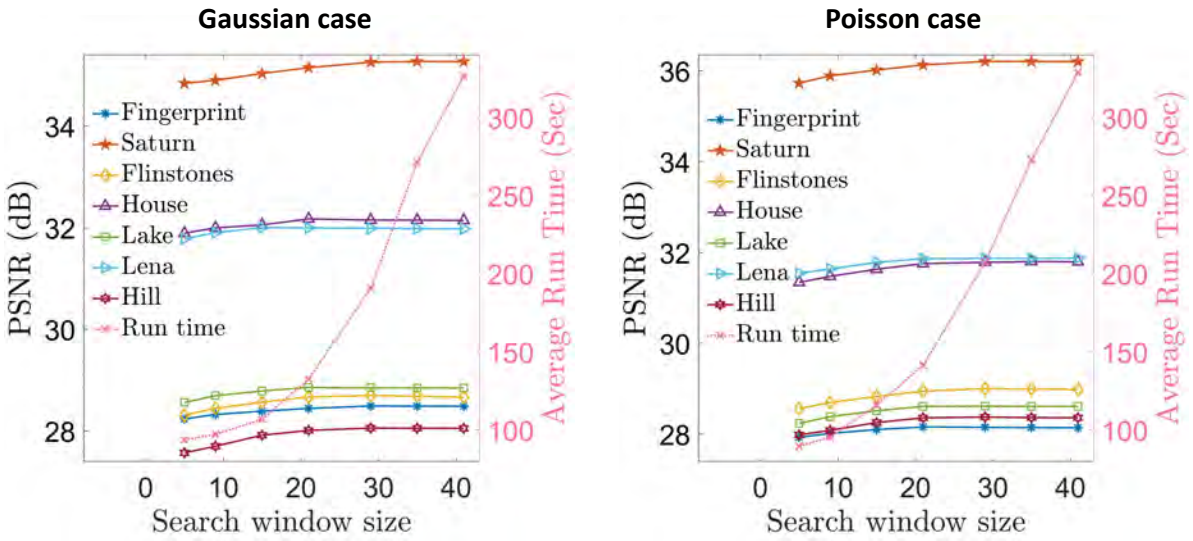

FIGURE 6.4. Denoising performance in terms of PSNR (left y-axis) and average run time (right y-axis) of De-QuIP as a function of the search window size for the first seven sample images in Fig. 6.3. The images hyperparameters $P_h = 7$ and others are estimated from the equations (6.9)-(6.12).

an adaptive approach [187]. In this work, we concentrate on the fixed size approach for examining the effect of the search window on De-QuIP.

Fig. 6.4 shows the denoising performance of De-QuIP in terms of PSNR as a function of the search window size for the Gaussian and Poisson noise cases. For these simulations, the patch size is kept fixed at 7×7 for all images. Note that in these simulations patches overlap, given that consecutive target patches are one pixel away from each other, both in the horizontal and vertical direction. In Fig. 6.4, one can see that in both cases, the denoising ability increases with the size of the search window before roughly stabilizing beyond a size 20×20 for both noise models. These observations show that the patch neighborhood is important to increase the denoising performance but larger search windows do not bring additional information about the neighborhood due to the inverse square nature of the interaction term. It is also important to notice that the computation time increases with the search window size, as shown in the right y-axis in Fig. 6.4. The use of a relatively moderate size search window is computationally more efficient while preserving the image attributes using the proposed interaction framework. Note that these results are consistent for other patch sizes. Therefore, for simplicity, in this work we choose a search window size of 15×15, 21×21 and 33×33 respectively for the patch sizes of 5×5, 7×7 and 11×11. One interesting observation can be drawn here, that the

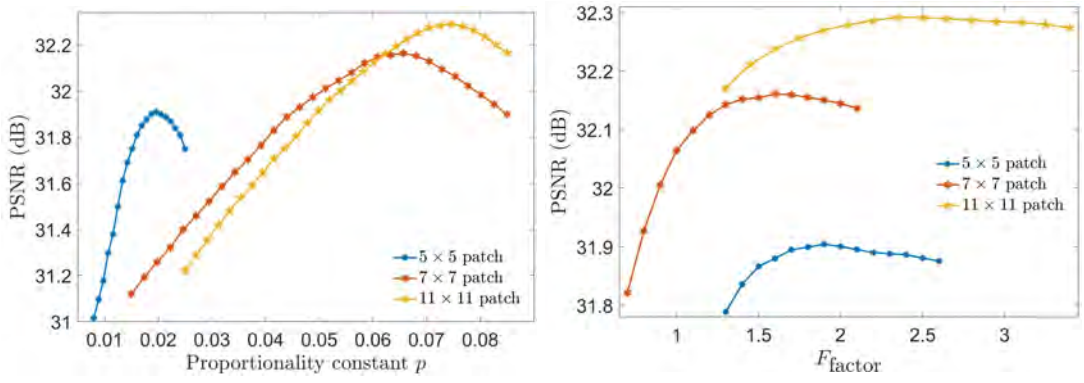

(a) PSNR vs p (b) PSNR vs F_{factor}

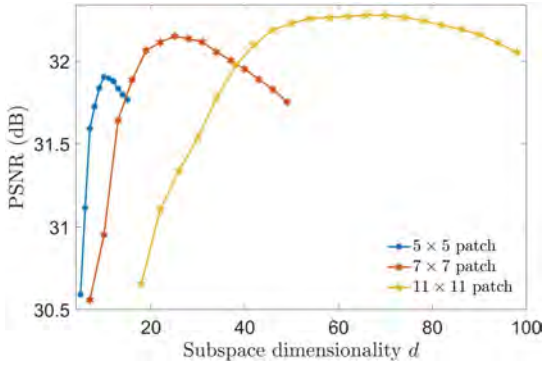

(c) PSNR vs d

FIGURE 6.5. Denoising performance of De-QuIP in terms of PSNR as a function of the hyperparameters for the *House* image corrupted with AWGN (SNR = 16dB) using three different patch sizes. All hyperparameters are estimated using equations (6.9)-(6.12).

search window size changes with the patch size and not with the noise model within the proposed algorithm.

6.4.1.3 Influence of the Proportionality Constant p

As mentioned above, the proportionality constant p regulates the interaction term in the effective potential, and consequently the shape of the basis vectors. Hence, there exists an optimal choice of p depending on the size of the patch for optimal performance of De-QuIP for a given noisy image. Fig. 6.5(a) presents the denoising performance in terms of PSNR as a function of p for the *House* image corrupted with AWGN (SNR = 16dB), for three different patch sizes. These optimal values also depend on the level of noise present in the image. These p values that maximize the output PSNRs for the first

seven sample images in Fig. 6.3 corrupted with different noise intensities are highlighted. These optimal p values are shown as a function of SNR in Fig. 6.6 using box-plots for a fixed patch size. The observations confirm that there is a tendency for optimal values to decrease as the noise level increases. The explicit details of these optimal values are reported in Table 6.2. A possible explanation for this phenomenon comes from the fact that dissimilarities increase with the noise intensity in a local-neighborhood. Hence, to balance the original potential (patch pixels) and the interactions in the effective potential, the hyperparameter p decreases.

The data in Fig. 6.6 enables rules to fix the p value closer to its optimal values. The distribution of the data gives an intuition about a possible linear relationship between the optimal p and the SNR. Therefore, the proportionality constant p can be chosen from the following rule:

$$p = m_1 \times (\mathrm{SNR}) + c_1. \tag{6.9}$$

TABLE 6.2. Optimal proportionality constant p for De-QuIP.

Sample	Input SNR(dB)	Gaussian case Patch size 5×5	Gaussian case Patch size 7×7	Gaussian case Patch size 11×11	Poisson case Patch size 5×5	Poisson case Patch size 7×7	Poisson case Patch size 11×11
house	22	0.0385	0.0750	0.0550	0.0109	0.0467	0.0800
	16	0.0197	0.0667	0.0700	0.0046	0.0325	0.0900
	8	0.0053	0.0600	0.0625	0.0064	0.0305	0.0500
	2	0.0001	0.0225	0.0475	0.00013	0.0034	0.0400
lake	22	0.0220	0.0900	0.0900	0.0057	0.0555	0.0600
	16	0.0130	0.0522	0.0936	0.0033	0.0269	0.0400
	8	0.0060	0.0460	0.0755	0.0018	0.0355	0.0499
	2	0.0001	0.0290	0.0573	0.00013	0.0096	0.0300
lena	22	0.0215	0.0950	0.1250	0.0156	0.0533	0.0625
	16	0.0107	0.0758	0.1100	0.0067	0.0317	0.0550
	8	0.0046	0.0467	0.0600	0.00031	0.0207	0.0775
	2	0.00001	0.0100	0.0400	0.00001	0.0010	0.0550
hill	22	0.0154	0.0643	0.1229	0.0089	0.0500	0.0900
	16	0.0139	0.0521	0.0888	0.0056	0.0400	0.0800
	8	0.0072	0.0375	0.0625	0.00088	0.0300	0.0629
	2	0.00001	0.0146	0.0340	0.00001	0.0055	0.0429
fingerprint	22	0.0500	0.0700	0.0450	0.0244	0.0600	0.1000
	16	0.0369	0.0657	0.0650	0.0133	0.0400	0.0833
	8	0.0041	0.0543	0.0900	0.00011	0.0350	0.0650
	2	0.0022	0.0110	0.0830	0.00005	0.0011	0.0500
saturn	22	0.0257	0.0700	0.1100	0.0100	0.0500	0.1083
	16	0.0021	0.0578	0.0900	0.0080	0.0400	0.0967
	8	0.0031	0.0234	0.0600	0.0006	0.0124	0.0617
	2	0.00001	0.0157	0.0500	0.00001	0.0010	0.0540
flintstones	22	0.0260	0.0931	0.0463	0.0089	0.0400	0.0500
	16	0.0183	0.0500	0.0304	0.0044	0.0225	0.0655
	8	0.0052	0.0308	0.0500	0.0006	0.0200	0.0525
	2	0.0016	0.0205	0.0500	0.00017	0.0126	0.0450

TABLE 6.3. Slope and intercept used in determining proportionality constant p for various patch sizes for Gaussian and Poisson noise models. Also, the associative ℓ_2 error, PSNR (dB) loss and SSIM loss in linear curve fitting to the optimal p.

		Size of the patches		
		5×5	7×7	11×11
Gaussian	Slope (m_1)	12.84×10^{-4}	30.96×10^{-4}	16.46×10^{-4}
	Intercept (c_1)	-35.96×10^{-4}	13.56×10^{-3}	50.40×10^{-3}
	ℓ_2 error for p fit	0.0327	0.0528	0.1196
	PSNR(dB) loss	0.278	0.306	0.179
	SSIM loss	0.0139	0.0172	0.0106
Poisson	Slope (m_1)	60.33×10^{-5}	21.00×10^{-4}	16.64×10^{-4}
	Intercept (c_1)	-21.85×10^{-4}	36.31×10^{-4}	44.23×10^{-3}
	ℓ_2 error for p fit	0.0189	0.0392	0.0811
	PSNR(dB) loss	0.380	0.422	0.485
	SSIM loss	0.0197	0.0185	0.0150

In Fig. 6.6, the best linear fits to the optimal p as a function of SNR are shown for three different patch sizes as well as for Gaussian and Poisson noise models. These linear fits give a robust way of choosing the suitable p for a given patch size and noise level.

The linear fit parameters are summarized in Table 6.3 together with the ℓ_2 error and the resulting average loss in the denoising performance in terms of PSNR and SSIM. One may notice that the denoising performance loss with rule (6.9) rather than the optimal choice is negligible. This is expected due to the smooth nature of the PSNR curve with a broad maxima shown in Fig. 6.5(a), which makes the De-QuIP resilient to small sub-optimalities in the adoption of p. Hence, it is anticipated that the parameters learned from the sample images to estimate p using (6.9), will be effective for a large set of images. These conclusions are valid for various cases of noise models and patch sizes, as shown in the simulations results. Furthermore, an adaptive approach of tuning p that depends on the image patch gives an alternative to the above rules and opens an interesting perspective for future investigation.

6.4.1.4 Influence of $\hbar^2/2m$ and the Subspace Dimensionality d

The last two hyperparameters to be analyzed are $\hbar^2/2m$ and the subspace dimensionality d. Although the utilization of these two hyperparameters seems to be different, the first one being used in the construction of the Hamiltonian operator and the other one acting as a threshold, there is a deep connection between them. In this subsection, we will explain this connection with experimental validation and propose rules for automated estimation of their optimal choices.

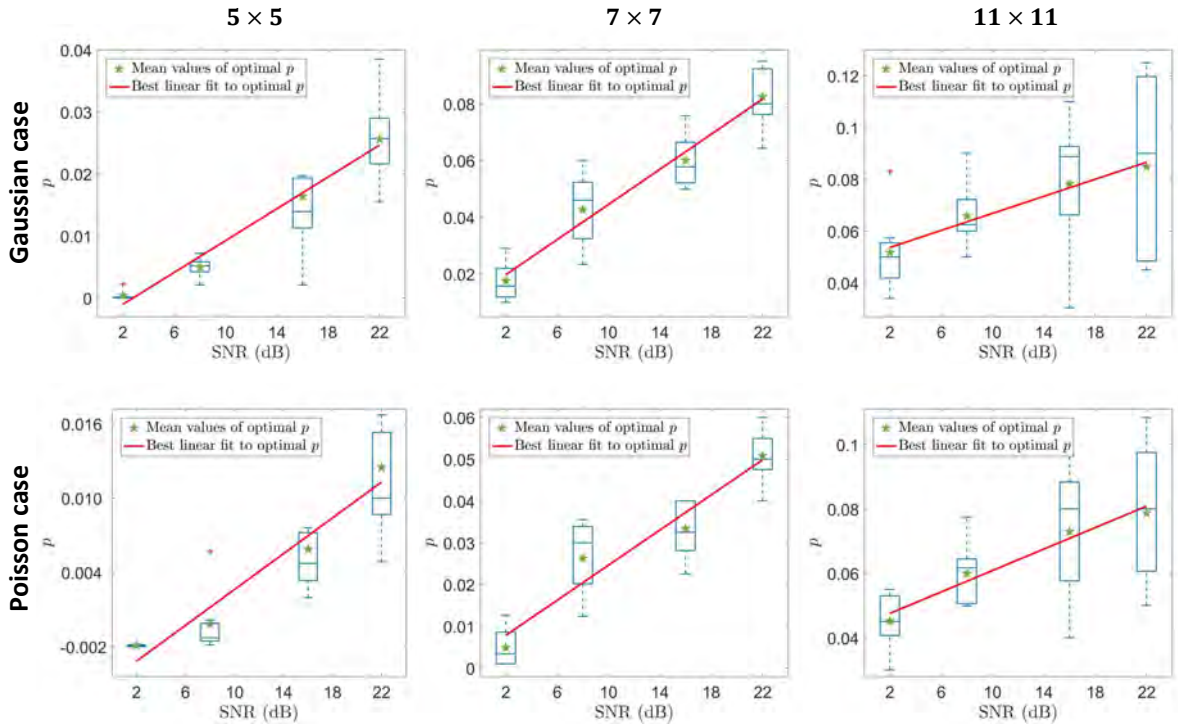

FIGURE 6.6. Optimal proportionality constant p value as a function of SNR for three patch sizes, where the three left and the three right graphs are associated with the case of Gaussian and Poisson noise models. The bars indicate the minimum and maximum values of the optimal p. The bottom and top edges of the blue boxes indicate the 25^{th} and 75^{th} percentiles and the central mark and green star indicate the median and mean values. The red line is the best linear curve fitted to the data points corresponding to the mean of the optimal p values.

As stated above in Subsection 6.2.1.1, the hyperparameter $\hbar^2/2m$ controls how the local frequencies of the basis vectors change with the image pixel values. For low values of $\hbar^2/2m$, the oscillation frequencies are very high, regardless of the low and high pixel values, due to the presence of a very high maximal oscillation in this limit which restricts the wave vectors from properly exploring higher pixel values. On the other side, increasing too much the values of $\hbar^2/2m$ decreases the ability of the basis vectors to distinguish between high and low values pixels. For more illustrations about the effect of this hyperparameter $\hbar^2/2m$ on the basis vectors, we refer readers to the previous Chapter 4. Therefore, the optimal $\hbar^2/2m$ value has a strong dependence on the maximum and minimum values of the pixels present in the image patch. Thus, it is more convenient

TABLE 6.4. Optimal F_{factor} values for De-QuIP.

Sample	Input SNR(dB)	Gaussian case Patch size 5×5	Gaussian case Patch size 7×7	Gaussian case Patch size 11×11	Poisson case Patch size 5×5	Poisson case Patch size 7×7	Poisson case Patch size 11×11
house	22	1.4714	2.4250	2.2000	1.7000	2.2667	2.6000
	16	1.9000	1.6733	2.3000	1.6000	1.9167	1.8500
	8	1.9800	1.5333	1.9833	1.9900	2.1000	1.0000
	2	1.5000	1.2000	1.7300	2.9000	1.9000	1.5800
lake	22	1.6000	2.1125	2.4000	1.4889	1.8000	1.6000
	16	1.5500	1.9633	2.8000	1.6333	1.9900	2.0000
	8	2.2000	1.4083	2.0650	2.5000	1.8500	2.0000
	2	1.6632	2.1000	2.3000	2.8333	2.6000	1.7000
lena	22	1.3850	1.9000	2.4000	1.6000	2.0400	2.5000
	16	1.8500	1.7800	2.3000	1.8000	1.8500	2.1000
	8	2.0000	1.5500	2.0200	1.9200	2.2667	1.7000
	2	1.2400	0.8571	2.1000	2.6500	2.2333	2.0000
hill	22	1.3570	1.5000	1.8000	1.6500	1.5182	1.9000
	16	2.4500	2.2500	2.0000	2.0000	2.2000	1.9400
	8	2.6222	2.7400	2.5000	3.0000	3.0000	2.2800
	2	1.6167	2.1444	2.0000	2.5000	2.9000	3.2000
fingerprint	22	1.2500	1.3800	1.4500	1.6000	1.5000	1.5000
	16	1.7000	1.7500	2.1000	1.5400	1.6000	2.3000
	8	3.3000	3.0000	1.8000	3.8000	3.0000	1.9000
	2	2.7000	2.0000	2.0000	3.8000	3.0000	3.6000
saturn	22	1.3500	1.3900	1.9000	1.5500	1.8778	2.2600
	16	1.7818	1.7000	1.7000	1.5600	1.4889	1.8000
	8	1.5909	1.8400	1.8000	2.1143	2.0000	1.9600
	2	1.6286	1.7100	1.7000	1.8333	1.6000	2.0429
flintstones	22	1.4000	1.5500	1.5000	1.8000	1.4000	1.5000
	16	1.9333	1.9000	1.9000	1.7000	1.8400	1.5000
	8	1.8000	2.0000	1.9000	3.0000	1.9700	1.9000
	2	3.0000	2.5750	1.8000	3.8000	2.9000	1.9000

to use an adaptive way to select $\hbar^2/2m$ that depends on the image patch to have the optimal performance of De-QuIP. Herein, it is possible to write the hyperparameter in terms of the difference between this maximum and minimum pixel values multiplied by a factor F_{factor}, for example, for the patch $\boldsymbol{A}$,

$$\hbar^2/2m = F_{\text{factor}} \times (\boldsymbol{A}_{\max} - \boldsymbol{A}_{\min}), \tag{6.10}$$

where $\boldsymbol{A}_{\max}$, $\boldsymbol{A}_{\min}$ are the maximum and minimum pixel values of the patch $\boldsymbol{A}$. Hence, the optimal choice of F_{factor} is needed to have the best possible output.

In this proposed scheme, the subspace dimensionality d is used as the threshold for truncating high energy wave solutions, which mostly carry noise information. Hence, an optimal choice of d exists for a noisy image that yields the best denoising output depending on the patch size. $\hbar^2/2m$ or say F_{factor} controls the frequency distribution across the basis vectors since the maximal frequency of a vector with energy E at the local pixel value V is $\sqrt{(E-V)/(\hbar^2/2m)}$. Hence, the maximal frequency decreases with

TABLE 6.5. Optimal subspace dimensionality d for De-QuIP.

Sample	Input SNR(dB)	Gaussian case Patch size 5×5	Gaussian case Patch size 7×7	Gaussian case Patch size 11×11	Poisson case Patch size 5×5	Poisson case Patch size 7×7	Poisson case Patch size 11×11
house	22	16	39	120	15	33	85
	16	10	24	111	10	25	74
	8	6	11	56	3	11	24
	2	3	4	24	2	6	18
lake	22	24	48	84	24	48	120
	16	21	40	64	22	36	101
	8	7	15	25	8	14	36
	2	3	7	11	3	6	24
lena	22	19	35	100	18	33	98
	16	12	21	58	11	22	90
	8	7	8	27	5	8	28
	2	2	4	12	2	4	17
hill	22	25	48	120	24	48	120
	16	20	40	111	22	43	115
	8	6	13	41	6	13	41
	2	3	6	11	2	6	11
fingerprint	22	13	28	86	13	26	86
	16	8	18	56	8	17	47
	8	4	9	28	4	8	18
	2	3	7	19	3	7	13
saturn	22	8	17	51	8	17	47
	16	7	11	30	8	12	30
	8	3	6	15	3	4	15
	2	2	5	7	2	3	7
flintstones	22	24	48	120	24	47	120
	16	13	41	118	14	37	118
	8	8	13	41	8	13	32
	2	5	10	25	4	8	24

increasing F_{factor}. As a consequence, low-energy basis vectors become more prominent to distinguish low and high pixel regions using different levels of frequency. Thus, the optimal subspace dimensionality d decreases as F_{factor} increases. These optimal choices vary with the image patch size and noise statistics. Table 6.4 and Table 6.5 show these optimal values that give the best output PSNRs for the first seven sample images. In Fig. 6.7, all these optimal values that give the best output PSNRs for the first seven sample images are shown as a scatter-plot of F_{factor} vs d, which clearly shows their inverse relationship, *i.e.*, d decreases with F_{factor}'s growth or vice-versa and validates our above arguments.

These experimental data enable an automated way of selecting the values of d and F_{factor} close to their optimalities. To do this, the optimal d values are shown in Fig. 6.8 as a function of SNR using box-plots for a fixed patch size, for the Gaussian and Poisson cases. The observation shows a very predictable behaviour of this optimal d as a function of SNR which is expected as it needs to be further thresholded as the noise increases. For a specific patch size, the optimal d and SNR follow a linear relationship. Therefore,

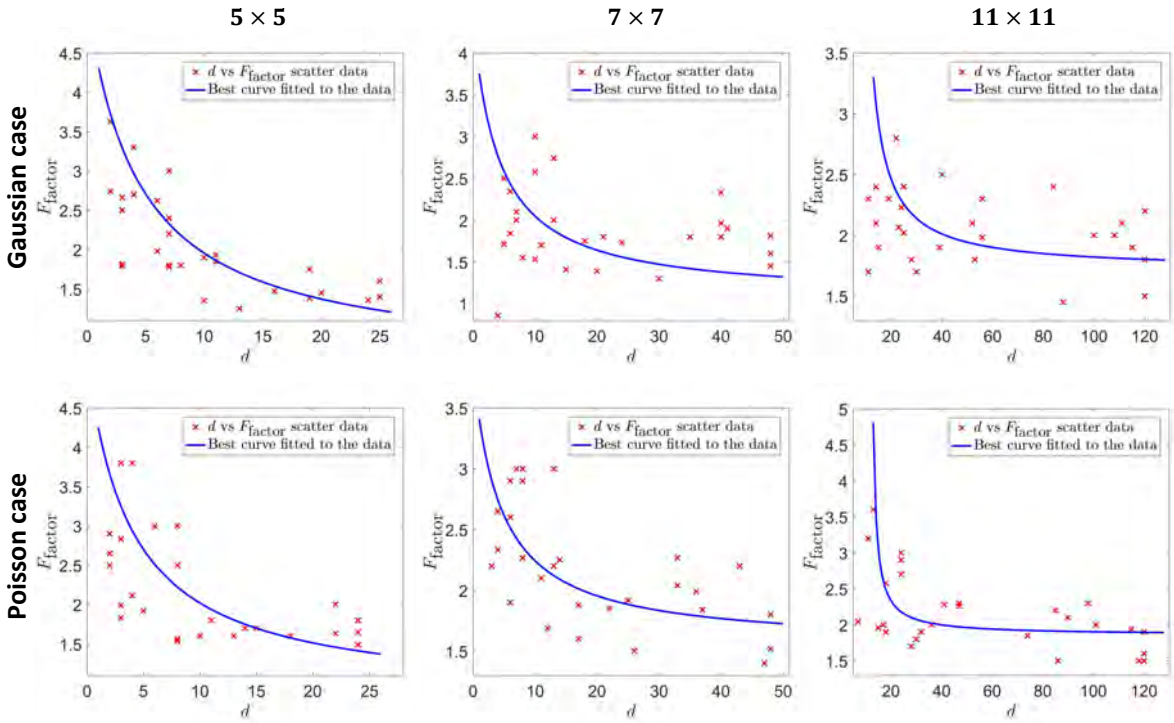

FIGURE 6.7. F_{factor} vs d scatter plot and the respective best-fitted curve of the form $(F_{\text{factor}} - l_1) = l_3/(d - l_2)$.

the subspace dimensionality d and F_{factor} can be inferred from the following two rules,

$$d = m_2 \times (\text{SNR}) + c_2, \tag{6.11}$$

$$F_{\text{factor}} - l_1 = l_3/(d - l_2). \tag{6.12}$$

Fig. 6.7 and Fig. 6.8 show the best-fitted curves to the optimal F_{factor} and d, and the respective fit parameters are regrouped in Table 6.6. These rules give an efficient way of selecting the hyperparameters close to their optimality depending on the size of the given patch and the intensity of the noise. Our data show that the respective costs in terms of performance loss are minimal, since the output PSNR curves are smooth and have broad maxima, shown in Figs. 6.5(b)-6.5(c) for the choice of F_{factor} and d, as discussed in Subsection 6.4.1.3 for the hyperparameter p. Hence, the rules for automated selecting hyperparameters are expected to be valid for other images as well.

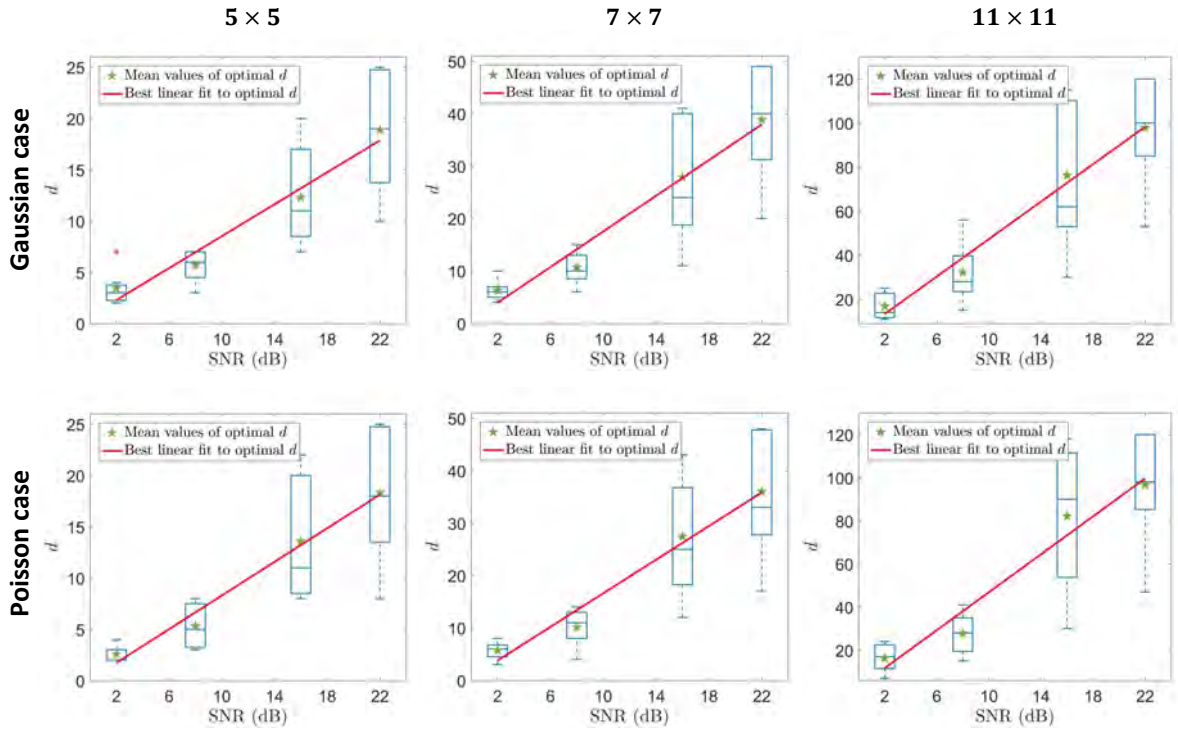

FIGURE 6.8. Optimal subspace dimensionality d value as a function of SNR for three patch sizes are shown for the Gaussian and Poisson noise models. Similar to Fig. 6.6, a box-plot diagram is used for the optimal d. The red line is the best linear curve fitted to the data points corresponding to the mean of the optimal d.

6.4.2 Denoising Efficiency of the Proposed Scheme in Comparison with Standard Methods

This subsection presents the denoising performance of the De-QuIP algorithm depending on the noise statistics and intensity, and also how this performance varies with patch size for the sample images. The denoising outputs using three patch sizes are summarized in Table 6.7. The numerical simulations show that 11×11 is the suitable patch size for most of the cases, but for low-level noise, smaller sizes give a small advantage. It is expected to have a better result with a large patch for a strong noise scenario since high noise intensity refers to an extreme random system and a large patch is more efficient to capture the similarity measures from this strong randomness. Obviously, the size should not be so large because it is affected by the phenomenon of localization, as illustrated in Subsubsection 6.2.2.5.

TABLE 6.6. Curve fitting parameters used in determining d and F_{factor} for various patch sizes for Gaussian and Poisson noise models. The table also includes the associative ℓ_2 errors, PSNR (dB) loss and SSIM loss in curve fitting to the optimal d and F_{factor}.

		Size of the patches		
		5×5	7×7	11×11
Gaussian	Slope (m_2)	0.7783	1.7000	4.2500
	Intercept (c_2)	0.7315	0.5345	4.8210
	ℓ_2 error for d fit	21.1673	43.3499	112.4127
	Parameter l_1	0.5287	1.2630	1.9161
	Parameter l_2	−4.4551	−4.1915	6.8223
	Parameter l_3	20.6204	13.9698	9.7995
	ℓ_2 error for F_{factor} fit	2.3845	2.6135	1.9334
	PSNR(dB) loss	0.416	0.361	0.209
	SSIM loss	0.0153	0.0129	0.0118
Poisson	Slope (m_2)	0.8202	1.6030	4.3990
	Intercept (c_2)	0.8621	0.5800	2.8900
	ℓ_2 error for d fit	23.2670	43.4135	115.9894
	Parameter l_1	0.8083	1.5391	1.8587
	Parameter l_2	−3.8975	−4.4288	11.6517
	Parameter l_3	16.8476	10.1560	3.9798
	ℓ_2 error for F_{factor} fit	3.3802	2.0652	2.2571
	PSNR(dB) loss	0.487	0.594	0.485
	SSIM loss	0.0175	0.0266	0.0386

As explained earlier, the De-QuIP follows a similar principle to the NLM approach. Comparisons with NLM-based state-of-the-art methods are thus provided in order to prove the efficiency of the proposed algorithm. However, for a comprehensive survey of the denoising ability of De-QuIP, rigorous comparisons with contemporary noise removal methods from the literature are also presented. For the recovery of Gaussian corrupted images, the following methods were used for comparison: NLM method using PCA called PND in [333], two patch-based PCA for NLM denoising methods referred to as PGPCA (global approach) and PLPCA (local approach) in [92], BM3D [82], dictionary learning (DL) method [123], graph signal processing (GSP) method [262], and finally, our earlier implementations of quantum adaptive basis (QAB) for image denoising based on the single particle theory from Chapter 4.

For the recovery of Poisson corrupted images, comparisons have been carried out with recent algorithms dedicated to the Poissonian model such as Poisson non-local PCA (PNLPCA) [296], BM3D consolidated with the Anscombe transform [238] leveled as ATBM3D, and finally the QAB from Chapter 4 method.

The proposed denoising algorithm has been extensively compared to other standard methods to demonstrate the accuracy of De-QuIP. Detailed quantitative evaluations in terms of PSNR and SSIM for both noise models are available in Tables 6.8-6.9. From

TABLE 6.7. Comparison of denoising performance of De-QuIP with different patch sizes for different noise levels.

		Gaussian case						Poisson case					
Sample	Input	5×5		7×7		11×11		5×5		7×7		11×11	
	SNR(dB)	PSNR(dB)	SSIM	PSNR(dB)	SSIM	PSNR(dB)	SSIM	PSNR(dB)	SSIM	PSNR(dB)	SSIM	PSNR(dB)	SSIM
house	22	35.30	0.88	35.45	0.89	35.58	0.89	34.94	0.87	35.10	0.88	35.14	0.88
	16	31.91	0.83	32.15	0.83	32.29	0.83	31.49	0.82	31.78	0.82	31.73	0.82
	8	26.85	0.72	27.45	0.75	27.91	0.76	26.45	0.72	27.02	0.74	27.27	0.75
	2	23.05	0.60	23.92	0.68	24.66	0.72	22.65	0.59	23.48	0.66	24.09	0.70
lake	22	33.23	0.92	33.16	0.91	32.80	0.90	33.09	0.91	33.04	0.90	32.72	0.90
	16	28.81	0.83	28.85	0.82	28.63	0.81	28.54	0.81	28.60	0.81	28.42	0.81
	8	24.05	0.69	24.19	0.71	24.37	0.69	23.75	0.66	23.98	0.68	24.11	0.68
	2	21.09	0.57	21.59	0.62	21.75	0.63	20.90	0.56	21.33	0.61	21.48	0.63
lena	22	35.05	0.89	35.21	0.89	35.34	0.90	34.86	0.88	35.05	0.89	35.16	0.89
	16	31.73	0.84	32.00	0.85	32.17	0.85	31.49	0.83	31.78	0.84	32.34	0.84
	8	26.17	0.71	27.67	0.78	28.00	0.78	26.93	0.74	27.40	0.77	27.61	0.76
	2	23.60	0.63	24.53	0.71	25.04	0.74	23.36	0.63	24.30	0.71	24.71	0.71
hill	22	31.54	0.82	31.58	0.83	31.55	0.83	32.01	0.82	32.16	0.83	32.13	0.83
	16	27.95	0.69	28.06	0.70	28.10	0.70	28.25	0.70	28.37	0.70	28.39	0.70
	8	24.42	0.55	24.49	0.55	24.61	0.55	24.58	0.55	24.63	0.55	23.58	0.54
	2	21.97	0.46	22.41	0.48	22.61	0.49	22.08	0.46	22.46	0.48	22.54	0.49
fingerprint	22	32.35	0.93	32.50	0.93	32.54	0.94	33.39	0.94	32.15	0.93	33.49	0.95
	16	28.12	0.86	28.46	0.87	28.65	0.87	28.63	0.87	28.16	0.86	28.24	0.86
	8	23.36	0.72	23.31	0.72	23.63	0.73	23.65	0.74	23.07	0.72	23.40	0.73
	2	20.03	0.59	19.80	0.57	20.01	0.58	19.90	0.59	19.58	0.56	19.56	0.56
saturn	22	38.94	0.89	39.36	0.92	39.53	0.94	40.64	0.97	40.85	0.98	40.87	0.98
	16	34.67	0.79	35.27	0.83	35.63	0.87	36.00	0.94	36.31	0.95	36.42	0.94
	8	28.94	0.61	29.87	0.67	30.60	0.74	30.44	0.89	31.00	0.90	31.40	0.89
	2	24.45	0.46	25.97	0.55	27.03	0.62	26.40	0.82	27.26	0.86	27.46	0.85
flintstones	22	32.20	0.87	32.16	0.87	31.97	0.86	33.20	0.88	33.08	0.88	32.99	0.88
	16	28.65	0.80	28.69	0.79	28.47	0.78	29.04	0.80	29.00	0.78	28.77	0.78
	8	23.48	0.67	23.78	0.68	23.70	0.66	23.44	0.65	23.84	0.68	23.64	0.64
	2	19.74	0.52	19.87	0.56	20.03	0.56	19.50	0.51	19.69	0.53	19.63	0.53

these results, on can observe that De-QuIP scheme significantly outperforms all NLM-based methods with an average gain of 1.1 to 2.6 dB in PSNR and 3 to 20% in SSIM. One can also observe that De-QuIP and BM3D-based methods stand out as the two best-performing algorithms for both Gaussian and Poissonian cases. The denoising performance of De-QuIP and BM3D-based methods are presented in Figs. 6.9-6.10 for visual inspection, where ground truth, noisy, and corresponding denoised images are shown. These results confirm the good performance of De-QuIP regardless of the noise model and intensity. In the denoised images, image features and details, for example, patterns (in *Fingerprint* and *Ridges*), sharp edges (in *Lake*, *Bridge*, *Cameraman* and *House*), smooth areas (in *Peppers*, *Flintstones*, and *Lena*), are well-preserved. Although BM3D and respectively ATBM3D are slightly more accurate in some of the experiments, a smoothing effect is present in their corresponding denoised images and becomes more prominent as the noise level increases. This effect is clearly visible around the windows and roof of the *Hill*, on the patterns of the *Fingerprint*, near the eye of the *Lena*, on the

face of the *Flintstones*, and around the sharp edges of the *House* images, while De-QuIP preserves all these image features in a better way and consequently provides a denoised image closer to the original one. This is due to the interaction term that allows De-QuIP to better extract the image information. Although, for the increasing noise intensity, some artefacts can be observed in the denoised images (for example in *House*, *Saturn*,

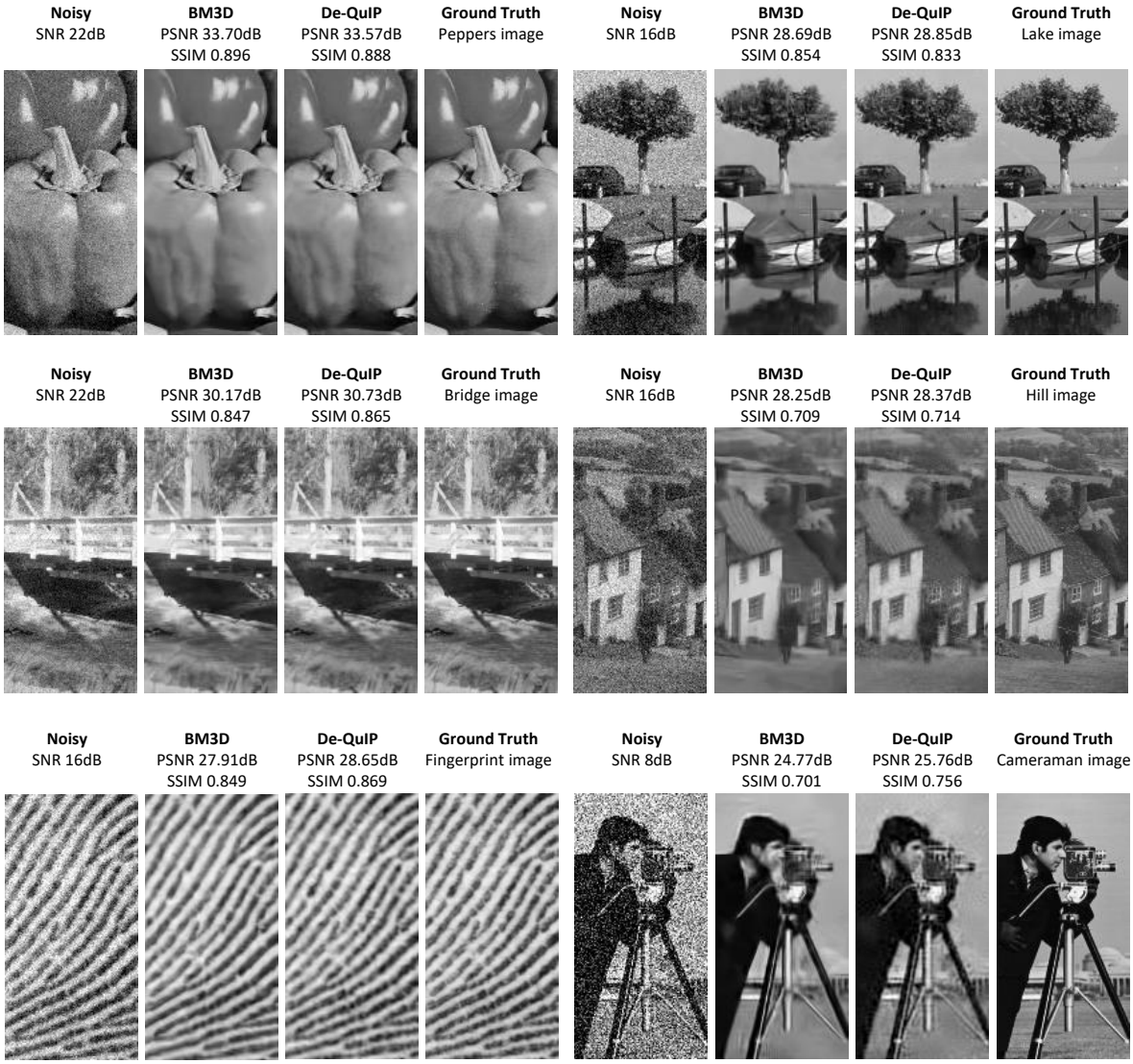

FIGURE 6.9. The Gaussian denoising results for different level of noise. The noisy, BM3D results, De-QuIP results, and ground-truth images are presented here accordingly. The BM3D and De-QuIP schemes are listed as these are always among the two best-performing methods.

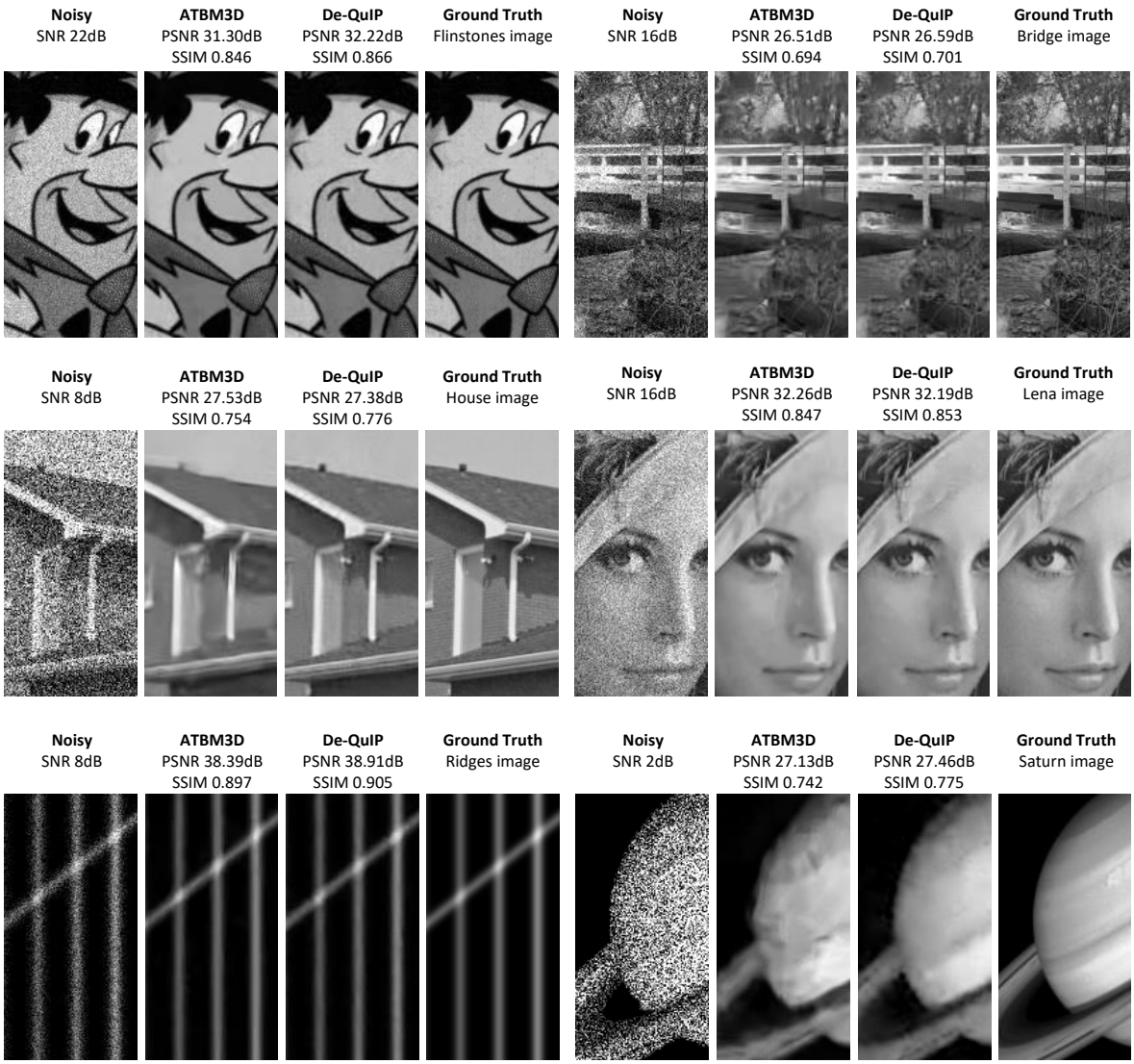

FIGURE 6.10. The Poissonian denoising results for different level of noise. The noisy, ATBM3D results, De-QuIP results, and ground-truth images are presented here accordingly. The ATBM3D and De-QuIP schemes are listed as these are always among the two best-performing methods.

Cameraman images) due to the presence of strong noise, they are very few and negligible for low-level noises.

For further inspection in Fig. 6.11, we show zoomed segments of the denoised results of the *Flintstones* image while corrupted with AWGN (SNR 16dB). Similarly, for Poisson corrupted (SNR 16dB) *Lake* image the zoomed segments of the denoised estimations

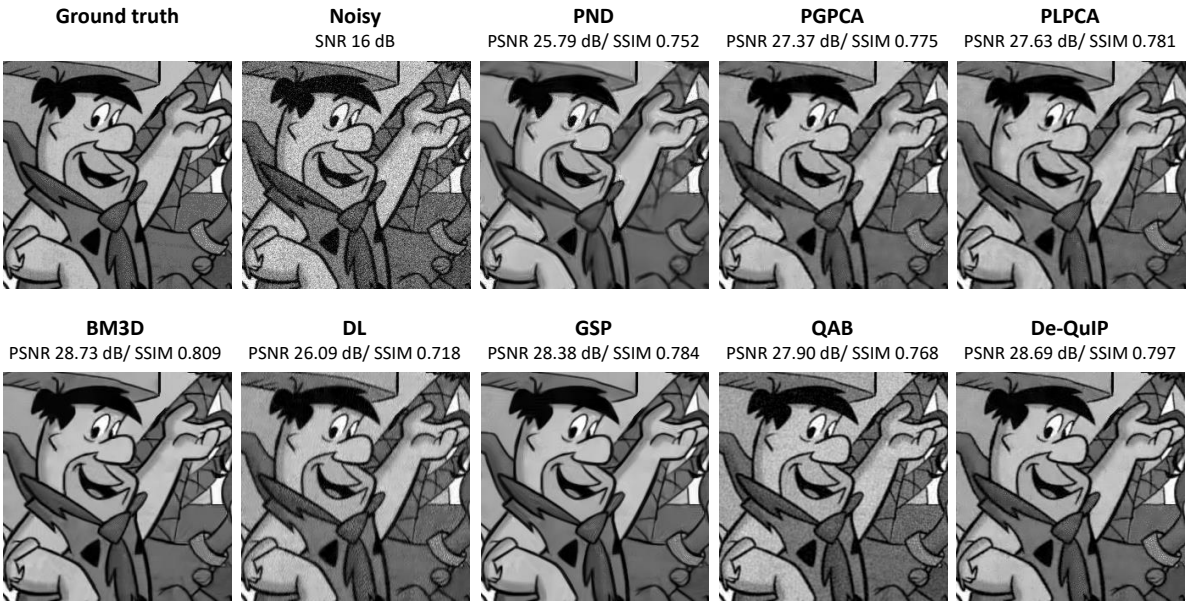

FIGURE 6.11. Zoomed segments of the denoised estimations of the *Flintstones* image while corrupted with AWGN (SNR 16dB) using different methods.

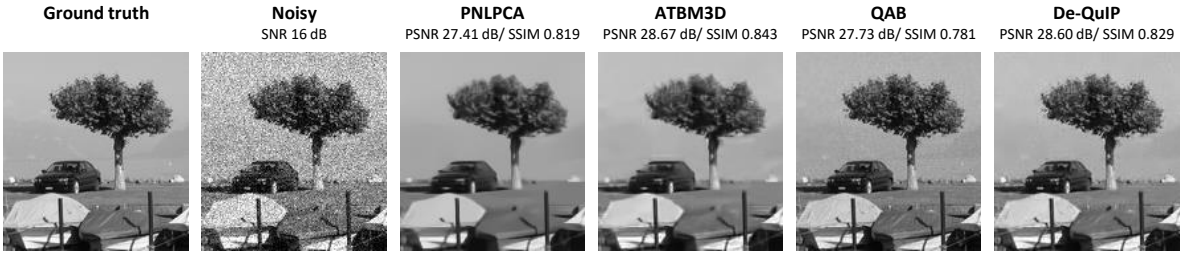

FIGURE 6.12. Zoomed segments of the denoised estimations of the *Lake* image while corrupted with Poisson noise (SNR 16dB) using different methods.

are shown in Fig. 6.12. Quantitative performance in terms of PSNR and SSIM adopting different methods for Gaussian and Poisson contaminated images are presented in Fig. 6.13 using box-plots as a function of SNR. The detailed quantitative performance related to these experiments are repoted in Tables 6.8-6.9.

Through visual and quantitative inspections of Figs. 6.11-6.12, it is clear that the proposed De-QuIP uniformly outperforms all the NLM-based approaches with a significant increase in terms of PSNR and SSIM. For Gaussian corrupted images, BM3D is still the best method in most cases, but De-QuIP allows competitive comparisons in all scenarios.

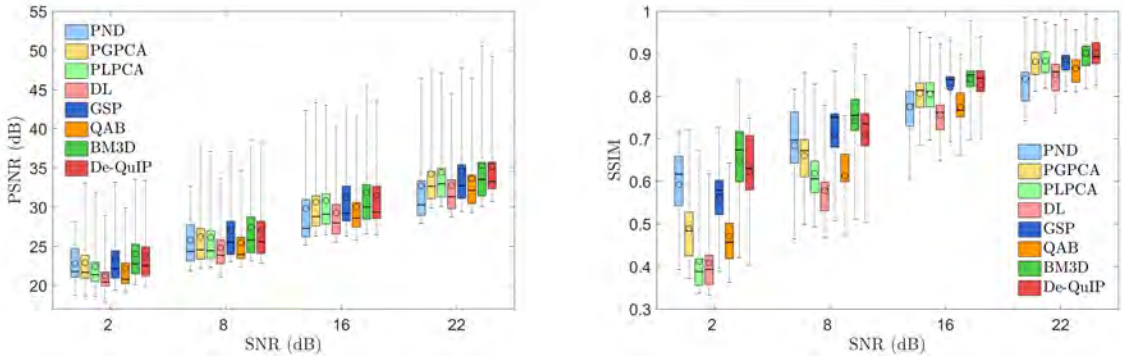

(a) Recovery of Gaussian corrupted images

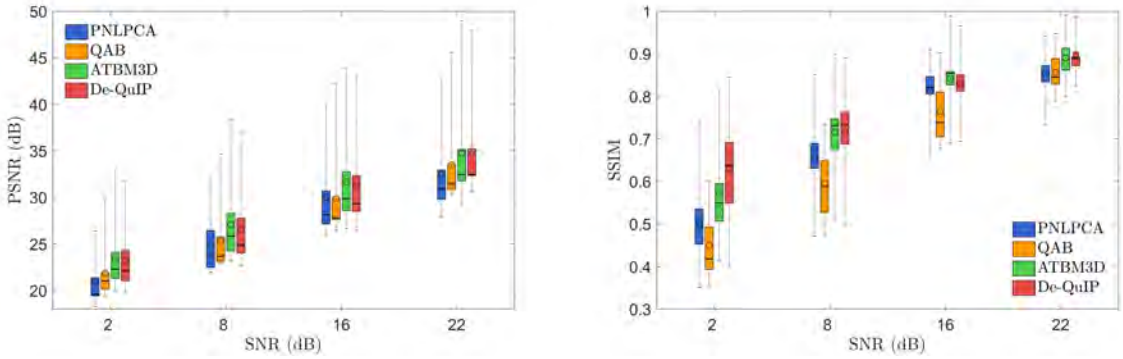

(b) Recovery of Poisson corrupted images

FIGURE 6.13. Quantitative denoising results using different methods for Gaussian and Poisson corrupted images with four different noise levels. The bottom and top edges of the boxes indicate the 25^{th} and 75^{th} percentiles, and the central black line and circle indicate the median and mean relative to the data points.

Furthermore, for both noise models, the positive effects of local similarity considerations are clearly visible in the Fig. 6.13 data of QAB and De-QuIP, as it gives much better PSNR and SSIM values with significantly fewer computations. The Figs. 6.11-6.12 show a pronounced gain in the qualitative performance of the proposed DeQuIP model against the QAB. Therefore, exploiting the structural details through interaction terms notably contributes to the preservation of image details, as verified by quantitative and visual assessments. Additionally, regardless of the noise intensity, De-QuIP always provides good PSNR and SSIM for the recovery of Gaussian corrupted images as shown in Fig 6.13(a), which is not the case with most algorithms, as highlighted by SSIM values. Although in Fig. 6.13, our results look comparable with BM3D, one should note that a beautification

TABLE 6.8. Quantitative denoising results for Gaussian corrupted images (average over 10 independent noise realizations). The best values are highlighted by color.

Sample	Input	Methods															
		PND		PGPCA		PLPCA		BM3D		DL		GSP		QAB		De-QuIP	
	SNR	PSNR	SSIM	PSNR	SSIM	PSNR	SSIM	PSNR	SSIM	PSNR	SSIM	PSNR	SSIM	PSNR	SSIM	PSNR	SSIM
house	22	33.17	0.831	34.28	0.863	34.80	0.866	35.89	0.896	32.86	0.827	35.70	0.891	33.77	0.856	35.60	0.892
	16	30.78	0.800	31.13	0.803	31.47	0.802	33.05	0.848	29.72	0.747	32.91	0.839	30.16	0.767	32.86	0.843
	8	27.52	0.753	26.83	0.672	26.65	0.605	28.73	0.786	25.31	0.587	28.19	0.760	25.71	0.601	28.13	0.764
	2	24.25	0.679	23.45	0.491	22.63	0.371	24.96	0.706	21.20	0.405	23.93	0.589	22.92	0.464	24.78	0.719
lake	22	30.29	0.855	32.36	0.895	32.56	0.895	33.07	0.919	30.90	0.863	32.09	0.913	32.22	0.878	33.27	0.926
	16	26.78	0.780	28.21	0.815	28.39	0.814	28.92	0.857	27.22	0.768	28.45	0.836	28.59	0.795	29.11	0.842
	8	23.61	0.697	23.87	0.653	23.77	0.606	24.43	0.739	23.25	0.588	24.30	0.722	24.24	0.599	24.52	0.705
	2	21.42	0.623	21.23	0.483	20.73	0.388	21.97	0.652	20.16	0.419	21.27	0.548	20.79	0.441	21.80	0.631
lena	22	33.52	0.858	34.78	0.881	35.04	0.883	35.50	0.898	34.08	0.868	35.09	0.893	34.36	0.876	35.81	0.904
	16	31.10	0.822	31.75	0.831	31.95	0.829	32.70	0.861	30.93	0.801	32.43	0.852	31.02	0.801	32.41	0.852
	8	27.94	0.773	27.65	0.716	27.35	0.648	28.75	0.799	26.34	0.638	28.18	0.767	26.61	0.657	28.31	0.778
	2	25.21	0.716	24.27	0.536	23.34	0.415	25.57	0.728	22.27	0.446	24.93	0.664	22.76	0.476	25.04	0.737
hill	22	29.35	0.742	30.98	0.812	31.29	0.819	31.36	0.818	29.80	0.761	30.97	0.811	30.56	0.810	31.59	0.826
	16	26.90	0.640	27.86	0.690	28.07	0.700	28.32	0.710	27.17	0.649	28.15	0.708	27.24	0.671	28.34	0.710
	8	24.34	0.534	24.55	0.539	24.42	0.515	24.98	0.575	23.85	0.478	24.86	0.571	23.91	0.492	24.78	0.563
	2	22.49	0.475	22.24	0.405	21.75	0.345	22.72	0.493	21.14	0.354	22.33	0.447	21.39	0.375	22.61	0.491
fingerprint	22	28.40	0.845	31.14	0.912	31.30	0.914	31.47	0.917	29.79	0.882	31.23	0.896	30.32	0.894	32.53	0.934
	16	25.57	0.757	27.27	0.830	27.46	0.835	27.92	0.850	25.97	0.783	26.99	0.824	27.16	0.815	28.61	0.868
	8	22.58	0.666	22.73	0.680	23.02	0.676	23.77	0.734	21.09	0.575	23.22	0.698	22.95	0.671	23.65	0.733
	2	20.05	0.563	18.92	0.471	19.50	0.474	20.73	0.613	17.85	0.385	20.21	0.546	20.04	0.527	20.56	0.605
saturn	22	40.95	0.955	39.32	0.935	39.63	0.929	42.26	0.970	37.55	0.891	41.20	0.943	38.63	0.916	39.70	0.937
	16	37.86	0.904	35.80	0.907	36.02	0.883	38.64	0.937	33.74	0.776	38.01	0.881	34.44	0.850	36.93	0.873
	8	32.23	0.775	30.70	0.753	30.09	0.647	33.16	0.861	28.00	0.541	32.58	0.757	29.44	0.712	31.25	0.735
	2	28.13	0.640	26.68	0.544	25.31	0.398	28.31	0.747	23.36	0.347	27.64	0.608	25.27	0.601	27.18	0.615
flintstones	22	28.54	0.766	30.62	0.827	30.83	0.831	31.31	0.847	29.15	0.793	30.91	0.841	30.34	0.811	32.20	0.865
	16	25.63	0.702	27.36	0.755	27.61	0.758	28.61	0.802	25.64	0.695	28.33	0.776	27.68	0.752	28.46	0.781
	8	21.86	0.620	22.15	0.586	22.31	0.567	23.96	0.705	21.12	0.520	23.61	0.662	22.54	0.561	23.67	0.662
	2	18.79	0.521	18.67	0.415	18.62	0.364	20.12	0.585	17.86	0.361	19.38	0.498	19.17	0.435	19.99	0.555
ridges	22	46.41	0.985	47.52	0.980	47.18	0.973	50.58	0.993	44.49	0.968	47.76	0.980	46.47	0.956	49.23	0.982
	16	42.32	0.961	43.34	0.950	42.97	0.938	45.37	0.978	40.17	0.922	42.60	0.931	41.44	0.898	43.56	0.940
	8	32.65	0.816	38.03	0.856	37.09	0.828	38.60	0.922	33.60	0.779	37.06	0.859	34.68	0.754	38.28	0.851
	2	25.99	0.599	33.07	0.720	31.91	0.672	33.56	0.837	28.97	0.618	33.15	0.727	29.86	0.643	33.39	0.749
peppers	22	31.23	0.842	32.83	0.871	33.06	0.872	33.79	0.897	31.32	0.840	33.34	0.891	32.08	0.849	33.52	0.888
	16	28.46	0.801	29.39	0.814	29.70	0.811	30.58	0.853	28.02	0.762	30.25	0.839	28.67	0.758	30.43	0.847
	8	24.54	0.744	24.93	0.674	25.03	0.639	26.24	0.771	23.96	0.608	26.07	0.752	23.94	0.612	26.19	0.755
	2	21.73	0.687	21.67	0.519	21.38	0.420	22.83	0.683	20.43	0.434	21.96	0.579	20.49	0.457	22.14	0.696
bridge	22	27.91	0.751	29.90	0.839	30.08	0.845	30.11	0.846	28.72	0.799	29.43	0.824	29.27	0.817	30.72	0.864
	16	25.16	0.608	26.28	0.685	26.46	0.697	26.57	0.698	25.52	0.655	26.33	0.693	25.78	0.662	26.49	0.699
	8	22.53	0.464	22.82	0.499	22.82	0.493	23.12	0.511	22.27	0.467	23.00	0.508	22.31	0.472	22.84	0.503
	2	20.69	0.393	20.61	0.372	20.29	0.337	21.00	0.421	19.71	0.333	20.60	0.389	20.04	0.362	20.72	0.403
cameraman	22	30.25	0.812	32.66	0.880	32.97	0.881	33.54	0.907	31.54	0.858	32.71	0.882	32.13	0.865	32.91	0.892
	16	27.29	0.757	28.78	0.793	29.08	0.792	29.99	0.843	27.98	0.758	29.17	0.840	28.18	0.751	29.36	0.841
	8	24.28	0.695	24.42	0.635	24.45	0.579	25.80	0.755	23.72	0.581	25.54	0.751	23.93	0.612	25.57	0.751
	2	21.78	0.617	21.45	0.434	21.03	0.347	22.77	0.674	20.28	0.393	22.13	0.597	20.51	0.402	22.49	0.636

happens in the BM3D outputs due to the smoothing effect as illustrated in Figs. 6.9-6.10, which is not present in our outcomes and makes our resultant image texture closer to the original one.

For Poisson corrupted images, De-QuIP provides better outcomes compared to the other methods. ATBM3D generates comparable PSNR and SSIM data in some scenarios, but the visual assessment clearly shows an extra smoothing effect present on the denoised image, which causes lower SSIM values for low SNR images as shown in Fig. 6.13(b). This is due to the process of data Gaussianization through the Anscombe transformation. In

TABLE 6.9. Quantitative denoising results for Poisson corrupted images (average over 10 independent noise realizations). The best values are highlighted by color.

Sample	Input	Methods							
		PNLPCA		ATBM3D		QAB		De-QuIP	
	SNR	PSNR	SSIM	PSNR	SSIM	PSNR	SSIM	PSNR	SSIM
house	22	33.19	0.848	35.36	0.879	32.85	0.833	35.27	0.879
	16	30.64	0.815	33.13	0.851	29.18	0.738	32.79	0.839
	8	26.72	0.706	28.48	0.731	25.63	0.619	27.72	0.757
	2	20.93	0.519	23.96	0.549	21.02	0.413	23.94	0.651
lake	22	30.23	0.884	32.13	0.913	31.21	0.845	32.43	0.892
	16	27.45	0.832	28.69	0.854	27.76	0.789	28.62	0.839
	8	22.42	0.675	24.50	0.698	23.29	0.567	24.28	0.707
	2	19.38	0.494	21.65	0.534	20.70	0.418	21.51	0.637
lena	22	32.68	0.852	34.92	0.886	34.29	0.872	35.15	0.889
	16	30.74	0.846	32.39	0.856	30.65	0.791	31.87	0.827
	8	26.19	0.686	28.08	0.751	25.83	0.617	27.78	0.768
	2	21.76	0.541	24.23	0.599	21.88	0.436	24.63	0.707
hill	22	30.88	0.792	31.81	0.813	30.89	0.824	31.69	0.824
	16	26.24	0.673	28.14	0.696	27.44	0.682	27.89	0.696
	8	22.95	0.535	24.98	0.555	24.45	0.494	24.71	0.548
	2	19.59	0.413	22.37	0.445	21.80	0.397	22.48	0.480
fingerprint	22	27.95	0.846	31.40	0.913	30.74	0.905	32.39	0.924
	16	26.81	0.820	28.41	0.860	27.62	0.829	28.36	0.862
	8	21.94	0.686	23.63	0.719	22.91	0.679	23.56	0.732
	2	19.42	0.538	20.16	0.569	20.07	0.549	20.01	0.565
saturn	22	39.36	0.942	41.15	0.976	38.94	0.906	40.96	0.978
	16	35.85	0.909	37.39	0.957	34.42	0.849	36.71	0.942
	8	28.55	0.851	30.82	0.874	28.75	0.714	30.31	0.890
	2	24.87	0.740	26.20	0.765	24.58	0.591	27.12	0.845
flintstones	22	30.08	0.820	31.72	0.843	30.29	0.789	32.28	0.864
	16	28.12	0.796	29.46	0.814	27.23	0.678	29.31	0.806
	8	22.51	0.631	23.93	0.650	23.67	0.529	23.76	0.668
	2	18.23	0.435	19.97	0.479	21.08	0.389	19.72	0.532
ridges	22	42.67	0.942	48.98	0.991	45.59	0.947	47.93	0.986
	16	39.95	0.894	43.88	0.988	42.23	0.902	42.97	0.965
	8	31.92	0.630	38.33	0.898	34.64	0.734	37.09	0.865
	2	26.42	0.491	33.00	0.815	29.83	0.602	31.79	0.816
peppers	22	31.85	0.860	33.35	0.893	31.42	0.816	33.32	0.889
	16	30.02	0.847	30.49	0.855	27.78	0.737	29.97	0.830
	8	25.08	0.693	25.97	0.743	23.02	0.587	25.45	0.737
	2	20.61	0.532	22.19	0.591	19.74	0.434	21.69	0.676
bridge	22	28.59	0.734	29.22	0.800	30.49	0.847	30.58	0.860
	16	25.99	0.660	26.61	0.690	26.44	0.689	26.50	0.694
	8	22.37	0.471	23.16	0.512	23.13	0.472	22.65	0.496
	2	19.46	0.351	20.94	0.413	20.17	0.352	20.56	0.398
cameraman	22	29.48	0.855	32.45	0.881	31.77	0.837	32.41	0.890
	16	28.03	0.821	29.86	0.839	27.78	0.720	28.76	0.818
	8	23.87	0.645	25.83	0.734	23.12	0.524	24.87	0.716
	2	19.39	0.470	22.37	0.546	19.41	0.359	22.08	0.612

addition, for increasing noise intensity, this Anscombe transformation loses its accuracy [112], which is clearly observable in the Fig. 6.13(b) in the cases of low SNR. On contrary. De-QuIP is a straightforward method without having any such transformation and efficiently shows good denoising performance in all situations. Similar to the Gaussian

case, De-QuIP outperforms PNLPCA, a NLM based method, by a large margin. This proves its adaptability for high as well as for low SNR images regardless of their noise statistics which can be viewed as a strong point in several practical applications.

6.5 Application to Ultrasound Image Despeckling

In this section, for further illustration of the potential of De-QuIP, we investigated its ability for real medical ultrasound (US) image despeckling. US imaging is an integral part of modern medical science as it gives harmless, non-invasive, real-time images in an affordable way. The main artefact affecting US images is a random granular pattern, the speckle, which is generated by random constructive and destructive interference between US waves. This phenomenon related to the acquisition system is used as a source of information about the tissues in several applications, but can also affect the interpretability of the images by diminishing their readability. Indeed, the speckle does not follow an additive rule and has a complex noise distribution. Therefore, the important task of estimating speckle-free US images, known as despeckling [228] in the relevant literature, has been extensively explored using various schemes [7, 211, 298, 393] to enhance the readability of the US images.

6.5.1 Ultrasound Image Despeckling Performance of De-QuIP

Despeckling performance of De-QuIP is investigated through a phantom as well as four real cancer and two non-cancer thyroid US images acquired with a 7.5 MHz linear probe. We are proposing a comprehensive study of this problem here. The estimated despeckled

TABLE 6.10. Quantitative despeckling results of real medical US images using different methods. The best values are highlighted by color.

Sample	Input	Methods							
		AD		Lee		NLM		De-QuIP	
	CNR	CNR	RL (%)	CNR	RL (%)	CNR	RL (%)	CNR	RL (%)
phantom	0.69	7.97	6.9	12.25	7.0	15.92	7.2	14.29	7.0
non-cancer 1	9.56	15.39	7.0	18.04	7.6	19.97	8.5	18.54	7.8
non-cancer 2	1.86	7.05	6.0	9.77	6.7	11.89	8.4	10.54	7.3
cancer 1	1.41	4.59	7.5	5.41	8.0	8.43	8.8	9.10	8.1
cancer 2	0.49	6.14	6.8	8.91	7.9	11.80	9.0	9.92	7.6
cancer 3	0.96	4.12	6.9	6.12	8.4	8.20	9.4	6.40	8.5
cancer 4	1.22	5.35	7.3	6.90	9.2	9.04	11.6	7.24	9.6

outcomes are compared with three existing despeckling algorithms, the anisotropic diffusion (AD) [393], Lee [211] and NLM [333] filters. For the quantitative analysis, the contrast-to-noise-ratio (CNR) and resolution loss (RL) are regrouped in Table 6.10. In Fig. 6.14, four US images are presented for visual demonstrations. Observation shows

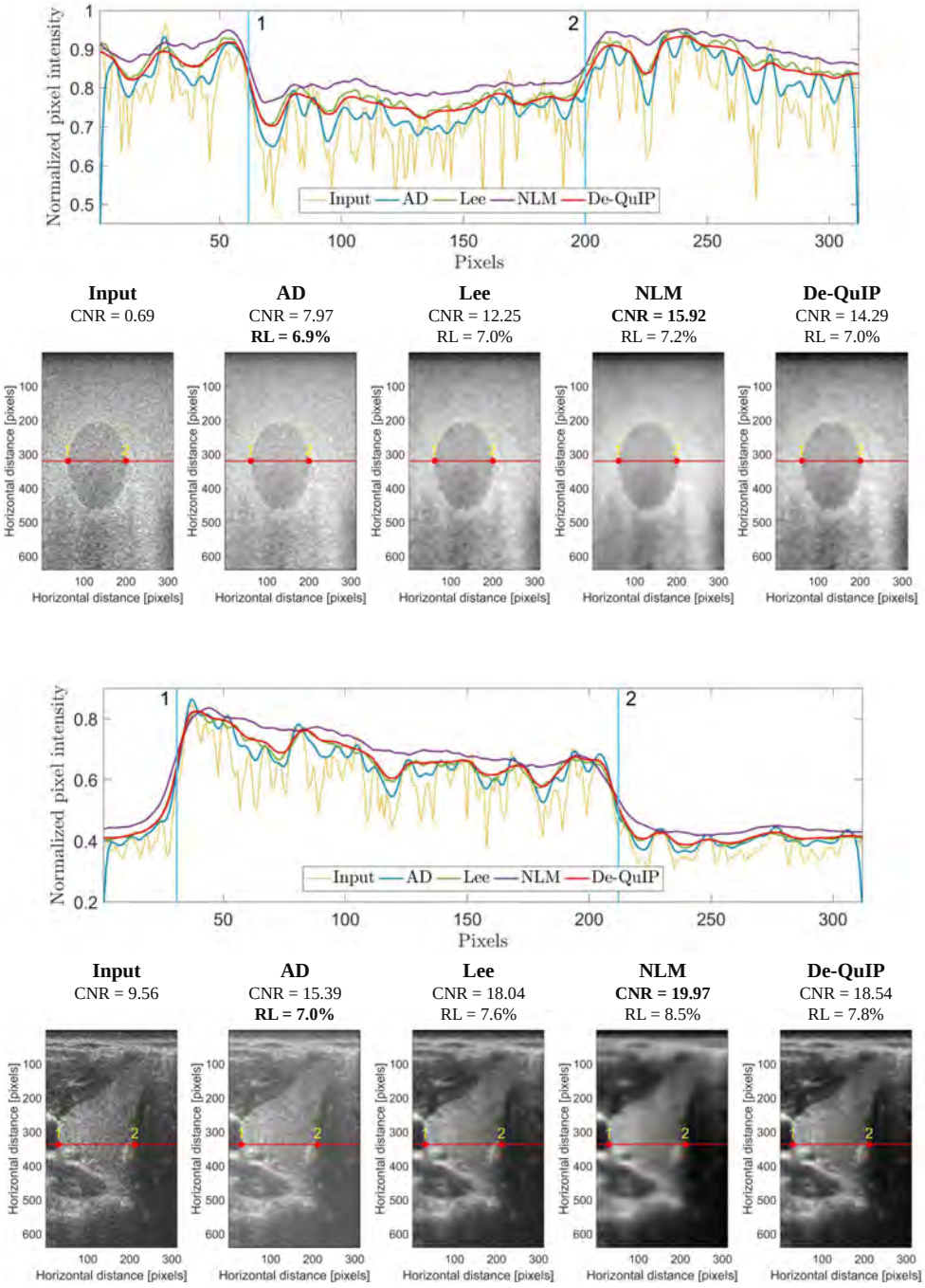

···Continued on next page.

· · · Continued from previous page.

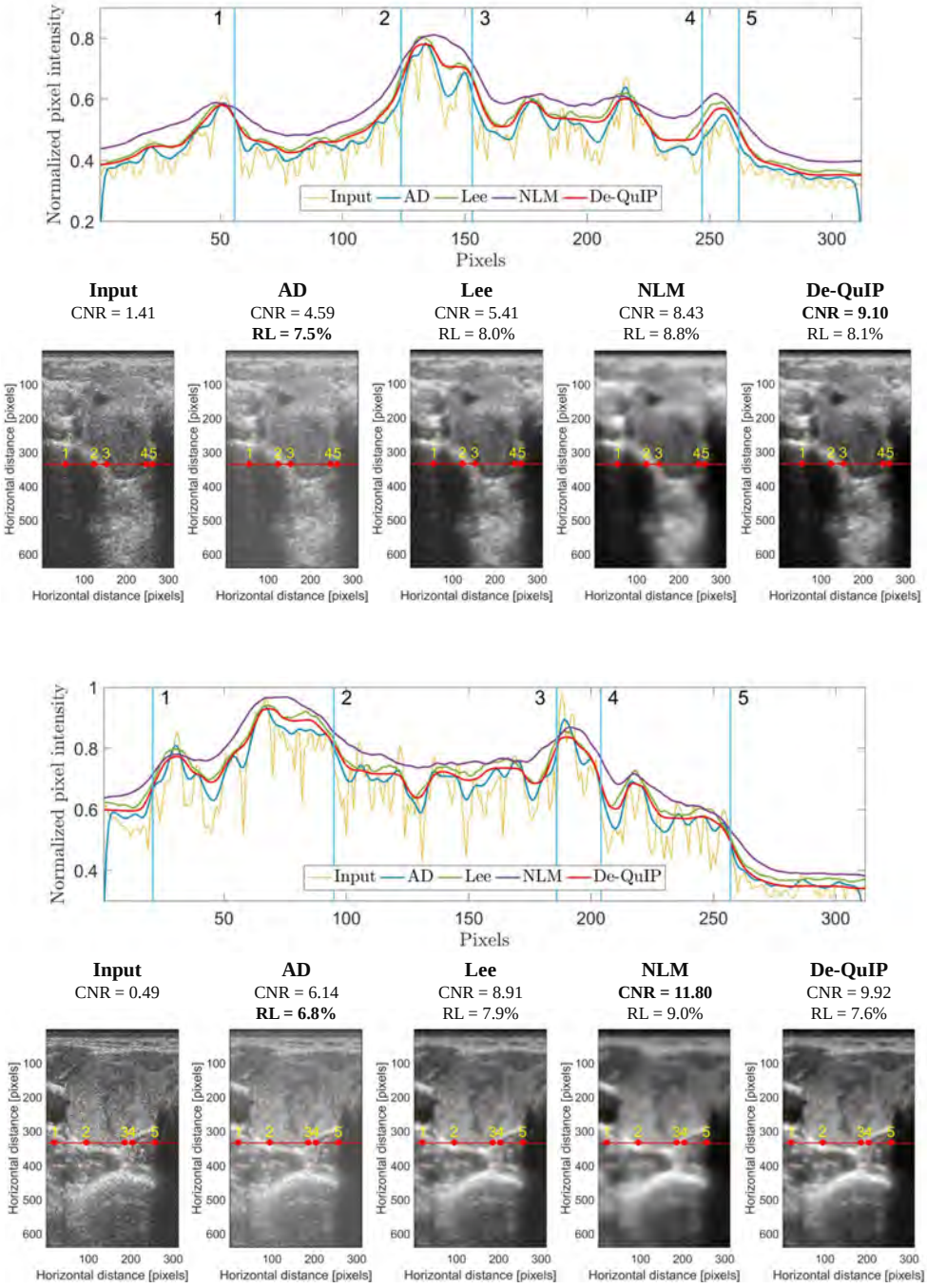

FIGURE 6.14. US image despeckling results using different methods. The first one is the phantom image, the second one is the non-cancer image, and the last two are associated with cancer images. The normalized pixel intensities of the extracted red lines from speckled and despeckled US images are shown.

that De-QuIP offers a better image contrast (higher CNR than AD, Lee and slightly lower than NLM, which over-smooths the images and yields poor resolution) while having less spatial resolution loss (De-QuIP has less spatial resolution loss compared to the native US image). Note that these images are chosen arbitrarily, that is, the quality of the results should not depend on the data tested.

6.6 Application to Clinical Dental Computed Tomography Image Super-Resolution

Medical image resolution, critical in number of clinical applications, is subject to physical limitations, such as the X-ray doses in the case of computed tomography (CT) considered herein. Therefore, enhancing spatial resolution in post-processing, referred to as super-resolution (SR) in the related literature, is an important research field. Most of the existing algorithms are based on modeling image degradation by specific operators such as blurring or downsampling, or on machine learning strategies requiring training databases. In this section, we focus on the first approach and in particular on algorithms exploiting the potential of image denoising in more complex image restoration tasks such as SR [286, 354]. More precisely, we propose two algorithms, both exploiting the De-QuIP denoiser and a computationally efficient way of handling simultaneously the decimation and blur operators based on their underlying properties in the Fourier domain within SR.

6.6.1 Image Super-Resolution Problem

The single image SR problem is a process of retrieval of an unknown high-resolution (HR) image $\boldsymbol{x} \in \mathbb{R}^{sN}$ from a noisy low-resolution (LR) and spatially decimated (by a factor $s > 1$) measurement $\boldsymbol{y} \in \mathbb{R}^{N}$, modeled as,

$$\boldsymbol{y} = \boldsymbol{S}\boldsymbol{G}\boldsymbol{x} + \boldsymbol{e}, \tag{6.13}$$

where $\boldsymbol{S} \in \mathbb{R}^{N \times sN}$ and $\boldsymbol{G} \in \mathbb{R}^{sN \times sN}$ are respectively the decimation and blurring/convolution operators, and $\boldsymbol{e} \in \mathbb{R}^{N}$ is an additive white Gaussian noise (AWGN). Note that $\boldsymbol{y}$, $\boldsymbol{x}$ and $\boldsymbol{e}$ are expressed in standard vectorized lexicographical order. $\boldsymbol{G}$ is assumed to be a block circulant matrix with circulant blocks (BCCB) for computation efficiency.

The maximum-a-posteriori (MAP) estimator formulates this highly ill-posed estimation problem as an optimization of a cost function formed by a data fidelity term

(quadratic herein given the Gaussian noise assumption) and a regularization term $g(\boldsymbol{x})$ resulting from an *a priori* statistical distribution of $\boldsymbol{x}$

$$\hat{\boldsymbol{x}} = \frac{1}{2}\arg\min_{\boldsymbol{x}} \ \|\boldsymbol{S}\boldsymbol{G}\boldsymbol{x} - \boldsymbol{y}\|_2^2 + \lambda g(\boldsymbol{x}), \tag{6.14}$$

where $\hat{\boldsymbol{x}}$ is the restored HR image and λ is a hyper-parameter. Therefore, a suitable prior based on strong assumptions about the HR image is crucial to obtain a reliable solution and leads to the question of the appropriate choice of this regularization term. Over the years, various regularization functions have been proposed in the literature, among which the most common are based on the sparsity of the HR image through an application-dependent transformation.

As an alternative to the explicit choice of the regularization, the Plug-and-Play (PnP) scheme [354] provides a way to turn an inverse problem into a chain of denoising processes and opens the possibilities for the existing state-of-the-art denoisers (*e.g.*, BM3D [82], TRND [71], etc.) to act as an underlying prior. Another scheme called Regularization by Denoising (RED) [286] follows similar principles. The good performance of these PnP and RED denoising engines [62, 77, 280, 281, 287, 330] as an underlying prior is discussed in Chapter 3 in detailed.

In this section we exploit these denoising engines using the De-QuIP denoiser to propose implicit regularization functions for solving the SR inverse problem expressed in (6.13). The following subsection introduce the main principle of De-QuIP denoiser and its implementation into SR PnP and RED algorithms.

6.6.2 Proposed Super-Resolution Algorithms using De-QuIP

6.6.2.1 Super-Resolution Plug-and-Play ADMM with De-QuIP

The PnP alternating direction method of multipliers (ADMM) scheme provides an elegant way to separate the problem (6.14) into an inversion step and a denoising process, where the latter is solved separately by an off-the-shelf denoiser. Thus the PnP scheme offers an intrinsic association between the regularization function and the denoising operator. Finding the MAP estimator (6.14) using ADMM with appropriate parameterization leads to the optimization problem:

$$\hat{\boldsymbol{x}} = \frac{1}{2}\arg\min_{\boldsymbol{x}} \ \|\boldsymbol{S}\boldsymbol{G}\boldsymbol{x} - \boldsymbol{y}\|_2^2 + \lambda g(\boldsymbol{v}), \ \text{ s.t. } \ \boldsymbol{x} = \boldsymbol{v}, \tag{6.15}$$

whose associated augmented Lagrangian function is,

$$\mathscr{L}_{(\boldsymbol{x},\boldsymbol{v},\boldsymbol{u})} = \frac{1}{2}\|\boldsymbol{S}\boldsymbol{G}\boldsymbol{x} - \boldsymbol{y}\|_2^2 + \lambda g(\boldsymbol{v}) + \frac{\beta}{2}\|\boldsymbol{x} - \boldsymbol{v} + \boldsymbol{u}\|_2^2, \tag{6.16}$$

where $\boldsymbol{u}$ and β are the Lagrangian multipliers and penalty parameter respectively. After variable splitting, we obtain:

$$\boldsymbol{x}^{k+1} = \arg\min_{\boldsymbol{x}} \|\boldsymbol{SGx} - \boldsymbol{y}\|_2^2 + \frac{\beta}{2}\left\|\boldsymbol{x} - \boldsymbol{v}^k + \boldsymbol{u}^k\right\|_2^2 \tag{6.17a}$$

$$\boldsymbol{v}^{k+1} = \arg\min_{\boldsymbol{v}} \ \lambda g(\boldsymbol{v}) + \frac{\beta}{2}\left\|\boldsymbol{x}^{k+1} - \boldsymbol{v} + \boldsymbol{u}^k\right\|_2^2 \tag{6.17b}$$

$$\boldsymbol{u}^{k+1} = \boldsymbol{u}^k + \boldsymbol{x}^{k+1} - \boldsymbol{v}^{k+1} \tag{6.17c}$$

Note that the first step (6.17a) has a closed-form solution as,

$$\boldsymbol{x}^{k+1} = \left(\boldsymbol{G}^H\boldsymbol{S}^H\boldsymbol{SG} + \beta\boldsymbol{I}\right)^{-1}\left(\boldsymbol{G}^H\boldsymbol{S}^H\boldsymbol{y} + \beta(\boldsymbol{v}^k - \boldsymbol{u}^k)\right), \tag{6.18}$$

Since $\boldsymbol{G}$ is BCCB, $\boldsymbol{G} = \boldsymbol{F}^H\boldsymbol{\Lambda}\boldsymbol{F}$ and $\boldsymbol{G}^H = \boldsymbol{F}^H\boldsymbol{\Lambda}^H\boldsymbol{F}$. Here $\boldsymbol{F}$ and $\boldsymbol{F}^H$ are respectively the Fourier and inverse Fourier transformations, $\boldsymbol{G}^H$ and $\boldsymbol{S}^H$ are associated with the conjugate transpose of $\boldsymbol{G}$ and $\boldsymbol{S}$, $\boldsymbol{\Lambda}$ is a diagonal matrix, whose diagonal elements are the Fourier transformation of the first column of $\boldsymbol{G}$, and $\boldsymbol{I} \in \mathbb{R}^{sN\times sN}$ is the identity matrix. Besides, it is worth mentioning that the decimation operator $\boldsymbol{S}$ prevents this analytical solution to be implemented efficiently in the Fourier domain. Consequently, most existing methods use a gradient descent algorithms to solve (6.18). However, following the work in [416], (6.18) maybe rewritten as,

$$\boldsymbol{x}^{k+1} = \boldsymbol{F}^H\left(\frac{1}{s}\underline{\boldsymbol{\Lambda}}^H\underline{\boldsymbol{\Lambda}} + \beta\boldsymbol{I}\right)^{-1}\boldsymbol{F}\left(\boldsymbol{G}^H\boldsymbol{S}^H\boldsymbol{y} + \beta(\boldsymbol{v}^k - \boldsymbol{u}^k)\right) \tag{6.19}$$

where $\underline{\boldsymbol{\Lambda}} \in \mathbb{C}^{N\times sN}$ is defined as $\underline{\boldsymbol{\Lambda}} = [\boldsymbol{\Lambda}_1, \boldsymbol{\Lambda}_2, \cdots, \boldsymbol{\Lambda}_s]$ and the blocks $\boldsymbol{\Lambda}_j \in \mathbb{C}^{N\times N}$ for $j = 1, 2, \cdots, s$ obey $\text{diag}\{\boldsymbol{\Lambda}_1, \boldsymbol{\Lambda}_2, \cdots, \boldsymbol{\Lambda}_s\} = \boldsymbol{\Lambda}$, which ensures a direct computational effective implementation to solve (6.18).

Moving to eq. (6.17b), that is associated with the denoising of the noisy image $\tilde{\boldsymbol{v}}^k = \boldsymbol{x}^{k+1} + \boldsymbol{u}^k$. Hence, following the PnP method we can apply the De-QuIP denoiser $\mathscr{D}$ (symbolic notation) for solving step (6.17b), this leads to

$$\boldsymbol{v}^{k+1} = \mathscr{D}\left(\tilde{\boldsymbol{v}}^k\right). \tag{6.20}$$

6.6.2.2 Super-Resolution Regularization by denoising with De-QuIP

The RED scheme [286] is an alternative to PnP ADMM which allows integration of denoising algorithms in more complex image restoration tasks such as SR. Unlike PnP, RED proposes an explicit construction of the regularization function of the form of an image-adaptive Laplacian based on an external denoiser. This regularization function

uses the inner product between the image and its denoising residual. Thus, considering De-QuIP denoiser $\mathscr{D}$ as the denoising operator, the associated RED-prior function is defined as $g(\boldsymbol{x}) = \frac{1}{2}\boldsymbol{x}^T(\boldsymbol{x} - \mathscr{D}(\boldsymbol{x}))$, and leads to, $\nabla g(\boldsymbol{x}) = (\boldsymbol{x} - \mathscr{D}(\boldsymbol{x}))$, *i.e.*, the gradient of the RED-prior is the denoising residual [286].

Similarly to the PnP scheme in Section 6.6.2.1, an ADMM-based algorithm can be designed to find the MAP estimator in (6.14) for the RED regularization function. The associated augmented Lagrangian function becomes

$$\mathscr{L}_{(\boldsymbol{x},\boldsymbol{v},\boldsymbol{u})} = \frac{1}{2}\|\boldsymbol{SG}\boldsymbol{x} - \boldsymbol{y}\|_2^2 + \frac{\lambda}{2}\boldsymbol{v}^T(\boldsymbol{v} - \mathscr{D}(\boldsymbol{v})) + \frac{\beta}{2}\|\boldsymbol{x} - \boldsymbol{v} + \boldsymbol{u}\|_2^2, \tag{6.21}$$

which leads to following iterative scheme:

$$\boldsymbol{x}^{k+1} = \arg\min_{\boldsymbol{x}} \|\boldsymbol{SG}\boldsymbol{x} - \boldsymbol{y}\|_2^2 + \frac{\beta}{2}\left\|\boldsymbol{x} - \boldsymbol{v}^k + \boldsymbol{u}^k\right\|_2^2, \tag{6.22a}$$

$$\boldsymbol{v}^{k+1} = \arg\min_{\boldsymbol{v}} \frac{\lambda}{2}\boldsymbol{v}^T(\boldsymbol{v} - \mathscr{D}(\boldsymbol{v})) + \frac{\beta}{2}\left\|\boldsymbol{x}^{k+1} - \boldsymbol{v} + \boldsymbol{u}^k\right\|_2^2, \tag{6.22b}$$

$$\boldsymbol{u}^{k+1} = \boldsymbol{u}^k + \boldsymbol{x}^{k+1} - \boldsymbol{v}^{k+1}. \tag{6.22c}$$

Notice that the step (6.22a) has the same analytical solution of the form (6.19) following the derivations proposed in [416]. Also, considering the property of RED gradient the second step (6.22b) leads to the following solution,

$$\boldsymbol{v}^{k+1} = \frac{1}{\lambda + \beta}\Big(\lambda\mathscr{D}(\boldsymbol{v}^k) + \beta(\boldsymbol{x}^{k+1} + \boldsymbol{u}^k)\Big), \tag{6.23}$$

where $\mathscr{D}$ represents the quantum adaptive denoiser De-QuIP.

6.6.3 Experimental Results on Clinical Dental Computed Tomography Images

This subsection regroups experiments of SR image reconstruction using the proposed algorithms PnP with De-QuIP and RED with De-QuIP, respectively denoted by PnP-De-QuIP and RED-De-QuIP, on dental CT data. In dental applications, cone beam CT (CBCT) is increasingly used in clinics, but suffers from low spatial resolution because of low X-ray dose requirements, for particular application such as endodontics that concerns the root canal. In this work, μCT, only available for extracted teeth given the small tube and the high radiation dose, is used to obtain the ground truth.

Three methods from the literature have been used to evaluate the efficiency of the proposed methods: i) a fast SR algorithm with total variation regularization [416] denoted

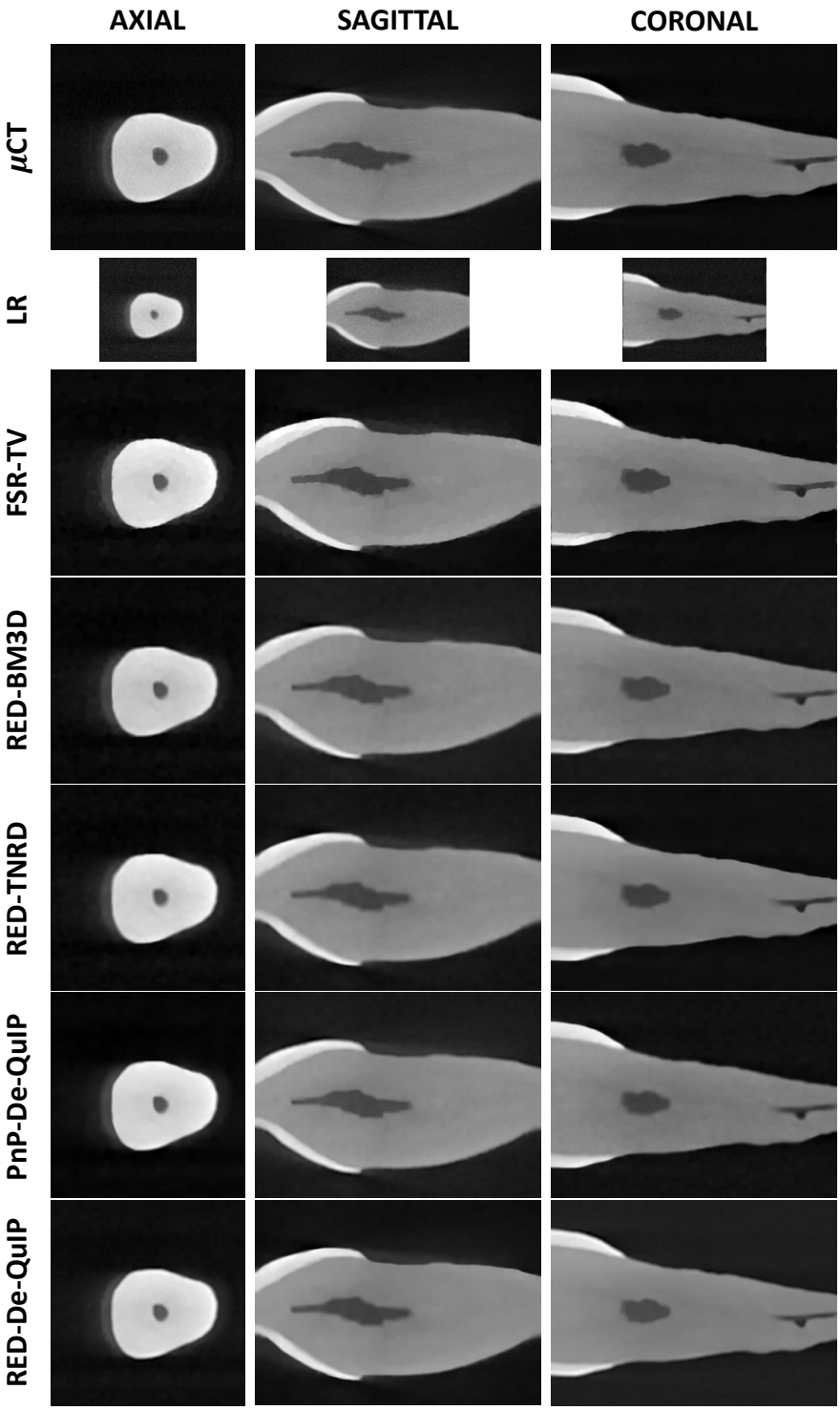

FIGURE 6.15. Restored μCT tooth images from axial, sagittal and coronal slices. The dark region inside the tooth corresponds to the canal root.

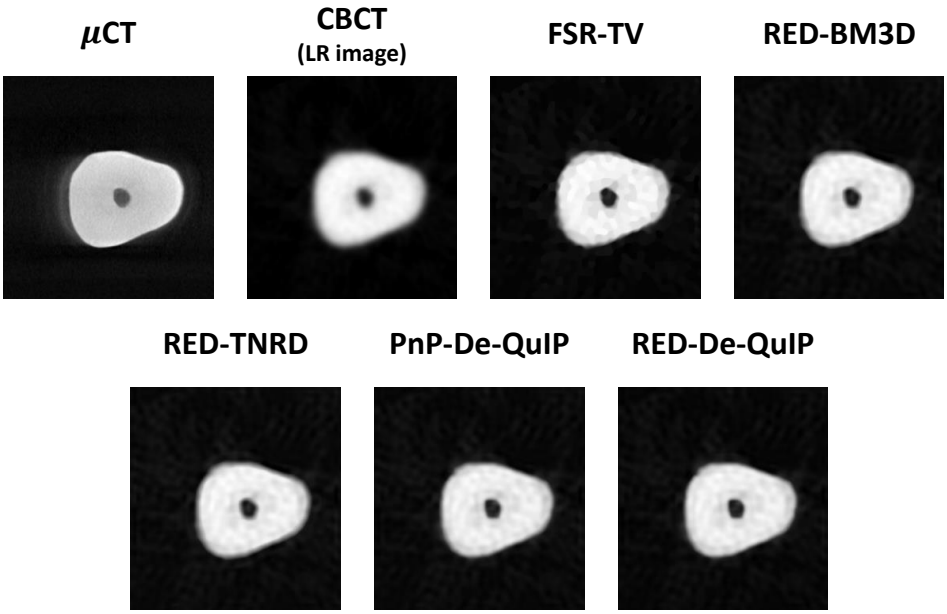

FIGURE 6.16. Restored CBCT tooth image from axial slice. The dark region inside the tooth corresponds to the canal root.

by FSR-TV, ii) the RED algorithm using BM3D denoiser [77] denoted by BM3D-RED, iii) RED algorithm using a convolutional neural network-based flexible learning denoising method, known as the trainable nonlinear reaction diffusion (TNRD) denoiser [286], referred as TNRD-RED.

The first experiment consists of three synthetic LR images created from the μCT dataset by using a 9×9 Gaussian blurring kernel with std of 3, decimation factor of 2 in each spatial direction, and contamination by an AWGN corresponding to blurred-signal-to-noise-ratio (BSNR) of 20 dB (Fig. 6.15). Within the second experiment, CBCT images were considered as the LR input of the SR algorithms. In this case, the ground truth is not directly available but was assimilated to μCT images acquired on the same tooth, given their very good spatial resolution and SNR (Fig. 6.16). Note that the point spread function, unknow for this experiment, was estimated from the CBCT image itself and approximated by a Gaussian kernel with std 6.2, 0.4 and 3.3 respectively for the axial, sagittal and coronal slices. Table 6.11 depicts the resulting peak-signal-to-noise-ratio (PSNR) and structure similarity (SSIM) of the restored μCT and CBCT images. The results show a slight gain in PSNR and SSIM compared to FSR-TV and RED-BM3D, and are comparable with RED-TNRD. The restored HR μCT and CBCT images are presented in Fig. 6.15 and Fig. 6.16 respectively. The displayed results justify the potential of the

TABLE 6.11. Quantitative SR results for dental tomography images. The best values are highlighted in bold.

	Methods	Output	Tooth Image Slices		
			Axial	Sagittal	Coronal
μCT	FSR-TV	PSNR(dB)	39.67	39.90	38.95
		SSIM	0.969	0.973	0.981
	RED-BM3D	PSNR(dB)	40.36	39.44	39.92
		SSIM	0.973	0.972	0.982
	RED-TNRD	PSNR(dB)	40.61	**40.05**	**40.88**
		SSIM	0.973	**0.974**	**0.983**
	PnP-De-QuIP	PSNR(dB)	40.68	39.96	40.63
		SSIM	**0.974**	**0.974**	**0.983**
	RED-De-QuIP	PSNR(dB)	**40.75**	39.98	40.71
		SSIM	**0.974**	**0.974**	**0.983**
CBCT	FSR-TV	PSNR(dB)	21.22	23.20	23.01
		SSIM	0.764	0.895	0.891
	RED-BM3D	PSNR(dB)	21.78	22.87	23.03
		SSIM	0.808	0.895	0.897
	RED-TNRD	PSNR(dB)	21.99	**23.60**	**23.39**
		SSIM	0.825	**0.899**	**0.899**
	PnP-De-QuIP	PSNR(dB)	22.07	23.42	23.37
		SSIM	0.829	0.898	**0.899**
	RED-De-QuIP	PSNR(dB)	**22.15**	23.56	**23.39**
		SSIM	**0.834**	**0.899**	**0.899**

proposed SR algorithms for enhancing the CBCT images, particularly for enhancing the region of interest, the dark region in the middle of the tooth, which is the canal root.

6.7 Conclusions

A novel image denoising algorithm inspired by the quantum many-body theory has been developed in this chapter. This gives a way to adapt the concept of interaction from the many-body physics to an imaging problem. More precisely, the interactions between image patches are nothing more than a reflection of the similarity-measures in a local image neighborhood and provide an efficient way to capture the local structures of real images. Through these interactions, structural details are transmitted on a patch-based adaptive basis created by the solutions of the Schrödinger equation of quantum mechanics, which can be exploited as filters for denoising the patches. The versatile nature of the adaptive basis that conveys the structural similarities of image

neighborhood, extends its scope of applications beyond AWGN without modification.

A rigorous comparison with contemporary methods exemplifies the denoising ability of our De-QuIP algorithm regardless of the image nature, noise statistics and intensity. Simulation results demonstrate that the proposed method clearly outperforms other schemes and gives a good comparison with the best outcome for both image independent and dependent noise models. Additionally, De-QuIP achieves much better results at a significantly less computational cost in comparison with the earlier single-particle based quantum scheme of Chapter 4. To make De-QuIP more robust, automated rules are discussed in this chapter to efficiently select the values of the hyperparameters close to the optimal ones when less information is available.

In real-life problems, De-QuIP shows good performance, for example in medical US image despeckling applications demonstrates its ability in handling multiplicative noise efficiently. Furthermore, we proposed two new SR algorithms combining the adaptive quantum denoiser De-QuIP and an analytical solution of the inversion step. This property increases the denoiser's efficiency while acting as a PnP or RED prior in a SR problem. Comparisons with standard techniques justify the potential of the proposed schemes in clinical dental computed tomography imaging applications.

6.7.1 Limitations

In this chapter, we have made a comprehensive study to optimize the relevant hyperparameter values and proposed automatic rules to tune them efficiently based on some physical intuitions. Despite these observations to guide the choice of hyperparameters, they are generally limited to the whole image and cannot be exploited patch-wise. It raises the question of using different hyperparameter values for different patches due to the nonlocal structure of the De-QuIP algorithm. Furthermore, patch-dependent hyperparameters may further enhance the adaptability of De-QuIP. In Chapter 7, we will address this issue.

6.7.2 Perspectives

Adaptation of this new quantum many-body idea opens up a new domain of future explorations. Since De-QuIP primarily has a non-local nature and significantly outperforms contemporary NLM-based methods, the first obvious perspective comes from the extension of this idea of interactions for collaborative patch denoising, as originally proposed in [82].

A second interesting point would be to embed this interaction architecture into a convolutional neural network, as explored with various schemes, such as a fast flexible learning method [71, 407], residual learning [405] and others, and study imaging problems through this many-body network where each node shows interaction with others. We will study this aspect in Chapter 7.

Further expansion of the framework in three dimensional data or RGB color images can be easily done by simply bypassing data across different processing channels. Finally, this work could be extended to other medical imaging problems, for example to 3D SR problems with image-dependent noise models, and one can also investigate the theoretical analysis of the method in the context of PnP and RED.

CHAPTER 7

DEEP UNFOLDED NETWORK FROM QUANTUM INTERACTIVE PATCHES FOR IMAGE RESTORATION

Contents

* This chapter presents materials from the submitted journal paper [116] and conference papers [115, 118].

Overview

This chapter presents a deep neural network called DIVA unfolding a baseline adaptive denoising algorithm (De-QuIP), relying on the theory of quantum many-body physics. Furthermore, it is shown that with very slight modifications, this network can be enhanced to solve more challenging image restoration tasks such as image deblurring, super-resolution and inpainting. Despite a compact and interpretable (from a physical perspective) architecture, the proposed deep learning network outperforms several recent algorithms from the literature, designed specifically for each task. The key ingredients of the proposed method are on one hand, its ability to handle non-local image structures through the patch-interaction term and the quantum-based Hamiltonian operator, and, on the other hand, its flexibility to adapt the hyperparameters patch-wisely, due to the training process. Finally, we show the ability of our approach to deal with clinical cardiac ultrasound images enhancement applications.

7.1 Introduction

7.1.1 Image Restoration Problem

Restoring a high-quality image from a degraded observation is a classic but still major challenge in imaging applications, such as medical imaging, remote sensing, low-level vision, surveillance, to cite few. Such a degradation process can be formulated as

$$\boldsymbol{Y} = \boldsymbol{O}\boldsymbol{X} + \boldsymbol{e}, \tag{7.1}$$

where, $\boldsymbol{Y}$ and $\boldsymbol{X}$ are the low quality observation and the underling true image respective, respectively, the degradation operator is $\boldsymbol{O}$, and $\boldsymbol{e}$ is associated with an additive noise. The Chapter 3 explains that the nature of the degradation operator $\boldsymbol{O}$ sets the tone of the restoration process of the latent high-quality image $\boldsymbol{X}$. More precisely, we get a denoising [82, 100, 106, 123], deblurring [58, 72, 84, 385] or super-resolution (SR) [141, 252, 416] problem if $\boldsymbol{O}$ is an identity, a blurring or a subsampling operator, respectively. In practice, the estimation of the latent image $\boldsymbol{X}$ from a degraded observation by neutralizing operator $\boldsymbol{O}$'s effects is a challenging ill-posed inverse problem and has been extensively studied over the years, yet remains an active field of research.

7.1.2 Related Works

Traditionally, the restoration process is framed as a model-based optimization problem from a Bayesian perspective, in which the desired solution is obtained by minimizing the sum of a regularization and a data fidelity term [10, 106, 123, 236, 260]. Later, data-driven non-local self-similarity (NLSS) filters [49, 82, 109, 197, 340, 394], in particular, non-local regularization approaches [102, 103, 328, 335] blending the NLSS and low-rank regularity, dominated the field due to their state-of-the-art restoration performances. However, these schemes require conducting a costlier computation process and manual tuning of several hyperparameters, which are the primary challenges of these strategies.

Based on deep convolutional neural networks (CNN), deep-learning (DL)-based strategies brought an alternative to the well-established model-based methods to counter such imaging problems [22, 96, 101, 301, 398, 405] and have proven efficiency in image restoration over the conventional model-based approaches, exploiting a training dataset in the learning process. However, a CNN network performance largely depends on the number of layers, the kernel size and the learning rate. Indeed, deeper network structures may provide better results but exponentially increase the training complexity

[162]. Thus, network structures are in most cases determined empirically, which makes them suffer from a lack of interpretation of their true functionality.

Very recently a new concept, known as unfolding [151], is gaining more attention due to its explanatory properties, while exploiting the computation power of CNN architecture. Gathering the advantages of both model and DL-based approaches, this framework constructs a DL network starting from a classical algorithm and has recently been successfully explored in the literature, leading to superior restoration performance over the classical methods [194, 212, 300, 313, 383].

7.1.3 Contributions

In this chapter, we advocate novel CNN architectures for image restoration problems, unfolding our recently introduced quantum mechanics-based adaptive denoising algorithm called De-QuIP in Chapter 6. It is shown that despite the promising performances in imaging domain, the quantum-single-particle-based frameworks cannot benefit from the structural features of the image like NLSS algorithms. In contrast, De-QuIP is based on the theory of many-body quantum systems, where each image patch behaves like a single particle system and interacts with its neighbors. This phenomenon of interaction preserves the image similarity/features from a local neighborhood. Indeed, use of this concept of interaction in De-QuIP brings an intrinsic non-local structure to the algorithm that notably enhances the denoising performance and has been extensively studied in Chapter 6. Despite its interesting performances, De-QuIP suffer from costly computational processes (*e.g.*, hyperparameters tuning and eigenvalue decomposition) like many other model-based schemes, which may limit its practical use.

In this chapter, we introduce a novel DL network unfolding the baseline De-QuIP algorithm, denoted as DIVA (Deep denoising by quantum InteractiVe pAtches) for image denoising problem. We further extend the network architecture to conduct a general image restoration task. The inclusion of the quantum interaction theory brings a non-local structure to the proposed CNN architecture. Indeed, in our depicted DL models, the fundamental aspects of quantum theory from the baseline De-QuIP algorithm are essentially preserved. Furthermore, the DL model efficiently resolves the hyperparameter tuning problem of the original De-QuIP scheme, harnessing the power of back-propagation. The integration of the key attributes of DL and quantum theory significantly enhances the functionality of our proposed networks due to their intrinsic versatility and enables our models to exhibit state-of-the-art performances for several restoration tasks. Herein, we present a robust generalized formalism by incorporating additional features in signif-

icant ways: (i) we initially propose a DL model, primarily designed for denoising, and further extend it to more complex image restoration tasks such as deblurring, super-resolution and inpainting, with a resilient generalized network architecture; (ii) we conduct a detailed investigation regarding the network diagram and add considerable analysis of the incorporated quantum background, tunable parameter number, and run time; (iii) we report a comprehensive survey of image restoration performance against benchmark methods for various imaging problems; (iv) we also conduct experiments with clinical cardiac ultrasound (US) images to demonstrate our model ability in real medical applications.

The remainder of the chapter is organized as follows. Section 7.2 reminds briefly the concepts of the baseline De-QuIP algorithm for self-consistency reasons. Section 7.3 first presents the proposed DIVA network for denoising and then extends it to an advanced model for other imaging tasks. The experimental settings and extensive evaluations are reported in Section 7.4. Section 7.5 summarizes findings related to clinical US image contrast enhancement problems. Section 7.6 outlines the overall remarks and possible future perspectives. Finally, Section 7.7 draws the conclusions.

7.2 Brief Review of Quantum Interactive Patches-Based Denoising

To facilitate the understanding of the proposed method, we briefly revisit the baseline De-QuIP algorithm as proposed in Chapter 6 for image denoising and its main properties.

7.2.1 The De-QuIP Scheme

Built on an underlying nonlocal architecture, De-QuIP offers an adaptive way of image denoising based on the theory of quantum many-body interaction. The theory of quantum many-body physics describes many-body quantum systems, where generally particle-to-particle interactions emerge. De-QuIP provides a framework for extending this concept of interaction to imaging problems. Effectively, De-QuIP divides an image into small patches, and each image patch acts as a single-particle system while interacting with its neighbors, *i.e.*, with neighboring patches, inside the whole image, similarly to a many-body system. Indeed, these interactions between neighbors reflect their mutual similarities that enhance the denoising performance of De-QuIP significantly.

Similar to any denoising method, the goal is to estimate the underlying clean image $\boldsymbol{X} \in \mathbb{R}^{M\times N}$ from a noisy observation $\boldsymbol{Y} \in \mathbb{R}^{M\times N}$. The respective vectorized representations of $\boldsymbol{X}$ and $\boldsymbol{Y}$ are denoted by $\boldsymbol{x} \in \mathbb{R}^{MN}$ and $\boldsymbol{y} \in \mathbb{R}^{MN}$ in lexicographical order. Based on the many-body quantum physics, the primary idea of De-QuIP algorithm is to construct an adaptive transformation using the wave solutions of the Schrödinger equation $H\boldsymbol{\psi}(z) = E\boldsymbol{\psi}(z)$, where the wave function $\boldsymbol{\psi}(z)$ describes a particle with energy E in a potential V, z being the spatial coordinate. In a many-body system, denoting by I the interaction, the Hamiltonian operator is $H = -(\hbar^2/2m)\nabla^2 + V + I$, where ∇ and $(\hbar^2/2m)$ are respectively the gradient operator and a function of the Planck's constant (this function acts as a hyperparameter in this formalism). For this patch-based imaging scheme, the potential V is represented by the original pixels' values of the image patch and the patch-similarity measures act as the interaction I. The set of eigenvectors of the Hamiltonian operator gives the adaptive transformations for the respective patch. Thus, for a system with multiple particles, the Hamiltonian operator $\boldsymbol{H}_a$ for the a-th patch is defined by:

$$\boldsymbol{H}_a = -\frac{\hbar^2}{2m}\nabla^2 + \boldsymbol{J}_a + \boldsymbol{I}_a, \tag{7.2}$$

where $\boldsymbol{J}_a$ and $\boldsymbol{I}_a$ are respectively the pixels' values and interaction term for the a-th patch. The corresponding set of eigenvectors $\boldsymbol{B}_a$ of $\boldsymbol{H}_a$ acts as the quantum adaptive basis for the a-th patch. The key steps of De-QuIP algorithm are as follows.

- ***Patch extraction:*** The patch extraction step primarily uncoils small patches from the observed image and assimilates their neighbors into their respective local groups. Let us denote by $\boldsymbol{J}_a$ a patch of size n^2 whose upper-left pixel position is a, and by Ω the set containing all such patches extracted from the image $\boldsymbol{y}$. For all $\boldsymbol{J}_a \in \Omega$, one creates a window of size $W \times W$ centered on $\boldsymbol{J}_a$ and accumulates all patches inside the window in a set denoted by $S_{\boldsymbol{J}_a}$ to create local groups.

- ***Total interaction:*** The goal of the interaction step is to preserve local structures/similarities by exploiting the local groups through a notion akin to the interactions in quantum mechanics. This step computes the interactions $\boldsymbol{L}_{ab}$, for all $\boldsymbol{J}_b \in S_{\boldsymbol{J}_a}$ and all $\boldsymbol{J}_a \in \Omega$, using power laws of physics, *i.e.*, interaction is linearly proportional to the pixel-wise difference $\boldsymbol{K}_{ab}^k = |\boldsymbol{J}_a^k - \boldsymbol{J}_b^k|$ for $k = 1, \cdots, n^2$ and inversely proportional to the square of the Euclidean distance D_{ab} between the patches. Summing over b gives the total interaction for the a-th patch

$$\boldsymbol{I}_a = p\sum_b \boldsymbol{L}_{ab} = p\sum_b \frac{\boldsymbol{K}_{ab}}{D_{ab}^2}, \quad \forall \boldsymbol{J}_a \in \Omega. \tag{7.3}$$

In this construction the proportionality constant p acts as a hyperparameter.

- ***Hamiltonian operator and adaptive basis:*** This step formulates the energy or Hamiltonian operators of the extracted patches by incorporating their total interaction with their neighbors in the local group using (7.2). The associated set of eigenvectors $\boldsymbol{B}_a$ of the Hamiltonian operator $\boldsymbol{H}_a$ operates as the adaptive basis for the current image patch $\boldsymbol{J}_a$.

- ***Thresholding:*** The thresholding is processed on the coefficients resulting from patch projections onto their respective adaptive basis. Hence, the noise is attenuated by projecting $\boldsymbol{J}_a$ onto $\boldsymbol{B}_a$ and performing hard/soft-thresholding $\mathscr{T}$ in energy. Finally, reverse projecting the truncated coefficients reinstates the denoised patch $\hat{\boldsymbol{J}}_a, \forall \boldsymbol{J}_a \in \Omega$.

- ***Patch accumulation:*** This step accumulates all the denoised patches to their original positions and normalizes them to reconstruct the estimated denoised image $\hat{\boldsymbol{x}}$. In the following, the patch extractor operator is denoted by $\boldsymbol{E}$, while the operation of accumulating the patches to form the denoised image is denoted by $\boldsymbol{E}^{-1}$.

In the De-QuIP framework, the preserved spatial information by the patch interaction phenomenon coherently passes through the Hamiltonian operator to the quantum adaptive basis and enables the algorithm to handle denoising tasks regardless of the noise intensity, statistics and image nature. Its application field is not limited to denoising tasks, and its efficiency has been illustrated in various imaging problems such as despeckling and super-resolution as shown in Chapter 6. Fig. 7.1(a) depicts the De-QuIP architecture, where interaction, proportionality constant, adaptive basis and thresholded coefficients are denoted by $\boldsymbol{L}$, $\boldsymbol{P}$, $\boldsymbol{B}$ and $\boldsymbol{R}$ respectively.

7.2.2 Shortcomings of De-QuIP

The major challenge of De-QuIP is its high computational cost of tuning the hyperparameters p, $(\hbar^2/2m)$ and energy threshold. In Chapter 6, the influence of these hyperparameters and strategies to optimize their values were discussed. Despite some rules that guided the choice of the hyperparameters, they remain general for the whole image and are not optimized to be applied patch-wise. Although De-QuIP demonstrates favorable outcomes despite these drawbacks, the intrinsic non-local architecture of the algorithm raises an obvious question of assigning patch-dependent hyperparameter values, which

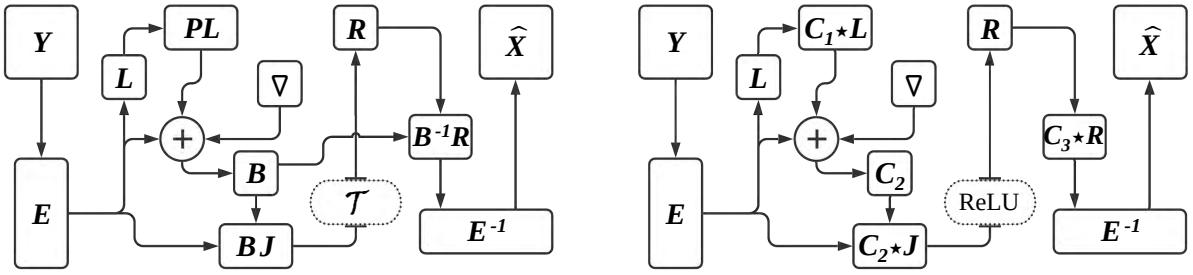

(a) De-QuIP algorithm (b) Deep unfolding of De-QuIP algorithm

FIGURE 7.1. Architectural comparison between De-QuIP and its DL counterpart.

can further enhance the adaptability of the model. However, manually tuning all the hyperparameters separately for each patch is practically impossible. The power of DL architecture removes this barrier by involving many parameters that can be learned during the training process.

Another challenge of De-QuIP is the computationally-expensive task of adaptive basis vector computation from the Hamiltonian operator. Furthermore, this adaptive basis is exploited to calculate the projection coefficients, bringing additional computational burden. A deep learning model can bypass all these bottlenecks by directly estimating the projection coefficients with the help of convolutional kernels. The subsequent section focuses on this deep-learning prospect of the De-QuIP algorithm, the main contribution of this chapter.

7.3 Proposed Deep Architectures for Image Restoration

This section presents deep unfolding strategies for image restoration problems built on the baseline De-QuIP algorithm. Depending on the image degradation operator $\boldsymbol{O}$, various imaging problems arise. If $\boldsymbol{O}$ is an identity operator, the image restoration problem is equivalent to a denoising task, whereas, depending on $\boldsymbol{O}$, it may turn into deblurring, super-resolution or inpainting, addressed herein. In the following, two deep architectures are introduced: the first addresses denoising, and the second more complex image restoration tasks. The first proposed network, referred to as DIVA, is a direct translation of the baseline De-QuIP algorithm into a deep learning model to handle denoising. To handle non-identity degradation operators $\boldsymbol{O}$, DIVA architecture is slightly

modified and denoted by DIVA advanced (DIVA-A). The subsequent subsections illustrate these two network architectures.

7.3.1 Proposed DIVA Architecture

The main idea behind the proposed unfolding strategy is to replace the matrix multiplication steps in De-QuIP by convolution layers. The analogy between the original algorithm and its unfolded version is illustrated in Fig. 7.1. The proposed DIVA network primarily stands upon eight main pillars.

- ***Extraction layer:*** Similar to the De-QuIP algorithm, the extraction layer in DIVA assembles all patches from a local window of size $W \times W$ centered at $\boldsymbol{J}_a$ in a local patch-group denoted as $S_{\boldsymbol{J}_a}, \forall \boldsymbol{J}_a \in \Omega$. Let the cardinality of $S_{\boldsymbol{J}_a}$ be κ, $\forall \boldsymbol{J}_a \in \Omega$ and ζ be the cardinality of Ω. The patch extraction operation from the local window can be defined as a matrix multiplication by $\boldsymbol{E}_{\boldsymbol{J}_a} \in \mathbb{R}^{n^2\kappa \times MN}$ for each $\boldsymbol{J}_a$. Therefore, mathematically, $\boldsymbol{G}_{\boldsymbol{J}_a} = \boldsymbol{E}_{\boldsymbol{J}_a}\boldsymbol{y}$, where $\boldsymbol{G}_{\boldsymbol{J}_a} \in \mathbb{R}^{n^2\kappa}$ is the concatenated vectorized local patch group for each $\boldsymbol{J}_a$. Thus, for the whole image, the patch extractor operator $\boldsymbol{E} \in \mathbb{R}^{\zeta n^2\kappa \times MN}$ is constructed by concatenating $\boldsymbol{E}_{\boldsymbol{J}_a} \in \mathbb{R}^{n^2\kappa \times MN}$ $\forall \boldsymbol{J}_a \in \Omega$. Finally, $\boldsymbol{J}_a$ and $\boldsymbol{G}_{\boldsymbol{J}_a}$ $\forall \boldsymbol{J}_a \in \Omega$ are concatenated and reshaped to construct matrices $\boldsymbol{J} \in \mathbb{R}^{\zeta \times n^2}$ and $\boldsymbol{G} \in \mathbb{R}^{\zeta \times n^2\kappa}$, further considered as inputs for the next layer.

- ***Interaction layer:*** This layer computes the interactions between patches for each local group $\boldsymbol{G}_{\boldsymbol{J}_a}$ following the power laws discussed in Sec. 7.2.1. But rather than considering a fixed hyperparameter value p as in (7.3), for each local group $\boldsymbol{G}_{\boldsymbol{J}_a}$ a different set of p_{ab}^k values is assigned for each pixel k ($k = 1, \cdots, n^2$) and patch b ($b = 1, \cdots, \kappa; \neq a$) respectively. Therefore, the total interaction can be expressed as

$$\boldsymbol{I}_a^k = \sum_{b=1, b\neq a}^{\kappa} p_{ab}^k \frac{\boldsymbol{K}_{ab}^k}{D_{ab}^2} = \sum_{b=1, b\neq a}^{\kappa} p_{ab}^k \boldsymbol{L}_{ab}^k, \text{for each } \boldsymbol{G}_{\boldsymbol{J}_a}. \tag{7.4}$$

  In matrix notation, $\boldsymbol{I}_a = \boldsymbol{P}_{ab}\boldsymbol{L}_{ab}$, for each $\boldsymbol{G}_{\boldsymbol{J}_a}$, where $\boldsymbol{I}_a \in \mathbb{R}^{n^2}$, $\boldsymbol{P}_{ab} \in \mathbb{R}^{n^2 \times n^2(\kappa-1)}$, and $\boldsymbol{L}_{ab} \in \mathbb{R}^{n^2(\kappa-1)}$ respectively denote the total interaction for patch $\boldsymbol{J}_a$, proportionality constant in local group $\boldsymbol{G}_{\boldsymbol{J}_a}$, and interaction between $\boldsymbol{J}_a$ and $\boldsymbol{J}_b$ patches. At this point, the main challenge is to tune the values of $\boldsymbol{P}_{ab}$ so that $\boldsymbol{I}_a$ can efficiently preserve the local information and incorporate them into the Hamiltonian. One may note that this process is equivalent to a convolution between $\boldsymbol{L}_{ab}$ and a learnable filter $\boldsymbol{C}_{1_a}$ of appropriate size. Hence, the local operation in the layer is,

$$\boldsymbol{I}_a = \boldsymbol{C}_{1_a} \star \boldsymbol{L}_{ab}, \;\; \forall \boldsymbol{G}_{\boldsymbol{J}_a}, \tag{7.5}$$

where $\star$ indicates the convolution product. This convolution layer is followed by a Rectified Linear Unit (ReLU) to truncate the insignificant contributions of the interactions. Finally, by concatenating $\boldsymbol{I}_a, \forall \boldsymbol{G}_{\boldsymbol{J}_a}$, one obtains $\boldsymbol{I} \in \mathbb{R}^{\varsigma \times n^2}$.

- ***Construct the Hamiltonian kernel:*** In the baseline architecture of De-QuIP, for each $\boldsymbol{J}_a$, the Hamiltonian/energy operator depends on the hyperparameter $(\hbar^2/2m)$ (*i.e.*, the Planck constant), the total interaction $\boldsymbol{I}_a$ and the original potential/pixels' values $\boldsymbol{J}_a$. This operator gives the adaptive basis $\boldsymbol{B}_a$ on which the noisy patch $\boldsymbol{J}_a$ is projected. The integration of the local interactions, bringing a non-local dimension to the formalism, is a core feature of De-QuIP.

  This physical attribute of the Hamiltonian operator is preserved in this step by constructing a kernel

$$\boldsymbol{C}_{2_a} = \left(\frac{\hbar^2}{2m}\right)_a \nabla^2 + \boldsymbol{J}_a + \boldsymbol{I}_a, \quad \forall \boldsymbol{J}_a \in \Omega, \tag{7.6}$$

  where different learnable values of $(\hbar^2/2m)_a$ are allotted instead of a constant one. This kernel $\boldsymbol{C}_{2_a}$ mimics the role of the adaptive basis $\boldsymbol{B}_a$ in the next layer in the shadow of a convolutional process. Note that throughout the learning process the kernel retains its original Hamiltonian structure which is a key ingredient of the original De-QuIP algorithm.

- ***Projection layer:*** This layer deals with the adaptive transformation of the noisy patch $\boldsymbol{J}_a$ on the associative quantum adaptive basis $\boldsymbol{B}_a$ for each $\boldsymbol{J}_a \in \Omega$, *i.e.*, $\boldsymbol{\alpha}_a = \boldsymbol{B}_a \boldsymbol{J}_a$, where $\boldsymbol{\alpha}_a \in \mathbb{R}^{n^2}$ are the projection coefficients of $\boldsymbol{J}_a$. In our proposed deep architecture, this process is conducted by performing convolution operations on $\boldsymbol{J}_a$ using a learnable kernel $\boldsymbol{C}_{2_a}$ built in the previous step, as:

$$\boldsymbol{\alpha}_a = \boldsymbol{C}_{2_a} \star \boldsymbol{J}_a, \quad \forall \boldsymbol{J}_a \in \Omega. \tag{7.7}$$

  Exploiting the power of a deep network, the convolution operation (7.7) removes the algebraically expensive processes, such as the computation of adaptive basis and projection coefficients, and uses the training dataset to directly estimate the projection coefficients. Finally, all $\boldsymbol{\alpha}_a$ are concatenated to form $\boldsymbol{\alpha} \in \mathbb{R}^{\zeta \times n^2}$, serving as input to the next layer.

- ***Thresholding layer:*** The thresholding layer handles the process of trimming the projection coefficients $\boldsymbol{\alpha}$. A nonlinear ReLU activation function φ is used as a thresholding function, which makes the denoising process more robust by adding

more flexibility than the baseline scheme, where thresholding was done in energy. Therefore, the shrunk coefficients $\boldsymbol{R}_a = \varphi(\boldsymbol{\alpha}_a)$ are obtained for each $\boldsymbol{J}_a \in \Omega$, further concatenated into $\boldsymbol{R} \in \mathbb{R}^{\zeta \times n^2}$, before stepping to the next layer.

- ***Inverse projection layer:*** In the original algorithm the denoised patch $\hat{\boldsymbol{J}}_a$ is created from the reduced coefficients $\boldsymbol{R}_a$ by inverse projecting onto the quantum adaptive basis $\boldsymbol{B}_a$ for each $\boldsymbol{J}_a \in \Omega$, *i.e.*, $\hat{\boldsymbol{J}}_a = \boldsymbol{B}_a^{-1}\boldsymbol{R}_a$. This step resembles a convolution process of $\boldsymbol{R}_a$ with a learnable kernel $\boldsymbol{C}_{3_a}$. Hence, the mathematical operation of the layer is defined as

$$\hat{\boldsymbol{J}}_a = \boldsymbol{C}_{3_a} \star \boldsymbol{R}_a, \quad \forall \boldsymbol{J}_a \in \Omega. \tag{7.8}$$

  Finally, before proceeding to the following layer, all outputs $\hat{\boldsymbol{J}}_a$ are concatenated to $\hat{\boldsymbol{J}} \in \mathbb{R}^{\zeta \times n^2}$.

  Note that in the baseline algorithm, the operator used in the inversion step was the inverse of the adaptive basis used in the projection process. This mutual dependence is highlighted in Fig. 7.1(a) by an arrow. In the proposed deep unfolded network, the learnable kernels $\boldsymbol{C}_{2_a}$ and $\boldsymbol{C}_{3_a}$ replaced respectively the original and inverse adaptive basis. The convolutional operations are useful to learn these kernels independently and are illustrated by removing the arrow in Fig. 7.1(b).

- ***Aggregation layer:*** Akin to the De-QuIP scheme, this layer conducts the $\boldsymbol{E}^{-1}$ operation to accumulate all the denoised patches and put them back to their initial positions in the image after normalization, and reconstructs the denoised image $\hat{\boldsymbol{x}}$. Note that overlapping patches are considered in the proposed formalism. Fig. 7.2(a) illustrates the proposed DIVA network architecture, highlighting all the layers described above.

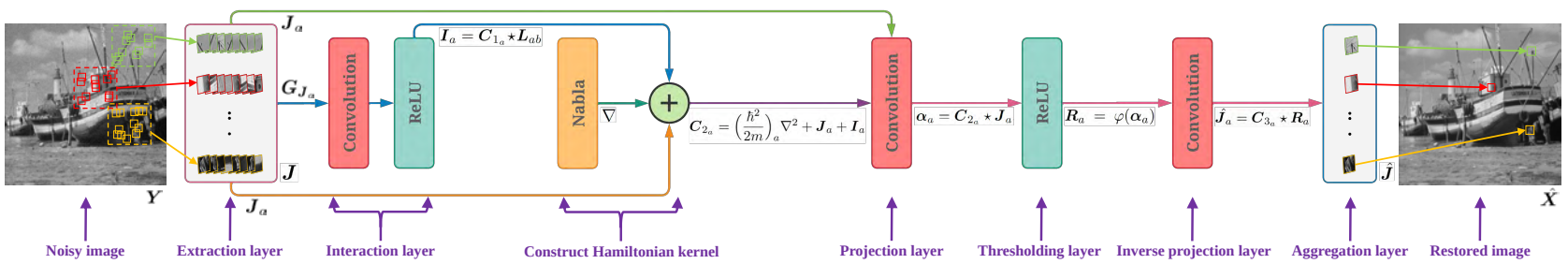

(a) Proposed DIVA network for image denoising.

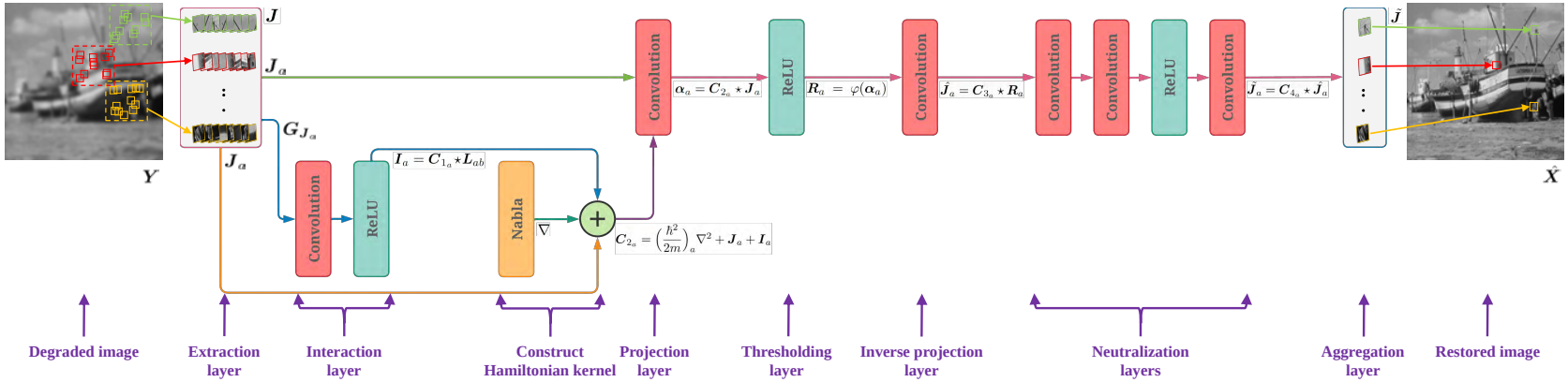

(b) Proposed DIVA-A network for image restoration.

FIGURE 7.2. The architectures of the proposed deep learning models. The corresponding operations for a patch $\boldsymbol{J}_a$ are indicated next to each block.

7.3.2 Proposed DIVA Advanced Network

An advanced version of the DIVA network introduced in the previous section is proposed hereafter. This network slightly differs from DIVA, and is adapted to image restoration tasks involving, in addition to noise, other degradation effects on the observed image $\boldsymbol{y}$, such as blur, pixel resolution loss or missing pixels. In the case of additive Gaussian noise, the effect of the noise and the additional degradation can be considered independently. Therefore, the DIVA network of Subsection 7.3.1 is extended by additional convolutional layers after the inversion process. In this way, the first part of the network eliminates the noise, and the second part neutralizes the effects of a nonidentity degradation operator.

The modified network referred to as DIVA-A primarily plugs a neutralization layer between the inverse projection and aggregation layers, as highlighted in Fig. 7.2(b).

- ***Neutralization layer:*** This layer corresponds to the restoration of the patch $\tilde{\boldsymbol{J}}_a$ by eliminating the influence of a degradation operator $\boldsymbol{O}_a$ from the patch $\hat{\boldsymbol{J}}_a$ reconstructed in the inverse projection layer for each $\boldsymbol{J}_a \in \Omega$, *i.e.*, $\tilde{\boldsymbol{J}}_a = \boldsymbol{O}_a^{-1}\hat{\boldsymbol{J}}_a$, where $\boldsymbol{O}_a$ denotes a degradation operator acting on a patch $\boldsymbol{J}_a$, $\forall \boldsymbol{J}_a \in \Omega$. This operation is analogous to a convolutional process of $\hat{\boldsymbol{J}}_a$ with a learnable kernel $\boldsymbol{C}_{4_a}$, defined as

  $$\tilde{\boldsymbol{J}}_a = \boldsymbol{C}_{4_a} \star \hat{\boldsymbol{J}}_a, \quad \forall \boldsymbol{J}_a \in \Omega. \tag{7.9}$$

  The proposed network conducts this operation by adding three convolutions with multiple learnable filters, and one ReLU function to remove any unwanted contribution (see Fig. 7.2(b)). The power of a CNN architecture is used to learn these filters that mimic the role of a degradation operator in this layer.

Before proceeding to the aggregation layer, all $\tilde{\boldsymbol{J}}_a$ are concatenated to obtain $\tilde{\boldsymbol{J}} \in \mathbb{R}^{\zeta \times n^2}$. Similar to the DIVA network, the aggregation layer assembles all recovered patches and outputs the restored image $\hat{\boldsymbol{x}}$.

7.3.3 Loss Function

The proposed networks are trained end-to-end, where the mean squared error (MSE) between the predicted and original residuals is adopted as the loss function [383]:

$$\mathscr{L}_\Theta = \frac{1}{MN} ||\mathscr{R}(\hat{\boldsymbol{x}};\Theta) - (\boldsymbol{y} - \boldsymbol{x})||_2^2, \tag{7.10}$$

where $\mathscr{R}(\hat{\boldsymbol{x}};\Theta)$ denotes the predicted residual by the network with parameter set Θ. This loss function allows our models to learn the disorders present in a distorted image without bothering about the features of the true image. Note that it is possible to use other loss functions.

7.4 Experimental Results

In this section, we analyze the proposed networks and illustrate their performance in various image restoration tasks, such as image denoising, deblurring, SR, and inpainting. Subsection 7.4.1 briefly summarizes the experimental settings used in the different contexts. Subsection 7.4.2 gives an overview of various benchmark methods considered for comparison purposes. An ablation study with/without considering the interaction layer and the Hamiltonian kernel within the proposed networks is conducted in Subsection 7.4.3, with an additional discussion on the parameter number, run time, and the depth of the network. Finally, Subsection 7.4.4 presents a quantitative and qualitative evaluation of our DL models on various image restoration problems.

7.4.1 Experimental Settings

7.4.1.1 Image Denoising

- ***Training data:*** The proposed DIVA network was trained for the Gaussian denoising task following [71, 405, 407], over a set of 400 gray-scale images of size 180×180 extracted from BSD400 dataset. All images were contaminated with additive white Gaussian noise (AWGN) with standard deviation σ, following two configurations: known and unknown σ. For the case of known σ, the training was conducted individually over six known noise levels, for $\sigma = 10, 15, 25, 50, 75$ and 100. To tackle an unknown noise level, DIVA was also trained blindly for a range of noise levels corresponding to $\sigma \in [5, 40]$. The corresponding model is referred as DIVA-blind.

- ***Testing data:*** The trained networks were tested on five standard benchmark datasets Set12, BSD68, Kodak, LIVE1 and Urban100, widely-used for denoising problems [405, 407].

7.4.1.2 Image Deblurring

- ***Training data:*** DIVA-A was trained separately for two types of blur kernels, *i.e.*, motion and Gaussian blur, using the recently released high-quality dataset DIV2K [9] that consists of 800 images. Eight real motion blur (MB) kernels [194, 215] and three Gaussian blur (GB) kernels [362] were considered with AWGN.
- ***Testing data:*** The models trained for motion blur were tested on four benchmark datasets Set10, Levin, Sun *et al.*, and Set12, used in [194, 254]. The BSD100 and Set16 datasets were considered for the Gaussian case, following [362].

7.4.1.3 Single Image Super-Resolution)

- ***Training data:*** Similar to the deblurring model, the high-quality DIV2K [9] dataset was used as training data for image SR application. Two degradation models were used to simulate low-resolution (LR) images for network training: (i) bicubic downsampling (BD), and (ii) Gaussian downsampling (GD). The scaling factor was set to x2, x3, and x4. For BD case [22], a LR image was simulated from the high-resolution (HR) image by adopting Matlab *imresize* function, whereas for GD scenario, the HR image was blurred by a Gaussian kernel of size 7×7 with standard deviation 1.6 before downsampling, similar to [22].
- ***Testing data:*** For testing, four widely-used benchmark datasets for image SR problem [12, 22, 331] Set5, Set14, BSD100, and Urban100, were used.

7.4.1.4 Image Inpainting

- ***Training data:*** The same 400 gray-scale images [405] exploited by the denoising model were used to conduct the training of the proposed DIVA-A model for image inpainting. Random pixel missing model was considered to generate LR images from HR ones. 20%, 50% and 80% rates of missing pixels were used.
- ***Testing data:*** Datasets Set5 and Set12 were used to evaluate the trained inpaining networks.

7.4.1.5 Quantitative Metrics

For the purpose of quantitative evalution, the peak-signal-to-noise-ratio (PSNR) and the structural similarity (SSIM) [366] computed between the true and the restored images were used.

7.4.1.6 Training Settings

All HR and simulated LR images were clipped between 0 and 1. The patch size was set to $n = 15$ with a local window of size $W = 35$ for the proposed image denoising model with known σ. For DIVA-blind and inpainting applications, these parameters were slightly modified to $n = 25$ and $W = 50$. For deblurring and SR, larger patch and window sizes were used, $n = 35$ and $W = 70$, to preserve more spatial information from the local neighborhood. Finally, all LR-HR patch pairs were augmented randomly by rotating 90 degree and flipping horizontally or vertically to generate training data pairs. The proposed models were trained in a supervised manner by exploiting these patch-pairs.

To conduct the training, the ADAM optimizer with a mini-batch size of 128 was employed. More precisely, the models were trained with an exponentially decaying learning rate ranging from 10^{-3} to 10^{-6} over 60 epochs. The proposed network architectures were implemented under the Keras and Keras-backend framework that relies on the TensorFlow library, and trained using NVIDIA GTX 1080 Ti GPU. The training process took about 6 hours for DIVA and 12 hours for DIVA-A to reach convergence for each experiment.

7.4.2 Comparison Methods

This subsection regroups the state-of-the-art methods used to conduct a comprehensive comparison to illustrate the potential of the proposed models in various imaging problems.

7.4.2.1 Image Denoising

The residual learning-based DnCNN [405] model is the benchmark for AWGN denoising, and its superiority over model-based (e.g., BM3D [82], NLM [49], etc.), and learning-based (e.g., TNRD [71], MLP [51], CSF [301] etc.) algorithms is well-established. In addition to DnCNN [405], our denoising model DIVA was also compared to two recently introduced DL-based networks, FFDNet [407] and IRCNN [402]. Furthermore, comparisons were carried out with a newly proposed deep unfolded scheme, BM3D-NET [383], as well as with the baseline De-QuIP algorithm as proposed in Chapter 6.

7.4.2.2 Image Deblurring and Super-Resolution

For image deblurring and SR problems, newly published leading methods from the literature were considered to illustrate the accuracy of DIVA-A architecture. In the

following, the relevant methods used for comparison purposes in different settings are listed.
(i) MB model: IDD-BM3D[84], FDN[199], VEMNet[254], DWDN[99], DRED-DUN[194];
(ii) GB model: IDD-BM3D[84], Son *et al.*[315], DEBCNN[362];
(iii) BD model: LapSRN[202], MemNet[331], CARN[12], DRLN[22];
(iv) GD model: IRCNN[402], DFAN[220], RDN[414], DRLN[22].

In image SR problems, the DRLN [22] is the new benchmark in the literature. It is already shown in the seminal paper that the DRLN [22] exhibits reference state-of-the-art performance for image SR.

Thus, the DRLN [22] was considered in the comparisons, avoiding to include all the other approaches. Similarly, for image deblurring, DWDN [99], DRED-DUN[194], and DEBCNN[362] were the best performing models in their fields. Hence, these models are selected for comparisons over other methods in the literature.

7.4.2.3 Image Inpainting

DIVA-A trained for image inpainting was compared against the DL prior based model IRCNN [402].

The pretrained models and the testing codes, made publicly available by the authors, were used for comparisons. Importantly, note that the proposed networks have been trained and tested exactly in the same conditions and on the same datasets as the comparison methods, thus ensuring a fair comparison.

7.4.3 Ablation Study and Model Analysis

This section regroups several ablation studies aiming at showing the importance of the layers inspired from quantum mechanics, and an in-depth analysis of the properties of the proposed networks.

7.4.3.1 Influence of the Interaction Layer

To show the effect of the interaction layer's integration in the Hamiltonian kernel, two versions of the DIVA network were trained for image denoising with $\sigma = 15$: the complete network as shown in Fig. 7.2(a), and the same network without the interaction layer. Fig. 7.3 plots the corresponding loss functions for these two network settings with respect to the number of epochs. One can see that using the interaction layer results into a faster and more stable convergence of the training process. Meanwhile, in the absence of this

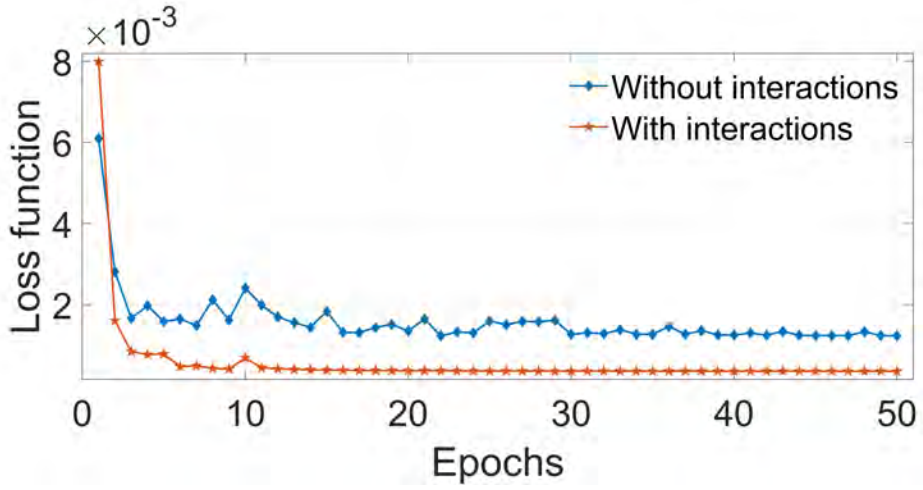

FIGURE 7.3. Loss function (MSE) with respect to epochs. Two specific models are trained for image denoising with $\sigma = 15$, with and without integrating the interaction layer in the proposed DIVA architecture for the ablation study.

layer, a strong periodic fluctuation can be observed. This is caused by the absence of a non-local architecture in the network, which helps stabilizing the convergence process.

The same ablation study was conducted for different depths of the projection layer, using the Hamiltonian convolutional kernel constructed with and without the interaction layer. From Table 7.1, one can see a clear improvement in denoising performance in the presence of the interaction layer. In addition, the interaction layer significantly reduces the depth of the network by extracting the local similarities/structures from the neighboring patches. Indeed, more local information can be transferred through this non-local architecture, which helps network structures with lower depth to be more efficient. On the contrary, the network without the interaction layer improves while increasing the depth. This is expected since a deeper network consists of a larger set of tunable parameters. Although a bigger set of parameters leads to a better outcome, the learning process becomes more computationally expensive. Thus, the integration of the interaction layer enhances the network performance with a reduced computational cost, giving an edge to the proposed models.

Note that, in absence of the interaction layer in the proposed model, the network does not consider the influence of neighboring patches on the target patch and loses its non-local nature. Thus, each patch behaves as a single particle quantum system, and all patches are independent. Hence, in this circumstance, the network without an interaction layer becomes an unfolded DL scheme of the baseline QAB algorithm as

TABLE 7.1. Ablation investigation of the projection layer's depth using Hamiltonian kernel with or without the interaction layer. The results (PSNR/SSIM) are obtained on Set12 contaminated with AWGN with $\sigma = 15$, in 50 epochs.

	Depth of the projection layer using Hamiltonian convolutional kernel									
	1	2	3	4	5	1	2	3	4	5
Interaction layer	✗	✗	✗	✗	✗	✓	✓	✓	✓	✓
PSNR (dB)	30.38	31.61	31.95	32.17	32.28	32.09	32.92	32.95	32.96	32.98
SSIM (%)	87.64	89.22	90.74	91.61	91.88	93.68	95.41	95.52	95.55	95.60

TABLE 7.2. Ablation study with/without using the Hamiltonian kernel in the network. The results (PSNR/SSIM) are obtained in 50 epochs on Set12 images contaminated with AWGN ($\sigma = 15$).

	Contribution of different components		
Hamiltonian kernel	✗	✓	✓
Interaction layer	✗	✗	✓
PSNR (dB)	29.30	31.61	32.92
SSIM (%)	86.82	89.22	95.41

proposed in Chapter 4, originally proposed for image denoising based on single-particle quantum theory. In Chapter 6, it has been shown that the baseline De-QuIP outperforms the conventional QAB algorithm significantly. This observation for the traditional De-QuIP algorithm is also consistent with results for our unfolded DL models, as reported in Fig. 7.3 and Table 7.1. Therefore, the consideration of the quantum interaction concept clearly enhances the model performance of both conventional and DL architectures.

7.4.3.2 Depth of the Projection Layer

Table 7.1 reports denoising performance on Set12 for $\sigma = 15$ for different depths of the projection layer within the Hamiltonian kernel. As expected, the denoising performance increases with the depth of the network, but this increment is less significant beyond depth 3. Assessing the trade-off between the network efficiency and the computational complexity, a depth of 2 was considered in the proposed DL models.

7.4.3.3 Ablation Study on the Hamiltonian Kernel

In the proposed models, the objective is to construct a Hamiltonian kernel to conduct the projection operation, while preserving the original attributes of the proposed Hamiltonian operator in the baseline De-QuIP algorithm. This Hamiltonian kernel is a sum of the

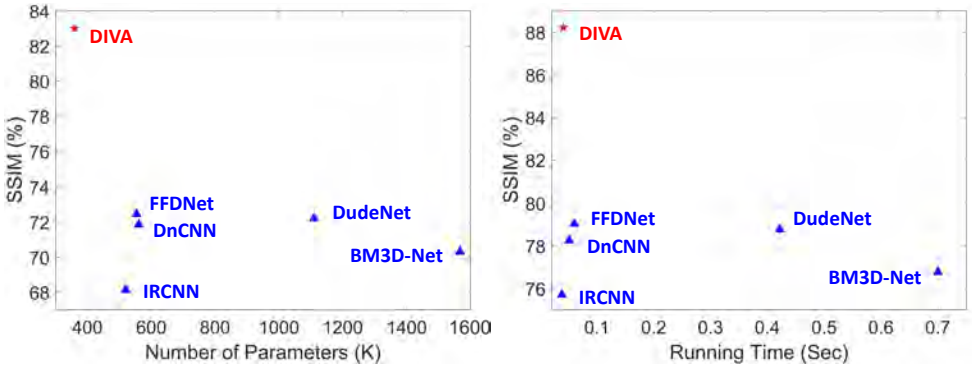

(a) Left: Denoising performance vs parameter number. Comparisons are presented on the BSD68 dataset with $\sigma = 50$. Right: Denoising performance vs run time. Comparisons are presented on the Set12 dataset with $\sigma = 50$.

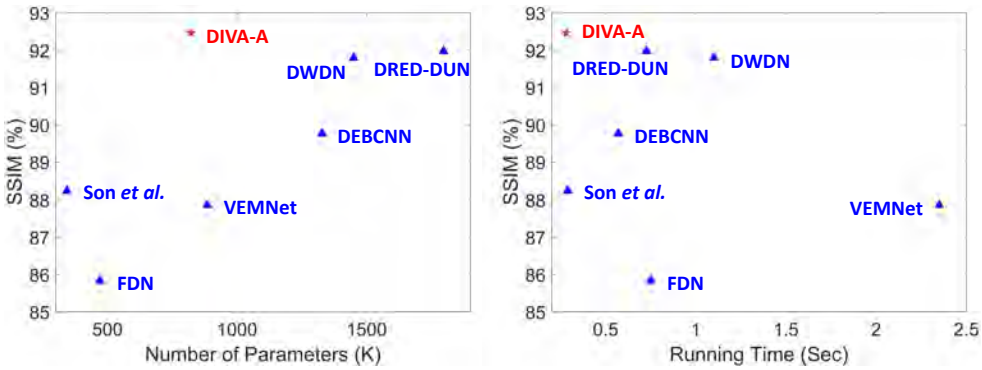

(b) Left: Deblurring performance vs parameter number. Comparisons are presented on the Levin dataset with motion blur and $\sigma = 7.65$. Right: Deblurring performance vs run time. Comparisons presented on the Levin dataset with motion blur and $\sigma = 7.65$.

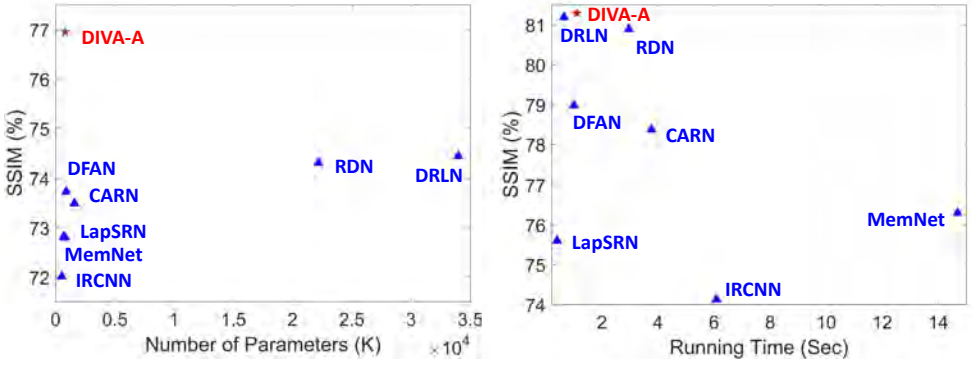

(c) Left: SR performance vs parameter number. Comparisons are presented on the BSD100 dataset for 4X SR. Right: SR performance vs run time. Comparisons are presented on the Urban100 dataset for 4X SR.

FIGURE 7.4. Performance versus parameter number and run time versus performance are presented for different methods for different tasks. The proposed methods give high performances in terms of SSIM(%) with fewer number of parameters and low computation time.

nabla operator, original pixels' values of the patch and the interactions with its neighbors, following equation (7.6). To illustrate the importance of this Hamiltonian structure in the proposed networks, an ablation investigation of this Hamiltonian kernel was conducted, through three network settings:(i) without the Hamiltonian kernel and interaction layer, (ii) with the Hamiltonian kernel but without the interaction layer, and (iii) with the Hamiltonian kernel including the interaction layer. For all settings, the depth of the projection layer was set to 2. Table 7.2 regroups the denoising results on Set12 for AWGN with $\sigma = 15$ for all these three configurations. From these results, one may observe that the accuracy of the network is significantly improved in the case where the Hamiltonian shape is preserved and includes the interactions between neighboring patches. This improvement is even further illustrated by the SSIM, that is more sensitive to the image structure than the PSNR, and thus more suitable to reflect the contribution of the interaction-based Hamiltonian operator. Furthermore, one may notice that with none of these two ingredients, the denoising performance is largely decreased. This can be explained by the fact that in this case, the resulting netwrok, very similar to DnCNN [405], needs far more layers to achieve good denoising results. Indeed, a network depth of 17 is suggested in [405], while, as mentionned previously, the proposed network depth can be reduced to 2. Therefore, the exploitation of the local information through the patch interaction, originally proposed in the baseline De-QuIP, and the attributes of the Hamiltonian kernel, make the proposed DL networks easily adaptable but resilient even for lower depth. In conclusion, this experiment illustrates the significance of the inclusion of the Hamiltonian kernel with the interaction layer in the proposed models.

7.4.3.4 Analysis of the Parameter Number and Runtime

The number of hyperparamers of a DL network plays a crucial role in its efficiency. Generally, a larger pool of parameters drives the model more resilient and leads to better performance. However, it also imposes an important computational load, in particular within the training process. Furthermore, an excessive number of parameters may lead to an over-fitting problem. Hence, a balanced trade-off between the learnable parameter number, the performance, and the computational cost becomes a crucial factor for an efficient DL model.

As detailed in the previous ablation studies, the proposed models exploit the Hamiltonian kernel, which is enriched by an intrinsic non-local architecture through the interaction layer. As a result, the resulting DL networks are able to process more information through fewer parameters and significantly reduce the cost of training with high

efficiency. Fig. 7.4 provides the performance in terms of SSIM(%) versus the number of parameters and the runtime of the proposed models against state-of-the-art methods, in the context of different image restoration problems. One can observe a significant gain in performance of DIVA model for image denoising (see Fig. 7.4(a)). DIVA increases SSIM by 10%, with almost half the number of parameters of its closest competitors FFDNet [407] and DnCNN [405]. For image deblurring problem (see Fig. 7.4(b)), DIVA-A requires only half of the parameters compared to its nearest rival DRED-DUN [194], but offers a 1% better SSIM value. Similarly, from Fig. 7.4(c), one can report a gain of 1-2% in SSIM for image SR by DIVA-A compared to the recently introduced DRLN network, whereas our model has 40 times less parameters than DRLN. Naturally, the proposed networks that need a reduced number of parameters to perform well, also offer a significantly reduced training cost. Fig. 7.4 presents the runtime comparisons against other standard models in various imaging tasks, showing that the proposed models are significantly faster. Note that similar results are achieved for image inpainting, but are not reported here since the comparison network is IRCNN, already included in the SR experiments. Hence, harnessing the benefits of the interaction layer and of the Hamiltonian kernel, the proposed DL models demonstrate better performance for image restoration with fewer parameters and more efficient computational costs.

7.4.4 Qualitative and Quantitative Image Restoration Results

7.4.4.1 Image Denoising

Table 7.3 summarizes the average PSNR and SSIM results of the different methods on six commonly used testing datasets with six different noise levels. One might notice that the proposed DIVA model uniformly outperforms all the state-of-the-art approaches, irrespective of the noise level and dataset. Compared to the deep unfolded BM3D network BM3D-NET, our model exhibits much better denoising performance with an average increment of 1.5dB PSNR and 4.5% SSIM for low noise levels and up to 2dB PSNR and 13% SSIM for higher σ. Note also that BM3D-NET was only available for four levels of noise. One can observe that the performance gain is much higher over the benchmark DnCNN and FFDNet networks for high noise cases. Precisely, DIVA outperforms these competing methods by 0.05-1.2dB PSNR and 4-18% SSIM in average and achieves the best denoising yields. Moreover, our blind denoising model DIVA-blind that, in contrast to the other networks, is not trained for a given (known) noise level, but for a range of σ, still gives comparable PSNR values and improved SSIM compared to the state-

TABLE 7.3. Image denoising results in terms of average PSNR (dB) and SSIM (%) values for five benchmark datasets contaminated by six noise levels ($\sigma = 10, 15, 25, 50, 75, 100$). For each experiment, the best values are in red and the second best values are in blue.

Dataset	σ	Input	Methods						
			DnCNN[405]	FFDNet[407]	IRCNN[402]	BM3D-NET[383]	De-QuIP	DIVA	DIVA-blind
Set12	10	28.16/82.87	34.76/92.69	34.64/92.71	33.62/91.83	33.27/91.97	33.45/91.03	34.80/96.77	34.68/94.56
	15	24.64/69.97	32.84/90.23	32.75/90.27	32.77/88.08	31.65/88.96	31.15/87.30	32.92/95.41	32.79/93.61
	25	20.20/49.68	30.42/86.14	30.42/86.34	30.38/84.23	29.77/85.09	28.65/81.23	30.47/93.00	30.36/90.73
	50	14.18/24.87	27.16/78.25	27.32/79.03	27.14/75.70	25.78/76.77	25.28/70.43	27.45/88.22	-/-
	75	10.66/14.75	25.15/71.71	25.49/73.52	23.75/67.46	-/-	23.44/63.69	25.63/84.31	-/-
	100	8.16/9.64	23.87/64.28	24.20/69.26	21.95/59.70	-/-	22.21/58.02	24.43/81.17	-/-
BSD68	10	28.15/83.57	33.87/92.71	33.75/92.66	33.74/90.57	32.74/91.73	32.67/90.65	33.94/96.21	33.80/94.38
	15	24.63/70.99	31.73/89.06	31.63/89.02	31.63/87.98	31.42/88.77	30.24/85.38	31.79/94.04	31.64/92.74
	25	20.19/50.70	29.22/82.78	29.19/82.89	29.15/79.51	28.95/81.42	27.83/77.35	29.34/90.07	29.19/87.44
	50	14.17/25.08	26.22/71.85	26.29/72.45	26.16/68.13	25.73/70.31	24.88/64.25	26.33/82.99	-/-
	75	10.65/14.61	24.63/64.69	24.78/65.86	22.87/60.05	-/-	23.33/56.55	24.87/77.81	-/-
	100	8.15/9.41	23.16/55.46	23.77/60.96	19.46/49.47	-/-	22.27/51.23	23.93/74.21	-/-
Kodak	10	28.14/81.24	34.86/92.17	34.81/92.20	34.76/87.91	32.39/91.01	33.56/89.95	34.91/96.35	34.82/94.75
	15	24.62/67.32	32.84/88.82	32.72/88.90	32.63/83.40	30.82/87.68	31.27/85.13	32.93/94.49	32.78/93.02
	25	20.18/45.89	30.43/83.15	30.37/83.42	30.29/78.07	28.55/81.62	28.83/77.64	30.55/91.16	30.30/87.89
	50	14.16/21.13	27.47/73.53	27.61/74.34	27.44/69.24	25.91/72.15	25.71/65.76	27.70/85.41	-/-
	75	10.64/11.91	25.77/67.34	25.96/68.80	23.85/61.75	-/-	24.07/59.02	26.16/81.36	-/-
	100	8.14/7.54	23.99/55.99	24.88/64.74	20.38/51.29	-/-	22.92/53.74	25.22/78.66	-/-
LIVE1	10	28.14/83.19	34.24/92.95	34.13/92.96	33.02/88.09	32.77/91.83	32.39/90.98	34.27/96.54	32.19/94.81
	15	24.62/70.46	32.11/89.68	32.01/89.71	30.42/81.32	30.46/88.74	29.96/85.96	32.19/94.65	31.97/92.69
	25	20.18/50.19	29.55/83.91	29.53/84.08	27.22/75.04	27.61/82.14	27.44/78.00	29.62/91.12	29.46/88.32
	50	14.16/25.03	26.40/73.34	26.51/74.03	23.05/66.92	24.75/71.60	24.28/64.73	26.63/84.54	-/-
	75	10.64/14.74	24.70/66.14	24.92/67.59	21.21/57.58	-/-	22.62/56.66	24.99/79.65	-/-
	100	8.14/9.59	22.39/50.10	23.81/62.74	19.59/48.28	-/-	21.51/50.87	23.99/76.23	-/-
Urban100	10	28.15/87.17	34.43/95.74	34.45/94.89	32.93/91.35	32.53/94.52	31.25/93.26	34.75/97.84	34.52/95.37
	15	24.63/77.13	32.17/93.36	32.42/92.73	30.30/88.77	30.65/91.99	29.53/88.60	32.51/96.52	32.26/94.11
	25	20.19/60.04	29.27/88.42	29.92/88.87	27.01/83.09	27.68/86.63	25.75/82.53	30.01/93.73	29.75/91.89
	50	14.17/34.98	25.46/77.82	26.52/80.57	22.79/71.51	23.99/75.34	22.81/68.02	26.67/87.80	-/-
	75	10.65/22.46	23.23/68.69	24.52/73.65	20.81/61.21	-/-	20.59/58.92	24.80/82.10	-/-
	100	8.15/15.38	22.04/62.85	23.08/67.59	18.79/53.57	-/-	19.65/50.51	23.39/77.37	-/-

∗*The symbol -/- denotes that the results were not provided in the original paper for a particular experiment.*

of-the-art approaches. In all the cases, one can observe a considerable improvement in SSIM enabled by the proposed network, which proves that it is better equipped for image structure and pattern preservation than other models. Utilization of this local information from neighboring patches enables our network to be resilient and adapted to high and low-level noise, giving us an edge over other models.

Furthermore, a notable gain of an average of 1.5-3dB PSNR and 5-26% SSIM is observed compared to the baseline De-QuIP method. This is a consequence of finely tuned hyperparameters values for each patch by harnessing the power of the backpropagation architecture.

Figs. 7.5- 7.7 illustrates denoising results for three images, *Girl*, *Castle* and *Parrot*, from three datasets, for σ = 25, 50 and 75 respectively. The qualitative analysis of the

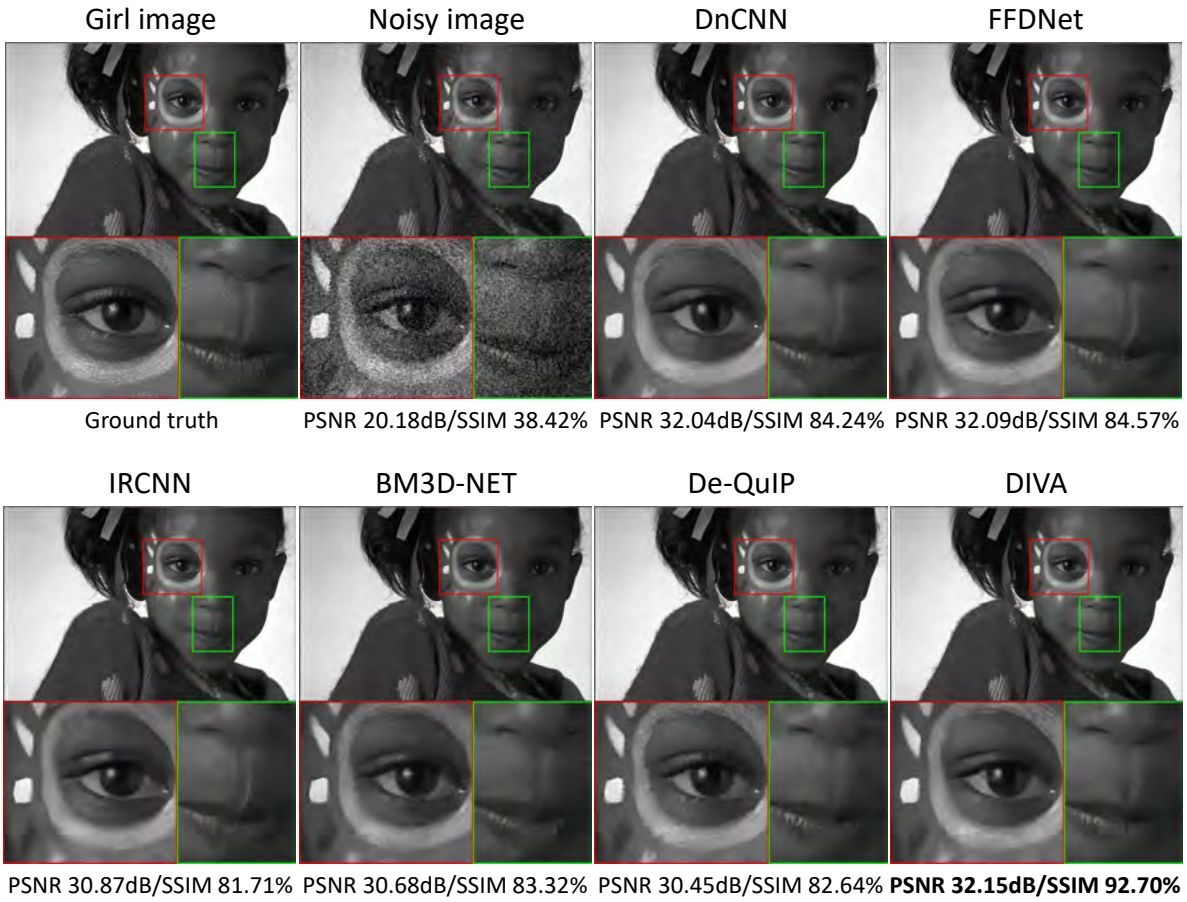

FIGURE 7.5. Denoising results using different methods for the *Girl* image contaminated with AWGN with $\sigma = 25$.

denoised images confirms the superiority of the proposed model. Indeed, all competing methods fail to recover the original textures around the eye and lips in *Girl* image, the sharp edges and peaks around the windows and roof in *Castle* image, and the patterns in *Parrot* image. IRCNN restores blurred edges, and BM3D-NET and De-QuIP generate some small artifacts. DnCNN and FFDNet give comparable PSNR, but low SSIM, caused by over-smoothed results, which were not able to retrieve small details. In contrast, DIVA is faithful to the ground truths and restores the images with the right consistency by capturing the subtle details more reliably.

Visual and quantitative inspections indicate that DIVA model conclusively outperforms its baseline method De-QuIP, as well as other advanced DL methods by a significant margin in terms of PSNR and SSIM. The DnCNN and FFDNet are the closest to DIVA, but struggle to preserve image textures accurately, mainly because of a smoothing effect.

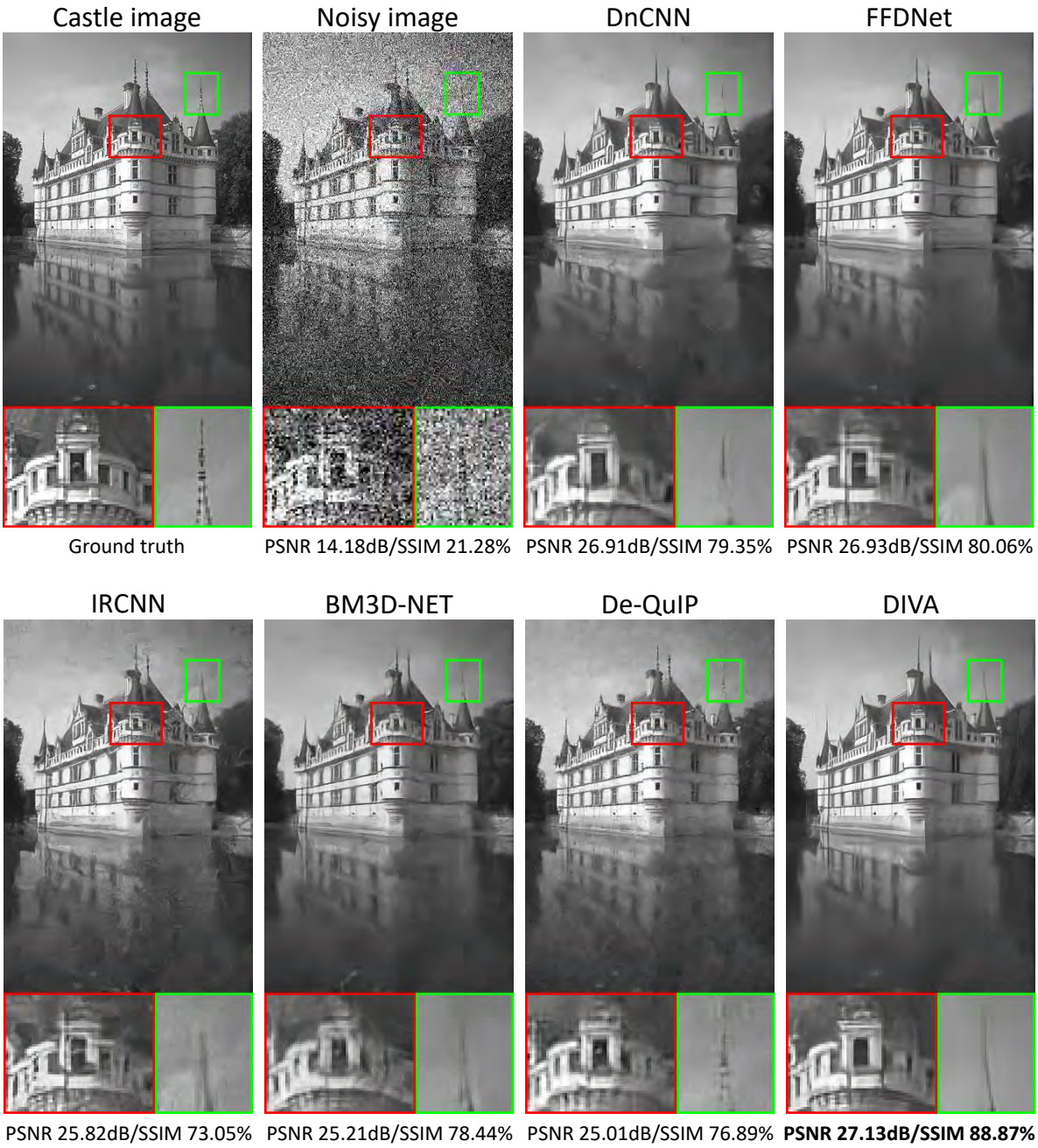

FIGURE 7.6. Denoising results using different methods for the *Castle* image contaminated with AWGN with $\sigma = 50$.

DIVA preserves most of the image fragments and textures in a better way without creating any visible artifacts and thus provides a denoised image closer to the ground truth.

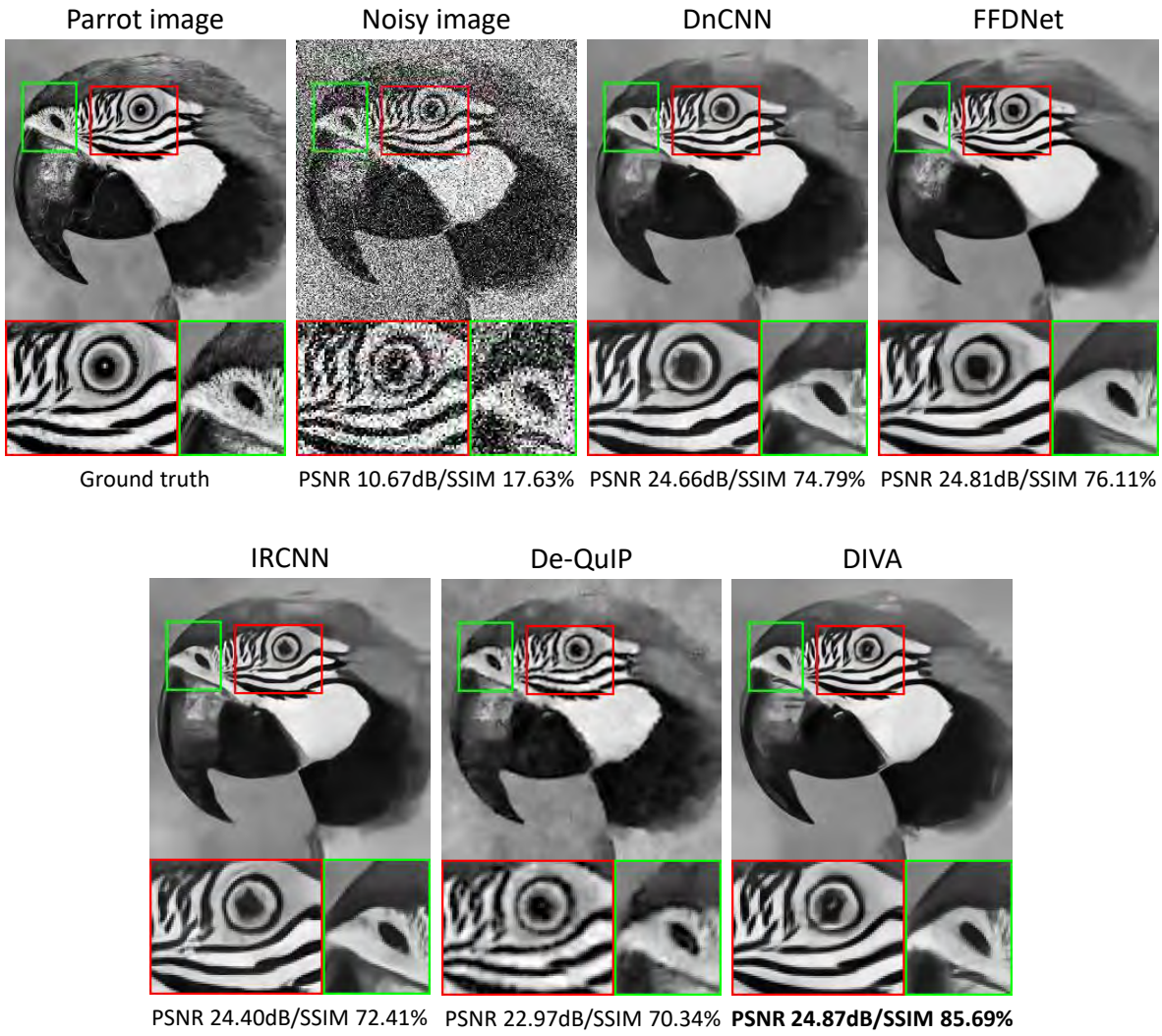

FIGURE 7.7. Denoising results using different methods for the *Parrot* image contaminated with AWGN with $\sigma = 75$.

7.4.4.2 Image Deblurring

Image deblurring results for Gaussian blur (GB) are illustrated on two benchmark datasets degraded with three different GB kernel settings of size 25×25: (i) GB kernel with standard deviation of 1.6 and AWGN with $\sigma = 2$, (ii) GB kernel with standard deviation of 3 and AWGN with $\sigma = 10$, (iii) GB kernel with standard deviation of 5 and AWGN with $\sigma = 10$. Table 7.4 regroups the average PSNRs and SSIMs obtained by all competing methods. One can observe that the benchmark DEBCNN method performs much better than the model-based IDD-BM3D and learning-based Son *et al.* [315] schemes. DIVA-A outperforms DEBCNN by 1.1 dB in PSNR and 2% in SSIM

TABLE 7.4. Deblurring results in terms of average PSNR (dB) and SSIM (%) values for two datasets degraded with three GB kernels and AWGN.

Dataset	kernel$_\sigma$	noise$_\sigma$	Methods			
			IDD-BM3D[84]	Son *et al.*[315]	DEBCNN[362]	DIVA-A
BSD100	1.6	2	27.17/86.14	23.18/73.47	28.47/87.90	29.97/89.65
	3	10	24.16/76.66	22.88/68.14	25.34/78.11	26.57/80.16
	5	10	22.75/71.74	22.17/65.92	22.79/71.94	23.73/74.09
Set16	1.6	2	30.85/93.41	29.87/93.29	31.34/94.39	32.38/95.37
	3	10	26.37/85.78	25.20/82.34	26.93/86.91	27.38/89.31
	5	10	24.23/82.24	23.63/80.55	27.28/82.76	28.11/87.22

TABLE 7.5. Deblurring results in terms of average PSNR (dB) and SSIM (%) values for four datasets degraded with standard MB kernels and AWGN.

Dataset	noise$_\sigma$	Methods					
		IDD-BM3D[84]	FDN[199]	VEMNet[254]	DWDN[99]	DRED-DUN[194]	DIVA-A
Set10	0	36.24/89.24	-/-	-/-	43.95/96.49	43.67/96.38	43.54/96.67
	2.55	30.75/86.63	-/-	31.71/89.95	33.28/93.12	33.16/92.97	33.03/93.54
	7.65	27.25/77.76	-/-	28.27/82.51	29.61/88.07	29.80/88.48	29.38/90.03
	12.75	25.71/71.38	-/-	26.62/77.68	26.92/83.16	27.49/84.05	27.42/85.79
Levin	0	37.48/94.68	-/-	-/-	46.13/97.63	45.56/97.27	46.19/97.76
	2.55	33.75/92.19	34.05/93.35	34.31/94.31	36.90/96.14	36.02/95.79	36.19/95.86
	7.65	29.26/85.78	29.77/85.83	30.50/87.86	32.77/91.79	32.87/91.97	33.12/92.46
	12.75	27.33/78.92	27.94/81.39	28.52/82.73	30.77/88.57	30.89/88.79	30.80/89.87
Sun *et al.*	0	37.14/90.42	-/-	-/-	43.10/97.19	42.49/97.08	42.65/97.36
	2.55	32.24/87.79	32.63/88.87	32.73/90.13	34.05/92.25	34.43/92.97	34.44/93.49
	7.65	28.74/77.86	28.97/78.42	29.41/81.08	29.11/86.31	29.88/87.28	30.30/89.14
	12.75	27.30/73.24	27.62/74.52	28.04/77.89	27.81/80.85	28.20/81.59	27.95/83.36
Set12	0	-/-	-/-	-/-	-/-	-/-	43.48/96.39
	2.55	31.43/88.14	31.43/89.17	31.93/90.19	-/-	-/-	33.77/92.58
	7.65	27.56/80.09	27.89/80.86	28.47/82.78	-/-	-/-	28.97/87.89
	12.75	25.95.74.88	26.28/76.24	26.77/78.13	-/-	-/-	27.28/84.45

∗*The symbol -/- denotes that the results were not provided in the original paper for a particular experiment.*

and 0.8 dB in PSNR and 2.6% in SSIM on average for BSD100 and Set16 datasets, respectively.

In Fig. 7.8, a qualitative evaluation shows that the proposed method not only generates better image contrast but also retrieves sharp edges with more details than the other approaches, like IDD-BM3D and Son *et al.* [315], where random artifacts and blurred edges are visible in the deblurred outputs. Our DL model restores the *Penguin* and *Horse* images with much sharper and more precise edges than the DEBCNN, for which edges look hazy. Thus, though DEBCNN and DIVA-A are the two best models in

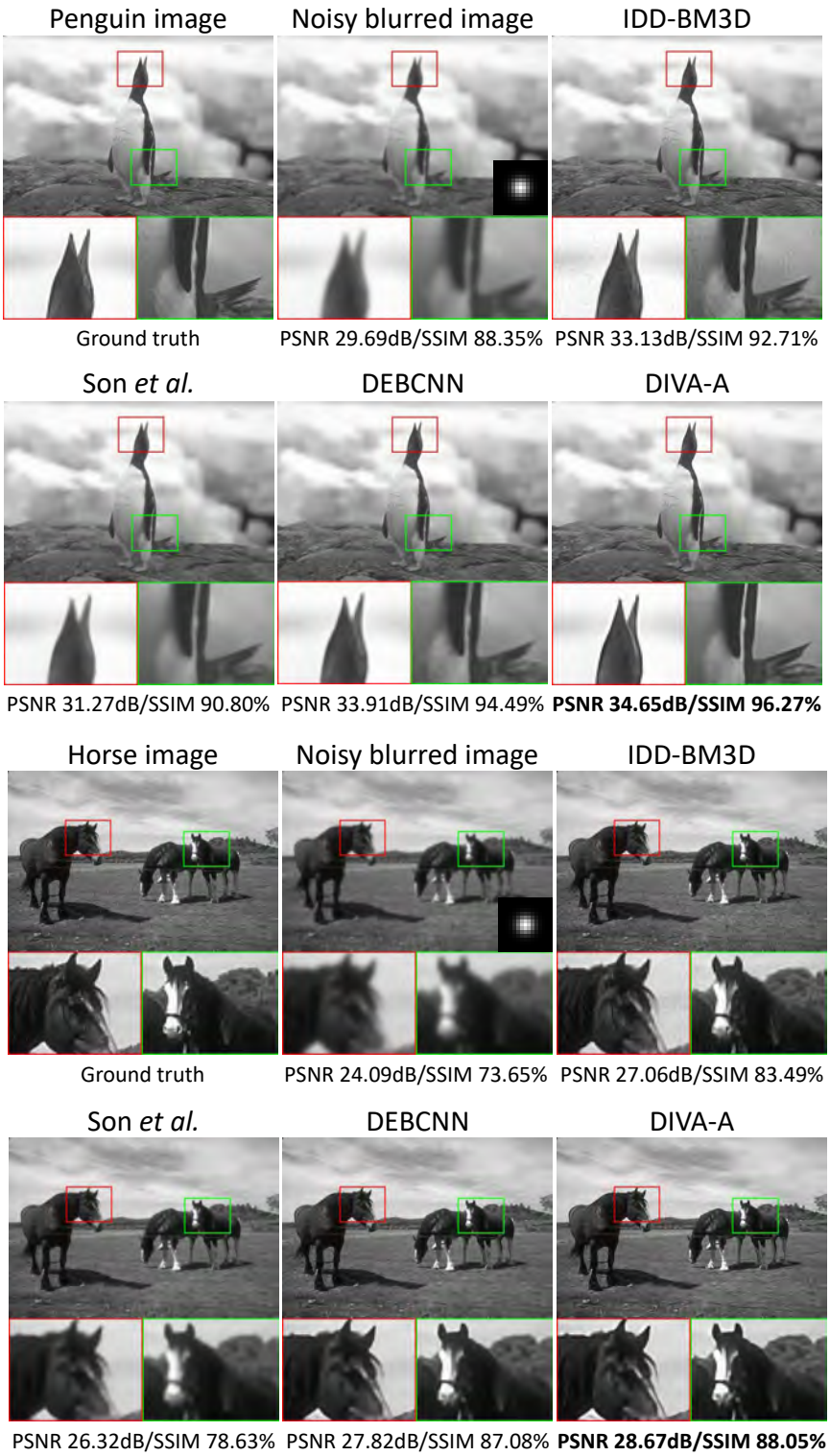

FIGURE 7.8. Image deblurring results for *Penguin* and *Horse* images degraded by a 25×25 GB kernel of standard deviation 1.6 with random AWGN of standard deviation 2.

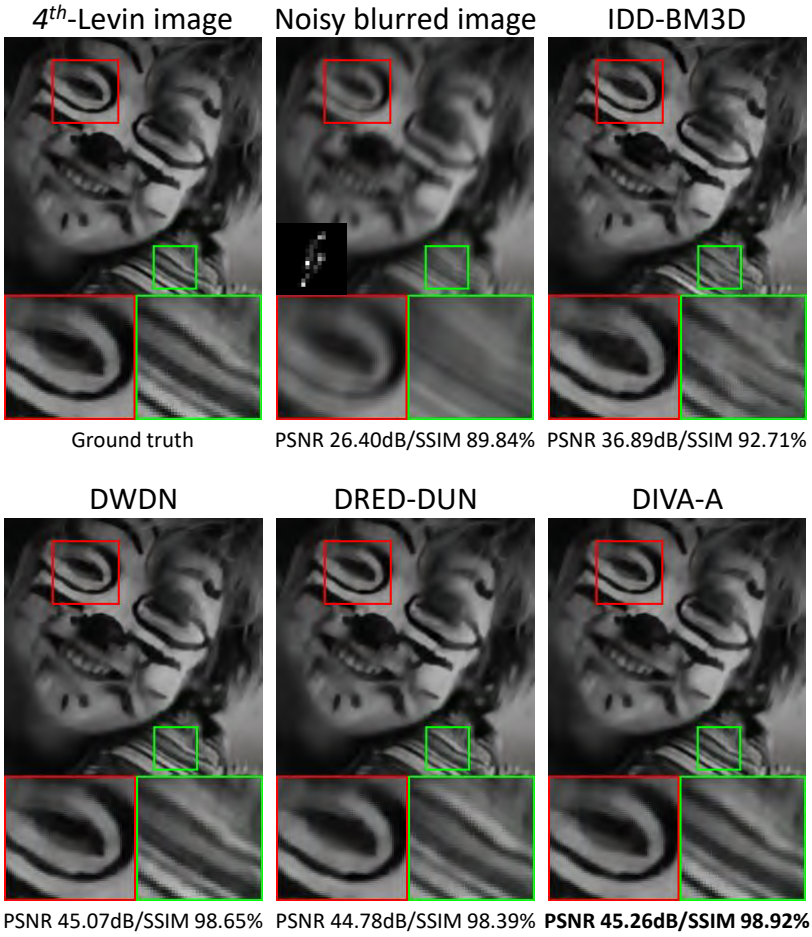

FIGURE 7.9. Deblurring results for 17×17 MB kernel. The restored *4th*-image from the Levin dataset with 17×17 motion blur kernel.

this setting, our model uniformly outperforms the sophisticated DEBCNN method for GB problems.

Table 7.5 gives the average deblurring performance of our method in terms of PSNRs and SSIMs in contrast to other standard models from the literature under eight commonly used motion blur (MB) kernels [194, 215] and four different noise levels. One should note that the code or trained models provided by the authors are used to generate these results. As the first observation, one can see that DWDN and DRED-DUN outperform the conventional IDD-BM3D, FDN and VEMNet for the Set10, Levin and Sun *et al.* datasets, which is consistent with the findings in [194]. Secondly, DWDN performs better in the case of low/no noise in terms of PSNRs compared to DRED-DUN and our proposed model. DRED-DUN is more accurate for high levels of noise. On the contrary, our proposed model exhibits the best SSIMs with a gain up to 0.15-1.8% against the DWDN and DRED-DUN for low as well as high noise levels and this efficiency increases

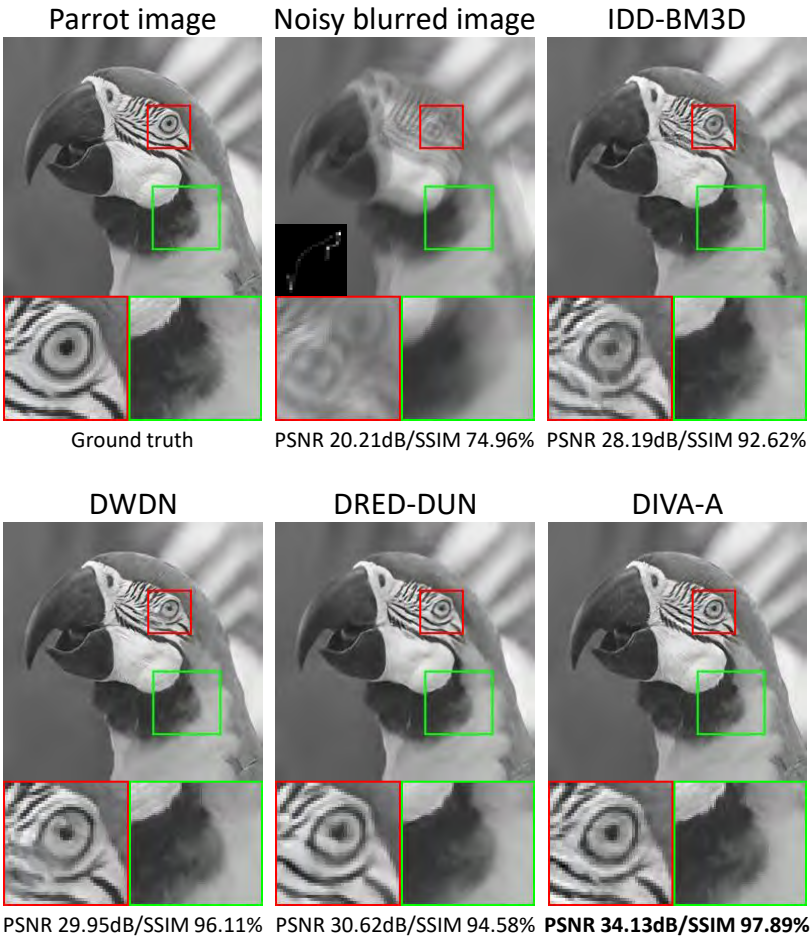

FIGURE 7.10. Deblurring results for 25×25 MB kernel. The restored *Parrot* images with 25×25 motion blur kernel.

with noise intensity. In terms of PSNR values, our model often stays in the top two and only fails to do so for Set10, where the average PSNR gaps between the best two methods and our model is very small. Noticeably, although DIVA-A sometimes offers slightly worse PSNRs than DWDN and DRED-DUN, it requires only half of the tunable parameters (shown in Fig. 7.4(b)). Finally for Set12, our model unilaterally dominates the comparison and exceeds its nearest rival VEMNet by up to an average of 1dB PSNR and 3.5% SSIM.

For visual assessment, restored images from images degraded with four different MB kernels are shown in Figs. 7.9, 7.10, 7.11, 7.12. Figs. 7.9, 7.10 show that for the *4th*-Levin, and *Parrot* images respectively under a MB kernel of size 17×17 and 25×25, the quality of the restored images by our model is considerably improved compared to the other

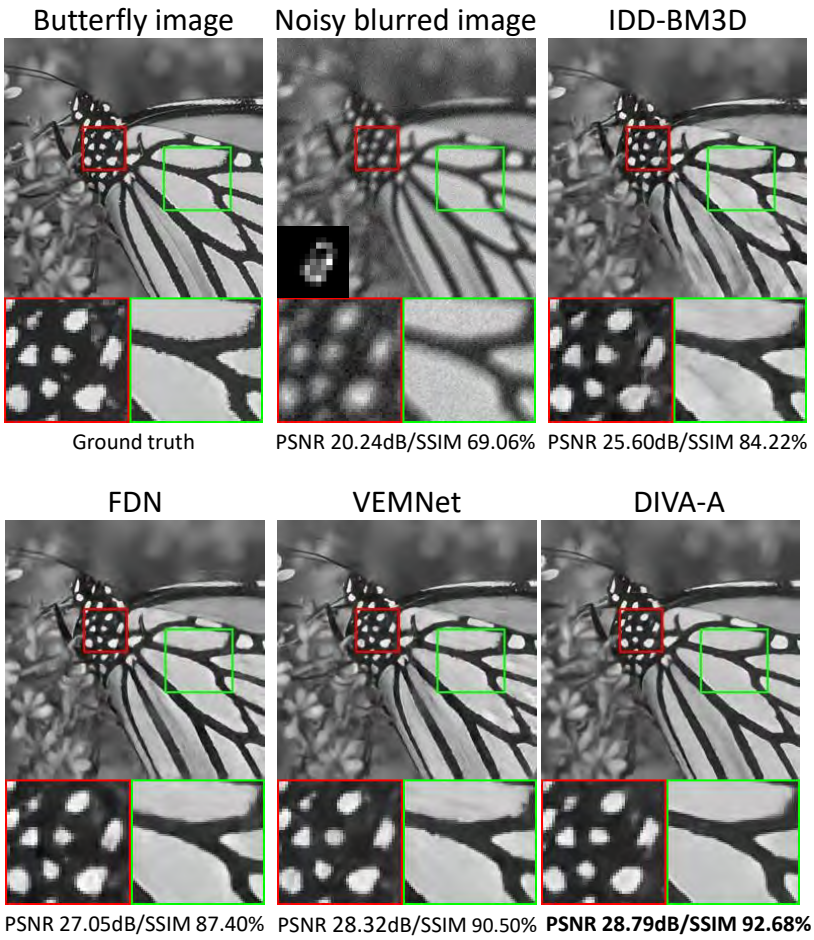

FIGURE 7.11. Deblurring results for 13×13 MB kernel. The restored *Butterfly* images with 13×13 motion blur kernel and Gaussian noise of standard deviation 7.65.

methods. In particular, the finer texture of the images is severely smoothed out by IDD-BM3D, DWDN and DRED-DUN, as shown in the zoomed boxes. Additionally, in Fig. 7.11, the *Butterfly* image is degraded by a moderate size 13×13 motion blur kernel with random Gaussian noise of standard deviation 7.65. Our proposed model for retrieving original image quality is significantly better than other competitors. For example, IDD-BM3D, FDN, and VEMNet fail to properly restore the pattern on the butterfly's wings and body, and show many distortions in the restored images, as visible in the zoomed boxes. Furthermore, the overall visual impression of the restored images is improved, as visible on the facial decorations, finer details on the wings and minute patterns that are better preserved with DIVA-A. Finally, Fig. 7.12 offers a similar conclusion for the restored *3th*-Levin image under a 23×23 MB kernel with AWGN with $\sigma = 2.55$. Thus,

FIGURE 7.12. Deblurring results for the *3rd*-image from the Levin dataset with motion blur kernel of size 23×23 and random AWGN $\sigma = 2.55$.

under MB kernels DIVA-A demonstrates a better efficiency in recovering edges and patterns of the original images. DWDM and DRED-DUN produce comparative results compared to our model, but with lower contrast. Quantitatively, our method is always among the best two approaches in this context.

7.4.4.3 Single Image Super-Resolution

This subsection presents super-resolution (SR) results for two standard downsampling operators, bicubic downsampling (BD) and Gaussian downsampling (GD). Tables 7.6, 7.7 regroup average PSNR and SSIM values of different methods on four datasets for BD

TABLE 7.6. SR results in terms of average PSNR (dB) and SSIM (%) values for 4 benchmark datasets degraded with bicubic downsampling with downsampling factors of 2, 3 and 4.

Dataset	Scale	Methods				
		LapSRN[202]	MemNet[331]	CARN[12]	DRLN[22]	DIVA-A
Set5	2x	37.52/95.91	37.78/95.97	37.76/95.90	38.27/96.16	37.42/97.43
	3x	33.82/92.27	34.09/92.48	34.29/92.55	34.78/93.03	33.14/93.36
	4x	31.54/88.50	31.74/88.93	32.13/89.37	32.63/90.02	30.87/90.02
Set14	2x	33.08/91.30	33.28/91.42	33.52/91.66	34.28/92.31	33.67/93.69
	3x	29.87/83.20	30.00/83.50	30.29/84.07	30.73/84.88	29.18/85.34
	4x	28.19/77.20	28.26/77.23	28.60/78.06	28.94/79.00	27.74/80.66
BSD100	2x	31.80/89.50	32.08/89.78	32.09/89.78	32.44/90.28	32.00/90.49
	3x	28.82/79.80	28.96/80.01	29.06/80.34	29.36/81.17	28.91/82.15
	4x	27.32/72.80	27.40/72.81	27.58/73.49	27.83/74.44	27.66/76.95
Urban100	2x	30.41/91.00	31.31/91.95	31.51/93.12	33.37/93.90	31.48/93.06
	3x	27.07/82.80	27.56/83.76	27.38/84.04	29.21/87.22	27.54/85.31
	4x	25.21/75.60	25.50/76.30	26.07/78.37	26.98/81.19	25.39/81.29

TABLE 7.7. SR results in terms of average PSNR (dB) and SSIM (%) values for 4 benchmark datasets degraded with GD by using a 7×7 GB kernel of standard deviation 1.6 with scaling factors of 2, 3 and 4.

Dataset	Scale	Methods				
		IRCNN[402]	DFAN[220]	RDN[414]	DRLN[22]	DIVA-A
Set5	2x	35.34/93.04	-/-	-/-	-/-	33.62/93.79
	3x	33.38/91.82	34.50/92.74	34.58/92.80	34.81/92.97	32.70/91.45
	4x	30.76/85.47	-/-	-/-	-/-	29.02/85.76
Set14	2x	31.98/88.49	-/-	-/-	-/-	30.88/90.65
	3x	29.63/82.81	30.43/84.19	30.53/84.47	30.81/84.87	28.97/83.47
	4x	27.73/74.12	-/-	-/-	-/-	26.86/76.01
BSD100	3x	28.65/79.22	29.17/80.58	29.23/80.79	29.40/81.21	28.26/80.65
Urban100	3x	26.77/81.54	28.27/85.26	28.46/85.82	29.11/86.97	27.72/84.92

∗*The symbol -/- denotes that the results were not provided in the original paper for a particular experiment.*

and GD respectively. One may observe that the recently introduced benchmark method DRLN [22] provides the best performance in both contexts. DRLN has a complex network architecture with dense residual Laplacian modules powered by 34 million parameters. In contrast, the proposed model has a much simpler architecture, and requires only 850K parameters approximately. Nevertheless, our model obtains the best SSIM for three datasets (*e.g.*, Set5, Set14 and BSD100) and among the top two SSIM for Urban100

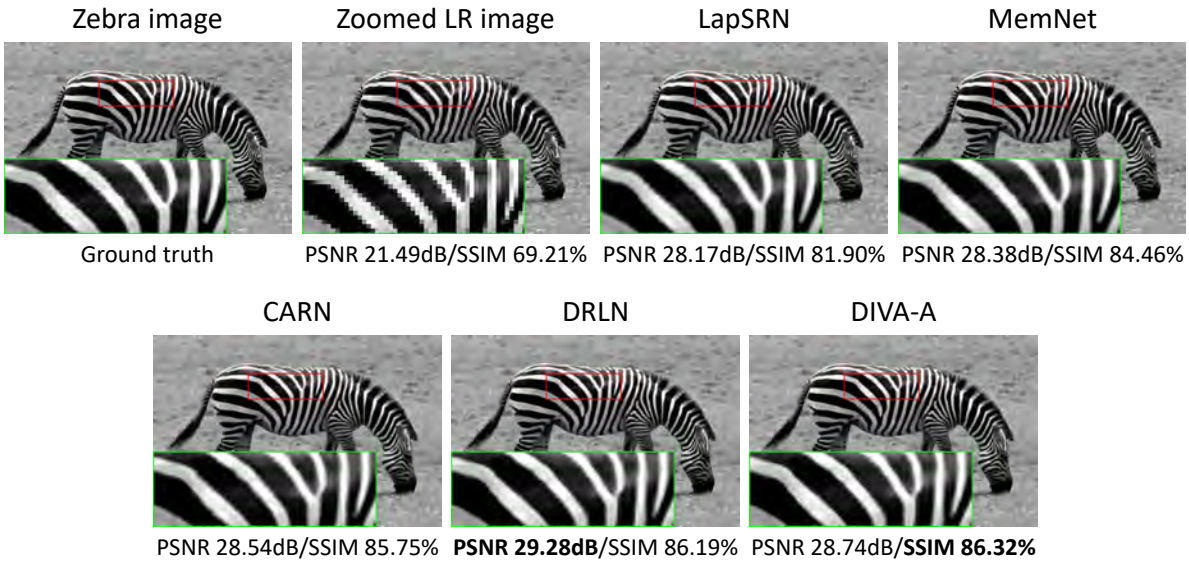

FIGURE 7.13. SR results for *Zebra* image for a bicubic downsampling with scaling factor 3.

images for BD. One can see an average gain of 1.5% SSIM by our method over DRLN in the BD scenario. For GD problems, our method struggles to produce competitive results against benchmark DRLN, RDN and DFAN approaches. Note that for SR problem our method upsamples the observed LR image by bicubic interpolation to obtain an initial HR image before enhancing it using the trained DL network.

The visual inspections of Figs. 7.13, 7.14, 7.15, 7.16, 7.17 and 7.18 illustrate the potential of our method for SR. Figs. 7.13 and 7.16 correspondingly display the restored HR images from the LR BD *Zebra*, *Baby-face*, *City-building* and *Fish* images with scale factors of 3 or 4. The visual effects of HR images recovered by our method are better than others and higher in accuracy. For example, in our retrieved HR images the stripes on the zebra's body, in *Baby-face* image the textures and shapes of eye, lips and nose, in *City-building* image the sharp edges of the windows, in *Fish* image the patterns on the fish and the shapes of the seagrass have better specifications than the other methods, such as LapSRN, MemNet, CARN. Figs. 7.17 and 7.18 show the reconstructed HR images from the LR *Book-cover* and *Flowers* images obtained by GD with scale factor of 2 and 3 respectively. In the degraded images, the small-scale details are nearly unrecognizable. Observation reveals that our method efficiently recovers the edges, patterns and texts of the original image from LR data. Moreover, our method strongly competes with the benchmark DRLN and beats it in some respects, especially in terms of overall visual

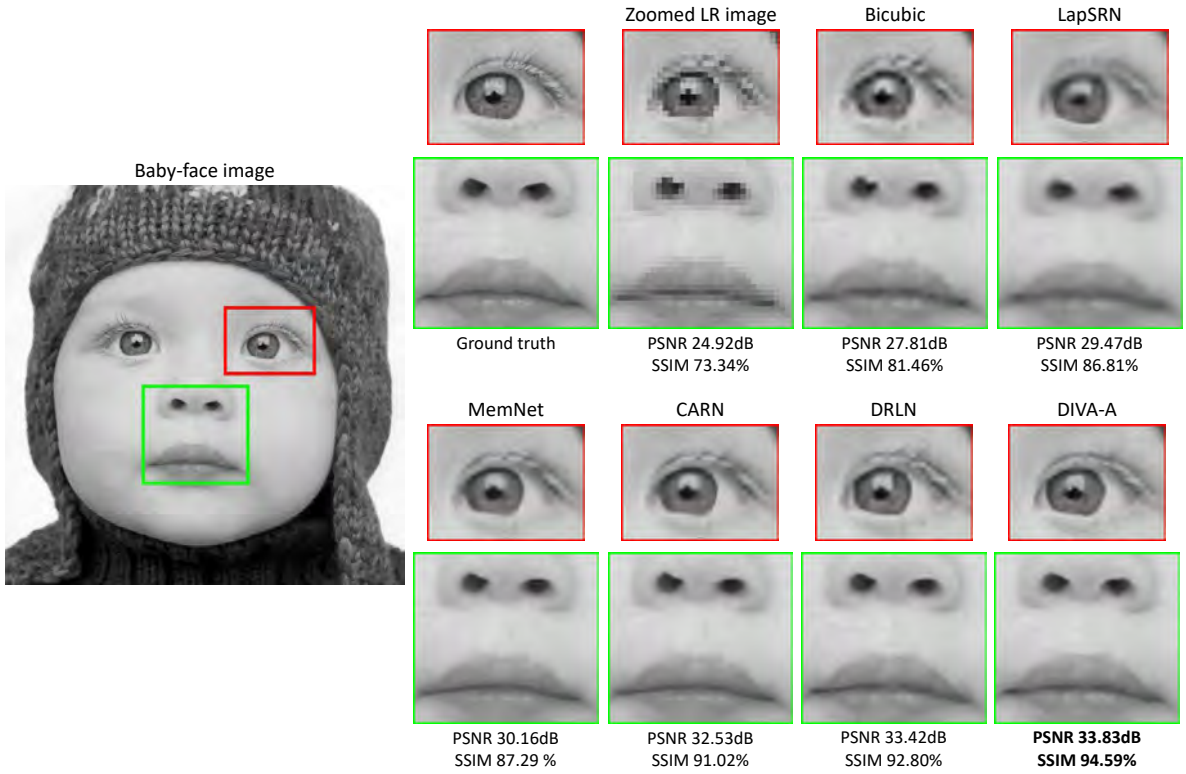

FIGURE 7.14. Two zoomed regions of the restored HR *Baby-face* images, extracted from SR results for a bicubic downsampling with scaling factor 4.

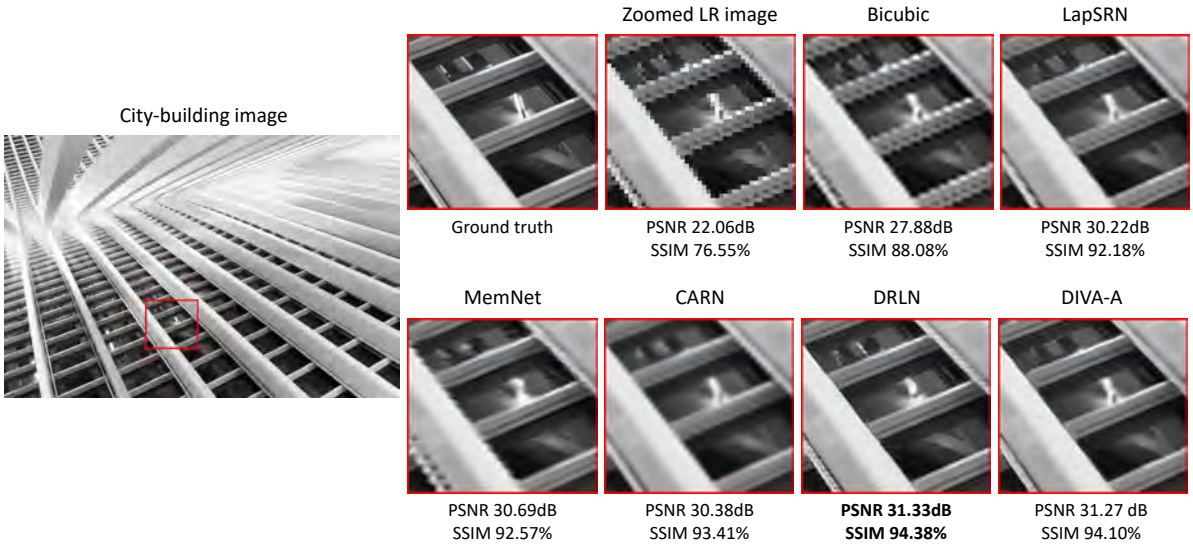

FIGURE 7.15. A zoomed regions of the restored HR *City-building* images, extracted from SR results for a bicubic downsampling with scaling factor 3.

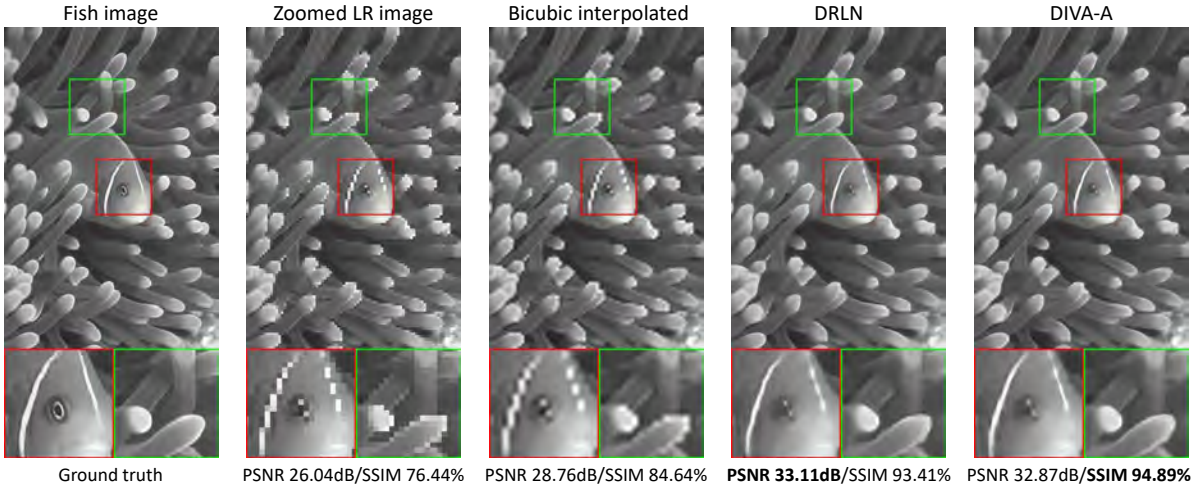

FIGURE 7.16. The restored HR *Fish* images from LR images generated by bicubic downsampling with scaling factor 4.

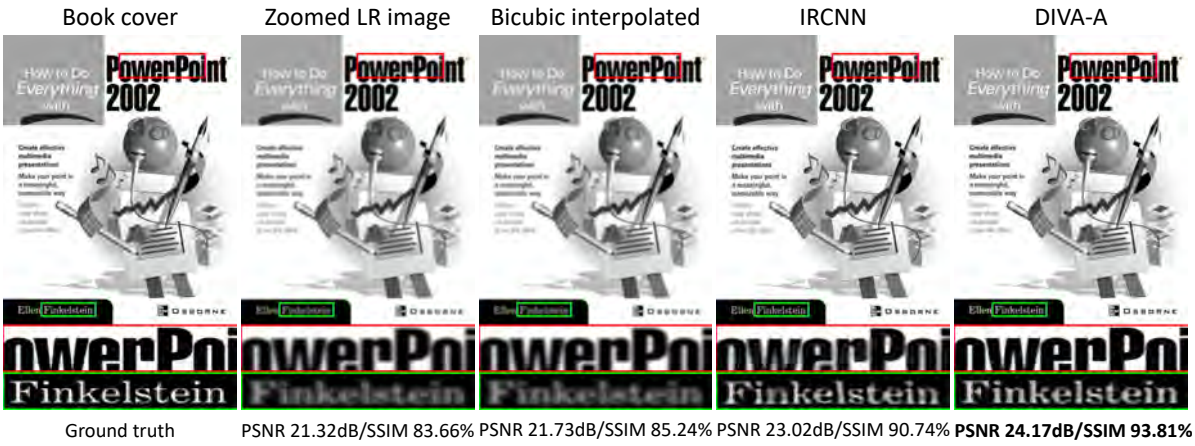

FIGURE 7.17. Restored HR *Book-cover* images from LR images generated by Gaussian downsampling under a 7×7 GB kernel of standard deviation 1.6 with scaling factor 2.

quality and preservation of the image structure compared to the state-of-the-art IRCNN, DFAN and RDN methods.

7.4.4.4 Image Inpainting

Table 7.8 illustrates our model performance in terms of average PSNR and SSIM on Set5 and Set12 datasets compared to the standard IRCNN network for image inpainting problems. Our model outperforms IRCNN in almost all situations when 20%, 50%, and

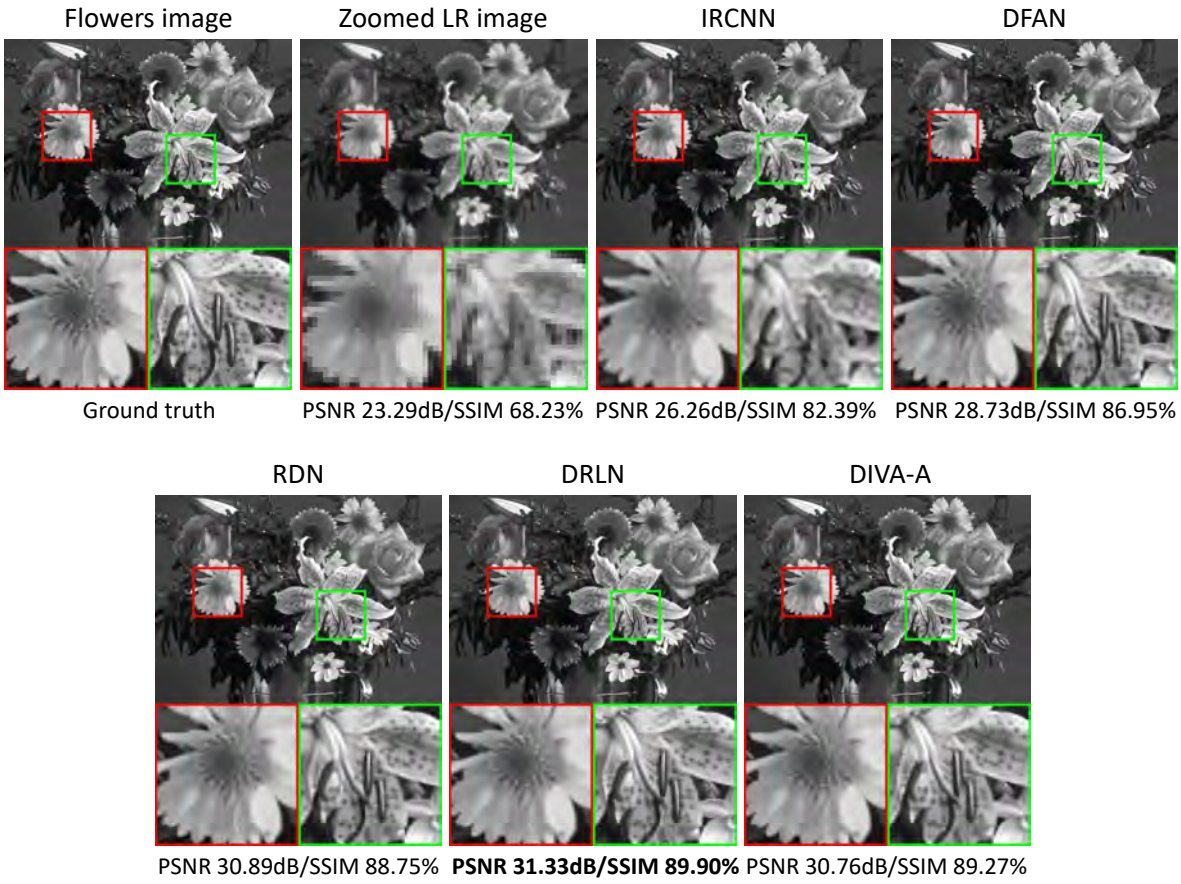

FIGURE 7.18. Restored HR *Flowers* images from LR images generated by Gaussian downsampling under a 7×7 Gaussian blur kernel of standard deviation 1.6 with scaling factor 3.

80% of random pixels are missing in the degraded observed images. DIVA-A provides a improvement of 0.2-1 dB in PSNR and 0.6-5.5% in SSIM over IRCNN and this gain increases with data lacking.

The visual analysis of Fig. 7.19 confirms the quantitative results. From the restored *F-16 Jet* image, it appears that our model efficiently reproduces the F-16 logo, borders and sharp edges despite 50% of data missing, whereas IRCNN fails to do so and loses/distorts many details in the restored output. Furthermore, in *Boat* image, despite 80% of data missing our model recovers minute details like the ropes and structures on the deck, on the contrary to the IRCNN model. Hence, our model can gather local information from the image neighborhood quite promisingly and delivers a high-quality restored image even with limited pixels available.

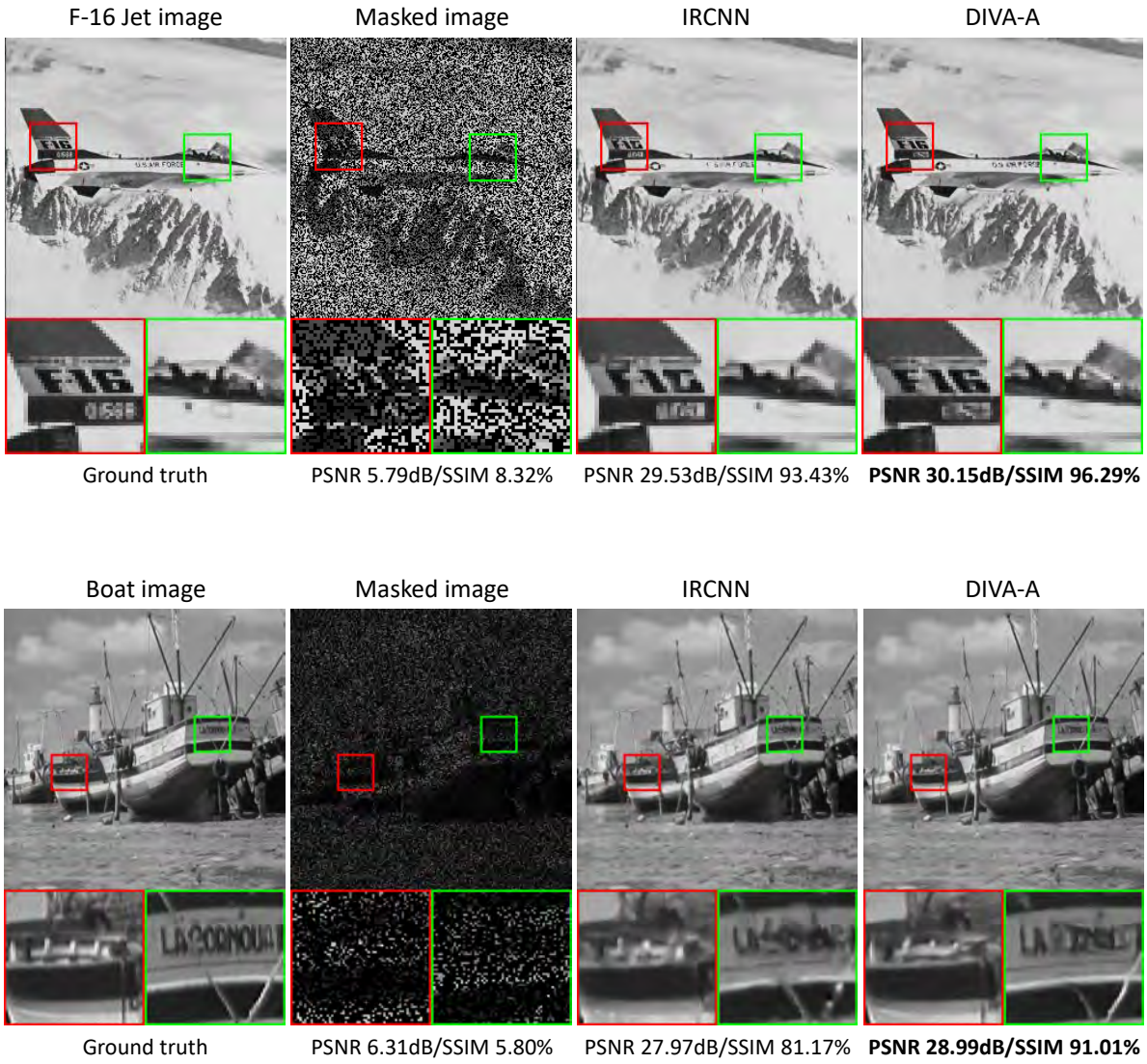

FIGURE 7.19. Image inpainting results by DIVA-A. The first row shows restored *F-16 Jet* images when 50% pixels' are missing and the second row shows restored *Boat* images when 80% pixels' are missing.

7.5 Adaptive Contrast Enhancement of Ultrasound Images

7.5.1 Background

Image enhancement, *i.e.*, contrast and spatial resolution improvement, have been extensively studied in ultrasound (US) imaging. Most techniques rely on adaptive beamforming to mitigate the drawbacks of delay-and-sum, despeckling to reduce speckle noise

TABLE 7.8. Image inpainting results in terms of average PSNR (dB) and SSIM (%) values for two benchmark datasets for respectively 20%, 50% and 80% pixels missing.

Dataset	Missing pixels'	Input	Methods	
			IRCNN[402]	DIVA-A
Set5	20%	13.33/38.61	41.62/98.67	41.85/99.24
	50%	9.34/23.44	35.57/95.87	36.08/97.84
	80%	7.29/12.40	29.41/88.54	30.38/94.01
Set12	20%	12.46/27.93	39.06/98.29	38.57/99.15
	50%	8.48/14.45	32.82/94.53	33.02/97.21
	80%	6.44/6.71	26.75/84.53	27.73/91.92

[110, 137, 211, 298, 394], or image deconvolution [244, 334] to increase spatial resolution by compensating the effect of the point spread function. Both model-based [13, 38] and machine learning-based [229, 247, 264, 265, 313] approaches have been proposed. The former rely on image formation models and statistical assumptions, while the latter offer more flexibility by learning the relationship between the observations and the target images.

7.5.2 Contributions

Our main objective is to address the US image enhancement problem by implementing our proposed deep unfolded network DIVA-A (see Subsection 7.3.2). In previous Chapter 6, we have already shown that the baseline De-QuIP algorithm demonstrates its ability in medical US image despeckling problem and offers a better image contrast compared to other state-of-the-art methods. In this section we will extend this by studying the clinical US image contrast enhancement problem using the deep unfolded version of original De-QuIP algorithm.

7.5.3 Network Training for Ultrasound Image Enhancement Tasks

Our proposed DIVA-A network was trained on 700 speckle-free image pairs. The clean images were extracted from 700 high-resolution human anatomy images (National Library of Medicine). The corresponding US images were simulated using SIMUS [76, 143] from MUST (MATLAB UltraSound Toolbox) [142], following a standard focused emission scheme. Patch size of 40 with a local window of size 70 were used during the

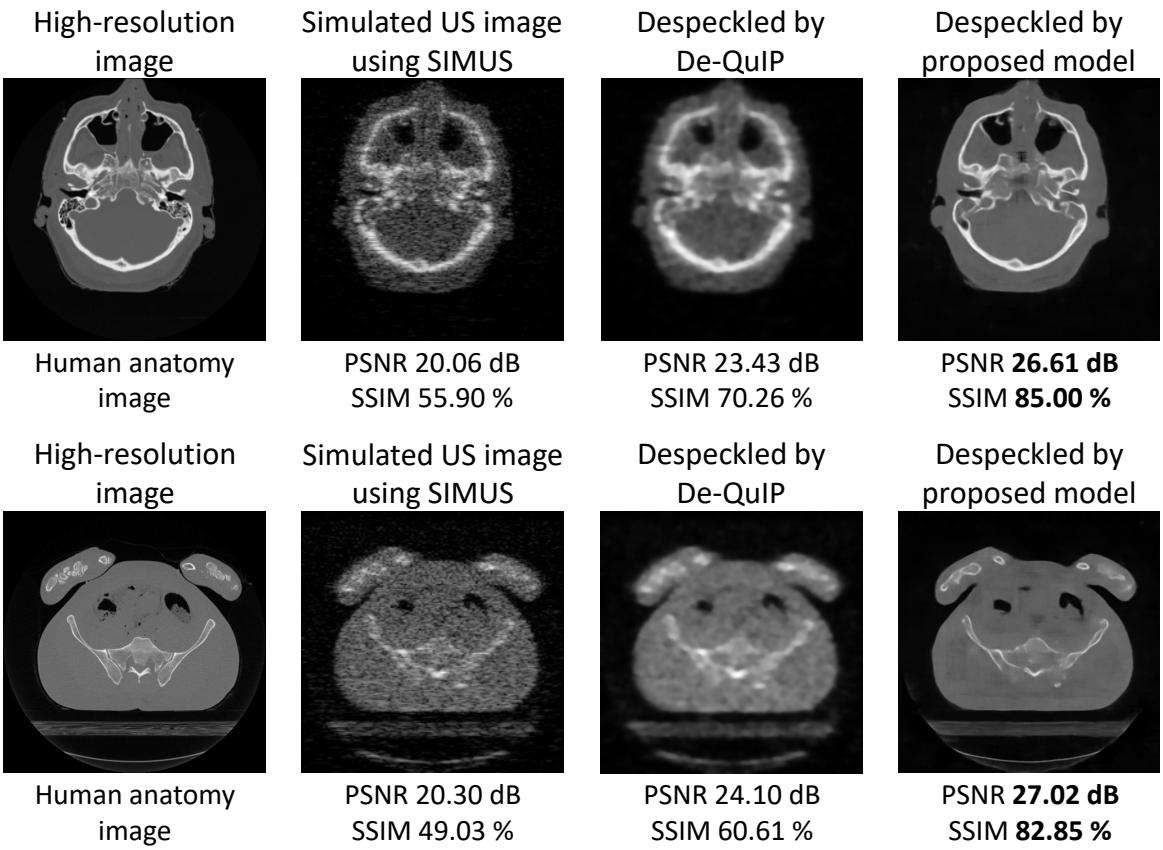

FIGURE 7.20. US image despeckling results using baseline De-QuIP and proposed unfolded deep-learning method DIVA-A for simulated US images.

training. The training was carried out in a supervised manner, with batches of size 256, using the Adam optimizer with an exponentially decaying learning rate ranging from 10^{-3} to 10^{-6} over 100 epochs. The training process took 15 hours to reach convergence using NVIDIA GTX 1080 Ti GPU implemented in Keras frameworks.

7.5.4 Experimental Results on Ultrasound Images

The potential of the proposed DIVA-A network is illustrated through simulated and real cardiac US image enhancement tasks.

Fig. 7.20 depicts despeckling results for simulated human anatomy US images using SIMUS, by original De-QuIP and the proposed DL methods, where peak-signal-to-noise ratio (PSNR) and structural similarity (SSIM) were calculated for quantitative assessment (the best values are in bold). These results prove that the proposed DL model offers a significant improvement in spatial resolution and contrast, with a negligible

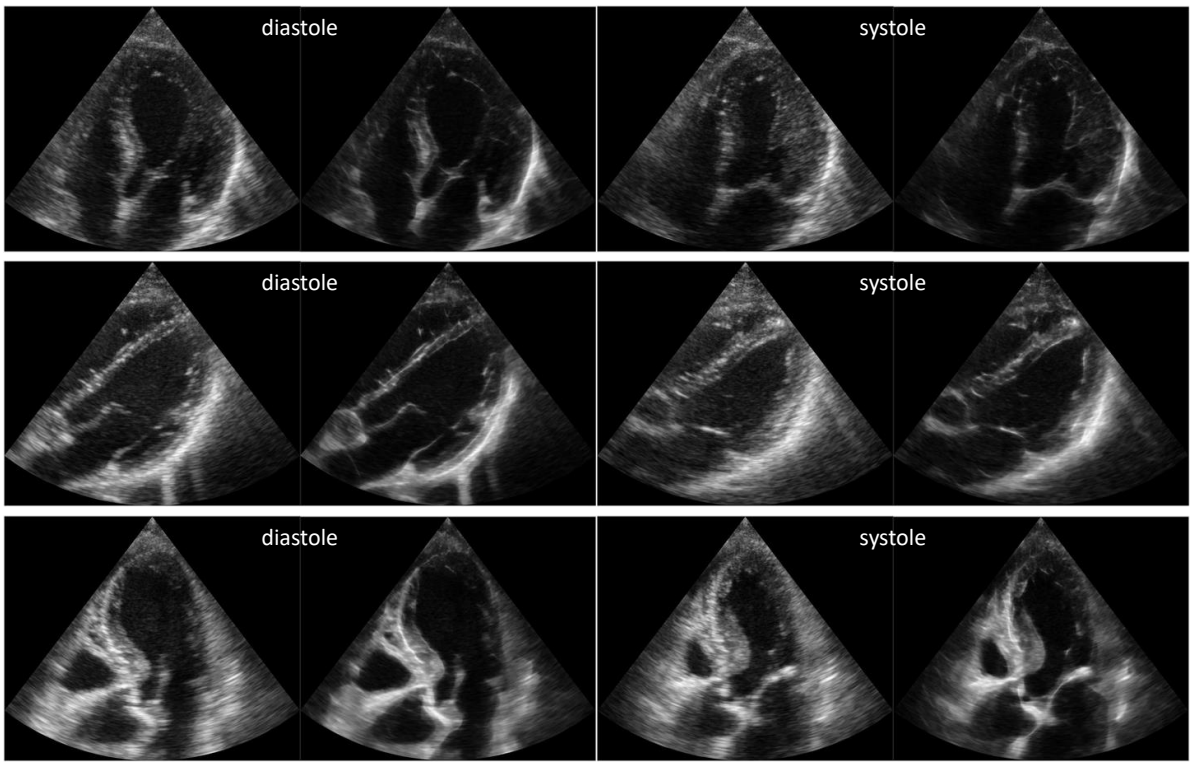

FIGURE 7.21. Snapshots in three patients during diastole and systole. The left-hand images are the original images acquired with a GE scanner and the right-hand images are the corresponding enhanced versions using our DIVA-A network.

presence of speckle compared to De-QuIP. Quantitative data follow similar conclusions.

Furthermore, the performance of our network was evaluated on >700 clinical cardiac images acquired in adults with a GE Vivid e95 during routine examinations. To obtain contrast-enhanced echocardiographic scans, we generated composite images by fusing the original and De-QuIP-derived images. Fig. 7.21 illustrates six of these cardiac images acquired from three patients during diastole and systole compared with their enhanced versions.

The enhanced images show a gain in contrast and resolution while preserving underlying structures and significantly reducing speckle. For more visual illustrations, three movies with these enhanced cardiac images are available in the GitHub file[1].

[1] github.com/SayantanDutta95/Cardiac-USimage-Enhancement

7.6 Discussions

In this section, we briefly recap the benefits and limitations of our proposed networks and future prospects in this regard.

7.6.1 Advantages

With the quantum principles of the baseline De-QuIP algorithm, our proposed DIVA/DIVA-A network provides an efficient DL method for image restoration following the deep unfolding philosophy. Indeed, the use of quantum concepts like patch interaction layer and Hamiltonian kernel makes our models better equipped than others. The local structure/similarities in an image neighborhood are preserved through the interaction layer exploiting the local patch groups that convey an intrinsic non-local network architecture. Processing of the local information by this interaction layer significantly enhances the performances of the network. It even yields a smaller network depth, leading to a good trade-off between the performance and computational cost, as portrayed in Subsection 7.4.3. Harnessing the power of back-propagation, our networks uniquely tune all hyperparameters, such as proportionality constant, Planck constant and thresholding energy, for each patch. This enables network adaptability with several image restoration tasks, and leads to promising performances. Moreover, our proposed network shows sophisticated performance in real medical US image enhancement problems. The enhanced images show a gain in contrast and resolution while preserving underlying structures and significantly reducing speckle.

7.6.2 Limitations

In the case of a challenging image degradation task, our method may sometimes struggle to produce a better recovered image than other benchmarks. To restore a Gaussian downsampled LR image, we notice that our DL model fails to compete in quantitative data against benchmark methods, like DRLN, RDN, and DFAN, as noted in Table 7.7. However, the overall visual efficiency of our method is good, as depicted in Fig. 7.17. From our observations, in presence of a strong decay, such as 'blur+downsampling', our method does not match the true pixels' intensity, which seems to be the main reason for the lower quantitative measures. Instead, our method utilizes the interaction layer to provide better visual quality by preserving the image structure, patterns, and textures with more details. Furthermore, our proposed models are trained in an end-to-end supervised

manner, *i.e.*, we need the clean-degraded image pairs for training. However it is worth-noting that the proposed method is much simpler and not specialized in a specific task as is the case for the other methods.

7.6.3 Perspectives

The quantum mechanics-based imaging methods open up a broad spectrum of future prospects. Following the limitations, the obvious direction would be an unsupervised DL network design, that essentially solves the training data problem and extends our reach to real-life applications more reliably [68, 89, 266]. Another possibility is to design a versatile network by stacking the proposed DIVA to build a deep and more complex architecture like UNet [194] and offer some attention mechanisms [22] to make the patch interaction robust while preserving the core philosophy. This complex network system should enhance the capacity of the proposed network in challenging degradation operators and even for blind imaging problems. Furthermore, the idea of quantum interaction can also be treated as a transformer in a deep architecture [367]. Another interesting prospect would be to explore imaging problems beyond the Gaussian model since baseline De-QuIP is well-adapted for such tasks without modifying the global architecture. Combining graph signal processing model with the proposed quantum-based interaction framework is also an interesting perspective [170].

7.7 Conclusions

This chapter introduces a novel neural network approach to solve image denoising problems, further extended to general image restoration tasks relying on the philosophy of quantum many-body theory. Our model recasts the baseline De-QuIP algorithm into a DL framework and optimizes the relevant parameters by exploiting the power of back-propagation approach. The proposed unfolded CNN architecture inherently employs various quantum mechanical components, such as interaction and Hamiltonian operator, from its baseline method to boost up the network performance while significantly reducing the training cost.

Integration of these key features from the quantum theory enables our proposed model to be well-adapted for handling several imaging problems efficiently. We conduct thorough ablation investigations and present extensive assessments regarding the network design. Finally, we perform comprehensive evaluations of our proposed

DL methods for various imaging problems, such as denoising, deblurring, single image super-resolution, and inpainting. In all cases, notable improvements were shown in the image restoration performance, especially overall visual quality, compared to standard well-established techniques from the literature.

Furthermore, in real-life problems, experimental results showed significant improvement in the resolution and contrast of the clinical cardiac data while preserving the essence of the baseline structure. Indeed, our DL model significantly reduces the speckle in the restored enhanced US images much better than its baseline De-QuIP algorithm.

CHAPTER 8

Conclusions and Perspectives

Contents

Overview

This chapter proposes a summary of the work of this thesis and outlines possible directions for future work on these topics.

8.1 Conclusions

The objective of this thesis was to explore new imaging methodologies based on a quantum mechanical framework, particularly for image restoration problems, borrowing principles and axioms of quantum mechanics. In contrast to the quantum computing and quantum information theory, quantum mechanics-based algorithms do not entirely depend on the physics associated with quantum mechanics and give us the freedom to impose quantum mechanical constraints that we find useful for imaging problems. Indeed, we showed that the implementation of such quantum principles in imaging problems significantly increases the performance of algorithms. Thus, exploiting the concepts of quantum physics, these algorithms were enabled to deal with real-life problems such as medical imaging, computer vision, etc, much better than some traditional methods.

The first work conducted in this thesis was introduced in Chapter 4, where we presented in detail a new approach of constructing a signal or image-dependent bases inspired by quantum mechanics tools, more precisely, by considering the signal or image as a potential in the discretized Schrödinger equation, the solution of which gives eigenvectors that form the proposed adaptive basis. The basis vectors automatically use a different range of frequencies to explore low potential valued regions compared to the regions corresponding to the high potential values. Therefore, thresholding the projection coefficients of the stretched signal or image on this basis treats the high and low values of the signal or image differently. To illustrate the potential of the proposed decomposition, denoising results were reported in the case of Gaussian, Poisson, and speckle noise and compared to state-of-the-art algorithms based on wavelet shrinkage, total variation regularization or patch-wise sparse coding in learned dictionaries, non-local means image denoising, and graph signal processing. The results showed that our denoising procedure outperforms standard methods in specific cases, and ranked among the best methods in most cases. In general, the method performed much better for signals or images with large contrasts in presence of Poisson-like noise. Furthermore, in real medical dental computed tomography images, our proposed method demonstrated the ability to enhance the noisy cone beam computed tomography images while preserving the canal root, which is the region of interest.

In Chapter 5, we proposed a new Plug-and-Play (PnP) alternating direction of multipliers (ADMM) scheme for Poisson deconvolution problems by embedding a computationally more efficient quantum adaptive denoiser than the one introduced in the previous Chapter 4. Numerical results showed the efficiency and good adaptability of

the proposed scheme compared to recent state-of-the-art techniques, for both high and low signal-to-noise ratio scenarios. This performance gain regardless of the amount of noise affecting the observations is explained by the flexibility of the embedded quantum denoiser constructed without anticipating any prior statistics about the noise, which is one of the main advantages of this method. Finally, we illustrated the efficiency of the proposed method in real fluorescence microscopy image enhancement tasks, which are intrinsically contaminated with Poisson-Gaussian noise.

In Chapter 6, we developed a new image denoising algorithm exploiting an image-dependent basis inspired by the quantum many-body theory. Based on patch analysis, the similarity measures in a local image neighborhood are formalized through a term akin to interaction in quantum mechanics that can efficiently preserve the local structures of real images. Through these interactions, structural details are transmitted on a patch-based adaptive basis created by the solutions of the Schrödinger equation of quantum mechanics, which can be exploited as filters for denoising the patches. The versatile nature of this adaptive basis extends the scope of its application to image-independent or image-dependent noise scenarios without any adjustment. We carried out a comprehensive comparison with contemporary methods to demonstrate the denoising capability of the proposed algorithm regardless of the image characteristics, noise statistics and intensity. Experimental results revealed that the proposed method convincingly beats other schemes and provides a better comparison with the best results for both image-independent and image-dependent noise models. Additionally, this newly proposed method, which is indeed a generalization of the earlier single-particle based quantum scheme of Chapter 4, achieved much better results at a significantly less computational cost in comparison with its first version of Chapter 4. In real-life problems, this newly proposed quantum mechanics-based algorithm demonstrated good performances, for example, in medical ultrasound image despeckling and clinical dental computed tomography image super-resolution applications.

Finally, in Chapter 7, we introduced an original deep-learning approach to solve image denoising problems, further extended to general image restoration tasks relying on the philosophy of quantum many-body theory. Our model unfolds the baseline adaptive denoising algorithm as proposed in previous Chapter 6, into a deep-learning framework and optimizes the relevant parameters by exploiting the power of back-propagation approach. Absorption of various quantum mechanical components from its baseline method significantly increased the network performance while reducing training costs. We have performed comprehensive evaluations of our proposed deep networks for various imaging

tasks, such as denoising, deblurring, single image super-resolution, and inpainting and observed notable improvements, especially in overall visual quality, compared to standard well-established techniques from the literature. Furthermore, experimental results with clinical cardiac ultrasound images showed significant improvement in the resolution and contrast while preserving underlying structures and significantly reducing speckles.

8.2 Future Perspectives

The quantum mechanics-based imaging methods open up a broad spectrum of future prospects. In this last section, we propose some subjects of interest that could lead to potentially valuable results. Some are ideas that suggest directions of research. Others are already planned as future work. We provide these perspectives as a list.

8.2.1 How to Design a Robust Deep-Learning Model

In this subsection, we propose some key elements that could allow to improve our proposed deep-learning methods presented in Chapter 7.

- **Network training:** Our proposed deep unfolded model DIVA/DIVA-A, as presented in Chapter 7, was trained in a supervised manner exploiting the pairs of clean and degraded images. In the absence of ground truth, training is no longer a straightforward process. The possible solutions of that is to design an unsupervised [16, 17, 68, 89, 266] deep-learning network by assigning a flexible prior model, or implement the framework of transfer learning [261, 349, 378] and domain adaptation [3, 29, 381]. Using such schemes essentially solves the training data problem and extends our reach to real-life applications more reliably.

- **Network architecture:** It is possible to design a more versatile network architecture implementing UNet [74, 194] or VNet [4, 279] frameworks while preserving the core philosophy of our proposed deep-learning model DIVA. Furthermore, the patch interaction framework can be offered as an attention mechanism [22] in the modified deep network. This complex network system should enhance the capacity of the proposed network in challenging degradation operators and even for blind imaging problems. Besides that, the idea of quantum interaction framework can also be treated as a transformer in a deep architecture [367], where the interactions between patches are defined by attention mechanism.

- **Loss Function:** The mean squared error (MSE) between the predicted and original residuals is adopted as the loss function in our network. Our models perform well with this loss function in terms of visual quality. But it is possible to use different other loss functions, for example, perceptual loss [184, 219, 276, 386], which exploits similarities between two images, that could significantly boost our model performances.

8.2.2 Other Quantum Mechanical Tools

Here we propose some quantum mechanical concepts that can be exploited in future for imaging problems.

- **Time-dependent Schrödinger equation:** As discussed in Chapter 2, in the time-dependent Schrödinger equation the Hamiltonian operator depends on time. Therefore, there are no stationary solutions of the Schrödinger equation anymore. However, for Hamiltonian periodic in time, one can use Floquet theory [30] and follow a similar formalism as in this thesis using eigenfunctions of the evolution operator over one period. This theory can be implemented for the processing of periodic signals [377].

- **Quantum Harmonic Oscillator:** For the image segmentation problem [391] proposed an idea to associate each pixel with a quantum harmonic oscillator, where the Hamiltonian operator is derived from the features extracted at the pixel level. In that scenario from the time evolution of an initial ground state, one can extract the image features and use them for segmentation. This idea of assigning image pixels with quantum harmonic oscillators can be further extended to other imaging problems.

8.2.3 Extension to Quantum Computing and Quantum Information Theory

In this thesis, we have studied the paradigm of quantum mechanics-based image processing algorithms where the computations are performed on conventional computers. In view of the recent developments in quantum information and computation, it is a natural idea to adapt these algorithms for quantum computers.

- **Quantum denoising:** We have recently begun to develop such an approach. Indeed, it is possible to build unitary operators to transform and store classical signals or images into quantum states by exploiting qubits and quantum logic gates [412]. We have thus constructed a computationally efficient denoising scheme in the line of the preceding methods by using various transformation and Grover's quantum search [153] on these quantum states to perform denoising. Finally, by taking quantum measurements, one can restore the denoised classical signals or images. Fig 8.1 illustrates a preliminary result for signal denoising using this prototype quantum algorithm. Although this work is still in progress, our results indicate that the proposed quantum algorithm gives comparable denoising results utilizing less computational power than its classical equivalent.

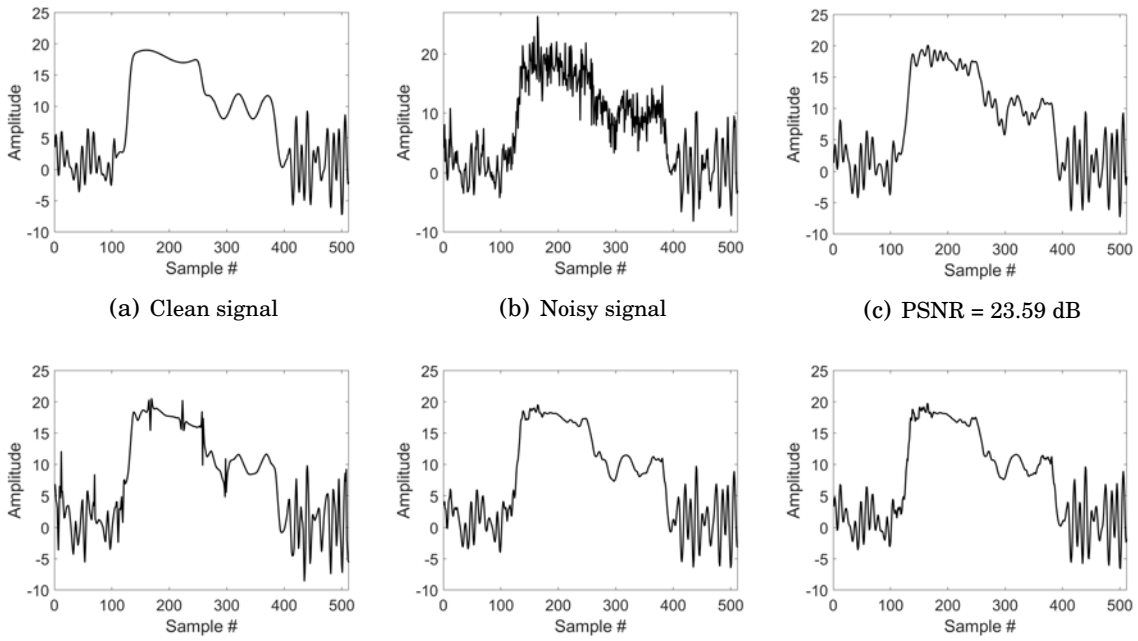

(a) Clean signal (b) Noisy signal (c) PSNR = 23.59 dB

(d) PSNR = 24.64 dB (e) PSNR = 27.63 dB (f) PSNR = 27.24 dB

FIGURE 8.1. Denoising results using a quantum algorithm (prototype) for synthetic signal corrupted with Poisson noise corresponding to a SNR of 15 dB. (a) Clean synthetic signal, (b) Signal corrupted with Poisson noise corresponding to a SNR of 15 dB. Denoising results obtained using, (c) Fourier transformation, (d) wavelet hard thresholding, (e) proposed quantum adaptive basis from Chapter 4 and (f) proposed quantum algorithm (prototype) for denoising.

APPENDIX

CODES

MatLab and **Python** implementations of the algorithms proposed in this thesis are available in my **GitHub** file:
`https://github.com/SayantanDutta95`

BIBLIOGRAPHY

[1] *Fluorescence microscopy image dataset*, http://tinyurl.com/y6mwqcjs.

[2] A. ABBAS, D. SUTTER, C. ZOUFAL, A. LUCCHI, A. FIGALLI, AND S. WOERNER, *The power of quantum neural networks*, Nature Computational Science, 1 (2021), pp. 403–409.

[3] C. ABBET, L. STUDER, A. FISCHER, H. DAWSON, I. ZLOBEC, B. BOZORGTABAR, AND J.-P. THIRAN, *Self-rule to adapt: Learning generalized features from sparsely-labeled data using unsupervised domain adaptation for colorectal cancer tissue phenotyping*, in Medical Imaging with Deep Learning, 2021.

[4] A. ABDOLLAHI, B. PRADHAN, AND A. ALAMRI, *Vnet: An end-to-end fully convolutional neural network for road extraction from high-resolution remote sensing data*, IEEE Access, 8 (2020), pp. 179424–179436.

[5] A. ABDULAZIZ, D. YAO, Y. ALTMANN, AND S. MCLAUGHLIN, *Blind deconvolution of images corrupted by gaussian noise using expectation propagation*, in 2021 29th European Signal Processing Conference (EUSIPCO), IEEE, 2021, pp. 1970–1974.

[6] S. ACHARD, P. BORGNAT, I. GANNAZ, AND M. ROUX, *Wavelet-Based Graph Inference Using Multiple Testing*, in Wavelets and Sparsity XVIII, D. V. D. Ville, M. Papadakis, and Y. M. Lu, eds., vol. 11138, International Society for Optics and Photonics, SPIE, 2019, p. 1113811.

[7] A. ACHIM, A. BEZERIANOS, AND P. TSAKALIDES, *Novel bayesian multiscale method for speckle removal in medical ultrasound images*, IEEE Transactions on Medical Imaging, 20 (2001), pp. 772–783.

[8] M. V. AFONSO, J. M. BIOUCAS-DIAS, AND M. A. T. FIGUEIREDO, *Fast image recovery using variable splitting and constrained optimization*, IEEE Transactions on Image Processing, 19 (2010), pp. 2345–2356.

[9] E. AGUSTSSON AND R. TIMOFTE, *NTIRE 2017 challenge on single image super-resolution: Dataset and study*, in Proceedings of the IEEE Conference on Computer Vision and Pattern Recognition Workshops (CVPRW), 2017, pp. 126–135.

[10] M. AHARON, M. ELAD, AND A. BRUCKSTEIN, *K-svd: An algorithm for designing overcomplete dictionaries for sparse representation*, IEEE Transactions on Signal Processing, 54 (2006), pp. 4311–4322.

[11] M. AHARON, M. ELAD, AND A. BRUCKSTEIN, *rmk-svd: An algorithm for designing overcomplete dictionaries for sparse representation*, IEEE Transactions on Signal Processing, 54 (2006), pp. 4311–4322.

[12] N. AHN, B. KANG, AND K. SOHN, *Fast, accurate, and lightweight super-resolution with cascading residual network*, in Proceedings of the European Conference on Computer Vision (ECCV), 2018, pp. 252–268.

[13] M. ALESSANDRINI, S. MAGGIO, J. POREE, L. DE MARCHI, N. SPECIALE, E. FRANCESCHINI, O. BERNARD, AND O. BASSET, *A restoration framework for ultrasonic tissue characterization*, IEEE Transactions on Ultrasonics, Ferroelectrics, and Frequency Control, 58 (2011), pp. 2344–2360.

[14] M. S. C. ALMEIDA AND M. A. T. FIGUEIREDO, *Deconvolving images with unknown boundaries using the alternating direction method of multipliers*, IEEE Transactions on Image Processing, 22 (2013), pp. 3074–3086.

[15] Y. ALTMANN, R. ASPDEN, M. PADGETT, AND S. MCLAUGHLIN, *A bayesian approach to denoising of single-photon binary images*, IEEE Transactions on Computational Imaging, 3 (2017), pp. 460–471.

[16] Y. ALTMANN, N. DOBIGEON, S. MCLAUGHLIN, AND J.-Y. TOURNERET, *Unsupervised nonlinear unmixing of hyperspectral images using gaussian processes*, in 2012 IEEE International Conference on Acoustics, Speech and Signal Processing (ICASSP), 2012, pp. 1249–1252.

[17] Y. ALTMANN, S. MCLAUGHLIN, AND M. PADGETT, *Unsupervised restoration of subsampled images constructed from geometric and binomial data*, in 2017

IEEE 7th International Workshop on Computational Advances in Multi-Sensor Adaptive Processing (CAMSAP), 2017, pp. 1–5.

[18] Y. ALTMANN, S. MCLAUGHLIN, M. PADGETT, V. GOYAL, A. HERO, AND D. FACCIO, *Quantum-inspired computational imaging*, Science, 361 (2018), p. 6403.

[19] P. W. ANDERSON, *Absence of diffusion in certain random lattices*, Physical review, 109 (1958), pp. 1492–1505.

[20] P. W. ANDERSON, *Ill-Condensed Matter: Les Houches 1978, Session XXXI*, R. Balian, R. Maynard, G. Toulouse, eds., North-Holland, New York, 1979.

[21] F. J. ANSCOMBE, *The transformation of poisson, binomial and negative-binomial data*, Biometrika, 35 (1948), pp. 246–254.

[22] S. ANWAR AND N. BARNES, *Densely residual laplacian super-resolution*, IEEE Transactions on Pattern Analysis and Machine Intelligence, 44 (2022), pp. 1192–1204.

[23] J.-F. AUJOL, G. AUBERT, AND L. BLANC-FÉRAUD, *Wavelet-based level set evolution for classification of textured images*, IEEE Transactions on Image Processing, 12 (2003), pp. 1634–1641.

[24] C. AYTEKIN, S. KIRANYAZ, AND M. GABBOUJ, *Quantum mechanics in computer vision: Automatic object extraction*, in IEEE International Conference on Image Processing, Sept 2013, pp. 2489–2493.

[25] Ç. AYTEKIN, S. KIRANYAZ, AND M. GABBOUJ, *Quantum mechanics in computer vision: Automatic object extraction*, in Proc. IEEE International Conference on Image Processing (ICIP), 2013, pp. 2489–2493.

[26] L. AZZARI AND A. FOI, *Variance stabilization for noisy+estimate combination in iterative poisson denoising*, IEEE Signal Processing Letters, 23 (2016), pp. 1086–1090.

[27] L. AZZARI AND A. FOI, *Variance stabilization in poisson image deblurring*, in 2017 IEEE 14th International Symposium on Biomedical Imaging (ISBI 2017), 2017, pp. 728–731.

[28] Y. BAI, W. CHEN, J. CHEN, AND W. GUO, *Deep learning methods for solving linear inverse problems: Research directions and paradigms*, Signal Processing, 177 (2020), p. 107729.

[29] A. BARBE, P. GONÇALVES, M. SEBBAN, P. BORGNAT, R. GRIBONVAL, AND T. VAYER, *Optimization of the diffusion time in graph diffused-wasserstein distances: Application to domain adaptation*, in 2021 IEEE 33rd International Conference on Tools with Artificial Intelligence (ICTAI), 2021, pp. 786–790.

[30] S. R. BARONE, M. A. NARCOWICH, AND F. J. NARCOWICH, *Floquet theory and applications*, Physical Review A, 15 (1977), p. 1109.

[31] H. H. BAUSCHKE AND P. L. COMBETTES, *Convex analysis and monotone operator theory in Hilbert spaces*, vol. 408, Springer, 2011.

[32] A. BECK AND M. TEBOULLE, *Fast gradient-based algorithms for constrained total variation image denoising and deblurring problems*, IEEE Transactions on Image Processing, 18 (2009), pp. 2419–2434.

[33] A. BECK AND M. TEBOULLE, *A fast iterative shrinkage-thresholding algorithm for linear inverse problems*, SIAM Journal on Imaging Sciences, 2 (2009), pp. 183–202.

[34] A. BECK AND M. TEBOULLE, *A fast iterative shrinkage-thresholding algorithm with application to wavelet-based image deblurring*, in 2009 IEEE International Conference on Acoustics, Speech and Signal Processing, 2009, pp. 693–696.

[35] J. F. BENDERS, *Partitioning procedures for solving mixed-variables programming problems*, Numerische mathematik, 4 (1962), pp. 238–252.

[36] Y. BENGIO, *Learning deep architectures for ai*, Foundations and Trends® in Machine Learning, 2 (2009), pp. 1–127.

[37] L. BÉTHUNE, Y. KALOGA, P. BORGNAT, A. GARIVIER, AND A. HABRARD, *Hierarchical and unsupervised graph representation learning with loukas's coarsening*, Algorithms, 13 (2020).

[38] K. BINAEE AND R. P. HASANZADEH, *An ultrasound image enhancement method using local gradient based fuzzy similarity*, Biomedical Signal Processing and Control, 13 (2014), pp. 89–101.

[39] J. M. BIOUCAS-DIAS AND M. A. T. FIGUEIREDO, *A new TwIST: Two-step iterative shrinkage/thresholding algorithms for image restoration*, IEEE Transactions on Image Processing, 16 (2007), pp. 2992–3004.

[40] M. BORGERDING, P. SCHNITER, AND S. RANGAN, *Amp-inspired deep networks for sparse linear inverse problems*, IEEE Transactions on Signal Processing, 65 (2017), pp. 4293–4308.

[41] J. BOULANGER, C. KERVRANN, P. BOUTHEMY, P. ELBAU, J.-B. SIBARITA, AND J. SALAMERO, *Patch-based nonlocal functional for denoising fluorescence microscopy image sequences*, IEEE Transactions on Medical Imaging, 29 (2010), pp. 442–454.

[42] S. BOYD, N. PARIKH, E. CHU, B. PELEATO, J. ECKSTEIN, ET AL., *Distributed optimization and statistical learning via the alternating direction method of multipliers*, Now Publishers, Inc., 2011.

[43] B. BOZORGTABAR, M. S. RAD, D. MAHAPATRA, AND J.-P. THIRAN, *Syndemo: Synergistic deep feature alignment for joint learning of depth and ego-motion*, in Proceedings of the IEEE/CVF International Conference on Computer Vision, 2019, pp. 4210–4219.

[44] S. BRANDT AND H. D. DAHMEN, *The Picture Book of Quantum Mechanics*, Springer New York, 2013.

[45] A. BRIASSOULI AND N. AHUJA, *Extraction and analysis of multiple periodic motions in video sequences*, IEEE Transactions on Pattern Analysis and Machine Intelligence, 29 (2007), pp. 1244–1261.

[46] A. BRIFMAN, Y. ROMANO, AND M. ELAD, *Turning a denoiser into a super-resolver using plug and play priors*, in 2016 IEEE International Conference on Image Processing (ICIP), 2016, pp. 1404–1408.

[47] A. BUADES, B. COLL, AND J.-M. MOREL, *A non-local algorithm for image denoising*, in 2005 IEEE Computer Society Conference on Computer Vision and Pattern Recognition (CVPR'05), vol. 2, 2005, pp. 60–65 vol. 2.

[48] A. BUADES, B. COLL, AND J.-M. MOREL, *A review of image denoising algorithms, with a new one*, SIAM Multiscale Multiscale Modeling & Simulation, 4 (2005), pp. 490–530.

[49] A. BUADES, B. COLL, AND J.-M. MOREL, *A review of image denoising algorithms, with a new one*, SIAM Multiscale Modeling and Simulation, 4 (2005), pp. 490–530.

[50] A. BUADES, B. COLL, AND J.-M. MOREL, *Nonlocal image and movie denoising*, International Journal of Computer Vision, 76 (2008), pp. 123–139.

[51] H. BURGER, C. SCHULER, AND S. HARMELING, *Image denoising: Can plain neural networks compete with BM3D?*, in IEEE Conference on Computer Vision and Pattern Recognition (CVPR), 2012, pp. 2392–2399.

[52] E. J. CANALES-RODRÍGUEZ, J. H. LEGARRETA, M. PIZZOLATO, G. RENSONNET, G. GIRARD, J. RAFAEL-PATINO, M. BARAKOVIC, D. ROMASCANO, Y. ALEMAN-GOMEZ, J. RADUA, ET AL., *Sparse wars: A survey and comparative study of spherical deconvolution algorithms for diffusion MRI*, NeuroImage, 184 (2019), pp. 140–160.

[53] E. CANDÉS, L. DEMANET, D. DONOHO, AND L. YING, *Fast discrete curvelet transforms*, Multiscale Modeling & Simulation, 5 (2006), pp. 861–899.

[54] M. CARLAVAN AND L. BLANC-FÉRAUD, *Sparse poisson noisy image deblurring*, IEEE Transactions on Image Processing, 21 (2012), pp. 1834–1846.

[55] M. CEREZO AND P. J. COLES, *Higher order derivatives of quantum neural networks with barren plateaus*, Quantum Science and Technology, 6 (2021), p. 035006.

[56] A. CHAHID, S. BHADURI, M. WALI, E. ACHTEN, H. SERRAI, AND T.-M. LALEG-KIRATI, *Semi-classical signal analysis method with soft-thresholding for mrs denoising*, in ISMRM 27th Annual meeting & exhibition, 2019.

[57] A. CHAHID, H. SERRAI, E. ACHTEN, AND T.-M. LALEG-KIRATI, *A new roi-based performance evaluation method for image denoising using the squared eigenfunctions of the schrödinger operator*, in 2018 40th Annual International Conference of the IEEE Engineering in Medicine and Biology Society (EMBC), IEEE, 2018, pp. 5579–5582.

[58] R. H. CHAN, M. TAO, AND X. YUAN, *Constrained total variation deblurring models and fast algorithms based on alternating direction method of multipliers*, SIAM Journal on Imaging Sciences, 6 (2013), pp. 680–697.

[59] S. H. CHAN, *Algorithm-induced prior for image restoration*, arXiv preprint arXiv:1602.00715, (2016).

[60] S. H. CHAN, *Performance analysis of plug-and-play admm: A graph signal processing perspective*, IEEE Transactions on Computational Imaging, 5 (2019), pp. 274–286.

[61] S. H. CHAN, R. KHOSHABEH, K. B. GIBSON, P. E. GILL, AND T. Q. NGUYEN, *An augmented lagrangian method for total variation video restoration*, IEEE Transactions on Image Processing, 20 (2011), pp. 3097–3111.

[62] S. H. CHAN, X. WANG, AND O. A. ELGENDY, *Plug-and-play admm for image restoration: Fixed-point convergence and applications*, IEEE Transactions on Computational Imaging, 3 (2017), pp. 84–98.

[63] S. H. CHAN, T. ZICKLER, AND Y. M. LU, *Understanding symmetric smoothing filters via gaussian mixtures*, in 2015 IEEE International Conference on Image Processing (ICIP), 2015, pp. 2500–2504.

[64] P. CHARBONNIER, L. BLANC-FÉRAUD, G. AUBERT, AND M. BARLAUD, *Deterministic edge-preserving regularization in computed imaging*, IEEE Transactions on Image Processing, 6 (1997), pp. 298–311.

[65] P. CHATTERJEE AND P. MILANFAR, *Is denoising dead?*, IEEE Transactions on Image Processing, 19 (2010), pp. 895–911.

[66] P. CHATTERJEE AND P. MILANFAR, *Patch-based near-optimal image denoising*, IEEE Transactions on Image Processing, 21 (2012), pp. 1635–1649.

[67] P. CHATTERJEE AND P. MILANFAR, *Patch-based near-optimal image denoising*, IEEE Transactions on Image Processing, 21 (2012), pp. 1635–1649.

[68] D. CHEN, J. TACHELLA, AND M. DAVIES, *Robust equivariant imaging: A fully unsupervised framework for learning to image from noisy and partial measurements*, in IEEE Conference on Computer Vision and Pattern Recognition (CVPR), June 2022, pp. 5647–5656.

[69] S. CHEN, A. HALIMI, X. REN, A. MCCARTHY, X. SU, S. MCLAUGHLIN, AND G. S. BULLER, *Learning non-local spatial correlations to restore sparse 3d single-photon data*, IEEE Transactions on Image Processing, 29 (2020), pp. 3119–3131.

[70] W. CHEN, D. WIPF, AND M. RODRIGUES, *Deep learning for linear inverse problems using the plug-and-play priors framework*, in ICASSP 2021 - 2021 IEEE International Conference on Acoustics, Speech and Signal Processing (ICASSP), 2021, pp. 8098–8102.

[71] Y. CHEN AND T. POCK, *Trainable nonlinear reaction diffusion: A flexible framework for fast and effective image restoration*, IEEE Transactions on Pattern Analysis and Machine Intelligence, 39 (2017), pp. 1256–1272.

[72] Z. CHEN, A. BASARAB, AND D. KOUAMÉ, *Compressive deconvolution in medical ultrasound imaging*, IEEE Transactions on Medical Imaging, 35 (2016), pp. 728–737.

[73] G. CHEUNG, E. MAGLI, Y. TANAKA, AND M. K. NG, *Graph spectral image processing*, Proceedings of the IEEE, 106 (2018), pp. 907–930.

[74] K. T. CHITTY-VENKATA, A. K. SOMANI, AND S. KOTHANDARAMAN, *Searching architecture and precision for u-net based image restoration tasks*, in 2021 IEEE International Conference on Image Processing (ICIP), 2021, pp. 1989–1993.

[75] A. CHOWDHURY, G. VERMA, C. RAO, A. SWAMI, AND S. SEGARRA, *Unfolding wmmse using graph neural networks for efficient power allocation*, IEEE Transactions on Wireless Communications, 20 (2021), pp. 6004–6017.

[76] A. CIGIER, F. VARRAY, AND D. GARCIA, *Simus: An open-source simulator for medical ultrasound imaging. part ii: Comparison with four simulators*, Computer Methods and Programs in Biomedicine, 220 (2022), p. 106774.

[77] R. COHEN, M. ELAD, AND P. MILANFAR, *Regularization by denoising via fixed-point projection (red-pro)*, SIAM Journal on Imaging Sciences, 14 (2021), pp. 1374–1406.

[78] R. COHEN, M. ELAD, AND P. MILANFAR, *Regularization by denoising via fixed-point projection (red-pro)*, SIAM Journal on Imaging Sciences, 14 (2021), pp. 1374–1406.

[79] C. COHEN-TANNOUDJI, B. DIU, AND F. LALOË, *Quantum Mechanics*, 1st ed, New York, NY, USA: Wiley, 1977.

[80] C. COHEN-TANNOUDJI, B. DIU, AND F. LALOË, *Quantum mechanics; 1st ed.*, Wiley, New York, NY, 1977.
Trans. of : Mécanique quantique. Paris : Hermann, 1973.

[81] I. CONG, S. CHOI, AND M. D. LUKIN, *Quantum convolutional neural networks*, Nature Physics, 15 (2019), pp. 1273–1278.

[82] K. DABOV, A. FOI, V. KATKOVNIK, AND K. EGIAZARIAN, *Image denoising by sparse 3-d transform-domain collaborative filtering*, IEEE Transactions on Image Processing, 16 (2007), pp. 2080–2095.

[83] K. DABOV, A. FOI, V. KATKOVNIK, AND K. EGIAZARIAN, *Bm3d image denoising with shape-adaptive principal component analysis*, in Signal Processing with Adaptive Sparse Structured Representations (SPARS), 2009, pp. 1–7.

[84] A. DANIELYAN, V. KATKOVNIK, AND K. EGIAZARIAN, *Bm3d frames and variational image deblurring*, IEEE Transactions on Image Processing, 21 (2012), pp. 1715–1728.

[85] G. DANTZIG, *Linear programming and extensions*, Princeton university press, 2016.

[86] G. B. DANTZIG AND P. WOLFE, *Decomposition principle for linear programs*, Operations research, 8 (1960), pp. 101–111.

[87] Y. DAR, A. M. BRUCKSTEIN, M. ELAD, AND R. GIRYES, *Postprocessing of compressed images via sequential denoising*, IEEE Transactions on Image Processing, 25 (2016), pp. 3044–3058.

[88] M. A. DAVENPORT AND M. B. WAKIN, *Analysis of orthogonal matching pursuit using the restricted isometry property*, IEEE Transactions on Information Theory, 56 (2010), pp. 4395–4401.

[89] F. DE MORSIER, M. BORGEAUD, V. GASS, J.-P. THIRAN, AND D. TUIA, *Kernel low-rank and sparse graph for unsupervised and semi-supervised classification of hyperspectral images*, IEEE Transactions on Geoscience and Remote Sensing, 54 (2016), pp. 3410–3420.

[90] F. DE VIEILLEVILLE, P. WEISS, V. LOBJOIS, AND D. KOUAMÉ, *Alternating direction method of multipliers applied to 3d light sheet fluorescence microscopy im-*

age deblurring using gpu hardware, in 2011 Annual International Conference of the IEEE Engineering in Medicine and Biology Society, 2011, pp. 4872–4875.

[91] C.-A. DELEDALLE, L. DENIS, AND F. TUPIN, *How to compare noisy patches? patch similarity beyond gaussian noise*, International journal of computer vision, 99 (2012), pp. 86–102.

[92] C.-A. DELEDALLE, J. SALMON, AND A. DALALYAN, *Image denoising with patch based pca: local versus global*, in Proceedings of BMVC, vol. 81, 2011, pp. 425–455.

[93] W. DENK, J. H. STRICKLER, AND W. W. WEBB, *Two-photon laser scanning fluorescence microscopy*, Science, 248 (1990), pp. 73–76.

[94] N. DEY, L. BLANC-FÉRAUD, C. ZIMMER, P. ROUX, Z. KAM, J.-C. OLIVO-MARIN, AND J. ZERUBIA, *Richardson–lucy algorithm with total variation regularization for 3d confocal microscope deconvolution*, Microscopy Research and Technique, 69 (2006), pp. 260–266.

[95] S. DIAMOND, V. SITZMANN, F. HEIDE, AND G. WETZSTEIN, *Unrolled optimization with deep priors*, arXiv preprint arXiv:1705.08041, (2017).

[96] C. DONG, C. LOY, K. HE, AND X. TANG, *Learning a deep convolutional network for image super-resolution*, in Proceedings of the European Conference on Computer Vision (ECCV), Springer International Publishing, 2014, pp. 184–199.

[97] C. DONG, C. LOY, K. HE, AND X. TANG, *Image super-resolution using deep convolutional networks*, IEEE Transactions on Pattern Analysis and Machine Intelligence, 38 (2016), pp. 295–307.

[98] C. DONG, C. LOY, AND X. TANG, *Accelerating the super-resolution convolutional neural network*, in Proceedings of the European conference on computer vision, Springer International Publishing, 2016, pp. 391–407.

[99] J. DONG, S. ROTH, AND B. SCHIELE, *Deep wiener deconvolution: Wiener meets deep learning for image deblurring*, Advances in Neural Information Processing Systems, 33 (2020), pp. 1048–1059.

[100] W. DONG, G. SHI, AND X. LI, *Nonlocal image restoration with bilateral variance estimation: A low-rank approach*, IEEE Transactions on Image Processing, 22 (2013), pp. 700–711.

[101] W. DONG, P. WANG, W. YIN, G. SHI, F. WU, AND X. LU, *Denoising prior driven deep neural network for image restoration*, IEEE Transactions on Pattern Analysis and Machine Intelligence, 41 (2019), pp. 2305–2318.

[102] W. DONG, L. ZHANG, G. SHI, AND X. LI, *Nonlocally centralized sparse representation for image restoration*, IEEE Transactions on Image Processing, 22 (2013), pp. 1620–1630.

[103] W. DONG, L. ZHANG, G. SHI, AND X. WU, *Image deblurring and super-resolution by adaptive sparse domain selection and adaptive regularization*, IEEE Transactions on Image Processing, 20 (2011), pp. 1838–1857.

[104] D. DONOHO, I. JOHNSTONE, G. KERKYACHARIAN, AND D. PICARD, *Wavelet shrinkage: asymptopia?*, Journal of the Royal Statistical Society, 57 (1995), pp. 301–337.

[105] D. L. DONOHO AND I. M. JOHNSTONE, *Adapting to unknown smoothness via wavelet shrinkage*, Journal of the American Statistical Association, 90 (1995), pp. 1200–1224.

[106] D. L. DONOHO AND J. M. JOHNSTONE, *Ideal spatial adaptation by wavelet whrinkage*, Biometrika, 81 (1994), pp. 425–455.

[107] Z. DU, H. ZHANG, X. CHEN, AND Y. YANG, *Convolutional plug-and-play sparse optimization for impulsive blind deconvolution*, Mechanical Systems and Signal Processing, 161 (2021), p. 107877.

[108] F.-X. DUPE, J. M. FADILI, AND J.-L. STARCK, *A proximal iteration for deconvolving poisson noisy images using sparse representations*, IEEE Transactions on Image Processing, 18 (2009), pp. 310–321.

[109] F. DURAND AND J. DORSEY, *Fast bilateral filtering for the display of high-dynamic-range images*, ACM Transactions on Graphics, 21 (2002), p. 257–266.

[110] S. DUTTA, A. BASARAB, B. GEORGEOT, AND D. KOUAMÉ, *Despeckling ultrasound images using quantum many-body physics*, in 2021 IEEE International Ultrasonics Symposium (IUS), 2021, pp. 1–4.

[111] S. DUTTA, A. BASARAB, B. GEORGEOT, AND D. KOUAMÉ, *Image denoising inspired by quantum many-body physics*, in 2021 28th IEEE International Conference on Image Processing (ICIP), 2021, pp. 1619–1623.

[112] S. DUTTA, A. BASARAB, B. GEORGEOT, AND D. KOUAMÉ, *Plug-and-play quantum adaptive denoiser for deconvolving poisson noisy images*, IEEE Access, 9 (2021), pp. 139771–139791.

[113] S. DUTTA, A. BASARAB, B. GEORGEOT, AND D. KOUAMÉ, *Poisson image deconvolution by a plug-and-play quantum denoising scheme*, in 2021 29th European Signal Processing Conference (EUSIPCO), 2021, pp. 646–650.

[114] S. DUTTA, A. BASARAB, B. GEORGEOT, AND D. KOUAMÉ, *Quantum mechanics-based signal and image representation: Application to denoising*, IEEE Open Journal of Signal Processing, 2 (2021), pp. 190–206.

[115] S. DUTTA, A. BASARAB, B. GEORGEOT, AND D. KOUAMÉ, *Deep unfolding of image denoising by quantum interactive patches*, in 2022 29th IEEE International Conference on Image Processing (ICIP), 2022, pp. 491–495.

[116] S. DUTTA, A. BASARAB, B. GEORGEOT, AND D. KOUAMÉ, *DIVA: Deep unfolded network from quantum interactive patches for image restoration*, Arxiv Preprint (Submitted), (2022), pp. 1–18.

[117] S. DUTTA, A. BASARAB, B. GEORGEOT, AND D. KOUAMÉ, *A novel image denoising algorithm using concepts of quantum many-body theory*, Signal Processing, 201 (2022), p. 108690.

[118] S. DUTTA, B. GEORGEOT, D. KOUAMÉ, D. GARCIA, AND A. BASARAB, *Adaptive contrast enhancement of cardiac ultrasound images using a deep unfolded many-body quantum algorithm*, in 2022 IEEE International Ultrasonics Symposium (IUS), 2022, pp. 1–4.

[119] S. DUTTA, N. K. TUADOR, J. MICHETTI, B. GEORGEOT, D. H. PHAM, A. BASARAB, AND D. KOUAMÉ, *Quantum denoising-based super-resolution algorithm applied to dental tomography images*, in 2022 IEEE 19th International Symposium on Biomedical Imaging (ISBI), 2022, pp. 1–4.

[120] J. ECKSTEIN AND D. P. BERTSEKAS, *On the douglas—rachford splitting method and the proximal point algorithm for maximal monotone operators*, Mathematical Programming, 55 (1992), pp. 293–318.

[121] A. EKERT AND R. JOZSA, *Quantum computation and shor's factoring algorithm*, Reviews of Modern Physics, 68 (1996), p. 733.

[122] M. ELAD, *On the origin of the bilateral filter and ways to improve it*, IEEE Transactions on Image Processing, 11 (2002), pp. 1141–1151.

[123] M. ELAD AND M. AHARON, *Image denoising via sparse and redundant representations over learned dictionaries*, IEEE Transactions on Image Processing, 15 (2006), pp. 3736–3745.

[124] M. ELAD AND M. AHARON, *Image denoising via sparse and redundant representations over learned dictionaries*, IEEE Transactions on Image Processing, 15 (2006), pp. 3736–3745.

[125] A. K. ELDALY, Y. ALTMANN, A. PERPERIDIS, N. KRSTAJIĆ, T. R. CHOUDHARY, K. DHALIWAL, AND S. MCLAUGHLIN, *Deconvolution and restoration of optical endomicroscopy images*, IEEE Transactions on Computational Imaging, 4 (2018), pp. 194–205.

[126] Y. C. ELDAR AND A. V. OPPENHEIM, *Quantum signal processing*, IEEE Signal Processing Magazine, 19 (2002), pp. 12–32.

[127] F. ELEIWI, T.-M. LALEG-KIRATI, S. KHELLADI, AND F. BAKIR, *A semi-classical signal analysis method for the analysis of turbomachinery flow unsteadiness*, International Journal of Mechanical and Mechatronics Engineering, 5 (2011), pp. 2102 – 2105.

[128] M.-J. FADILI AND J.-L. STARCK, *Monotone operator splitting for optimization problems in sparse recovery*, in 2009 16th IEEE International Conference on Image Processing (ICIP), 2009, pp. 1461–1464.

[129] J. A. FESSLER AND A. O. HERO, *Penalized maximum-likelihood image reconstruction using space-alternating generalized em algorithms*, IEEE Transactions on Image Processing, 4 (1995), pp. 1417–1429.

[130] R. FEYNMAN, R. LEIGHTON, AND M. SANDS, *The Feynman Lectures on Physics*, Addison-Wesley world student series, Addison-Wesley, 1977.

[131] R. P. FEYNMAN, *Quantum mechanical computers.*, Foundations of Physics, 16 (1986), pp. 507–532.

[132] R. P. FEYNMAN, R. B. LEIGHTON, AND M. SANDS, *The Feynman lectures on physics; New millennium ed.*, Basic Books, New York, NY, 2010.
Originally published 1963-1965.

[133] M. A. T. FIGUEIREDO AND J. M. BIOUCAS-DIAS, *Restoration of poissonian images using alternating direction optimization*, IEEE Transactions on Image Processing, 19 (2010), pp. 3133–3145.

[134] M. FISZ, *The limiting distribution of a function of two independent random variables and its statistical application*, in Colloquium Mathematicum, vol. 3, 1955, pp. 138–146.

[135] A. FOI, S. ALENIUS, M. TRIMECHE, V. KATKOVNIK, AND K. EGIAZARIAN, *A spatially adaptive poissonian image deblurring*, in IEEE International Conference on Image Processing 2005, vol. 1, 2005, pp. I–925.

[136] I. FROSIO AND J. KAUTZ, *Statistical nearest neighbors for image denoising*, IEEE Transactions on Image Processing, 28 (2019), pp. 723–738.

[137] V. S. FROST, J. A. STILES, K. S. SHANMUGAN, AND J. C. HOLTZMAN, *A model for radar images and its application to adaptive digital filtering of multiplicative noise*, IEEE Transactions on Pattern Analysis and Machine Intelligence, PAMI-4 (1982), pp. 157–166.

[138] P. FRYZLEWICZ AND G. P. NASON, *Poisson intensity estimation using wavelets and the fisz transformation*, (2001).

[139] D. GABAY, *Chapter ix applications of the method of multipliers to variational inequalities*, in Augmented Lagrangian Methods: Applications to the Numerical Solution of Boundary-Value Problems, M. Fortin and R. Glowinski, eds., vol. 15 of Studies in Mathematics and Its Applications, Elsevier, 1983, pp. 299–331.

[140] D. GABAY AND B. MERCIER, *A dual algorithm for the solution of nonlinear variational problems via finite element approximation*, Computers & Mathematics with Applications, 2 (1976), pp. 17–40.

[141] X. GAO, K. ZHANG, D. TAO, AND X. LI, *Image super-resolution with sparse neighbor embedding*, IEEE Transactions on Image Processing, 21 (2012), pp. 3194–3205.

[142] D. GARCIA, *Make the most of must, an open-source matlab ultrasound toolbox*, in 2022 IEEE International Ultrasonics Symposium (IUS), 2022, pp. 1–4.

[143] D. GARCIA, *Simus: An open-source simulator for medical ultrasound imaging. part i: Theory & examples*, Computer Methods and Programs in Biomedicine, 218 (2022), p. 106726.

[144] A. GHOSHAL, *Basics of Quantum Mechanics*, 2016.

[145] R. GIRYES, Y. C. ELDAR, A. M. BRONSTEIN, AND G. SAPIRO, *Tradeoffs between convergence speed and reconstruction accuracy in inverse problems*, IEEE Transactions on Signal Processing, 66 (2018), pp. 1676–1690.

[146] R. GLOWINSKI AND A. MARROCO, *Sur l'approximation, par éléments finis d'ordre un, et la résolution, par pénalisation-dualité d'une classe de problèmes de dirichlet non linéaires*, ESAIM: Mathematical Modelling and Numerical Analysis-Modélisation Mathématique et Analyse Numérique, 9 (1975), pp. 41–76.

[147] D. GNANADURAI AND V. SADASIVAM, *Image de-noising using double density wavelet transform based adaptive thresholding technique*, International Journal of Wavelets, Multiresolution and Information Processing, 3 (2005), pp. 141–152.

[148] H. GOLDSTEIN, C. POOLE, AND J. SAFKO, *Classical Mechanics*, Pearson, 2002.

[149] D. GONG, Z. ZHANG, Q. SHI, A. VAN DEN HENGEL, C. SHEN, AND Y. ZHANG, *Learning deep gradient descent optimization for image deconvolution*, IEEE Transactions on Neural Networks and Learning Systems, 31 (2020), pp. 5468–5482.

[150] GOOGLE, *Fluorescence Microscopy Images*.

[151] K. GREGOR AND Y. LECUN, *Learning fast approximations of sparse coding*, in Proceedings of the 27th International Conference on International Conference on Machine Learning, 2010, p. 399–406.

[152] D. J. GRIFFITHS AND D. F. SCHROETER, *Introduction to Quantum Mechanics*, Cambridge University Press, 2018.

[153] L. K. GROVER, *Quantum mechanics helps in searching for a needle in a haystack*, Physical Review Letters, 79 (1997), p. 325.

[154] S. GU, Q. XIE, D. MENG, W. ZUO, X. FENG, AND L. ZHANG, *Weighted nuclear norm minimization and its applications to low level vision*, International Journal of Computer Vision, 121 (2017), pp. 183–208.

[155] S. GUO, Z. YAN, K. ZHANG, W. ZUO, AND L. ZHANG, *Toward convolutional blind denoising of real photographs*, in Proceedings of the IEEE/CVF Conference on Computer Vision and Pattern Recognition (CVPR), June 2019, pp. 1712–1722.

[156] R. HAMON, P. BORGNAT, P. FLANDRIN, AND C. ROBARDET, *Extraction of temporal network structures from graph-based signals*, IEEE Transactions on Signal and Information Processing over Networks, 2 (2016), pp. 215–226.

[157] A. HAMZA AND H. KRIM, *Image denoising: a nonlinear robust statistical approach*, IEEE Transactions on Signal Processing, 49 (2001), pp. 3045–3054.

[158] Z. T. HARMANY, R. F. MARCIA, AND R. M. WILLETT, *This is spiral-tap: Sparse poisson intensity reconstruction algorithms—theory and practice*, IEEE Transactions on Image Processing, 21 (2012), pp. 1084–1096.

[159] B. HE AND X. YUAN, *On non-ergodic convergence rate of douglas–rachford alternating direction method of multipliers*, Numerische Mathematik, 130 (2015), pp. 567–577.

[160] K. HE, J. SUN, AND X. TANG, *Guided image filtering*, IEEE Transactions on Pattern Analysis and Machine Intelligence, 35 (2013), pp. 1397–1409.

[161] K. HE, X. ZHANG, S. REN, AND J. SUN, *Delving deep into rectifiers: Surpassing human-level performance on imagenet classification*, in Proceedings of the IEEE International Conference on Computer Vision (ICCV), 2015, pp. 1026–1034.

[162] K. HE, X. ZHANG, S. REN, AND J. SUN, *Deep residual learning for image recognition*, in IEEE Conference on Computer Vision and Pattern Recognition (CVPR), June 2016, pp. 770–778.

[163] F. HEIDE, M. STEINBERGER, Y.-T. TSAI, M. ROUF, D. PAJĄK, D. REDDY, O. GALLO, J. LIU, W. HEIDRICH, K. EGIAZARIAN, J. KAUTZ, AND K. PULLI, *Flexisp: A flexible camera image processing framework*, ACM Transactions on Graphics, 33 (2014), pp. 1–13.

[164] B. HELFFER AND T.-M. LALEG-KIRATI, *On semi-classical questions related to signal analysis*, Asymptotic Analysis, 75 (2011), pp. 125–144.

[165] M. R. HESTENES, *Multiplier and gradient methods*, Journal of optimization theory and applications, 4 (1969), pp. 303–320.

[166] D. HILBERT, J. VON NEUMANN, AND L. NORDHEIM, *Über die grundlagen der quantenmechanik*, Mathematische Annalen, 98 (1928), pp. 1–30.

[167] M. HONG, Z.-Q. LUO, AND M. RAZAVIYAYN, *Convergence analysis of alternating direction method of multipliers for a family of nonconvex problems*, SIAM Journal on Optimization, 26 (2016), pp. 337–364.

[168] M. HOURANI, A. BASARAB, D. KOUAMÉ, J.-M. GIRAULT, AND J.-Y. TOURNERET, *Restoration of ultrasonic images using non-linear system identification and deconvolution*, in 2018 IEEE 15th International Symposium on Biomedical Imaging (ISBI 2018), 2018, pp. 1166–1169.

[169] Y. HU, J. LIU, X. XU, AND U. S. KAMILOV, *Monotonically convergent regularization by denoising*, arXiv preprint arXiv:2202.04961, (2022).

[170] F. HUA, C. RICHARD, J. CHEN, H. WANG, P. BORGNAT, AND P. GONÇALVES, *Learning combination of graph filters for graph signal modeling*, IEEE Signal Processing Letters, 26 (2019), pp. 1912–1916.

[171] T. HUA, J. CHEN, D. PEI, W. ZHANG, AND N. ZHOU, *Quantum image encryption algorithm based on image correlation decomposition*, International Journal of Theoretical Physics, 54 (2015), pp. 526–537.

[172] A. M. ILIYASU, *Towards realising secure and efficient image and video processing applications on quantum computers*, Entropy, 15 (2013), pp. 2874–2974.

[173] A. M. ILIYASU, P. Q. LE, F. DONG, AND K. HIROTA, *Watermarking and authentication of quantum images based on restricted geometric transformations*, Information Sciences, 186 (2012), pp. 126–149.

[174] A. JALOBEANU, L. BLANC-FÉRAUD, AND J. ZERUBIA, *Satellite image deblurring using complex wavelet packets*, International Journal of Computer Vision, 51 (2003), pp. 205–217.

[175] A. JALOBEANU, L. BLANC-FERAUD, AND J. ZERUBIA, *An adaptive gaussian model for satellite image deblurring*, IEEE Transactions on Image Processing, 13 (2004), pp. 613–621.

[176] N. JIANG, Y. DANG, AND J. WANG, *Quantum image matching*, Quantum Information Processing, 15 (2016), pp. 3543–3572.

[177] N. JIANG, J. WANG, AND Y. MU, *Quantum image scaling up based on nearest-neighbor interpolation with integer scaling ratio*, Quantum Information Processing, 14 (2015), pp. 4001–4026.

[178] N. JIANG AND L. WANG, *Analysis and improvement of the quantum arnold image scrambling*, Quantum Information Processing, 13 (2014), pp. 1545–1551.

[179] N. JIANG AND L. WANG, *Quantum image scaling using nearest neighbor interpolation*, Quantum Information Processing, 14 (2015), pp. 1559–1571.

[180] N. JIANG, W. WU, L. WANG, AND N. ZHAO, *Quantum image pseudocolor coding based on the density-stratified method*, Quantum Information Processing, 14 (2015), pp. 1735–1755.

[181] N. JIANG, W.-Y. WU, AND L. WANG, *The quantum realization of arnold and fibonacci image scrambling*, Quantum Information Processing, 13 (2014), pp. 1223–1236.

[182] N. JIANG, N. ZHAO, AND L. WANG, *LSB based quantum image steganography algorithm*, International Journal of Theoretical Physics, 55 (2016), pp. 107–123.

[183] K. H. JIN, M. T. MCCANN, E. FROUSTEY, AND M. UNSER, *Deep convolutional neural network for inverse problems in imaging*, IEEE Transactions on Image Processing, 26 (2017), pp. 4509–4522.

[184] J. JOHNSON, A. ALAHI, AND L. FEI-FEI, *Perceptual losses for real-time style transfer and super-resolution*, in Computer Vision – ECCV 2016, Cham, 2016, Springer International Publishing, pp. 694–711.

[185] Z. KAISSERLI, T.-M. LALEG-KIRATI, AND A. LAHMAR-BENBERNOU, *A novel algorithm for image representation using discrete spectrum of the schrödinger operator*, Digital Signal Processing, 40 (2015), pp. 80–87.

[186] U. S. KAMILOV, C. A. BOUMAN, G. T. BUZZARD, AND B. WOHLBERG, *Plug-and-play methods for integrating physical and learned models in computational imaging*, arXiv preprint arXiv:2203.17061, (2022).

[187] C. KERVRANN AND J. BOULANGER, *Optimal spatial adaptation for patch-based image denoising*, IEEE Transactions on Image Processing, 15 (2006), pp. 2866–2878.

[188] A. KHERADMAND AND P. MILANFAR, *A general framework for kernel similarity-based image denoising*, in 2013 IEEE Global Conference on Signal and Information Processing, 2013, pp. 415–418.

[189] S. KHOBAHI AND M. SOLTANALIAN, *Model-based deep learning for one-bit compressive sensing*, IEEE Transactions on Signal Processing, 68 (2020), pp. 5292–5307.

[190] J. KIM, J. LEE, AND K. LEE, *Accurate image super-resolution using very deep convolutional networks*, in IEEE Conference on Computer Vision and Pattern Recognition (CVPR), June 2016, pp. 1646–1654.

[191] S. KIM, *Pde-based image restoration: a hybrid model and color image denoising*, IEEE Transactions on Image Processing, 15 (2006), pp. 1163–1170.

[192] S. KIRANYAZ, T. INCE, A. IOSIFIDIS, AND M. GABBOUJ, *Operational neural networks*, Neural Computing and Applications, 32 (2020), pp. 6645–6668.

[193] C. KNAUS AND M. ZWICKER, *Progressive image denoising*, IEEE Transactions on Image Processing, 23 (2014), pp. 3114–3125.

[194] S. KONG, W. WANG, X. FENG, AND X. JIA, *Deep red unfolding network for image restoration*, IEEE Transactions on Image Processing, 31 (2022), pp. 852–867.

[195] J. KOO, A. HALIMI, AND S. MCLAUGHLIN, *A bayesian based deep unrolling algorithm for single-photon lidar systems*, arXiv preprint arXiv:2201.10910, (2022).

[196] Y. KOPSINIS AND S. MCLAUGHLIN, *Development of emd-based denoising methods inspired by wavelet thresholding*, IEEE Transactions on Signal Processing, 57 (2009), pp. 1351–1362.

[197] F. KOU, W. CHEN, C. WEN, AND Z. LI, *Gradient domain guided image filtering*, IEEE Transactions on Image Processing, 24 (2015), pp. 4528–4539.

[198] B. KRAMER, G. BERGMANN, AND Y. BRUYNSERAEDE, *Anderson Localization, Interaction, and Transport Phenomena: Proceedings of the International Conference, August 23–28, 1984 Braunschweig, Fed. Rep. of Germany*, vol. 61, Springer, New York, 1985.

[199] J. KRUSE, C. ROTHER, AND U. SCHMIDT, *Learning to push the limits of efficient FFT-based image deconvolution*, in Proceedings of the IEEE International Conference on Computer Vision, 2017, pp. 4596–4604.

[200] C. KWAN, J. H. CHOI, S. CHAN, J. ZHOU, AND B. BUDAVARI, *Resolution enhancement for hyperspectral images: A super-resolution and fusion approach*, in 2017 IEEE International Conference on Acoustics, Speech and Signal Processing (ICASSP), 2017, pp. 6180–6184.

[201] A. LAGENDIJK, B. VAN TIGGELEN, AND D. S. WIERSMA, *Fifty years of anderson localization*, Physics Today, 62 (2009), pp. 24–29.

[202] W.-S. LAI, J.-B. HUANG, N. AHUJA, AND M.-H. YANG, *Deep laplacian pyramid networks for fast and accurate super-resolution*, in IEEE Conference on Computer Vision and Pattern Recognition (CVPR), 2017, pp. 5835–5843.

[203] T.-M. LALEG-KIRATI, E. CRÉPEAU, AND M. SORINE, *Semi-classical signal analysis*, Mathematics of Control, Signals, and Systems, 25 (2013), pp. 37–61.

[204] T.-M. LALEG-KIRATI, J. ZHANG, E. ACHTEN, AND H. SERRAI, *Spectral data de-noising using semi-classical signal analysis: application to localized mrs*, NMR in Biomedicine, 29 (2016), pp. 1477–1485.

[205] L. LANDAU AND E. LIFSHITZ, *Quantum Mechanics: Non-Relativistic Theory*, Course of Theoretical Physics, Elsevier Science, 1991.

[206] L. D. LANDAU AND L. M. LIFSHITZ, *Quantum Mechanics Non-Relativistic Theory, Third Edition*, Butterworth-Heinemann, 1981.

[207] P. Q. LE, A. M. ILIYASU, F. DONG, AND K. HIROTA, *Fast geometric transformations on quantum images*, IAENG International Journal of Applied Mathematics, 40 (2010).

[208] M. LEBRUN, A. BUADES, AND J.-M. MOREL, *A nonlocal bayesian image denoising algorithm*, SIAM Journal on Imaging Sciences, 6 (2013), pp. 1665–1688.

[209] M. LEBRUN, M. COLOM, A. BUADES, AND J.-M. MOREL, *Secrets of image denoising cuisine*, Acta Numerica, 21 (2012), pp. 475–576.

[210] Y. LECUN, Y. BENGIO, AND G. HINTON, *Deep learning*, Nature, 521 (2015), pp. 436–444.

[211] J.-S. LEE, *Digital image enhancement and noise filtering by use of local statistics*, IEEE Transactions on Pattern Analysis and Machine Intelligence, PAMI-2 (1980), pp. 165–168.

[212] S. LEFKIMMIATIS, *Non-local color image denoising with convolutional neural networks*, in IEEE Conference on Computer Vision and Pattern Recognition (CVPR), July 2017, pp. 3587–3596.

[213] A. LEVIN AND B. NADLER, *Natural image denoising: Optimality and inherent bounds*, in Proceedings of the IEEE Computer Society Conference on Computer Vision and Pattern Recognition, 2011, pp. 2833–2840.

[214] A. LEVIN, B. NADLER, F. DURAND, AND W. T. FREEMAN, *Patch complexity, finite pixel correlations and optimal denoising*, in European Conference on Computer Vision, Berlin, Heidelberg, 2012, Springer Berlin Heidelberg, pp. 73–86.

[215] A. LEVIN, Y. WEISS, F. DURAND, AND W. FREEMAN, *Efficient marginal likelihood optimization in blind deconvolution*, in IEEE Conference on Computer Vision and Pattern Recognition (CVPR), 2011, pp. 2657–2664.

[216] F. LI, Y. RU, AND X. LV, *Patch-based weighted scad prior for rician noise removal*, Journal of Scientific Computing, 90 (2021), pp. 1573–7691.

[217] H.-Q. LI, S.-Q. WANG, AND C.-Z. DENG, *New image denoising method based wavelet and curvelet transform*, in 2009 WASE International Conference on Information Engineering, vol. 1, 2009, pp. 136–139.

[218] H.-S. LI, Z. QINGXIN, S. LAN, C.-Y. SHEN, R. ZHOU, AND J. MO, *Image storage, retrieval, compression and segmentation in a quantum system*, Quantum Information Processing, 12 (2013), pp. 2269–2290.

[219] M. LI, W. HSU, X. XIE, J. CONG, AND W. GAO, *SACNN: Self-attention convolutional neural network for low-dose ct denoising with self-supervised perceptual loss network*, IEEE Transactions on Medical Imaging, 39 (2020), pp. 2289–2301.

[220] S. LI, G. ZHANG, Z. LUO, AND J. LIU, *Dfan: Dual feature aggregation network for lightweight image super-resolution*, Wireless Communications and Mobile Computing, 44 (2022), pp. 1530–8669.

[221] Y. LI, M. TOFIGHI, J. GENG, V. MONGA, AND Y. ELDAR, *Deep algorithm unrolling for blind image deblurring*, arXiv preprint arXiv:1902.03493, (2019).

[222] Y. LI, M. TOFIGHI, J. GENG, V. MONGA, AND Y. C. ELDAR, *Efficient and interpretable deep blind image deblurring via algorithm unrolling*, IEEE Transactions on Computational Imaging, 6 (2020), pp. 666–681.

[223] D. LIANG, J. CHENG, Z. KE, AND L. YING, *Deep magnetic resonance image reconstruction: Inverse problems meet neural networks*, IEEE Signal Processing Magazine, 37 (2020), pp. 141–151.

[224] B. LIM, S. SON, H. KIM, S. NAH, AND K. LEE, *Enhanced deep residual networks for single image super-resolution*, in Proceedings of the IEEE Conference on Computer Vision and Pattern Recognition Workshops (CVPRW), July 2017, pp. 1132–1140.

[225] B. LIU AND J. LIU, *Non-local mean filtering algorithm based on deep learning*, MATEC Web of Conferences, 232 (2018), p. 03025.

[226] J. LIU, X. XU, W. GAN, S. SHOUSHTARI, AND U. S. KAMILOV, *Online deep equilibrium learning for regularization by denoising*, arXiv preprint arXiv:2205.13051, (2022).

[227] P. LIU, F. HUANG, G. LI, AND Z. LIU, *Remote-sensing image denoising using partial differential equations and auxiliary images as priors*, IEEE Geoscience and Remote Sensing Letters, 9 (2012), pp. 358–362.

[228] S. LIU, L. GAO, Y. LEI, M. WANG, Q. HU, X. MA, AND Y. ZHANG, *Sar speckle removal using hybrid frequency modulations*, IEEE Transactions on Geoscience and Remote Sensing, 59 (2021), pp. 3956–3966.

[229] X. LIU, T. ZHOU, M. LU, Y. YANG, Q. HE, AND J. LUO, *Deep learning for ultrasound localization microscopy*, IEEE Transactions on Medical Imaging, 39 (2020), pp. 3064–3078.

[230] W. LU, J. DUAN, Z. QIU, Z. PAN, R. W. LIU, AND L. BAI, *Implementation of high-order variational models made easy for image processing*, Mathematical Methods in the Applied Sciences, 39 (2016), pp. 4208–4233.

[231] A. LUCAS, M. ILIADIS, R. MOLINA, AND A. K. KATSAGGELOS, *Using deep neural networks for inverse problems in imaging: Beyond analytical methods*, IEEE Signal Processing Magazine, 35 (2018), pp. 20–36.

[232] G. MAHAN AND K. SUBBASWAMY, *Local Density Theory of Polarizability*, Physics of Solids and Liquids, Springer US, 2013.

[233] M. MAHMOUDI AND G. SAPIRO, *Fast image and video denoising via nonlocal means of similar neighborhoods*, IEEE Signal Processing Letters, 12 (2005), pp. 839–842.

[234] J. MAIRAL, F. BACH, J. PONCE, G. SAPIRO, AND A. ZISSERMAN, *Non-local sparse models for image restoration*, in 2009 IEEE 12th International Conference on Computer Vision, 2009, pp. 2272–2279.

[235] J. MAIRAL, F. BACH, J. PONCE, G. SAPIRO, AND A. ZISSERMAN, *Non-local sparse models for image restoration*, in 2009 IEEE 12th International Conference on Computer Vision, 2009, pp. 2272–2279.

[236] J. MAIRAL, M. ELAD, AND G. SAPIRO, *Sparse representation for color image restoration*, IEEE Transactions on Image Processing, 17 (2008), pp. 53–69.

[237] M. MAKITALO AND A. FOI, *A closed-form approximation of the exact unbiased inverse of the anscombe variance-stabilizing transformation*, IEEE Transactions on Image Processing, 20 (2011), pp. 2697–2698.

[238] M. MAKITALO AND A. FOI, *Optimal inversion of the anscombe transformation in low-count poisson image denoising*, IEEE Transactions on Image Processing, 20 (2011), pp. 99–109.

[239] M. MAKITALO AND A. FOI, *Optimal inversion of the anscombe transformation in low-count poisson image denoising*, IEEE Transactions on Image Processing, 20 (2011), pp. 99–109.

[240] J. MALIK, S. KIRANYAZ, AND M. GABBOUJ, *Image denoising by super neurons: Why go deep?*, arXiv preprint arXiv:2111.14948, (2021).

[241] J. MALIK, S. KIRANYAZ, AND M. GABBOUJ, *Self-organized operational neural networks for severe image restoration problems*, Neural Networks, 135 (2021), pp. 201–211.

[242] P. A. MARTIN AND F. ROTHEN, *Many-Body Problems and Quantum Field Theory*, Springer Berlin, Heidelberg, 2004.

[243] F. G. MEYER AND X. SHEN, *Perturbation of the eigenvectors of the graph laplacian: Application to image denoising*, Applied and Computational Harmonic Analysis, 36 (2014), pp. 326–334.

[244] O. V. MICHAILOVICH AND D. ADAM, *A novel approach to the 2-d blind deconvolution problem in medical ultrasound*, IEEE Transactions on Medical Imaging, 24 (2005), pp. 86–104.

[245] J. MICHETTI, A. BASARAB, M. TRAN, F. DIEMER, AND D. KOUAMÉ, *Cone-beam computed tomography contrast validation of an artificial periodontal phantom for use in endodontics*, in 2015 37th Annual International Conference of the IEEE Engineering in Medicine and Biology Society (EMBC), IEEE, 2015, pp. 7905–7908.

[246] P. MILANFAR, *Symmetrizing smoothing filters*, SIAM Journal on Imaging Sciences, 6 (2013), pp. 263–284.

[247] D. MISHRA, S. CHAUDHURY, M. SARKAR, AND A. S. SOIN, *Ultrasound image enhancement using structure oriented adversarial network*, IEEE Signal Processing Letters, 25 (2018), pp. 1349–1353.

[248] J.-J. MOREAU, *Proximité et dualité dans un espace hilbertien*, Bulletin de la Société mathématique de France, 93 (1965), pp. 273–299.

[249] R. MORIN, A. BASARAB, AND D. KOUAMÉ, *Alternating direction method of multipliers framework for super-resolution in ultrasound imaging*, in 2012 9th IEEE International Symposium on Biomedical Imaging (ISBI), 2012, pp. 1595–1598.

[250] I. MOSSERI, M. ZONTAK, AND M. IRANI, *Combining the power of internal and external denoising*, in IEEE International Conference on Computational Photography (ICCP), 2013, pp. 1–9.

[251] M. C. MOTWANI, M. C. GADIYA, R. C. MOTWANI, AND F. C. HARRIS, *Survey of image denoising techniques*, in Proceedings of GSPX, vol. 27, 2004, pp. 27–30.

[252] S. MUDUNURI AND S. BISWAS, *Low resolution face recognition across variations in pose and illumination*, IEEE Transactions on Pattern Analysis and Machine Intelligence, 38 (2016), pp. 1034–1040.

[253] S. NAM, Y. HWANG, Y. MATSUSHITA, AND S. J. KIM, *A holistic approach to cross-channel image noise modeling and its application to image denoising*, in Proceedings of the IEEE Conference on Computer Vision and Pattern Recognition (CVPR), 2016, pp. 1683–1691.

[254] Y. NAN, Y. QUAN, AND H. JI, *Variational-em-based deep learning for noise-blind image deblurring*, in IEEE Conference on Computer Vision and Pattern Recognition (CVPR), 2020, pp. 3623–3632.

[255] NASA, *James Webb Telescope Images*.

[256] D. NEEDELL AND J. A. TROPP, *Cosamp: Iterative signal recovery from incomplete and inaccurate samples*, Applied and Computational Harmonic Analysis, 26 (2009), pp. 301–321.

[257] N. D. M. NEIL ASHCROFT, *Solid State Physics*, Saunders College Ed., 1976.

[258] R. D. NOWAK AND E. D. KOLACZYK, *A statistical multiscale framework for poisson inverse problems*, IEEE Transactions on Information Theory, 46 (2000), pp. 1811–1825.

[259] A. ORTEGA, P. FROSSARD, J. KOVAČEVIĆ, J. M. F. MOURA, AND P. VANDERGHEYNST, *Graph signal processing: Overview, challenges, and applications*, Proceedings of the IEEE, 106 (2018), pp. 808–828.

[260] S. OSHER, M. BURGER, D. GOLDFARB, J. XU, AND W. YIN, *An iterative regularization method for total variation-based image restoration*, SIAM Multiscale Modeling & Simulation, 4 (2005), pp. 460–489.

[261] S. J. PAN AND Q. YANG, *A survey on transfer learning*, IEEE Transactions on Knowledge and Data Engineering, 22 (2010), pp. 1345–1359.

[262] J. PANG AND G. CHEUNG, *Graph laplacian regularization for image denoising: Analysis in the continuous domain*, IEEE Transactions on Image Processing, 26 (2017), pp. 1770–1785.

[263] J. PAWLEY, *Handbook of biological confocal microscopy*, vol. 236, New York, NY, USA: Springer, 2006.

[264] D. PERDIOS, A. BESSON, M. ARDITI, AND J.-P. THIRAN, *A deep learning approach to ultrasound image recovery*, in 2017 IEEE International Ultrasonics Symposium (IUS), 2017, pp. 1–4.

[265] D. PERDIOS, M. VONLANTHEN, F. MARTINEZ, M. ARDITI, AND J.-P. THIRAN, *Deep learning based ultrasound image reconstruction method: A time coherence study*, in 2019 IEEE International Ultrasonics Symposium (IUS), 2019, pp. 448–451.

[266] M. PEREYRA AND S. MCLAUGHLIN, *Fast unsupervised bayesian image segmentation with adaptive spatial regularisation*, IEEE Transactions on Image Processing, 26 (2017), pp. 2577–2587.

[267] P. PERONA AND J. MALIK, *Scale-space and edge detection using anisotropic diffusion*, IEEE Transactions on Pattern Analysis and Machine Intelligence, 12 (1990), pp. 629–639.

[268] G. PEYRÉ, *The numerical tours of signal processing*, Computing in Science & Engineering, 13 (2011), pp. 94–97.

[269] N. PIERAZZO AND M. RAIS, *Boosting "shotgun denoising" by patch normalization*, in 2013 IEEE International Conference on Image Processing, 2013, pp. 1115–1119.

[270] E. PILIOURAS AND T.-M. LALEG-KIRATI, *Quantum-based interval selection of the semi-classical signal analysis method*, in 2020 28th European Signal Processing Conference (EUSIPCO), 2021, pp. 2294–2298.

[271] A. PIZURICA AND W. PHILIPS, *Estimating the probability of the presence of a signal of interest in multiresolution single- and multiband image denoising*, IEEE Transactions on Image Processing, 15 (2006), pp. 654–665.

[272] H. V. POOR, *An introduction to signal detection and estimation*, New York, NY, USA: Springer, 2013.

[273] J. PORTILLA, V. STRELA, M. J. WAINWRIGHT, AND E. P. SIMONCELLI, *Image denoising using scale mixtures of gaussians in the wavelet domain*, IEEE Transactions on Image Processing, 12 (2003), pp. 1338–1351.

[274] M. J. D. POWELL, *A method for nonlinear constraints in minimization problems*, Optimization, (1969), pp. 283–298.

[275] M. R. SPIEGEL, *Theory and Problems of Theoretical Mechanics (schaum's Outline Ed.)*, McGraw-Hill, 2021.

[276] M. S. RAD, B. BOZORGTABAR, U.-V. MARTI, M. BASLER, H. K. EKENEL, AND J.-P. THIRAN, *Srobb: Targeted perceptual loss for single image super-resolution*, in Proceedings of the IEEE/CVF International Conference on Computer Vision, 2019, pp. 2710–2719.

[277] H. RAGUET, J. FADILI, AND G. PEYRÉ, *A generalized forward-backward splitting*, SIAM Journal on Imaging Sciences, 6 (2013), pp. 1199–1226.

[278] B. RAJAEI, *An Analysis and Improvement of the BLS-GSM Denoising Method*, Image Processing On Line, 4 (2014), pp. 44–70.

[279] D. RASTOGI, P. JOHRI, AND V. TIWARI, *Brain tumor segmentation and tumor prediction using 2d-vnet deep learning architecture*, in 2021 10th International Conference on System Modeling & Advancement in Research Trends (SMART), 2021, pp. 723–732.

[280] E. T. REEHORST AND P. SCHNITER, *Regularization by denoising: Clarifications and new interpretations*, IEEE Transactions on Computational Imaging, 5 (2019), pp. 52–67.

[281] E. T. REEHORST AND P. SCHNITER, *Regularization by denoising: Clarifications and new interpretations*, IEEE Transactions on Computational Imaging, 5 (2019), pp. 52–67.

[282] B. RICAUD, P. BORGNAT, N. TREMBLAY, P. GONÇALVES, AND P. VANDERGHEYNST, *Fourier could be a data scientist: From graph fourier transform to signal processing on graphs*, Comptes Rendus Physique, 20 (2019), pp. 474–488.

[283] J. H. RICK CHANG, C.-L. LI, B. POCZOS, B. V. K. VIJAYA KUMAR, AND A. C. SANKARANARAYANAN, *One network to solve them all–solving linear inverse problems using deep projection models*, in Proceedings of the IEEE International Conference on Computer Vision, 2017, pp. 5888–5897.

[284] D. ROCCHESSO AND M. MANNONE, *Embryo of a quantum vocal theory of sound*, vol. 15, Udine, 2018.

[285] D. ROCCHESSO AND M. MANNONE, *A quantum vocal theory of sound*, Quantum Information Processing, 19 (2020), pp. 1–28.

[286] Y. ROMANO, M. ELAD, AND P. MILANFAR, *The little engine that could: Regularization by denoising (red)*, SIAM Journal on Imaging Sciences, 10 (2017), pp. 1804–1844.

[287] A. ROND, R. GIRYES, AND M. ELAD, *Poisson inverse problems by the plug-and-play scheme*, Journal of Visual Communication and Image Representation, 41 (2016), pp. 96–108.

[288] S. RUDER, *An overview of gradient descent optimization algorithms*, arXiv preprint arXiv:1609.04747, (2016).

[289] L. I. RUDIN AND S. OSHER, *Total variation based image restoration with free local constraints*, in Proceedings of 1st International Conference on Image Processing, vol. 1, IEEE, 1994, pp. 31–35.

[290] L. I. RUDIN, S. OSHER, AND E. FATEMI, *Nonlinear total variation based noise removal algorithms*, Physica D: Nonlinear Phenomena, 60 (1992), pp. 259–268.

[291] A. RUGET, S. MCLAUGHLIN, R. K. HENDERSON, I. GYONGY, A. HALIMI, AND J. LEACH, *Robust and guided super-resolution for single-photon depth imaging via a deep network*, in 2021 29th European Signal Processing Conference (EUSIPCO), 2021, pp. 716–720.

[292] A. RUGET, S. MCLAUGHLIN, R. K. HENDERSON, I. GYONGY, A. HALIMI, AND J. LEACH, *Robust super-resolution depth imaging via a multi-feature fusion deep network*, Optics Express, 29 (2021), pp. 11917–11937.

[293] E. RYU, J. LIU, S. WANG, X. CHEN, Z. WANG, AND W. YIN, *Plug-and-play methods provably converge with properly trained denoisers*, in Proceedings of

the 36th International Conference on Machine Learning, K. Chaudhuri and R. Salakhutdinov, eds., vol. 97 of Proceedings of Machine Learning Research, PMLR, 09–15 Jun 2019, pp. 5546–5557.

[294] M. U. SADIQ, J. P. SIMMONS, AND C. A. BOUMAN, *Model based image reconstruction with physics based priors*, in 2016 IEEE International Conference on Image Processing (ICIP), 2016, pp. 3176–3179.

[295] S. K. SAHOO AND A. MAKUR, *Signal recovery from random measurements via extended orthogonal matching pursuit*, IEEE Transactions on Signal Processing, 63 (2015), pp. 2572–2581.

[296] J. SALMON, Z. HARMANY, C.-A. DELEDALLE, AND R. WILLETT, *Poisson noise reduction with non-local pca*, Journal of mathematical imaging and vision, 48 (2014), pp. 279–294.

[297] A. SANDRYHAILA AND J. MOURA, *Discrete signal processing on graphs*, IEEE Transactions on Signal Processing, 61 (2013), pp. 1644–1656.

[298] C. A. N. SANTOS, D. L. N. MARTINS, AND N. D. A. MASCARENHAS, *Ultrasound image despeckling using stochastic distance-based bm3d*, IEEE Transactions on Image Processing, 26 (2017), pp. 2632–2643.

[299] P. SARDER AND A. NEHORAI, *Deconvolution methods for 3-d fluorescence microscopy images*, IEEE Signal Processing Magazine, 23 (2006), pp. 32–45.

[300] M. SCETBON, M. ELAD, AND P. MILANFAR, *Deep k-svd denoising*, IEEE Transactions on Image Processing, 30 (2021), pp. 5944–5955.

[301] U. SCHMIDT AND S. ROTH, *Shrinkage fields for effective image restoration*, in IEEE Conference on Computer Vision and Pattern Recognition (CVPR), June 2014, pp. 2774–2781.

[302] E. SCHRÖDINGER, *An undulatory theory of the mechanics of atoms and molecules*, Physical Review, 28 (1926), p. 1049.

[303] C. J. SCHULER, H. CHRISTOPHER BURGER, S. HARMELING, AND B. SCHOLKOPF, *A machine learning approach for non-blind image deconvolution*, in Proceedings of the IEEE Conference on Computer Vision and Pattern Recognition (CVPR), June 2013.

[304] C. J. SCHULER, M. HIRSCH, S. HARMELING, AND B. SCHÖLKOPF, *Learning to deblur*, IEEE Transactions on Pattern Analysis and Machine Intelligence, 38 (2016), pp. 1439–1451.

[305] S. SETZER, G. STEIDL, AND T. TEUBER, *Deblurring poissonian images by split bregman techniques*, Journal of Visual Communication and Image Representation, 21 (2010), pp. 193–199.

[306] R. SHANKAR, *Principles of Quantum Mechanics*, Springer US, 2012.

[307] S. SHEKKIZHAR AND A. ORTEGA, *Efficient graph construction for image representation*, in 2020 IEEE International Conference on Image Processing (ICIP), 2020, pp. 1956–1960.

[308] N. SHLEZINGER, J. WHANG, Y. C. ELDAR, AND A. G. DIMAKIS, *Model-based deep learning*, arXiv preprint arXiv:2012.08405, (2020).

[309] P. W. SHOR, *Algorithms for quantum computation: Discrete logarithms and factoring*, in Proceedings 35th Annual Symposium on Foundations of Computer Science, Ieee, 1994, pp. 124–134.

[310] D. SHUMAN, S. NARANG, P. FROSSARD, A. ORTEGA, AND P. VANDERGHEYNST, *The emerging field of signal processing on graphs: Extending high-dimensional data analysis to networks and other irregular domains*, IEEE Signal Processing Magazine, 30 (2013), pp. 83–98.

[311] D. SILVER, J. SCHRITTWIESER, K. SIMONYAN, I. ANTONOGLOU, A. HUANG, A. GUEZ, T. HUBERT, L. BAKER, M. LAI, A. BOLTON, Y. CHEN, T. LILLICRAP, F. HUI, L. SIFRE, G. VAN DEN DRIESSCHE, T. GRAEPEL, AND D. HASSABIS, *Mastering the game of go without human knowledge*, Nature, 550 (2017), pp. 354–359.

[312] R. SMITH, A. BASARAB, B. GEORGEOT, AND D. KOUAMÉ, *Adaptive transform via quantum signal processing: application to signal and image denoising*, in 2018 25th IEEE International Conference on Image Processing (ICIP), 2018, pp. 1523–1527.

[313] O. SOLOMON, R. COHEN, Y. ZHANG, Y. YANG, Q. HE, J. LUO, R. J. VAN SLOUN, AND Y. C. ELDAR, *Deep unfolded robust PCA with application to clutter sup-*

pression in ultrasound, IEEE Transactions on Medical Imaging, 39 (2020), pp. 1051–1063.

[314] H. SOMMERHOFF, A. KOLB, AND M. MOELLER, *Energy dissipation with plug-and-play priors*, in NeurIPS Workshop on Solving Inverse Problems with Deep Networks, 2019.

[315] H. SON AND S. LEE, *Fast non-blind deconvolution via regularized residual networks with long/short skip-connections*, in 2017 IEEE International Conference on Computational Photography (ICCP), 2017, pp. 1–10.

[316] X. SONG, S. WANG, A. A ABD EL-LATIF, AND X. NIU, *Dynamic watermarking scheme for quantum images based on hadamard transform*, Multimedia Systems, 20 (2014), pp. 379–388.

[317] X.-H. SONG, S. WANG, S. LIU, A. EL-LATIF, A. AHMED, AND X.-M. NIU, *A dynamic watermarking scheme for quantum images using quantum wavelet transform*, Quantum Information Processing, 12 (2013), pp. 3689–3706.

[318] E. SOUBIES, L. BLANC-FÉRAUD, AND G. AUBERT, *A continuous exact \ell_0 penalty (CEL0) for least squares regularized problem*, SIAM Journal on Imaging Sciences, 8 (2015), pp. 1607–1639.

[319] S. SREEHARI, S. V. VENKATAKRISHNAN, B. WOHLBERG, G. T. BUZZARD, L. F. DRUMMY, J. P. SIMMONS, AND C. A. BOUMAN, *Plug-and-play priors for bright field electron tomography and sparse interpolation*, IEEE Transactions on Computational Imaging, 2 (2016), pp. 408–423.

[320] J.-L. STARCK, E. CANDÉS, AND D. DONOHO, *The curvelet transform for image denoising*, IEEE Transactions on Image Processing, 11 (2002), pp. 670–684.

[321] J.-L. STARCK, D. L. DONOHO, AND E. J. CANDÉS, *Astronomical image representation by the curvelet transform*, Astronomy & Astrophysics, 398 (2003), pp. 785–800.

[322] J.-L. STARCK AND F. MURTAGH, *Astronomical image and data analysis*, Berlin, Germany: Springer-Verlag, 2007.

[323] J.-L. STARCK, E. PANTIN, AND F. MURTAGH, *Deconvolution in astronomy: A review*, Publications of the Astronomical Society of the Pacific, 114 (2002), pp. 1051–1069.

[324] A. STEANE, *Quantum computing*, Reports on Progress in Physics, 61 (1998), p. 117.

[325] G. STEIDL AND T. TEUBER, *Removing multiplicative noise by douglas-rachford splitting methods*, Journal of Mathematical Imaging and Vision, 36 (2010), pp. 168–184.

[326] R. J. STERITI AND M. A. FIDDY, *Blind beconvolution of images by use of neural networks*, Optics letters, 19 (1994), pp. 575–577.

[327] J. SU, X. GUO, C. LIU, AND L. LI, *A new trend of quantum image representations*, IEEE Access, 8 (2020), pp. 214520–214537.

[328] J. SUN, J. SUN, Z. XU, AND H.-Y. SHUM, *Gradient profile prior and its applications in image super-resolution and enhancement*, IEEE Transactions on Image Processing, 20 (2011), pp. 1529–1542.

[329] Y. SUN, J. LIU, AND U. KAMILOV, *Block coordinate regularization by denoising*, in Advances in Neural Information Processing Systems, H. Wallach, H. Larochelle, A. Beygelzimer, F. d'Alché-Buc, E. Fox, and R. Garnett, eds., vol. 32, Curran Associates, Inc., 2019.

[330] Y. SUN, J. LIU, Y. SUN, B. WOHLBERG, AND U. KAMILOV, *Async-RED: A provably convergent asynchronous block parallel stochastic method using deep denoising priors*, in International Conference on Learning Representations, 2021.

[331] Y. TAI, J. YANG, X. LIU, AND C. XU, *Memnet: A persistent memory network for image restoration*, in IEEE Conference on Computer Vision and Pattern Recognition (CVPR), 2017, pp. 4549–4557.

[332] M. TAO, J. YANG, AND B. HE, *Alternating direction algorithms for total variation deconvolution in image reconstruction*, TR0918, Department of Mathematics, Nanjing University, (2009).

[333] T. TASDIZEN, *Principal neighborhood dictionaries for nonlocal means image denoising*, IEEE Transactions on Image Processing, 18 (2009), pp. 2649–2660.

[334] T. TAXT AND J. STRAND, *Two-dimensional noise-robust blind deconvolution of ultrasound images*, IEEE Transactions on Ultrasonics, Ferroelectrics, and Frequency Control, 48 (2001), pp. 861–866.

[335] A. M. TEODORO, J. M. BIOUCAS-DIAS, AND M. A. T. FIGUEIREDO, *Image restoration and reconstruction using variable splitting and class-adapted image priors*, in 2016 IEEE International Conference on Image Processing (ICIP), 2016, pp. 3518–3522.

[336] A. M. TEODORO, J. M. BIOUCAS-DIAS, AND M. A. T. FIGUEIREDO, *Image restoration with locally selected class-adapted models*, in 2016 IEEE 26th International Workshop on Machine Learning for Signal Processing (MLSP), 2016, pp. 1–6.

[337] A. M. TEODORO, J. M. BIOUCAS-DIAS, AND M. A. T. FIGUEIREDO, *Scene-adapted plug-and-play algorithm with convergence guarantees*, in 2017 IEEE 27th International Workshop on Machine Learning for Signal Processing (MLSP), 2017, pp. 1–6.

[338] A. M. TEODORO, J. M. BIOUCAS-DIAS, AND M. A. T. FIGUEIREDO, *A convergent image fusion algorithm using scene-adapted gaussian-mixture-based denoising*, IEEE Transactions on Image Processing, 28 (2019), pp. 451–463.

[339] R. TIMOFTE, V. DE SMET, AND L. VAN GOOL, *A+: adjusted anchored neighborhood regression for fast super-resolution*, in Asian Conference on Computer Vision, Springer, 2014, pp. 111–126.

[340] C. TOMASI AND R. MANDUCHI, *Bilateral filtering for gray and color images*, in Sixth International Conference on Computer Vision (IEEE Cat. No.98CH36271), 1998, pp. 839–846.

[341] S. TOURBIER, X. BRESSON, P. HAGMANN, J.-P. THIRAN, R. MEULI, AND M. B. CUADRA, *An efficient total variation algorithm for super-resolution in fetal brain MRI with adaptive regularization*, NeuroImage, 118 (2015), pp. 584–597.

[342] N. TREMBLAY AND P. BORGNAT, *Subgraph-based filterbanks for graph signals*, IEEE Transactions on Signal Processing, 64 (2016), pp. 3827–3840.

[343] N. TREMBLAY, P. GONÇALVES, AND P. BORGNAT, *Chapter 11 - design of graph filters and filterbanks*, in Cooperative and Graph Signal Processing, Academic Press, 2018, pp. 299–324.

[344] N. TREMBLAY, G. PUY, P. BORGNAT, R. GRIBONVAL, AND P. VANDERGHEYNST, *Accelerated spectral clustering using graph filtering of random signals*, in 2016

IEEE International Conference on Acoustics, Speech and Signal Processing (ICASSP), 2016, pp. 4094–4098.

[345] J. A. TROPP AND A. C. GILBERT, *Signal recovery from random measurements via orthogonal matching pursuit*, IEEE Transactions on Information Theory, 53 (2007), pp. 4655–4666.

[346] D. ULYANOV, A. VEDALDI, AND V. LEMPITSKY, *Deep image prior*, in Proceedings of the IEEE Conference on Computer Vision and Pattern Recognition (CVPR), 2018, pp. 9446–9454.

[347] V. S. UNNI, S. GHOSH, AND K. N. CHAUDHURY, *Linearized admm and fast nonlocal denoising for efficient plug-and-play restoration*, in 2018 IEEE Global Conference on Signal and Information Processing (GlobalSIP), 2018, pp. 11–15.

[348] D. VALSESIA, G. FRACASTORO, AND E. MAGLI, *Deep graph-convolutional image denoising*, IEEE Transactions on Image Processing, 29 (2020), pp. 8226–8237.

[349] J. M. VALVERDE, V. IMANI, A. ABDOLLAHZADEH, R. DE FEO, M. PRAKASH, R. CISZEK, AND J. TOHKA, *Transfer learning in magnetic resonance brain imaging: A systematic review*, Journal of Imaging, 7 (2021).

[350] D. VAN DE VILLE AND M. KOCHER, *Sure-based non-local means*, IEEE Signal Processing Letters, 16 (2009), pp. 973–976.

[351] R. VAN SLOUN, R. COHEN, AND Y. ELDAR, *Deep learning in ultrasound imaging*, Proceedings of the IEEE, 108 (2020), pp. 11–29.

[352] S. VASU, V. R. MALIGIREDDY, AND A. RAJAGOPALAN, *Non-blind deblurring: Handling kernel uncertainty with cnns*, in Proceedings of the IEEE Conference on Computer Vision and Pattern Recognition (CVPR), 2018, pp. 3272–3281.

[353] S. E. VENEGAS-ANDRACA AND J. L. BALL, *Processing images in entangled quantum systems*, Quantum Information Processing, 9 (2010), pp. 1–11.

[354] S. V. VENKATAKRISHNAN, C. A. BOUMAN, AND B. WOHLBERG, *Plug-and-play priors for model based reconstruction*, in 2013 IEEE Global Conference on Signal and Information Processing, 2013, pp. 945–948.

[355] R. VIGNESH, B. OH, AND C.-C. KUO, *Fast non-local means (nlm) computation with probabilistic early termination*, IEEE Signal Processing Letters, 17 (2010), pp. 277–280.

[356] P. VINCENT, H. LAROCHELLE, I. LAJOIE, Y. BENGIO, P.-A. MANZAGOL, AND L. BOTTOU, *Stacked denoising autoencoders: Learning useful representations in a deep network with a local denoising criterion*, Journal of Machine Learning Research, 11 (2010), p. 3371–3408.

[357] O. VINYALS, I. BABUSCHKIN, W. M. CZARNECKI, M. MATHIEU, A. DUDZIK, J. CHUNG, D. H. CHOI, R. POWELL, T. EWALDS, P. GEORGIEV, J. OH, D. HORGAN, M. KROISS, I. DANIHELKA, A. HUANG, L. SIFRE, T. CAI, J. P. AGAPIOU, M. JADERBERG, A. S. VEZHNEVETS, R. LEBLOND, T. POHLEN, V. DALIBARD, D. BUDDEN, Y. SULSKY, J. MOLLOY, T. L. PAINE, C. GULCEHRE, Z. WANG, T. PFAFF, Y. WU, R. RING, D. YOGATAMA, D. WÜNSCH, K. MCKINNEY, O. SMITH, T. SCHAUL, T. LILLICRAP, K. KAVUKCUOGLU, D. HASSABIS, C. APPS, AND D. SILVER, *Grandmaster level in starcraft ii using multi-agent reinforcement learning*, Nature, 575 (2019), pp. 350–354.

[358] J. VON NEUMANN, *Mathematical Foundations of Quantum Mechanics*, Princeton University Press, 1955.

[359] J. VON NEUMANN, *Mathematische Begründung der Quantenmechanik: in Collected Works, Vol. I*, MacMillan, New York, 1961.

[360] K. K. WAN, *Quantum Mechanics: A Fundamental Approach*, Jenny Stanford Publishing Pte. Ltd., 2019.

[361] J. WANG, N. JIANG, AND L. WANG, *Quantum image translation*, Quantum Information Processing, 14 (2015), pp. 1589–1604.

[362] R. WANG AND D. TAO, *Training very deep cnns for general non-blind deconvolution*, IEEE Transactions on Image Processing, 27 (2018), pp. 2897–2910.

[363] S. WANG, X. SONG, AND X. NIU, *A novel encryption algorithm for quantum images based on quantum wavelet transform and diffusion*, in Intelligent Data analysis and its Applications, Volume II, Springer, 2014, pp. 243–250.

[364] X. WANG AND S. H. CHAN, *Parameter-free plug-and-play admm for image restoration*, in 2017 IEEE International Conference on Acoustics, Speech and Signal Processing (ICASSP), 2017, pp. 1323–1327.

[365] Z. WANG, A. C. BOVIK, H. R. SHEIKH, AND E. P. SIMONCELLI, *Image quality assessment: from error visibility to structural similarity*, IEEE Transactions on Image Processing, 13 (2004), pp. 600–612.

[366] Z. WANG, A. C. BOVIK, H. R. SHEIKH, AND E. P. SIMONCELLI, *Image quality assessment: from error visibility to structural similarity*, IEEE Transactions on Image Processing, 13 (2004), pp. 600–612.

[367] Z. WANG, X. CUN, J. BAO, W. ZHOU, J. LIU, AND H. LI, *Uformer: A general u-shaped transformer for image restoration*, in IEEE Conference on Computer Vision and Pattern Recognition (CVPR), June 2022, pp. 17683–17693.

[368] Z. WANG, D. LIU, J. YANG, W. HAN, AND T. HUANG, *Deep networks for image super-resolution with sparse prior*, in Proceedings of the IEEE international conference on computer vision, 2015, pp. 370–378.

[369] J. WEICKERT, *Theoretical foundations of anisotropic diffusion in image processing*, in Theoretical Foundations of Computer Vision, Vienna, 1996, Springer Vienna, pp. 221–236.

[370] J. WEICKERT ET AL., *Anisotropic Diffusion in Image Processing*, vol. 1, Teubner Stuttgart, 1998.

[371] P. WEISS, L. BLANC-FÉRAUD, AND G. AUBERT, *Efficient schemes for total variation minimization under constraints in image processing*, SIAM journal on Scientific Computing, 31 (2009), pp. 2047–2080.

[372] N. WIENER, N. WIENER, C. MATHEMATICIAN, N. WIENER, N. WIENER, AND C. MATHÉMATICIEN, *Extrapolation, Interpolation, and Smoothing of Stationary Time Series: with Engineering Applications*, vol. 113, MIT press Cambridge, MA, 1949.

[373] WIKIPEDIA, *Double Slits Experiment*.

[374] R. M. WILLETT AND R. D. NOWAK, *Fast multiresolution photon-limited image reconstruction*, in 2004 2nd IEEE International Symposium on Biomedical Imaging: Nano to Macro (IEEE Cat No. 04EX821), 2004, pp. 1192–1195 Vol. 2.

[375] S. J. WRIGHT, R. D. NOWAK, AND M. A. T. FIGUEIREDO, *Sparse reconstruction by separable approximation*, IEEE Transactions on Signal Processing, 57 (2009), pp. 2479–2493.

[376] Z. WU, Y. SUN, J. LIU, AND U. KAMILOV, *Online regularization by denoising with applications to phase retrieval*, in Proceedings of the IEEE/CVF International Conference on Computer Vision (ICCV) Workshops, Oct 2019.

[377] J. XI AND J. F. CHICHARO, *A new algorithm for improving the accuracy of periodic signal analysis*, IEEE Transactions on Instrumentation and Measurement, 45 (1996), pp. 827–831.

[378] L. XIAO, F. HEIDE, W. HEIDRICH, B. SCHÖLKOPF, AND M. HIRSCH, *Discriminative transfer learning for general image restoration*, IEEE Transactions on Image Processing, 27 (2018), pp. 4091–4104.

[379] L. XU, J. REN, C. LIU, AND J. JIA, *Deep convolutional neural network for image deconvolution*, in Proceedings of Advances in Neural Information Processing Systems, vol. 27, Curran Associates, Inc., 2014, pp. 1790–1798.

[380] X. XU, Y. SUN, J. LIU, B. WOHLBERG, AND U. S. KAMILOV, *Provable convergence of plug-and-play priors with mmse denoisers*, IEEE Signal Processing Letters, 27 (2020), pp. 1280–1284.

[381] B. YAN, C. MA, B. BARE, W. TAN, AND S. C. HOI, *Disparity-aware domain adaptation in stereo image restoration*, in Proceedings of the IEEE/CVF Conference on Computer Vision and Pattern Recognition, 2020, pp. 13179–13187.

[382] F. YAN, A. M. ILIYASU, AND S. E. VENEGAS-ANDRACA, *A survey of quantum image representations*, Quantum Information Processing, 15 (2016), pp. 1–35.

[383] D. YANG AND J. SUN, *BM3D-Net: A convolutional neural network for transform-domain collaborative filtering*, IEEE Signal Processing Letters, 25 (2018), pp. 55–59.

[384] J. YANG, Y. ZHANG, AND W. YIN, *An efficient tvl1 algorithm for deblurring multichannel images corrupted by impulsive noise*, SIAM Journal on Scientific Computing, 31 (2009), pp. 2842–2865.

[385] J. YANG, Y. ZHANG, AND W. YIN, *A fast alternating direction method for tvl1-l2 signal reconstruction from partial fourier data*, IEEE Journal of Selected Topics in Signal Processing, 4 (2010), pp. 288–297.

[386] Q. YANG, P. YAN, Y. ZHANG, H. YU, Y. SHI, X. MOU, M. K. KALRA, Y. ZHANG, L. SUN, AND G. WANG, *Low-dose ct image denoising using a generative adversarial network with wasserstein distance and perceptual loss*, IEEE Transactions on Medical Imaging, 37 (2018), pp. 1348–1357.

[387] Y. YANG, J. SUN, H. LI, AND Z. XU, *Admm-csnet: A deep learning approach for image compressive sensing*, IEEE Transactions on Pattern Analysis and Machine Intelligence, 42 (2020), pp. 521–538.

[388] X.-W. YAO, H. WANG, Z. LIAO, M.-C. CHEN, J. PAN, J. LI, K. ZHANG, X. LIN, Z. WANG, Z. LUO, W. ZHENG, J. LI, M. ZHAO, X. PENG, AND D. SUTER, *Quantum image processing and its application to edge detection: Theory and experiment*, Physical Review X, 7 (2017), p. 031041.

[389] A. YOUSSRY, A. EL-RAFEI, AND S. ELRAMLY, *A quantum mechanics-based framework for image processing and its application to image segmentation*, Quantum Information Processing, 14 (2015), pp. 3613–3638.

[390] A. YOUSSRY, A. EL-RAFEI, AND S. ELRAMLY, *A quantum mechanics-based algorithm for vessel segmentation in retinal images*, Quantum Information Processing, 15 (2016), pp. 2303–2323.

[391] A. YOUSSRY, A. EL-RAFEI, AND R.-G. ZHOU, *A continuous-variable quantum-inspired algorithm for classical image segmentation*, Quantum Machine Intelligence, 1 (2019), pp. 97–111.

[392] C. YU, C. ZHANG, AND L. XIE, *A blind deconvolution approach to ultrasound imaging*, IEEE Transactions on Ultrasonics, Ferroelectrics, and Frequency Control, 59 (2012), pp. 271–280.

[393] Y. YU AND S. ACTON, *Speckle reducing anisotropic diffusion*, IEEE Transactions on Image Processing, 11 (2002), pp. 1260–1270.

[394] Y. YU AND S. T. ACTON, *Speckle reducing anisotropic diffusion*, IEEE Transactions on Image Processing, 11 (2002), pp. 1260–1270.

[395] S. YUAN, X. MAO, L. CHEN, AND Y. XUE, *Quantum digital image processing algorithms based on quantum measurement*, Optik, 124 (2013), pp. 6386–6390.

[396] Z. ZHA, B. WEN, X. YUAN, J. ZHOU, J. ZHOU, AND C. ZHU, *Triply complementary priors for image restoration*, IEEE Transactions on Image Processing, 30 (2021), pp. 5819–5834.

[397] Z. ZHA, B. WEN, X. YUAN, J. ZHOU, AND C. ZHU, *Image restoration via reconciliation of group sparsity and low-rank models*, IEEE Transactions on Image Processing, 30 (2021), pp. 5223–5238.

[398] Z. ZHA, B. WEN, X. YUAN, J. ZHOU, C. ZHU, AND A. KOT, *Low-rankness guided group sparse representation for image restoration*, IEEE Transactions on Neural Networks and Learning Systems, (2022), pp. 1–15.

[399] Z. ZHA, X. YUAN, B. WEN, J. ZHANG, AND C. ZHU, *Nonconvex structural sparsity residual constraint for image restoration*, IEEE Transactions on Cybernetics, (2021), pp. 1–14.

[400] Z. ZHA, X. YUAN, B. WEN, J. ZHOU, J. ZHANG, AND C. ZHU, *From rank estimation to rank approximation: Rank residual constraint for image restoration*, IEEE Transactions on Image Processing, 29 (2020), pp. 3254–3269.

[401] Z. ZHA, X. YUAN, J. ZHOU, C. ZHU, AND B. WEN, *Image restoration via simultaneous nonlocal self-similarity priors*, IEEE Transactions on Image Processing, 29 (2020), pp. 8561–8576.

[402] J. ZHANG, J. PAN, W.-S. LAI, R. W. H. LAU, AND M.-H. YANG, *Learning fully convolutional networks for iterative non-blind deconvolution*, in Proceedings of the IEEE Conference on Computer Vision and Pattern Recognition (CVPR), 2017, pp. 3817–3825.

[403] K. ZHANG, L. GOOL, AND R. TIMOFTE, *Deep unfolding network for image super-resolution*, in IEEE Conference on Computer Vision and Pattern Recognition (CVPR), 2020, pp. 3217–3226.

[404] K. ZHANG, Y. LI, W. ZUO, L. ZHANG, L. VAN GOOL, AND R. TIMOFTE, *Plug-and-play image restoration with deep denoiser prior*, IEEE Transactions on Pattern Analysis and Machine Intelligence, (2021), pp. 1–1.

[405] K. ZHANG, W. ZUO, Y. CHEN, D. MENG, AND L. ZHANG, *Beyond a gaussian denoiser: Residual learning of deep cnn for image denoising*, IEEE Transactions on Image Processing, 26 (2017), pp. 3142–3155.

[406] K. ZHANG, W. ZUO, S. GU, AND L. ZHANG, *Learning deep CNN denoiser prior for image restoration*, in Proceedings of the IEEE conference on computer vision and pattern recognition (CVPR), 2017, pp. 3929–3938.

[407] K. ZHANG, W. ZUO, AND L. ZHANG, *FFDNet: Toward a fast and flexible solution for cnn-based image denoising*, IEEE Transactions on Image Processing, 27 (2018), pp. 4608–4622.

[408] M. ZHANG AND B. K. GUNTURK, *Multiresolution bilateral filtering for image denoising*, IEEE Transactions on Image Processing, 17 (2008), pp. 2324–2333.

[409] W.-W. ZHANG, F. GAO, B. LIU, Q.-Y. WEN, AND H. CHEN, *A watermark strategy for quantum images based on quantum fourier transform*, Quantum Information Processing, 12 (2013), pp. 793–803.

[410] Y. ZHANG, K. LI, K. LI, L. WANG, B. ZHONG, AND Y. FU, *Image super-resolution using very deep residual channel attention networks*, in Proceedings of the European Conference on Computer Vision (ECCV), September 2018, pp. 294–310.

[411] Y. ZHANG, X. LI, G. ZHAO, B. LU, AND C. C. CAVALCANTE, *Signal reconstruction of compressed sensing based on alternating direction method of multipliers*, Circuits, Systems, and Signal Processing, 39 (2020), pp. 307–323.

[412] Y. ZHANG, K. LU, Y. GAO, AND M. WANG, *NEQR: A novel enhanced quantum representation of digital images*, Quantum information processing, 12 (2013), pp. 2833–2860.

[413] Y. ZHANG, K. LU, K. XU, Y. GAO, AND R. WILSON, *Local feature point extraction for quantum images*, Quantum Information Processing, 14 (2015), pp. 1573–1588.

[414] Y. ZHANG, Y. TIAN, Y. KONG, B. ZHONG, AND Y. FU, *Residual dense network for image restoration*, IEEE Transactions on Pattern Analysis and Machine Intelligence, 43 (2021), pp. 2480–2495.

[415] Y. ZHANG, Y. ZHU, E. NICHOLS, Q. WANG, S. ZHANG, C. SMITH, AND S. HOWARD, *A poisson-gaussian denoising dataset with real fluorescence microscopy images*, in Proceedings of the IEEE/CVF Conference on Computer Vision and Pattern Recognition (CVPR), 2019, pp. 11710–11718.

[416] N. ZHAO, Q. WEI, A. BASARAB, N. DOBIGEON, D. KOUAMÉ, AND J. Y. TOURNERET, *Fast single image super-resolution using a new analytical solution for $\ell_2 - \ell_2$ problems*, IEEE Transactions on Image Processing, 25 (2016), pp. 3683–3697.

[417] R.-G. ZHOU, Q. WU, M.-Q. ZHANG, AND C.-Y. SHEN, *Quantum image encryption and decryption algorithms based on quantum image geometric transformations*, International Journal of Theoretical Physics, 52 (2013), pp. 1802–1817.

[418] D. ZORAN AND Y. WEISS, *From learning models of natural image patches to whole image restoration*, in 2011 International Conference on Computer Vision, 2011, pp. 479–486.

[419] C. ZUO, L. JOVANOV, B. GOOSSENS, H. LUONG, W. PHILIPS, Y. LIU, AND M. ZHANG, *Image denoising using quadtree-based nonlocal means with locally adaptive principal component analysis*, IEEE Signal Processing Letters, 23 (2016), pp. 434–438.

ওঁ অসতো মা সদগময় |
তমসো মা জ্যোতির্গময় |
মৃত্যর্মা অমৃতমঃ গময় |
ওঁ শান্তি শান্তি শান্তি ||

- বৃহদারণ্যক উপনিষদ (যাজ্ঞবল্ক্য)

In Latin script:

Om asato maa sad-gamaya |
Tamaso maa jyotir-gamaya |
Mrtyor-maa amrtam gamaya |
Om shanti shanti shanti ||

- Brihadaranyaka Upanishads (by Yajnavalkya)

Meaning:

"Lead us from ignorance to knowledge, from darkness to light and from death to immortality."

Titre: Nouvelles Approches de Restauration d'Images Inspirées des Concepts de la Mécanique Quantique

Mots clés: Mécanique quantique, Interaction quantique à plusieurs corps, Transformation adaptative, Équation de Schrödinger, Apprentissage profond, Débruitage quantique, Traitement d'image quantique, Imagerie médicale, Restauration d'images, Imagerie computationnelle.

Résumé:
La décomposition d'images numériques en d'autres bases ou dictionnaires que les domaines temporel ou spatial est une approche très courante et efficace dans le traitement et l'analyse d'images. Une telle décomposition est couramment obtenue à l'aide de transformations fixes (par exemple, Fourier ou ondelettes) ou de dictionnaires appris à partir de bases de données d'exemple ou à partir du signal ou de l'image eux-mêmes. Ces dernières années, avec la croissance de la puissance de calcul, les stratégies exploitant la redondance des patchs extraits d'une ou de plusieurs images pour faciliter leur décomposition parcimonieuse sont devenues très populaire, notamment grâce à leur efficacité à restaurer des images. Un des objectifs de cette thèse est de savoir comment concevoir une telle transformation adaptative à l'aide de principes de la mécanique quantique.
Cette thèse explore de nouvelles approches de construction de telles bases dépendantes de l'image inspirées de la mécanique quantique. Tout d'abord, nous construisons une base dépendante de l'image en utilisant les solutions d'onde de l'équation de Schrödinger. En particulier, en considérant l'image comme un potentiel dans l'équation de Schrödinger discrétisée, nous obtenons les solutions d'onde qui constitue une base et qui joue le rôle de transformée. L'efficacité de la décomposition proposée est illustrée par des résultats de débruitage dans le cas des bruits Gaussiens, de Poisson et de speckle et par comparaison aux algorithmes de l'état de l'art. Cette décomposition adaptative est ensuite généralisée en s'inspirant de la théorie quantique à plusieurs corps. Sur la base de l'analyse par patchs, les mesures de similarité dans un voisinage d'image local sont formalisées par un terme apparenté à l'interaction en mécanique quantique qui peut efficacement préserver les structures locales des images. La nature polyvalente de cette base adaptative étend la portée de son application à des scénarios de bruit indépendants ou dépendants de l'image sans aucun ajustement. Nous effectuons une comparaison rigoureuse avec les méthodes existantes pour démontrer la capacité de débruitage de l'algorithme proposé, quelles que soient les caractéristiques de l'image, les statistiques de bruit et l'intensité. Nous montrons la capacité de nos approches à traiter des données médicales réelles telles que le débruitage d'images de tomodensitométrie dentaire clinique et les applications de despeckling d'images d'échographie médicale. Nous étendons encore notre travail aux tâches de déconvolution d'image et de super-résolution en exploitant nos algorithmes de débruitage adaptatifs quantiques proposés. En particulier, suite à des développements récents, nous imposons ces débruiteurs externes comme fonction préalable au sein des approches de type Plug-and-Play et Régularisation par Débruitage.
Enfin, nous présentons une architecture de réseau neuronal profond dépliant notre proposition d'algorithme de débruitage adaptatif, reposant sur la théorie de la physique quantique à plusieurs corps. Les ingrédients clés de la méthode proposée sont d'une part, sa capacité à gérer des structures d'image non locales à travers le terme d'interaction patch et l'opérateur Hamiltonien quantique, et, d'autre part, sa flexibilité pour adapter les hyperparamètres aux caractéristiques de chaque patch. De plus, il est démontré qu'avec de très légères modifications, ce réseau peut être amélioré pour résoudre des tâches de restauration d'image plus difficiles telles que le défloutage d'image, la super-résolution et l'inpainting. Malgré une architecture compacte et interprétable (d'un point de vue physique), le réseau d'apprentissage profond proposé améliore plusieurs algorithmes de référence récents de la littérature, conçus spécifiquement pour chaque tâche. Enfin, nous abordons le problème de l'amélioration des image échocardiographiques clinique pour démontrer le potentiel de notre réseau profond dans des applications médicales réelles.

Title: Novel Prospects of Image Restoration Inspired by Concepts of Quantum Mechanics

Keywords: Quantum Mechanics, Quantum many-body interaction, Adaptive transformation, Schrödinger equation, Deep learning, Deep unfolding, Quantum denoising, Quantum image processing, Medical imaging, Image restoration, Computational imaging.

Abstract: Decomposition of digital images into other basis or dictionaries than time or space domains is a very common and effective approach in image processing and analysis. Such a decomposition is commonly obtained using fixed transformations (*e.g.*, Fourier or wavelet) or dictionaries learned from example databases or from the signal or image itself. In recent years, with the growth of computing power, data-driven strategies exploiting the redundancy within patches extracted from one or several images to increase sparsity have become more prominent. They have demonstrated very promising image restoration results. The question to pursue in this thesis is how to design such an adaptive transformation based on principles of quantum mechanics.
In this thesis, we explore new possibilities of constructing such image-dependent bases inspired by quantum mechanics. First, we construct an image-dependent basis using the wave solutions of the Schrödinger equation, in particular, by considering the image as a potential in the discretized Schrödinger equation. The efficiency of the proposed decomposition is illustrated through denoising results in the case of Gaussian, Poisson, and speckle noises and compared to the state-of-the-art algorithms. We further generalize our proposed adaptive basis by exploiting the data-driven strategy inspired by quantum many-body theory. Based on patch analysis, the similarity measures in a local image neighborhood are formalized through a term akin to interaction in quantum mechanics that can efficiently preserve the local structures of real images. The versatile nature of this adaptive basis extends the scope of its application to image-independent or image-dependent noise scenarios without any adjustment. We carry out a rigorous comparison with contemporary methods to demonstrate the denoising capability of the proposed algorithm regardless of the image characteristics, noise statistics and intensity. We show the ability of our approaches to deal with real-medical data such as clinical dental computed tomography image denoising and medical ultrasound image despeckling applications. We further extend our work to image deconvolution and super-resolution tasks exploiting our proposed quantum adaptive denoisers. In particular, following recent developments, we impose these external denoisers as a prior functions within the Plug-and-Play and Regularization by Denoising approaches.
Lastly, we present a deep neural network architecture unfolding our proposed baseline adaptive denoising algorithm, relying on the theory of quantum many-body physics. The key ingredients of the proposed method are on one hand, its ability to handle non-local image structures through the patch-interaction term and the quantum-based Hamiltonian operator, and, on the other hand, its flexibility to adapt the hyperparameters patch wisely, due to the training process. Furthermore, it is shown that with very slight modifications, this network can be enhanced to solve more challenging image restoration tasks such as image deblurring, super-resolution and inpainting. Despite a compact and interpretable (from a physical perspective) architecture, the proposed deep learning network outperforms several recent benchmark algorithms from the literature, designed specifically for each task. Finally, we address the problem of clinical cardiac ultrasound image enhancement to demonstrate the potential of our proposed deep unfolded network in real-world medical applications.

Université Toulouse 3 Paul Sabatier
118 Rte de Narbonne, 31062 Toulouse, France

UNIVERSITÉ TOULOUSE III PAUL SABATIER
Université de Toulouse